The Neural Correlates of Visual Hallucinations in Parkinson's Disease

Thesis submitted for the Degree of Doctor of Philosophy

Angeliki Zarkali

University College London

Queen Square Institute of Neurology

2021

Declaration

I, Angeliki Zarkali confirm that the work presented in this thesis is my own. Where information has been derived from other sources, I confirm that this has been indicated in the thesis.

Acknowledgements

Above all, I thank all the study participants and their families for kindly donating their time and energy to make this work possible. I hope that this work will make a contribution to the search for new treatments for Parkinson's disease. I would also like to thank Alzheimer's Research UK for awarding me a clinical research training fellowship allowing me to do this work.

I want to thank my supervisors, Rimona Weil and Geraint Rees for their sound advice, guidance, mentorship, and support on each new endeavour. They provided me with amazing examples and gave me the confidence and space to grow as a researcher; I am truly grateful to both for their support.

I would also like to thank the amazing researchers that I had the opportunity to collaborate with at UCL: Peter McColgan, Andrew Lees, Mina Ryten and Suzanne Reeves. They each provided their unique perspective and expertise and I have learnt so much from them. Many other colleagues shared their skills and experiences with me: Louise Leyland, George Thomas, Regina Reynolds, Maryam Shoai and many others. Thank you for taking time out of your busy schedule to help me!

Finally, I would like to thank my family. My partner Stam, for supporting me no matter what, my parents for always believing me and all my friends and family for being there for me when I needed a break.

Abstract

Visual hallucinations are common in Parkinson's disease (PD) and linked to worse outcomes: increased mortality, higher carer burden, cognitive decline, and worse quality of life. Recent functional studies have aided our understanding, showing large-scale brain network imbalance in PD hallucinations. Imbalance of different influences on visual perception also occurs, with impaired accumulation of feedforward signals from the eyes and visual parts of the brain. Whether feedback signals from higher brain control centres are also affected is unknown and the mechanisms driving network imbalance in PD hallucinations remain unclear.

In this thesis I will clarify the computational and structural changes underlying PD hallucinations and link these to functional abnormalities and regional changes at the cellular level. To achieve this, I will employ behavioural testing, diffusion weighted imaging, structural and functional MRI in PD patients with and without hallucinations. I will quantify the use of prior knowledge during a visual learning task and show that PD with hallucinations over-rely on feedback signals. I will examine underlying structural connectivity changes at baseline and longitudinally and will show that posterior thalamic connections are affected early, with frontal connections remaining relatively preserved. I will show that PD hallucinations are associated with a subnetwork of reduced structural connectivity strength, affecting areas crucial for switching the brain between functional states. I will assess the role of the thalamus as a potential driver of network-level changes and show preferential medial thalamus involvement. I will utilise data from the Allen Institute transcription atlas and show how differences in regional gene expression in health contributes

to the selective vulnerability of specific white matter connections in PD hallucinations.

These findings reveal the structural correlates of visual hallucinations in PD, link these to functional and behavioural changes and provide insights into the cellular mechanisms that drive regional vulnerability, ultimately leading to hallucinations.

Impact Statement

This thesis aims to shed light onto the mechanisms of visual hallucinations in Parkinson's disease to facilitate further research and inform the design of clinical trials. The findings of this thesis have significant potential impacts on research.

Although it is established that Parkinson's-hallucinations are associated with deficits in visual processing, I showed for the time that patients with hallucinations over-rely on feedback signals, with overweighting of prior knowledge when viewing ambiguous visual stimuli. In addition, I clarified the underlying changes in white matter structure in patients with Parkinson's and hallucinations both at the white matter tract and network level, linking the imbalance of feedforward and feedback signals to underlying structural connectivity changes. This provides new information on the neural mechanisms of visual hallucinations in Parkinson's disease.

The finding of evolving longitudinal white matter changes in patients with Parkinson's hallucinations with relatively preserved grey matter provides further in-vivo evidence that white matter changes may precede grey matter changes in Parkinson's and highlights the importance of biomarkers targeting the white matter. Clarifying the imaging correlates of Parkinson's-hallucinations could also inform the design of future clinical trials: aiding patient recruitment or assessing response to treatments under investigation.

Using emerging analytical frameworks such as network control theory, I was able to examine the effect that structural connectivity changes have on brain function. The finding that brain regions important for switching the brain between different states are preferentially affected in Parkinson's patients with hallucinations and the predisposition for a segregated, less connected substate of functional connectivity, provide support for

mechanistic models of visual hallucinations implicating attentional network imbalance and furthers our understanding of how hallucinations are generated in Parkinson's. Linking the regional distribution of structural brain changes identified by imaging, to regional expression of genes, I shed light on the biological processes and cell types driving regional vulnerability of these regions; this could inform future molecular-level research into potential therapeutic targets.

The medial mediodorsal thalamic subnucleus was identified as a region showing white and, later, grey matter changes in Parkinson's patients with hallucinations, with changes correlating with hallucination severity. This subnucleus plays a role in regulating prefrontal cortex function (and therefore feedback signals) and could be a potential therapeutic target for deep brain stimulation. Finally, correlating regional structural changes with regional neurotransmitter density and receptor gene expression, specific neurotransmitter receptors were identified as possible neuromodulatory targets, potentially opening new avenues for treatments of this highly distressing symptom.

This thesis' findings have implications for the mechanisms of hallucinations in other conditions, as similar pathways may be disrupted, and may influence research in schizophrenia, delirium and other dementias.

The work described in this thesis has led to 8 first author publications in high-impact, peer-reviewed journals including *Brain*, *Movement Disorders* and *Neurology*. In addition, this work was presented at national and international conferences, facilitating dissemination to the global scientific community. Finally, I have disseminated my findings to people with Parkinson's and their families through the Lewy body disease Rare Dementia Support Group, and a UCL Lunch Hour Lecture.

Publications

Zarkali A, Weil RS. Beyond dopamine: Further evidence of cholinergic dysfunction in Parkinson's disease (Commentary on Keo et al., 2021). Eur J Neurosci. 2021 May 7. doi: 10.1111/ejn.15269. PMID: 33960522.

Zarkali A, McColgan P, Ryten M, Reynolds R, Leyland LA, Lees AJ, Rees G, Weil RS. Organisational and neuromodulatory underpinnings of structural-functional connectivity decoupling in Parkinson's disease. Nature Commun Biol. 2021 Jan 19;4(1):86. doi: 10.1038/s42003-020-01622-9. PMID: 33469150.

Zarkali A, Mccolgan P, Leyland LA, Lees AJ, Rees G, Weil RS. Visual Dysfunction predicts cognitive impairment and white matter degeneration in Parkinson's Disease. Mov Disord. 2021 May;36(5):1191-1202. doi: 10.1002/mds.28477. PMID: 33421201.

Zarkali A, McColgan P, Ryten M, Reynolds R, Leyland LA, Lees AJ, Rees G, Weil RS. Differences in network controllability and regional gene expression underlie hallucinations in Parkinson's disease. Brain. 2020 Dec 5;143(11):3435-3448. doi: 10.1093/brain/awaa270. PMID: 33118028.

Zarkali A, McColgan P, Ryten M, Reynolds RH, Leyland LA, Lees AJ, Rees G, Weil RS. Dementia risk in Parkinson’s disease is associated with interhemispheric connectivity loss and determined by regional gene expression, NeuroImage: Clinical 2020; 28:102470. doi: 10.1016/j.nicl.2020.102470. PMID: 33395965.

Zarkali A, McColgan P, Leyland L-A, Lees AJ, Rees G, Weil RS. Fibre-specific white matter reductions in Parkinson’s hallucinations and visual dysfunction. Neurology 2020 Apr 7;94(14):e1525-e1538. doi: 10.1212/WNL.0000000000009014. PMID: 32094242.

Zarkali A, Adams RA, Psarras S, Leyland LA, Rees G, Weil RS. Increased weighting on prior knowledge in Lewy Body-associated visual hallucinations. Brain Commun. 2019;1(1):fcz007. doi: 10.1093/braincomms/fcz007. PMID: 31886459.

Zarkali A, Lees AJ, Weil RS. Flickering Stimuli Do Not Reliably Induce Visual Hallucinations in Parkinson's Disease. J Parkinsons Dis. 2019;6:14. doi: 10.3233/JPD-191635. PMID: 31227657.

Thomas GEC, **Zarkali A,** Ryten M, Shmueli K, Martinez ALG, Leyland LA, McColgan P, Acosta-Cabronero J, Lees AJ, Weil RS. Regional brain

iron and gene expression provide insights into neurodegeneration in Parkinson's disease. Brain. 2021 Mar 11:awab084. doi: 10.1093/brain/awab084. PMID: 33704443.

Oxtoby NP, Leyland LA, Aksman LM, Thomas GEC, Bunting EL, Wijeratne PA, Young AL, **Zarkali A**, Tan MXT, Bremner FD, Keane PA, Morris HR, Schrag AE, Alexander DC & Weil RS. Sequence of clinical and neurodegeneration events in Parkinson's disease progression. Brain 2021 Apr 12;144(3):975-988. doi: 10.1093/brain/awaa461. PMID: 33543247.

Foley JA, Dore C, **Zarkali A**, Livingston G, Cipolotti L, Mummery CJ, Weil RS. Evaluation of START (STrAtegies for RelaTives) adapted for carers of people with Lewy body dementia. Future Healthc J. 2020 Oct;7(3):e27-e29. doi: 10.7861/fhj.2020-0003. PMID: 33094242.

TABLE OF CONTENTS

“Knowledge of the fact differs from knowledge of the reason for the fact.”

Aristotle, Αναλυτικά Ύστερα ~384BC

1. Introduction

1.1 Thesis aims

Although traditionally thought of as a movement disorder, non motor symptoms and particularly visual hallucinations are extremely common and distressing in Parkinson's disease (PD) and are associated with worse outcomes (Fénelon *et al.*, 2000; Aarsland *et al.*, 2007). Despite this the neural correlates of hallucinations are not clearly understood and there are no effective treatments to date.

Neuroimaging and pathological studies so far have failed to identify a single brain region responsible for PD-associated visual hallucinations with multiple spatially distinct regions exhibiting changes in gray matter volume and thickness, white matter connectivity or functional activation (Pezzoli *et al.*, 2017). Indeed, increasing evidence suggests that visual hallucinations originate from imbalance between large scale whole brain networks (Muller *et al.*, 2014), particularly imbalance between feedforward signals (sensory evidence from our eyes and lower level visual areas) and feedback signals (from higher order brain areas to areas further down the cortical hierarchy) (Powers *et al.*, 2016).

Visuospatial deficits and reduced accumulation of sensory evidence have been described in patients with Parkinson's and visual hallucinations (O'Callaghan *et al.*, 2017) but changes in feedback signals have not been demonstrated. In this thesis I aim to quantify the use of prior knowledge (mediated by feedback signals) in patients with PD with and without hallucinations and test whether overweighting of prior knowledge also contributes to hallucinations.

Feedback and feedforward signals are communicated between regions through white matter connections. Additionally, there is evidence that changes in white matter may occur early in PD (Chung *et al.*, 2009) and imaging techniques to assess white matter changes may therefore be more sensitive. In this thesis I will evaluate the micro-structural and macro-structural white matter changes associated with PD-hallucinations and assess the longitudinal progression of white and gray matter changes in patients with compared to those without hallucinations.

To better understand why specific white matter connections are vulnerable, I will characterise how the structural brain network changes in patients with PD-hallucinations and examine whether regional gene expression profiles of the healthy brain relate to regional white matter connectivity loss in PD-hallucinations.

Finally, to better understand the effect that changes in white matter structure have on brain function, I will clarify how functional dynamic connectivity changes in PD with hallucinations. I will then use network control theory to model the transitions between states of functional connectivity in patients with and without hallucinations. I will correlate these with neurotransmitter systems using regional density profiles and gene expression profiles from healthy brains.

1.2 Introduction

Hallucinations are common in PD, affecting 30-70% of patients (Fénelon *et al.*, 2000; Hely *et al.*, 2008). Although hallucinations can occur in all sensory modalities, visual hallucinations are the most frequent, most typical of PD and occur earlier in the disease process (Fénelon *et al.*, 2000; ffytche *et al.*, 2017; Clegg *et al.*, 2018). The spectrum of PD-associated visual hallucinations is wide, ranging from minor hallucinations, such as passage

hallucinations (a fleeting image or brief vision of a person, animal, or object passing within the periphery of the visual field) and visual illusions/misperceptions (e.g., mistaking a pile of clothes in the room corner for a dog) (*Figure 1.1*) to complex, well-structured visual scenes (ffytche *et al.*, 2017) (*Figure 1.2*). Both types of hallucinations commonly co-occur (Fénelon *et al.*, 2011; Lenka *et al.*, 2019) and minor hallucinations almost always precede the onset of complex visual hallucinations (Mack *et al.*, 2012; Lenka *et al.*, 2019). In addition, insight into whether experienced images are real or not is initially preserved but often withers during the course of the disease (Fénelon *et al.*, 2000; Weil *et al.*, 2016).

Figure 1. 1 Example of a misperception.

Misperceptions can occur normally but are exaggerated in PD patients.

From Towel or Dog?:
https://www.reddit.com/r/funny/comments/gw6ow9/towel_or_dog/

Figure 1. 2. Charles Doyle, Self portrait 1832-93.

One of the sketchbooks used by the artist during his residence in the Royal Montrose Lunatic Asylum in Scotland. Although it is not known whether Charles Doyle was affected by Parkinson's disease, the painting is a good representation of the complex visual hallucinations associated with Parkinson's. Descriptions of hallucinations from study participants include:

"Strange people come in the house at night; I cannot see their legs and they sit around staring. They go away when we turn on the lights."

"I can often see little cats running around on the floor towards me. Sometimes I can feel them touching my legs. They keep me company."

Painting downloaded from the V&A with permission.

Visual hallucinations are thought to be specific to the presence of Lewy Body pathology and can therefore be a useful discriminator of PD from other parkinsonian syndromes such as Multiple System Atrophy or Progressive Supranuclear Palsy (Williams *et al.*, 2008). Additionally, it is well established that visual hallucinations are linked with negative outcomes. They are frequently distressing, distracting and a harbinger of dementia (Hobson and Meara, 2004; Galvin *et al.*, 2006). Furthermore, they are associated with increased mortality (Goetz and Stebbins, 1995), increased carer burden (Aarsland *et al.*, 2000) and worse quality of life (McKinlay *et al.*, 2007). They are also the strongest predictor of nursing home placement in people with PD (Aarsland *et al.*, 2000). Despite their impact on patients and families, our understanding of how visual hallucinations are produced remains limited (Weil *et al.*, 2016; Onofrj *et al.*, 2019).

1.3. Parkinson's hallucinations: a disorder of brain networks

Early theoretical models for visual hallucinations in PD proposed that the presence of hallucinations was a result of pharmacological treatment, specifically levodopa administration (Moskovitz *et al.*, 1978; Poewe, 2003). However, visual hallucinations can be seen in early disease, even in untreated patients and irrespective of levodopa doses (Barnes and David, 2001; Biglan *et al.*, 2007).

Other theoretical models trying to attribute visual hallucinations in PD to a single deficit have also been disproven. The *Dream Intrusion Model* considers the source of hallucinated images to be endogenous imagery produced during dreaming, potentially associated with Rapid Eye Movement (REM) sleep intrusions during wakefulness (Arnulf *et al.*, 2000; Manni *et al.*, 2002). Although the risk of visual hallucinations is increased

in patients with REM sleep behaviour disorder (Lee and Weintraub, 2012) and there is a temporal link of hallucinations with sleep (Manni *et al.*, 2002), visual hallucinations in PD often occur in association with non-REM sleep or in polysomnographically proven wakefulness (Lee and Weintraub, 2012) and therefore cannot be explained by the *Dream Intrusion Model*.

Another proposed mechanism of PD-associated hallucinations is a deficit in reality monitoring (Barnes *et al.*, 2003). Patients with PD and visual hallucinations perform worse than non-hallucinators in judging the source of an item in visual and memory tasks, despite similar performance in item recognition and rely more on a sense of familiarity (recognising an item as being presented before but not specifically remembering its previous presentation) (Barnes *et al.*, 2003). These results were interpreted as a bias toward attributing an internally generated event to an external source, which could give rise to a hallucinated image. However, this model, similar to other single-cause models, does not explain the widespread cognitive deficits and pathological changes seen in PD-associated hallucinations (Muller *et al.*, 2014).

In addition, multiple brain regions are affected in patients with visual hallucinations associated with Parkinson's and more generally Lewy body disease, suggesting a more complex multi-region pathology giving rise to PD-hallucinations. Lewy body pathology has been demonstrated in the amygdala and parahyppocampal gyrus (Harding *et al.*, 2002; Papapetropoulos *et al.*, 2006), inferior temporal cortex (Harding *et al.*, 2002; Papapetropoulos *et al.*, 2006; Gallagher *et al.*, 2011), superior and lateral frontal cortex (Gallagher *et al.*, 2011), inferior parietal cortex and cingulate cortex (Papapetropoulos *et al.*, 2006) in patients with PD-hallucinations. Increased tau and amyloid pathology has also been seen in patients with PD and visual hallucinations within the frontal cortex, parietal cortex and hippocampus (Jacobson *et al.*, 2014) and PD patients with visual

hallucinations show reduced amyloid in their cerebrospinal fluid (CSF), suggestive of Alzheimer's like pathology (Ffytche *et al.*, 2017).

Similarly, neuroimaging studies have also shown a diverse pattern of changes affecting many spatially and functionally distinct regions. Studies assessing gray matter volume using Voxel Based Morphometry (VBM), have shown diverse and inconsistent results: gray matter volume reduction has been reported in several areas including the lingual gyrus, cingulate, superior parietal lobule, precuneus, hippocampi and superior frontal lobule (Ramírez-Ruiz *et al.*, 2007; Ibarretxe-Bilbao *et al.*, 2008, 2010; Meppelink *et al.*, 2011; Janzen *et al.*, 2012; Watanabe *et al.*, 2013; Goldman *et al.*, 2014; Pagonabarraga *et al.*, 2014). Although different criteria for defining hallucinations and diverse methodology (for example, whole brain vs regions of interest analyses and different correction methods for multiple comparisons) may play a role in the difference in results (Lenka *et al.*, 2015), and gray matter volume loss may be a relatively late occurrence in the disease process, these findings further support the idea that visual hallucinations in PD do not originate from damage in a single brain region.

To account for these multidimensional changes, more recent models of PD hallucinations have adopted a more integrated approach focusing on the interplay between networks rather than single cognitive domains or brain regions. These models suggest that PD-associated hallucinations arise due to a shift in the relative effects of different networks (Muller *et al.*, 2014). Indeed, imbalance of large scale brain networks has been increasingly shown in association with PD-hallucinations across multiple different types of brain networks: computational brain networks, functional brain networks and structural brain networks.

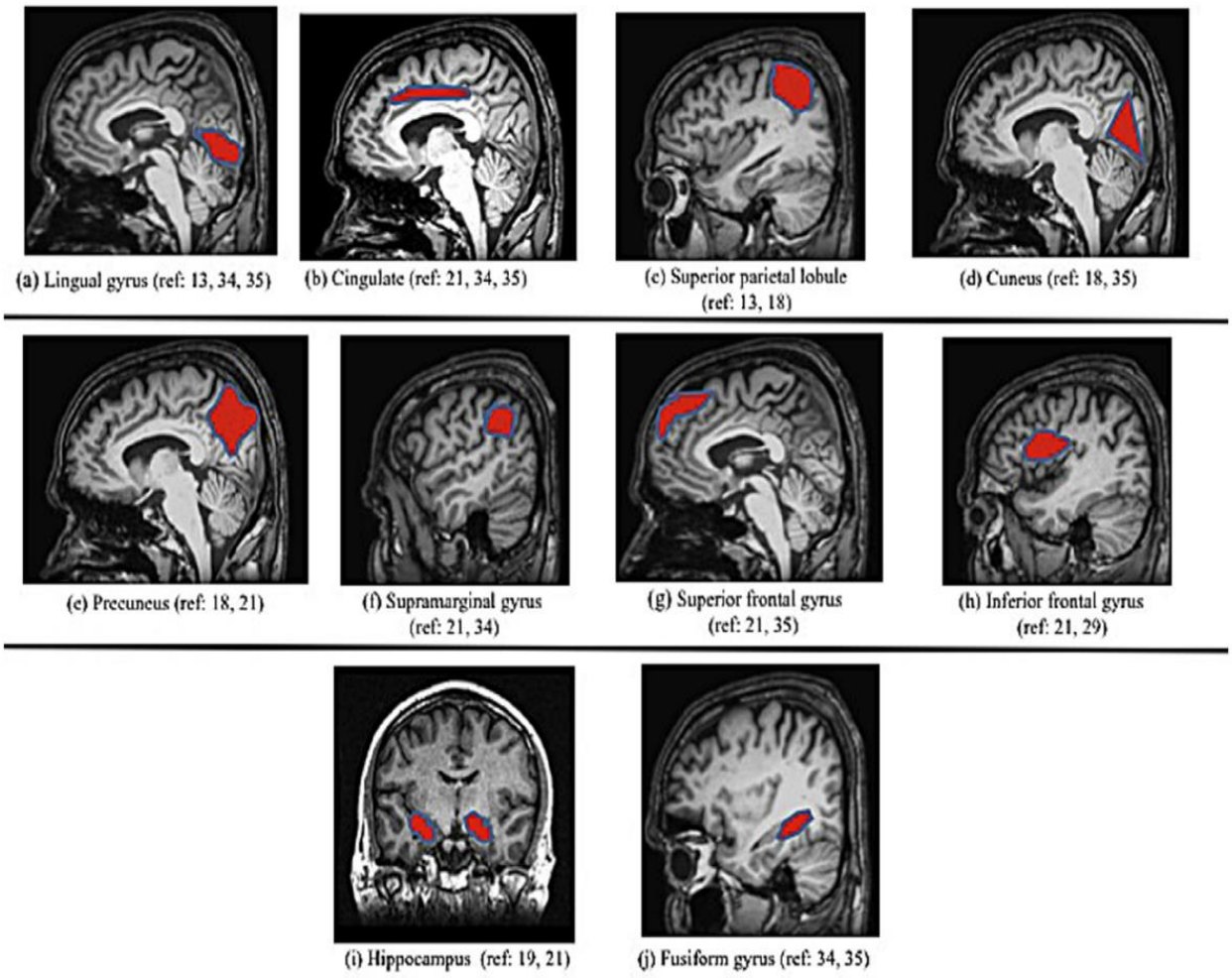

Figure 1. 3. Variable and inconsistent results of gray matter atrophy from Voxel Based Morphometry (VBM) studies in patients with Parkinson's hallucinations

Pictured in red are regions that have been reported to show grey matter atrophy in more than two VBM studies, in a recent meta-analysis of visual hallucinations in Parkinson's disease. From: (Lenka et al., 2015)

1.4. Computational brain networks

Perception in the human brain can be studied in the framework of predictive coding: here perception is seen as the adoption of a hypothesis explaining the cause of a sensation, an inference that takes into account both expectations from prior knowledge and sensory input (Friston and Kiebel, 2009; Cavanagh, 2011; Parr *et al.*, 2018). Priors are constantly compared to incoming sensory evidence across the cortical hierarchy and prediction errors are computed. If the priors are more precise than the sensory inputs themselves they will dominate inference, ignoring prediction errors (Friston and Kiebel, 2009; Feldman and Friston, 2010; Teufel *et al.*, 2013). In contrast, if prediction errors are more precise, they will dominate priors and update to a new belief or inference.

Hierarchical predictive coding as the basis of human perception is supported by experimental evidence in the healthy brain (Walsh *et al.*, 2020). In each level of the cortical hierarchy distinct neural populations exist giving rise to distinct feedforward and feedback connections (Markov *et al.*, 2014) and oscillating at different frequencies (Bastos *et al.*, 2015). Additionally, unexpected stimuli or omission of expected stimuli (therefore increased prediction error) lead to increased neural responses (de Lange *et al.*, 2018) and expectations can induce signals in early sensory regions (Kok *et al.*, 2016). There is therefore evidence that expectations or priors directly affect perception and that the brain has cell populations and neuroanatomical connections whose activity is consistent with the predictive coding model.

In this context, visual hallucinations, or experiencing visual percepts that are not objectively there, can be thought of as false inference which arises when the integration of sensory input and prior knowledge is altered (Fletcher and Frith, 2009; Adams *et al.*, 2013; Powers *et al.*, 2016; Corlett *et al.*, 2019). This framework has been applied to the study of hallucinations in non-

neurodegenerative diseases. Hallucinations experienced by healthy individuals or in the context of psychiatric illness are associated with a shift towards prior knowledge and away from sensory evidence (Teufel *et al.*, 2015; Alderson-Day *et al.*, 2017; Davies *et al.*, 2018; Stuke *et al.*, 2021). Conditioned auditory hallucinations (via sensory conditioning establishing a visual stimulus as a predictor for a near-threshold auditory stimulus) in healthy individuals are also mediated by strong priors and those individuals with a prior diagnosis of psychosis were more susceptible (Powers *et al.*, 2017). In addition to a propensity to hallucinate when stimuli are noisy (Powers *et al.*, 2017), this relative increase in the weighting of prior knowledge in people who experience hallucinations is linked with improved performance in disambiguating ambiguous visual and auditory signals (Teufel et al., 2015; Alderson-Day et al., 2017; Davies et al., 2018). Higher weighted priors could also be the product of lower precision of sensory evidence and there are several ways that imbalance between feedforward and feedback signals could lead to hallucinations (*Figure 1.4*).

Abnormal integration of priors with sensory information could also underlie hallucinations in neurodegeneration. Several visual-processing deficits have been described in PD including contrast sensitivity (Davidsdottir *et al.*, 2005; Silva *et al.*, 2005), colour vision (Silva *et al.*, 2005; Matar *et al.*, 2019), attention (Norton *et al.*, 2015), biological motion and skew (Jaywant *et al.*, 2016; Weil *et al.*, 2017), visual evoked potentials (Murphy *et al.*, 2020), even visual acuity (Hamedani *et al.*, 2020; Han *et al.*, 2020). The presence of visual-processing deficits is increased in PD patients with visual hallucinations (Diederich *et al.*, 2005; Weil *et al.*, 2016; Matar *et al.*, 2019) and sensory evidence accumulation is impaired in patients with PD and visual hallucinations (O'Callaghan *et al.*, 2017).

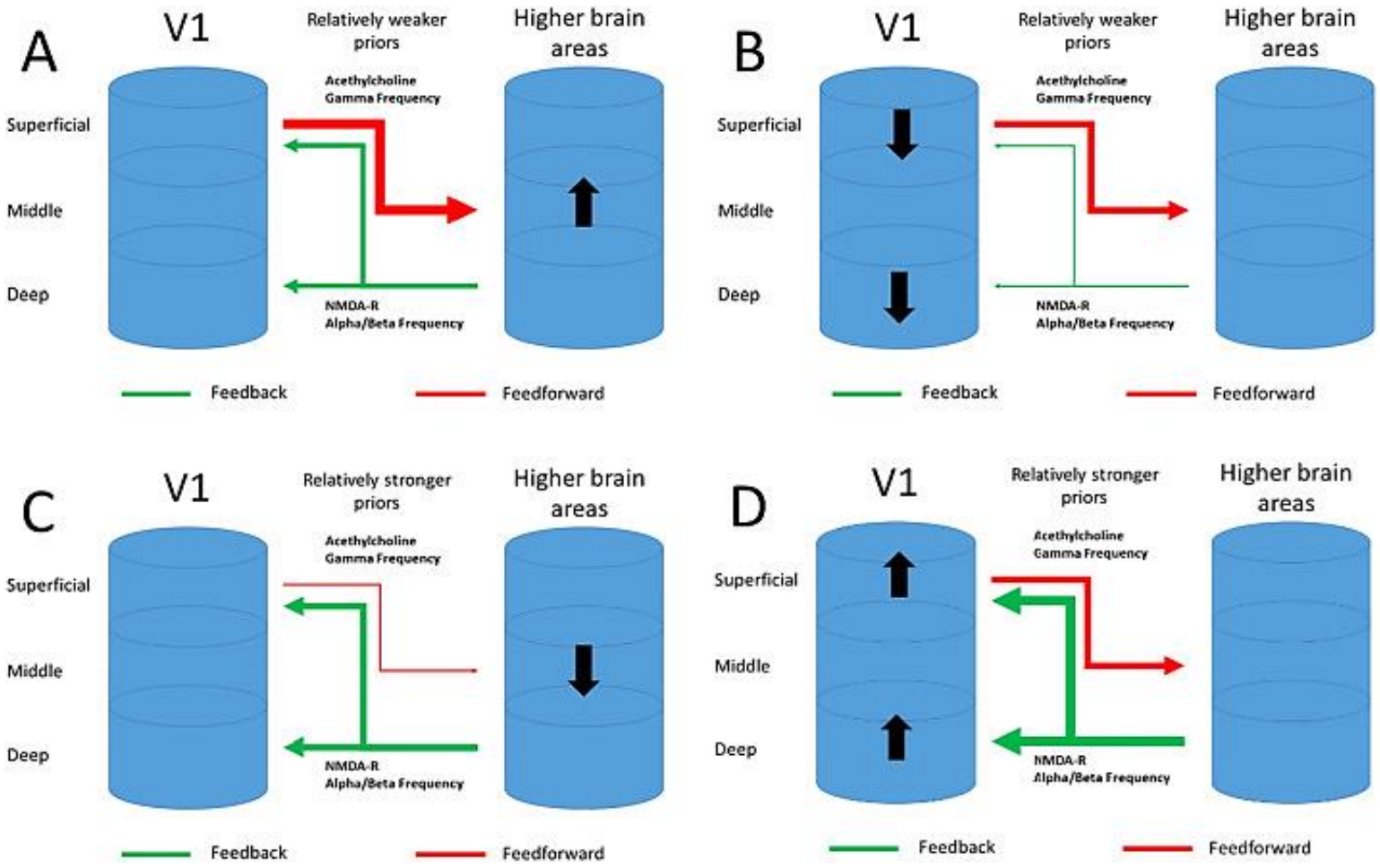

Figure 1. 4. Hypotheses for hierarchical computational model disruption in psychosis.

Lower sensory regions like the visual cortex (V1) communicate with higher brain areas via feedforward signals (red arrows) and higher brain regions communicate their prior expectations through feedback connections (green arrows). The thickness of the arrows represents their relative weighting; changes in this can lead to hallucinations.

Hallucinations can be the result of increased weighting of sensory evidence (A), or decreased weighting of priors (B), although there is less evidence to support this. Hallucinations could also be the result of relative increase in precision of priors (C) in addition to relative decrease in precision of sensory evidence, or finally they could be the results of just increased weighting of priors (D).

From (Haarsma et al., 2020)

However hallucinations can also occur in patients without any lower or higher visual deficits (Gallagher *et al.*, 2011; Weil *et al.*, 2016) making a solely feedforward explanation for the occurrence of hallucinations less attractive. Increased likelihood of visuoperceptual deficits in PD patients with hallucinations is in favour of a relative lower precision of sensory evidence (Figure 1.4, panel C) but whether prior knowledge is also overweighted is not yet clear. A recent study showed that patients with PD and presence hallucinations (the sensation that somebody is nearby when no one is present) but not those with visual hallucinations were more sensitive to robotic-induced presence hallucination when exposed to conflicting sensorimotor information suggesting stronger priors (Bernasconi *et al.*, 2021). This study however did not assess visual perception and whether priors are overweighted in visual hallucinations as well is not yet known. Quantifying the use of prior knowledge in PD-associated hallucinations could provide important insights in how the balance of feedforward and feedback processes becomes impaired in PD giving rise to visual hallucinations.

1.5. Functional brain networks

Functional brain networks are also imbalanced in patients with PD and visual hallucinations, giving rise to a recent attractive theoretical model which suggests that hallucinations in PD are the result of breakdown in the connectivity of networks involved in attention and conscious perception (Shine *et al.*, 2014): the Dorsal Attention Network (DAN) involved in tasks requiring exogenous attention, the Ventral Attention Network (VAN) responsible for salience monitoring, and the Default Mode Network (DMN) which is activated during internally focused tasks (*Figure 1.5*).

The *Attentional Networks hypothesis* suggests that visual hallucinations in Parkinson's disease are caused by overactivity of the DMN and VAN reinforcing false images that remain unchecked due to a failure to engage the DAN. The resulting over-reliance on the DMN, which has been repeatedly observed in PD-associated hallucinations (Yao *et al.*, 2014; Shine *et al.*, 2015; Onofrj *et al.*, 2017), leads to hallucinated images as the DMN is poorly suited to interpret ambiguous sensory images.

Increased connectivity between the regions participating in the DMN, specifically the right middle frontal gyrus, bilateral posterior cingulate and precuneus (Yao *et al.*, 2014) as well as between DMN and the visual system is seen in PD patients with hallucinations (Shine *et al.*, 2015). A different study showed decoupling of DMN activity with increased connectivity of the posterior cingulate cortex posterior regions of task-positive networks and visual association areas, which correlated with the severity of the hallucinations (Bejr-Kasem *et al.*, 2019). Other regions within the DMN such as the inferior partietal lobule and posterior cingulate also exhibit aberrant functional connectivity in PD patients with visual hallucinations (Franciotti *et al.*, 2015).

Similar changes are seen in association with cognitive impairment with increased connectivity of the DMN to occipital and parietal regions in PD patients with mild cognitive impairment (Baggio *et al.*, 2015; Abós *et al.*, 2017) and increased within-DMN connectivity in patients with Lewy body dementia (Schumacher *et al.*, 2018). DMN decoupling has also been described in association with the psychedelic drug LSD which can also cause visual hallucinations (Carhart-Harris *et al.*, 2016). And preserved metabolism of the posterior cingulate cortex, a key region of the DMN, is an established feature of Parkinson's dementia and Dementia with Lewy bodies where visual hallucinations are prominent (Whitwell *et al.*, 2017).

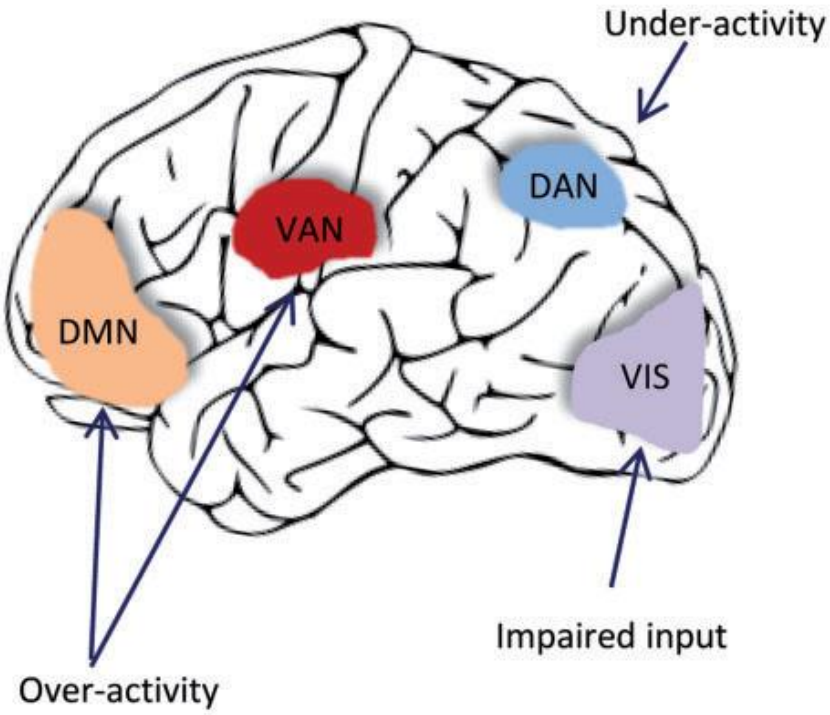

Figure 1. 5 The attentional network model of PD-associated hallucinations

Large scale functional networks show imbalance in PD with visual hallucinations. According to attentional network model, visual hallucinations in PD arise due to over-reliance on the DMN in processing ambiguous stimuli (due to impaired input from the VIS) with aberrant DMN activation and relative reduced DAN recruitment.

DAN: Dorsal attentional network, VAN: Ventral attentional network, DMN: Default mode network, VIS: visual cortex

From: (Weil et al., 2016).

The DMN plays a key role in self-referential thought, internally generated imagery and integration of sensory evidence with prior sensations (Callard and Margulies, 2014) and altered DMN connectivity is in keeping with relatively stronger/overweighted priors in PD-hallucinations. Although the attentional network hypothesis is supported by increasing evidence of functional network disruption in PD hallucinators, the mechanisms that drive this functional network imbalance are less clear.

1.6. Structural Brain Networks

Although, as discussed above, functional imaging studies have significantly advanced our understanding of visual hallucinations in PD (Shine *et al.*, 2014, 2015; Yao *et al.*, 2014, Hepp *et al.*, 2017*b*), less is known about the structural brain changes in PD-associated hallucinations. However, deriving inferences about the structure of physical brain connections from activation patterns seen in functional MRI is indirect and prone to assumptions (Vázquez-Rodríguez *et al.*, 2019). Given that structural connectivity impacts functional connectivity and is likely to be more reflective of the brain anatomy (Goñi *et al.*, 2014; Messé *et al.*, 2015; Vázquez-Rodríguez *et al.*, 2019), structural imaging techniques could be a powerful tool to investigate hallucinations in vivo.

The majority of structural imaging studies of PD-associated hallucinations so far have focused on gray matter (GM) volume using Voxel Based Morphometry (VBM), with diverse and inconsistent results as previously discussed (*Figure 1.3*). As atrophy was described in association with PD-hallucinations in many spatially distinct locations, subsequent studies employed network lesion mapping to attempt to identify common neuroanatomical substrates. This combines atrophy maps with resting state functional connectivity estimates from healthy human brains to assess

whether the areas of atrophy participate in a common functional network (Boes *et al.*, 2015). Using network lesion mapping, a recent study has shown that brain lesions that lead to visual hallucinations were connected to the lateral geniculate nucleus of the thalamus (Kim *et al.*, 2019), similarly a networked centered in the lateral geniculate nucleus was identified to be associated with PD-hallucinations in a meta-analysis of studies assessing GM volume (Weil *et al.*, 2019).

However, GM loss is a relatively late event in PD, limiting the sensitivity of imaging methods assessing GM. In contrast axonal changes seem to occur relatively early. Axonal dystrophic changes occur even before axonal loss, suggesting that alpha-synuclein accumulation in the axonal compartment happens early in the disease process (Chung *et al.*, 2009). Exogenous alpha-synuclein in neuronal cultures leads to formation of endogenous pathology that starts within the axon (Volpicelli-Daley *et al.*, 2011). Mouse models for leucine rich repeat kinase 2 (LRRK2) gene, the commonest genetic cause of PD, exhibit axonal pathology before neurite loss (Li *et al.*, 2009). Therefore, techniques sensitive to axonal changes, such as diffusion weighted imaging (DWI), are most likely to detect early structural changes in PD-associated hallucinations.

DWI allows non-invasive in vivo study of WM architecture (Le Bihan *et al.*, 2001) (*for details see Chapter 2*). It is usually analysed using the diffusion tensor model (diffusion tensor imaging (DTI)) that uses metrics averaged across voxels to derive measures such as fractional anisotropy (FA) and mean diffusivity (MD). DTI studies of visual hallucinations in PD have shown altered WM integrity within the optic nerve and optic radiation (Lee *et al.*, 2016) and tracts from the cholinergic nucleus basalis of Meynert to parietal and occipital cortical regions (Hepp *et al.*, 2017*a*) in tract of interest analysis. In addition, broadly reduced connectivity strength has also been reported in PD hallucinations, preferentially affecting nodes of the “diverse

club", areas that are proposed to integrate across more specialist modules (Hall *et al.*, 2019).

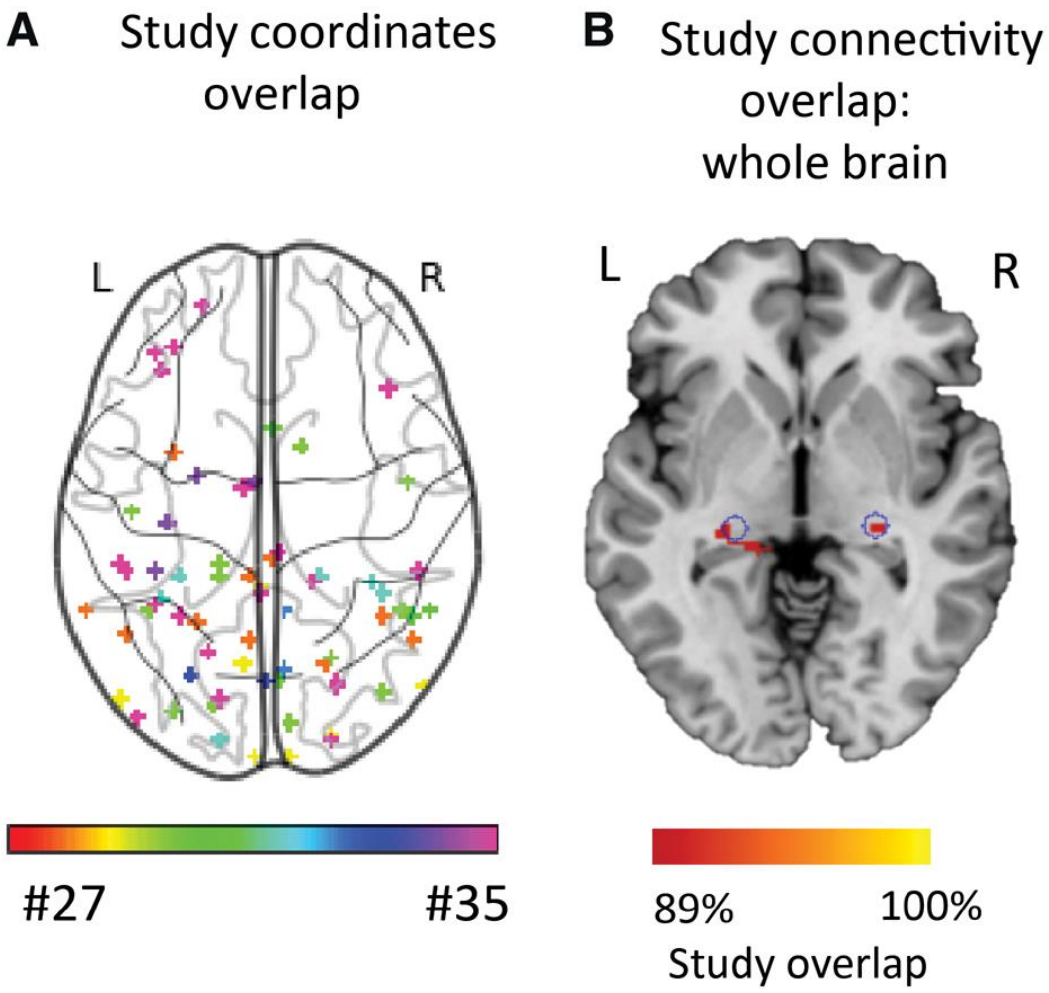

Figure 1. 6. Network of visual hallucinations identified by network lesion mapping.

A. Coordinates of gray matter atrophy across all included studies in this meta-analysis. Each study is represented by a different colour.

B. Network overlap of functional whole-brain connectivity maps: this overlaps on the lateral geniculate nucleus bilaterally.

From: (Weil et al., 2019).

However, classical DTI-based approaches have only limited ability to model crossing fibres, (Jbabdi *et al.*, 2010; Tournier *et al.*, 2011; Jones *et al.*, 2013) making them difficult to interpret, and limiting their specificity, especially in regions containing crossing fibres, which amount to up to 90% of brain white matter (Jeurissen *et al.*, 2013). Additionally, although providing insights to the structural changes that accompany visual hallucinations in PD, DWI studies have not directly examined the impact that these changes have on functional dynamics or the factors that make specific brain regions more vulnerable to white matter loss.

1.7. Drivers of network imbalance

Computational, functional and structural brain networks become imbalanced in PD to produce visual hallucinations. Impaired transition or switching between different functional network activation has been proposed as possible driver, for example failure to disengage the DMN and/or failure to activate the DAN (Muller *et al.*, 2014). However, the drivers behind this impaired between-states transition remain unclear.

Recently, the thalamus has been postulated as a possible driver of network imbalance in PD-hallucinations (Onofrj *et al.*, 2019; Russo *et al.*, 2019). The thalamus is a particularly well-connected brain region and plays a crucial role in filtering sensory information, primarily via connections with its first order nuclei like the lateral geniculate nucleus; this has been identified as a possible key region in studies using network lesion mapping as previously described (Kim *et al.*, 2019; Weil *et al.*, 2019).

In addition, higher order thalamic nuclei such as the mediodorsal thalamic nucleus regulate the function of crucial DMN brain regions including the prefrontal cortex (PFC) (Mitchell, 2015; Anastasiades *et al.*, 2021). Reduced

connectivity or degeneration of the mediodorsal thalamus could lead to unregulated PFC activity and subsequently increased feedback signals to regions lower in the cortical hierarchy. Changes in thalamic-PFC connectivity have been described in association with hallucinations in the context of psychiatric disease (Anticevic *et al.*, 2014).

In PD-associated visual hallucinations, the thalamus shows hypometabolism and atrophy (Nishio *et al.*, 2017) and alpha-synuclein pathology is particularly evident in the thalamus including associative and higher order nuclei in patients with PD (Halliday, 2009). In addition, both in PD dementia and Dementia with Lewy Bodies, theta rhythms, which are considered as a marker of thalamocortical dysfunction gradually evolve as the disease progresses and predict cognitive decline (Bonanni *et al.*, 2008). Theta rhythms have also been recorded during active hallucinations in PD (Dauwan *et al.*, 2019). This evidence of thalamocortical dysfunction in association with PD-hallucinations has lead to the hypothesis that loss of thalamic modulation leads to DMN decoupling and aberrant activation. However the specific spatial profile of thalamic involvement in PD-hallucinations remains unclear, understanding the specific grey matter changes within thalamic subnuclei as well as white matter connectivity changes from the thalamus to the cortex could provide useful insights to the mechanisms of PD-associated hallucinations.

1.8. Bridging brain structure and function

Although advances in WM imaging such as high tensor models can improve the fidelity of structural brain connectivity and similarly, functional MRI can provide an improved estimate of brain activation during tasks or rest, our understanding of how brain structure gives rise to behaviour remains

limited (Mišić and Sporns, 2016). Structural connectivity provides a principled way to represent the organization of brain networks, and to a large extent predicts brain activation patterns at rest (Messé *et al.*, 2015) but it cannot model the relationship between brain structure and behaviour.

Additionally, recent evidence suggest that structure-function relationships may differ across brain regions (Vázquez-Rodríguez *et al.*, 2019). The relationship between structural and functional connectivity also varies during aging. Stronger coupling of structural and functional connectivity is seen during brain maturation from infancy to adolescence (Hagmann *et al.*, 2010) and continues to increase with age (Betzel *et al.*, 2014). Altered structural-functional connectivity coupling has been described in the presence of neurological and psychiatric disease (Zhang *et al.*, 2011; Cocchi *et al.*, 2014; Koubiyr *et al.*, 2019) and has been correlated with cognitive function (Baum *et al.*, 2020). Understanding the link between structural connectivity and activation (functional) coupling of brain regions is critical to understanding the link between structural degeneration and behavioral change in neurodegeneration.

Several analytical methods can be used to examine the relationship between structural and functional connectivity. One method to achieve this is by concurrent, longitudinal investigation of brain structural and functional connectivity; similar approaches have provided useful insights in Huntington's disease (McColgan *et al.*, 2017).

An alternative approach is provided by network control theory, a powerful emerging framework that combines structural connectivity measures and linear estimates of local dynamics to provide a metric of the extent of influence of one part of the network over other parts of the brain and in changing brain states; this is termed controllability (Gu *et al.*, 2015). Network control theory can therefore determine regions responsible for

shifting the brain between difference functional states using structural imaging data. Given the emphasis on shifts between brain networks as a key driver of PD hallucinations (Muller *et al.*, 2014), brain controllability is likely to provide important insights into how hallucinations arise in PD. Network control theory can also directly model how the structural connectome guides transitions between functional states (Gu *et al.*, 2015, 2017; Betzel *et al.*, 2016); this could be particularly useful in better understanding how specific changes in functional connectivity that underly PD-hallucinations may occur.

Given the complex and multidimensional changes seen in PD-associated hallucinations in brain structure, function and behaviour, multivariate approaches are likely needed, linking multiple brain variables and phenotypic data (Mišić and Sporns, 2016).

1.9 Linking changes in brain networks to molecular processes and neurotransmitter systems

As previously discussed network neuroscience can provide useful insights to the brain structural and functional changes that underly hallucinations in PD. Until recently, these changes in macroscopic brain networks were abstract and difficult to relate to changes in structure and function at the cellular level. The creation of the Allen Human Brain Atlas (AHBA) by the Allen Institute of Brain Science (Hawrylycz *et al.*, 2015) provides a way to link regional changes identified by brain imaging to regional gene expression. AHBA contains a database of expression levels of 20,737 genes across the human brain. It was constructed postmortem from the brains of 6 human donors with no history of psychiatric or neuropathological disorders. RNA was extracted from 900 anatomically defined regions represented by 58,692 probes. Importantly, prior to RNA sampling, donors' brains

underwent postmortem MRI; this allowed all samples to be labelled in MRI space resulting to a regional gene expression map of the healthy human brain that can be associated with MRI-derived metrics.

Using data from AHBA, studies have shown that spatially and functionally correlated brain regions share similar gene expression profiles (Richiardi *et al.*, 2015; Krienen *et al.*, 2016). Similar gradients of cortical organisation following the rostro-caudal axis seem to guide both regional gene expression (Bernard *et al.*, 2012) and structural and functional connectivity (Paquola *et al.*, 2019) as well as cyto-architecture and cellular composition (Fornito *et al.*, 2019). Regional gene expression also seems to drive connectivity between regions and connectome topology (Fornito *et al.*, 2019); correlating changes in structural and functional connectivity measures to regional gene expression differences provides a unique opportunity to assess brain structure and function across scales.

Studies correlating imaging with regional gene expression have already provided useful insights to the drivers of regional vulnerability in the presence of disease: in schizophrenia (Romme *et al.*, 2017), Huntington's disease (McColgan *et al.*, 2018), autism (Romero-Garcia *et al.*, 2019). In PD, differential expression of predetermined candidate genes is associated with cortical atrophy patterns (Freeze *et al.*, 2018, 2019) and functional connectivity loss (Rittman *et al.*, 2016).

In this thesis, I will use data from AHBA to investigate the gene expression profiles associated with regional vulnerability to connectivity loss in PD patients with visual hallucinations. This will provide insights to the biological processes and cell-types involved in PD-hallucinations. Using gene expression data for neurotransmitter receptors, in combination with neurotransmitter density profiles from PET-derived atlases from healthy brains (Dukart *et al.*, 2021), I will also assess whether specific

neurotransmitter systems are important in the transitioning between functional states and could be therefore crucial in the temporal dynamic changes underlying hallucinations in PD.

2. General Methods

2.1 Introduction

This chapter describes the patient cohorts that were included in this thesis, including the clinical assessments performed, basics of MRI, including the acquisition and processing of diffusion weighting imaging and resting state functional data (fMRI), the specific acquisition and quality control of imaging data, and pre-processing steps for structural, diffusion weighted imaging and fMRI data. These methods were used in several of the experiments presented in this thesis. Additional methods were used in specific individual studies, such as a visual learning task and signal detection theory; these are described in the relevant chapters. As there was some variability in included participants and methods in individual experiments, each data chapter of this thesis also contains a methods section, describing the relevant methods used in more detail.

2.2 Study cohorts

Two main cohorts were used in this thesis:

- **Lewy Body Disease (LBD) cohort (n=57):** Chapter 3.
  Including patients (n=37) with a diagnosis of either Parkinson's disease (PD) or Dementia with Lewy Bodies (DLB) and age-matched controls (n=20).
- **Vision in Parkinson's disease (VIPD) cohort (n=135):** Chapters 4, 5 and 6.
  Including patients with Parkinson's disease (n=100) and age-matched controls (n=35).

Both cohorts were recruited to the National Hospital for Neurology and Neurosurgery (NHNN) under the Vision in Parkinson's disease study (PD Rimona Weil, NRES Queen Square Ethics Committee reference 15/LO/00476. Patients with PD or DLB were recruited from clinics in NHNN or affiliated hospitals, as well as the Queen Square Movement Disorders Consortium database and Parkinson's UK. Controls were recruited from spouses of patients taking part in the study, the UCL Institute of Cognitive Neuroscience volunteer databases and newspaper advertisements.

The LBD cohort underwent a single study visit, including a visual learning task (described in Chapter 3), as well as questionnaires and clinical assessments. The VIPD cohort underwent 3 study visits, at Baseline, at 18 months (Visit 2) and at 36 months (Visit 3; this is still underway). Each visit included the same questionnaires and clinical assessments as the LBD cohort, blood test sampling, and brain imaging. The VIPD study protocol is seen in *Table 2.1.*

The author personally recruited and tested all participants of the LBD cohort (n=57) within a period of 6 months. In addition, the author contributed to the recruitment and testing of participants in the VIPD cohort, in the second and third study visits. All participants received a detailed information sheet summarising the study objectives and design as well as potential risks prior to the study. Prior to testing, all participants gave written informed consent.

Table 2.1. Vision in Parkinson's disease study protocol

Assessments	Baseline Visit	Visit 2	Visit 3
Behavioural & Clinical Measures	Consent Demographics & History Questionnaires Cognitive testing Motor assessments Visual testing	Consent Demographics & History Questionnaires Cognitive testing Motor assessments Visual testing	Consent Demographics & History Questionnaires Cognitive testing Motor assessments Visual testing
Blood tests	Genetic testing and neurofilament light	Neurofilament light	Neurofilament light and plasma tau
Brain imaging	MP2RAGE, diffusion weighted imaging, resting state functional MRI, Quantitative susceptibility mapping	MP2RAGE, diffusion weighted imaging	MP2RAGE, diffusion weighted imaging, resting state functional MRI, Quantitative susceptibility mapping

Questionnaires

All participants reported details on demographics as well as a patient history questionnaire providing information including: PD/DLB diagnosis, medications, other medical history, family history and past education. Participants with a diagnosis of PD/DLB were also screened on each study visit for symptoms and signs that would raise the suspicion of an atypical parkinsonian syndrome (frequent falls, gaze palsy, severe autonomic dysfunction etc). Controls were also assessed and were excluded if they had a history of neurological disorders or head injury; they were also excluded from later visits if a subsequent diagnosis of mild cognitive impairment (MCI) or dementia was made.

All participants with PD satisfied the United Kingdom Parkinson's Disease Society Brain Bank criteria for Parkinson's disease, the Movement Disorder Society criteria for Parkinson's disease dementia or the Dementia with Lewy Bodies Consortium Criteria for DLB (Gibb and Lees, 1988; Emre et al., 2007; McKeith et al., 2017). Patients with LBD were classified as hallucinators (VH) if they scored ≥1 on question 2 of the Movement Disorder Society Unified Parkinson's Disease Rating Scale (UPDRS: "Over the past week have you seen, heard, smelled or felt things that were not really there?") (Goetz *et al.*, 2008).

Participants also provided detailed information on experienced hallucinatory phenomena using the University of Miami Parkinson's Disease Hallucinations Questionnaire (UM-PDHQ) (Papapetropoulos et al., 2008). The questionnaire is seen in *Appendix 1*. It provides quantitative information on both the severity and the frequency of hallucinations across all sensory modalities but focusing on visual hallucinations and has been validated for use in PD (Papapetropoulos et al., 2008). Participants also completed a questionnaire on mood, the Hospital Anxiety and Depression Scale (HADS)

(Zigmond and Snaith, 1983); this is an easy to use, quick self-assessment questionnaire and has been shown to be a reliable screening tool for depression and anxiety in an outpatient setting (Hansson *et al.*, 2009). The REM Sleep Behaviour Disorder Screening Questionnaire (RBDSQ) was also administered to gather information on sleep (Stiasny-Kolster et al., 2007, as REM sleep behaviour disorder is a condition often presenting as an early manifestation of PD and patients with PD and REM sleep behaviour disorder may have increased risk of cognitive impairment (Mao et al., 2020). VIPD participants on Visit 3 also completed the Clinician Assessment of Fluctuation (Walker *et al.*, 2000) questionnaire which provides information on cognitive fluctuations.

Cognitive assessments

Both general and domain-specific measures of cognition were collected at each study visit. General cognition was assessed using the Mini-Mental State Examination (MMSE) and Montreal Cognitive Assessment (MoCA) (Dalrymple-Alford *et al.*, 2010; Creavin *et al.*, 2016). Domain specific cognitive assessments were also performed using two tests per cognitive domain as per the recent Movement Disorder Society recommendations for assessment of cognitive impairment and dementia in PD (Litvan *et al.*, 2012). Specific cognitive tasks per domain included:

- Attention: Digit span backwards (Wechsler, D, 2008) and Stroop: Naming (Stroop, 1935)
- Executive function: Stroop Interference (Stroop, 1935) and Category fluency (Rende *et al.*, 2002)
- Memory: Word Recognition Task (Warrington, 1984) and Logical Memory (Wechsler, D, 2008)
- Language: Graded Naming Task(Warrington, 1997) and Letter fluency (Rende *et al.*, 2002), and

- Visuospatial: Benton's Judgment of Line (Benton *et al.*, 1978) and the Hooper Visual Organization Test (Hooper, 1983).

Parkinson's dementia was defined as diagnosis of PD and a MoCA score ≤25 as per the Movement Disorder Society Task Force Criteria (Emre *et al.*, 2007). PD with Mild Cognitive Impairment (PD-MCI) was defined as impaired performance (<1.5 standard deviation SD of control performance) on at least two domain neuropsychological tests (Litvan *et al.*, 2012). A composite cognitive z score (averaged across the 5 individual cognitive domains) was also computed for each participant (Maiti *et al.*, 2020).

For the study visit of the LBD cohort and the Baseline Visit and most of Visit 2 of the VIPD cohort, cognitive assessments and questionnaires were completed in person by the author or another trained member of the study team. For Visit 3 and part of Visit 2 of the VIPD cohort, the cognitive assessments and questionnaires were performed remotely due to coronavirus restrictions; this allowed data collection to continue during lockdown but also limit the time participants spent in person and minimise fatigue and anxiety for participants.

Visual assessments

All participants underwent visual assessments at each study visit; these were performed during in-person visits. Visual acuity was assessed using the LogMAR at a distance of 2m (Sloan, 1959), colour vision using the D15 (Farnsworth, 1947) and contrast sensitivity using the Pelli-Robson test at a distance of 1m (Pelli *et al.*, 1988). For both visual acuity and contrast sensitivity, each eye was tested separately and binocularly with glasses and the best score was selected for further analyses.

Disease specific measures

Disease specific measures were also collected for participants with PD/DLB. The Movement Disorder Society revision of the Unified

Parkinson's Disease Rating Scale (UPDRS), was used to assess motor function: this comprises of a questionnaire as well as a motor examination (Goetz *et al.*, 2008). Smell was assessed using Sniffin' Sticks (Hummel *et al.*, 1997). Levodopa dose equivalence scores (LEDD) were also calculated for all participants with PD or DLB (Tomlinson *et al.*, 2010).

Table 2.2. Levodopa equivalent doses for drugs used to treat parkinsonian symptoms (adapted from (Tomlinson *et al.*, 2010)).

Drug class	Drug	Total LED (mg/100mg Levodopa)
Levodopa	Levodopa	100
	Controlled release Levodopa	133
	Duodopa	90
COMT inhibitors	Entacapone	Levodopa dose × 0.33
	Tolcapone	Levodopa dose × 0.5
Dopamine agonists	Pramipexole	1mg salt
	Ropinirole	5
	Rotigotine	3.3
MAO-B inhibitors	Selegiline 10mg (oral)	10
	Rasagiline	1
Other	Amantadine	100
	Apomorphine (infusion or intermittent injections)	10

COMT: catechol-O-methyl transferase; MAO-B: monoamine oxidase type B.

2.3. Principles of MRI

Magnetic resonance imaging (MRI) produces images from the nuclei of hydrogen ions. Hydrogen ions are found in the majority of human tissue as tissues are mostly composed of fat and water, both containing hydrogen atoms. The nucleus of a hydrogen ion consists of a singly positively charged proton which is constantly spinning thereby generating a magnetic field. The magnetic fields of hydrogen protons are normally randomly orientated, but when an external magnetic field (B0) is applied, they become aligned either in parallel or antiparallel to the external magnetic field. The majority of protons becomes aligned parallel to the external magnetic field (as this requires less energy) leading to a change in the protons' rotational axis. The frequency of this rotational change (how many times the protons spins around its axis per second) or Larmor frequency is determined by:

$$\omega_0 = \gamma B_0$$

where γ is a constant, the gyromagnetic ratio, of a particular element (hydrogen in this case) and B0 is the strength of the externally applied magnetic field. Protons that are spinning in parallel to B0 gradually cancel each other out in all directions other than the z-axis along B0, thereby resulting in a sum magnetic field which parallels B0 or longitudinal magnetisation.

When a radiofrequency pulse (RF) is applied at the Larmor frequency, energy is transferred from the RF pulse to the protons, a phenomenon called magnetic resonance. The protons move to a higher energy state and become antiparallel to the external magnetic field B0; in addition the RF pulse causes the protons to move in the same direction at the same time, or *in phase*. This results to a new sum magnetic field transverse to B0 (in the x-y plane) which moves at the Larmor frequency. Because the transverse field is

moving, if a conductive received coil is placed in its proximity an electrical current will be generated forming an MR signal. When the RF pulse is switched off the protons gradually fall out of phase and return to a lower energy state, this is known as relaxation. Relaxation occurs in two ways: longitudinal relation (or T1, "Time 1") when the longitudinal magnetization protons start moving from the higher to the lower energy state and transverse relaxation (or T2, "Time 2") when the transverse sum magnetic field begins to dissipate as the protons dephase. Both types of relaxation occur simultaneously and result to the signal decaying in direction and magnitude over time. The MR signal generated from the spiraling sum magnetization vector is termed free induction decay. As the magnetic field gradients that are used to localise the MR signal can further disrupt free induction decay, the MR signal is measured in the form of an echo signal. This is done either by an additional 180^{o} RF pulse applied after the initial 90^{o} pulse (*spin echo*) or by refocusing a magnetic field gradient (*gradient echo*).

Formation of MR images

Differences in the relaxation times (T1 and T2) between different tissues lead to different signal intensities between them. When the main difference in between-tissue signal intensity is attributed mainly due to differences in T1 relaxation time this is a T1-weighted image; these are primarily generated by manipulating the repetition time (TR), or the time between two RF pulses. Shorter TR allows T1 relaxation differences to develop before the next RF pulse. When the main difference in signal intensity is caused by spin-spin interactions within tissues or T2 relaxation, this is called a T2-weighted image. Longer times between the application of the RF pulse and the induction of the signal in the coil (echo time or TE) are needed to maximise these local differences between different tissue types. Therefore, longer TR and TE generate a T2-weighted image whilst shorter TR and TE

generates a T1-weighted image. T2 relaxation is also affected by inhomogeneity within the local magnetic field due to tissue inhomogeneity (T2* relaxation). MR signal intensity can of course be influenced by many other parameters as well including proton density, blood flow, repetition time, echo time, and magnetic susceptibility. However in the case of T1 and T2 weighted images, relaxation time is the most important determinant of signal intensity.

The MRI signal then needs to be localised in space, which is achieved by three magnetic field gradients applied across three axes:

1) a slice selection gradient field. Thich is generated along a chosen axis to alter the strength of B0 so that protons within the gradient field have different Larmor frequencies. As the RF pulse is applied as a range rather than a single frequency, this field leads to a slice of a specific thickness being excited.

2) a phase encoding gradient. After the RF pulse is applied protons are in phase. Applying a phase-encoding gradient along another axis causes some protons to spin faster than other depending on their position on this gradient. When the gradient is switched off, all of the protons are exposed to the same magnetic field again (they therefore have the same frequency) but are now out of phase and can be differentiated.

3) a frequency encoding gradient, applied with and perpendicular to the phase encoding gradient. This helps to differentiate the signal from protons with different frequencies, as it alters the protons rotational frequencies depending on their position on the gradient.

This pulse sequence is repeated many times with each repetition increasing the phase encoding gradient (keeping the slice selection and frequency encoding gradient the same). Each repetition of the phase encoding generates a signal echo, stored in “k-space” as a line of data in the matrix.

Data in “k-space” undergo Fourier transform and are finally converted into an image (Currie *et al.*, 2013).

2.4. Diffusion Weighted imaging

Diffusion weighted imaging (DWI) is acquired using Echo-planar imaging (EPI) which allows the acquisition of multiple signal echoes from one TR; this shortens acquisition times and also reduces artifacts due to in-scanner motion (Mansfield, 1977; Poustchi-Amin *et al.*, 2001). EPI is based on a rapidly oscillating frequency encoding gradient (rather than static); each oscillation then corresponds to signal echo, or one line of data in “k-space”.

In DWI, the intensity of the MR signal depends on the diffusion of water molecules in a magnetic field. This can be measured using a pulsed gradient spin echo sequence which adds two additional gradient pulses to an EPI sequence causing a phase shift (Stejskal and Tanner, 1965). The phase shift resulting from the diffusion encoding gradient varies across the gradient and therefore diffusion, causing displacement will lead to higher phase shift, so reduced intensity of the MR signal. The gradient is commonly defined by its diffusion weighting, or b-value:

$$b = \gamma^2 G^2 \delta^2 (\Delta - \frac{\delta}{3})$$

where γ is the gyromagnetic ratio, G is the amplitude of the diffusion gradient, δ the duration of the diffusion gradient and Δ the diffusion time interval (Hagmann *et al.*, 2006). By repeating gradient pulses in multiple directions more data points are acquired, and the resulting diffusion image is more detailed.

Diffusion tensor imaging

The classical method of modelling DWI data is diffusion tensor imaging (DTI) which is based on the assumption that water molecules show anisotropic diffusion, with a diffusion tensor represented as an ellipsoid parallel to the axon in white matter (the main direction of diffusion is parallel to the axon) (*Figure 2.1*). This distribution can be described mathematically as a 3x3 matrix as diffusion occurs in 6 planes and can be modelled from 6 data points; it can be then decomposed into 3 eigenvectors λ_1, λ_2 and λ_3 (*Figure 2.1*). The diffusion tensor will differ between different tissue types (*Figure 2.1*) and to a lesser degree within the white matter itself thereby providing information on white matter integrity and structure with metrics such as fractional anisotropy (FA), the directional preference of diffusion and mean diffusivity (MD), the average diffusion rate across all directions (Le Bihan *et al.*, 2001).

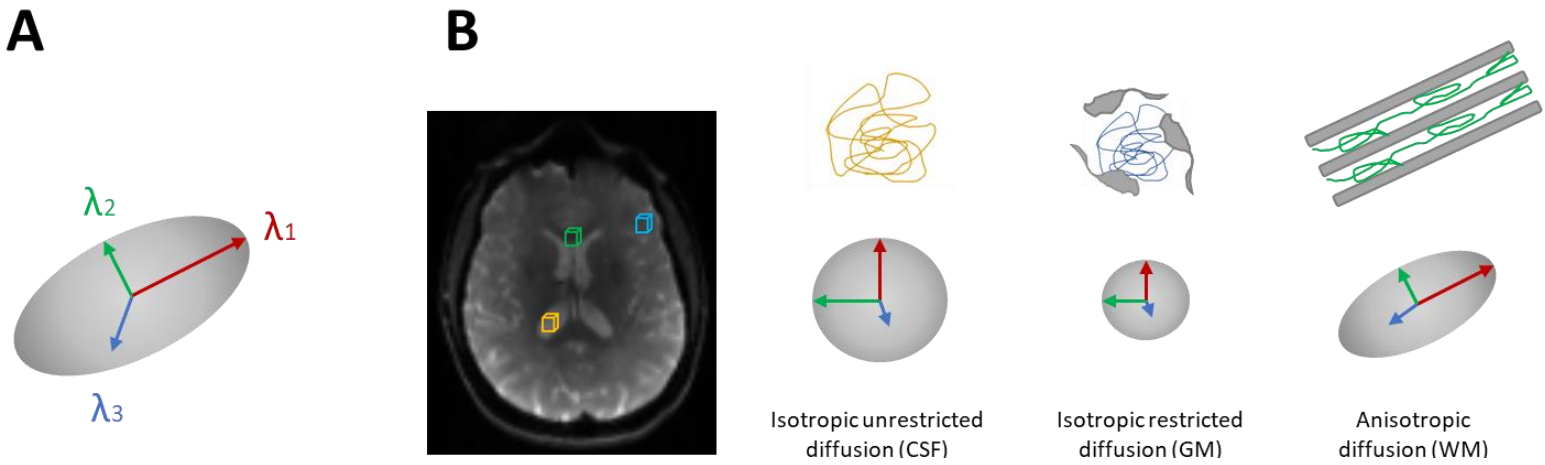

Figure 2. 1. The Diffusion Tensor

A. The diffusion tensor as an ellipsoid with eigenvectors λ_1, λ_2 and λ_3 in the principle axes of diffusion

B. Differences in tissue type result in different orientation and anisotropy of diffusion. Within the cerebrospinal fluid (CSF), diffusion is unrestricted and isotropic, within the grey matter (GM) diffusion is still relatively isotropic but less free or restricted, and in the white matter (WM) diffusion is less restricted along the axon and is anisotropic.

The diffusion tensor model is simple and performs well when all white matter fibres within a voxel are oriented in the same direction. However when white matter fibres are oriented perpendicular to each other (crossing fibres) the diffusion tensor will not be able to disentangle different directions of diffusion and derived metrics will not be able to assess the integrity of underlying white matter. In addition, DTI will not be able to track and delineate the underlying white matter pathways in regions of crossing fibres potentially resulting to spurious connections. As crossing fibres may be found in 70-90% of white matter (Jeurissen *et al.*, 2013), other models that can account for different white matter orientations are needed (Tournier *et al.*, 2011).

Constrained spherical deconvolution

Several models have been developed in recent years to overcome the problem of crossing fibres; one such model includes constrained spherical deconvolution (CSD). CSD is based on the principle that the DWI signal from all fibre populations is similar: the main signal follows the main axis of the fibres and is relatively preserved across fibres. Based on this principle, the DWI signal for a canonical fibre population is the sum of the signals of all the fibre population within a voxel, The observed DWI signal can therefore be deconvolved to calculate the fibre orientation distribution (FOD) for each fibre population within a voxel after calculating the response function: the signal attenuation from individual fibre populations across the z axis (*Figure 2.2*).

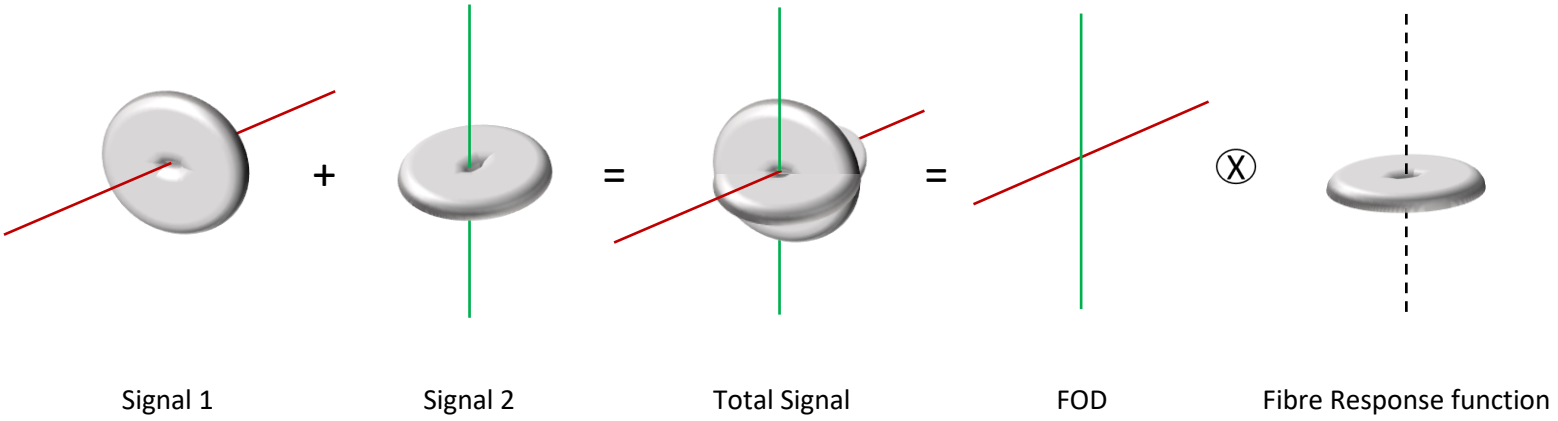

Figure 2. 2. Spherical deconvolution.

The signal from multiple separate white matter fibre populations within a voxel contributes to the total observed signal from DWI. Given the assumption that all fibre populations show the same signal profile, this is equivalent to the convolution of the spere of a fibre orientation distribution (FOD) with the fibre response function.

Adapted from Dell'Acqua and Tournier, 2019.

CSD uses spherical harmonics to calculate the coefficients of the fibre orientation density function that minimise the least-squares fit of the predicted signal within a given voxel and the sum of squares of the negative amplitudes (Dell'Acqua and Tournier, 2019). This is a computationally efficient approach (Tournier *et al.*, 2007) and is very high performing compared to other algorithms (Ramirez-Manzanares *et al.*, 2011; Neher *et al.*, 2015). By including additional compartments in the model, an extension of CSD termed multi-shell multi-tissue CSF can also account for signal from non white matter tissues providing an even more accurate estimation of FODs (Jeurissen *et al.*, 2014; Hollander, T. *et al.*, 2016).

The response function of each tissue type (white matter, grey matter and cerebrospinal fluid) is calculated with the dwi2response command at MRtrix (Tournier *et al.*, 2019) and then spherical deconvolution of the response function is performed using the command dwi2fod resulting in the FOD; this applies a non-negativity constraint to the algorithm as negative FODs are not biologically plausible (Tournier *et al.*, 2007; White and Dale, 2009).

Advanced acquisition protocols including multi-shell data with at least 3 different b-values is needed for multi-shell multi-tissue CSD; this was possible for the acquired DWI data used in this thesis therefore allowing for a more accurate FOD estimation. In addition, a high b-value (b=2000 s/mm^2) was acquired; higher b-values further improve CSD performance (Tournier *et al.*, 2007).

Fixel-based analysis

Based on CSD, Fixel-based analysis is an emerging framework that derives quantitative metrics within specific fibre populations within voxels (which is termed *fixel*) instead of comparing measures averaged across voxels (Raffelt *et al.*, 2017).

Fixel based analysis can be used to derive three quantitative metrics at a subject level (*Figure 2.3*):

- ***Fibre density (FD) or apparent fibre density:*** FD is calculated as the integral of each fixel's FOD amplitude and is proportional to the intra-axonal volume of fibre bundles aligned with that fixel. FD is therefore sensitive to within-voxel changes and is a measure of microstructural white matter changes within a tract (Raffelt *et al.*, 2012).

- ***Fibre cross-section (FC):*** FC is calculated as the extent of distortion (change in fixel orientation) that needs to be applied to each fixel to spatially normalise the subject to the study template:

$$\boldsymbol{FC_f = \frac{det(J)}{||J\widehat{v_f}||}}$$

  where det is the matrix determinant, $\boldsymbol{\widehat{v}_f}$ is the vector of the direction of fixel f, and J is the Jacobian matrix at the fixel's location within the voxel. FC is therefore a relative metric of bundle cross-section and is calculated based on a study template. Values of > 1 compared to the template, imply larger cross-section in that subject than average and lower values suggest atrophy of a tract (Raffelt *et al.*, 2017). FC provides information on the relative size of fibre bundlers and is therefore a metric of macrostructural changes within the white matter (Raffelt *et al.*, 2017).
- ***Combined measure of fibre density and cross-section (FDC)***: FDC is calculated as FDC = FD * FC for each fixel. As such it takes into account both macrostructural (reduced FC) and microstructural (reduced FD) changes and is an overall measure of a white matter fibre's ability to relay information (Raffelt *et al.*, 2017).

In *Chapters 4* and 5 of this thesis I describe fixel-based analysis across the whole white matter in the VIPD cohort, specifically examining changes in white matter macro- and micro-structure in patients with PD with and without hallucinations. In addition, CSD was used to derive FODs that were then used for tractography and structural connectome construction, described in *Chapters 6 and 7.*

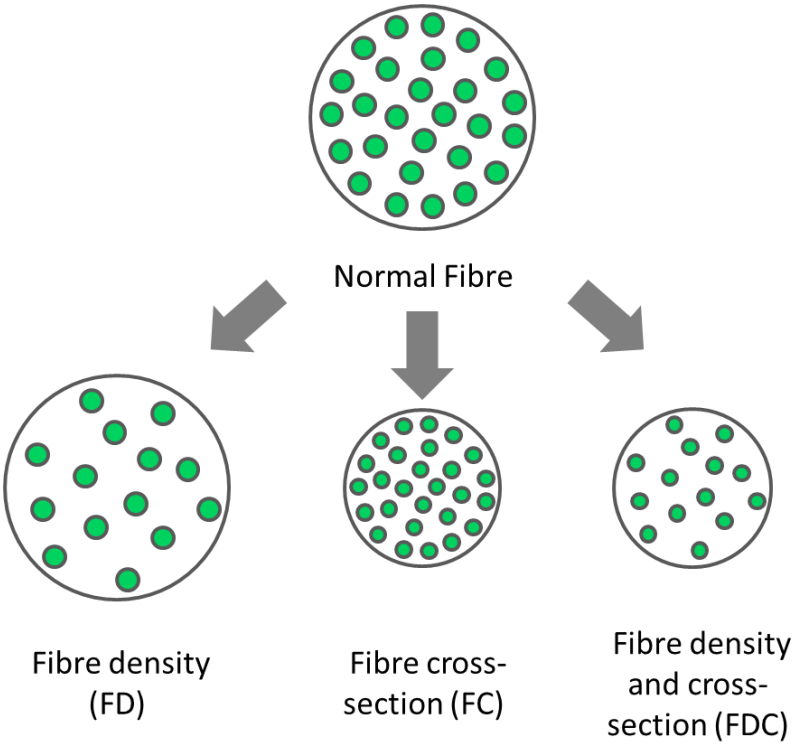

Figure 2.3. Metrics derived from Fixel-based analysis

A normal white matter fibre is shown on the top in a diagrammatic cross-section. In the presence of degeneration, this fibre can become less dense or show microstructural changes (reduced fibre density or FD), can show macrostructural changes or become thinner (reduced fibre cross-section or FC) or can show both micro- and macro-structural changes (reduced combined FDC metric).

2.5. Functional MRI

As with the case of DWI, functional MRI images are acquired using EPI acquisitions. Functional MRI is based on the principle that oxygenated and deoxygenated forms of haemoglobin have different properties: deoxyhaemoglobin is paramagnetic whilst oxyhaemoglobin is weakly diamagnetic (Pauling and Coryell, 1936). Therefore deoxyhaemoglobin induces a magnetic field parallel to the external field B0 whilst oxyhaemoglobin has minimal effect on the signal. This means that regions with high deoxyhaemoglobin will show reduced T2 and T2* weighted MR signal; this is the basis of the Blood Oxygen Level Dependent (BOLD) signal.

Metabolic demands (for example hypoglycaemia or anaesthesia) lead to changes in cerebral blood flow and subsequent increased BOLD signal (Ogawa *et al.*, 1990, 1992; Turner *et al.*, 1991). Increased neuronal activity also leads to increased blood flow. This haemodynamic response to neuronal activity occurs in 3 stages: 1) first there is an initial decrease in BOLD signal below baseline as oxygen consumption leads to increased deoxyhaemoglobin, 2) then a large increase of BOLD signal occurs due to increased blood flow leading to a net increase in oxyhaemoglobin and 3) finally, the BOLD signal returns below the baseline as blood supply is again diminished.

The basis of the haemodynamic response is not fully understood. Both increased oxygen consumption and increased glucose consumption due to neuronal activity have been postulated (Heeger and Ress, 2002). However the BOLD response has been observed in the presence of both hyperoxia and hyperglycaemia (Wolf *et al.*, 1997; Lindauer *et al.*, 2010). The relative delay in peak blood flow after increased neuronal activity also suggests that neurons can meet any increased needs for oxygen or glucose irrespective of

blood flow. Multiple other factors including astrocyte-induced vasodilatation, replenishing nutrient stores, or neurotransmitter control, have been postulated, however it is likely that many factors contribute to the BOLD response (Hillman, 2014). Although the basis of the BOLD response is not clear, the relationship between neuronal activity and BOLD response has been clearly demonstrated (Logothetis *et al.*, 2001) and measuring BOLD signal can therefore be an indirect measure of underlying neuronal activity.

Resting state functional MRI (rsfMRI)

Even in the absence of an explicit task, temporally correlated low-frequency variations in regional BOLD signal (therefore in regional blood flow and underlying neuronal activity) are seen across spatially remote brain regions (Biswal *et al.*, 1995). These fluctuations are correlated with fluctuations in underlying neuronal activity measured by electrophysiology (Shmuel and Leopold, 2008) and with activation patterns seen during tasks (Smith *et al.*, 2009). Additionally, patterns of co-activations between brain regions, or resting state networks are stable and reproducible across individuals and in multiple samples (Rosazza and Minati, 2011). rsfMRI is advantageous in clinical populations, as no specific task is required; this can be particularly useful in patients with cognitive impairment as in the VIPD cohort.

Functional connectivity (or co-activation patterns between regions) during rest is not static but has been shown to fluctuate over time (Chang and Glover, 2010). This dynamic or time-varying functional connectivity where the brain switches between different dynamic states (Hutchison *et al.*, 2013; Allen *et al.*, 2014; Shine *et al.*, 2016) may be more representative of cognitive states than static approaches (Liégeois *et al.*, 2019). Several analysis methods have been developed to assess the dynamic aspects of spontaneous brain activity captured using rsfMRI. In *Chapter 7* I use one

such method, applying sliding temporal windows, to assess the differences in temporal dynamics between patients with Parkinson's with and without hallucinations.

2.6. MRI data acquisition

All MRI data for the VIPD cohort were acquired in the same 3T Siemens scanner with a 64-channel coil, performed in the Wellcome Centre for Human Neuroimaging, 12 Queen Square.

Resting state functional (rsfMRI) was acquired using the following parameters: gradient-echo EPI, TR=70 ms, TE=30 ms, flip angle=90°, FOV=192×192, voxel size=3x3x2.5 mm, 105 volumes. During rsfMRI, participants were instructed to lie quietly with their eyes open and try to avoid falling asleep. This was confirmed by monitoring and post-scan debriefing. The total acquisition time for rsfMRI was approximately 9 minutes.

Diffusion-weighted imaging (DWI) was acquired using the following parameters: b=50s/mm2 /17 directions, b=300s/mm2 /8 directions, b=1000s/mm2 /64 directions, b=2000s/mm2 /64 directions, 2x2x2mm isotropic voxels, TE=3260ms, TR=58ms, 72 slices, 2mm thickness, acceleration factor=2. Acquisition time for DWI was approximately 11 minutes. Importantly DWI acquisition included more than 3 b-values and a maximum b-value >1000; this allowed for the application of multi-shell multi-tissue CSD and improved the fidelity and performance of acquired fixel-based analysis metrics and subsequent tractography.

Structural MPRAGE data (magnetization prepared rapid acquisition gradient echo) was acquired using: 1×1×1mm voxel, TE=3.34ms,

TR=2530ms, flip angle=7°. Acquisition time for MPRAGE was approximately 9 minutes.

2.7. MRI Quality Control

Prior to MRI pre-processing, all volumes of raw datasets for all acquisitions were visually inspected. Each volume was evaluated for the presence of artefact and any scan with ≥15 volumes containing artefacts was excluded (Roalf *et al.*, 2016).

rsfMRI is particularly sensitive to artefacts arising from head motion, as even sub-millimiter movements can distort derived estimates of functional connectivity independent of the chosen analysis approach (Power *et al.*, 2012, 2014; Van Dijk *et al.*, 2012) which can distort group differences. Additional quality assurance steps were taken to minimise the effect of motion artefact, using the MRI quality control tool (MRIQC) (Esteban *et al.*, 2017). Framewise displacements, the subtle in-scanner movements from volume-to-volume were calculated using MRIQC. Rotational displacements were calculated as the displacement on the surface of a sphere with radius 50 mm (the approximate mean distance from the cerebral cortex to the centre of the head) using the following equation:

$$FD_i = |\Delta d_{ix}| + |\Delta d_{iy}| + |\Delta d_{iz}| + |\Delta a_i| + |\Delta \beta_i| + |\Delta \gamma_i|$$

where $\Delta d_{ix} = d_{(i-1)x} - d_{ix}$ and similarly for all the rigid body parameters (Δd_{iy}, Δd_{iy}, a_i, β_i and γ_i) (Power *et al.*, 2012).

Stringent criteria were adopted to exclude high motion participants, as this has been shown to be both effective and efficient with higher reliability in detecting group differences (Parkes *et al.*, 2018). Specifically, participants were excluded from rsfMRI analyses if any of the following criteria was

met: 1) mean frame-wise displacement >0.3mm, 2) any frame-wise displacement >5mm, or 3) outliers >30% of the whole sample.

In addition to excluding high motion participants, image quality metrics were extracted for both functional images and structural images and compared across the groups of interest to ensure that any group differences were not a result of systematic differences in image quality. Specifically the following measures were used as measures of noise:

- **Coefficient of joint variation (CJV):** CJV has been proposed as an objective, quantitative measure of intensity non-uniformity. It is calculated as:

$$CJV = \frac{\sigma(WM) + \sigma(GM)}{\mu(WM) - \mu(GM)}$$

  where σ is the standard deviation and μ is the mean intensity of a given tissue class, WM is white matter and GM is grey matter. Large intensity non-uniformity and head motion will result in higher values, therefore lower values indicate better image quality (Ganzetti *et al.*, 2016).
- **Signal to noise ratio (SNR):** This is an important measure of noise, calculated within the tissue mask of the gray matter (GM) as:

$$SNR = \frac{\mu(GM)}{\sigma(AIR)}$$

  where σ is the standard deviation and μ is the mean intensity of a given tissue class (Magnotta *et al.*, 2006).
- **Entropy focus criterion (EFC):** EFC is a metric of ghosting and blurring induced by head motion; this is indirectly assessed by the Shannon entropy of voxel intensities and calculated as:

$$E = -\sum_{j=1}^{S} \frac{B_j}{B_{max}} \ln\left[\frac{B_j}{B_{max}}\right]$$

where S is the total number of pixels, B_j is the modulus of the value of the jth image pixel and B_{max} is equal to:

$$B_{max} = \sqrt{\sum_{j=1}^{S} B_j^2}$$

EFC is then calculated by normalising the entropy criterion E by the maximum entropy allowing comparison across images (Atkinson *et al.*, 1997).

2.8. MRI data pre-processing

Structural T1-weighted images

Following quality control, structural images underwent pre-processing and automatic segmentation using FreeSurfer v6.0 (https://freesurfer.net/). Automatic segmentation is particularly advantageous when dealing with large sample sizes, reducing time whilst maintaining accuracy and improving reproducibility. The Freesurfer implementation is based on a probabilistic model using a surface-based coordinate system to calculate the probability of a specific anatomical structure occurring in a specific brain region as well as the probability that a structure contains specific MR properties (Fischl *et al.*, 1999). Freesurfer combines these with prior knowledge about anatomical location, to label cortical and subcortical structures according to a specific atlas, as well as to derive structural measurements. The choice of atlas or parcellation used in the studies presented in this thesis differed according to the specific research question; the specific parcellation and reasons for choosing it will be discussed in individual chapters.

Irrespective of parcellation choice, the Freesurfer pipeline performs the following steps:

- Skull stripping is first performed: signal from non-brain tissue is removed
- The T1-weighted image is registered to Talairach space (Talairach and Tournoux, 1988) through affine registration (preserved global image features)
- Intensity normalisation: the signal intensity of white and grey matter is homogenised. This allows for better subsequent distinction between tissue types and improves segmentation results.
- Initial labelling of cortical and subcortical structures.
- Bias field correction: tissue types are classified and a bias-free image created. The residual image is generated by subtracting the bias-free image from the original one; this is used to estimate the bias field (Gispert *et al.*, 2004).
- Non-linear registration of the T1-weighted image to the Talairach atlas. Cortical and subcortical structures are then re-labelled.

For the purposes of longitudinal analysis in *Chapter 5*, the dedicated longitudinal pipeline from Freesurfer was used (Reuter et al., 2012) after the Baseline and Visit 2 scans for each VIPD participant were processed with default parameters following the above pipeline. An unbiased within-subject template image was created for each participant using inverse consistent registration and taking into account both the Baseline and Visit 2 image. Subsequent processing steps were initialized from the within-subject template, thereby increasing accuracy and statistical power (Reuter et al., 2012). After longitudinal processing, surface reconstructions of the template and of images at Baseline and Visit 2 were inspected, corrected, and reprocessed where necessary.

Diffusion weighted images

Following quality control steps described previously, DWI images underwent denoising (Veraart *et al.*, 2016) using the dwidenoise command and removal of Gibbs ringing artefacts (Kellner *et al.*, 2016) using the mrdegibbs command in MRtrix (Tournier *et al.*, 2019). Motion and distortion correction was then performed using the dwipreproc pipeline in MRtrix (Tournier *et al.*, 2019). This performs the following corrections:

- EPI distortion correction (Holland *et al.*, 2010) using two b0 images one acquired in the phase encoded direction (PE) and one in the reversed direction.
- B0-field inhomogeneity correction using FSL's topup tool (Andersson *et al.*, 2003)
- Eddy-current and movement distortion correction (Andersson and Sotiropoulos, 2016) using FSL's eddy tool. This shows better performance than previous methods (Graham *et al.*, 2016).

Then DWI images underwent bias field correction (Tustison *et al.*, 2010) using the dwibiascorrect command. This improves subsequent brain mask estimation. Finally, a brain mask was estimated using the dwi2mask command; this removes non-brain matter from the image. After brain mask calculation, each mask was visually inspected to assess whether non-brain matter was included or whether brain matter was inappropriately removed from the image; masks were manually corrected if required.

The response function was then estimated for each participant's grey matter, white matter and cerebrospinal fluid using dwi2response followed by a group averaged white matter response function estimation (Tournier *et al.*, 2013). The DWI spatial resolution of diffusion weighted images was then upsampled to a voxel size of 1.3 mm^3 using cubic interpolation as this has been shown to improve anatomical contrast and downstream template

building, registration and statistics and is recommended for fixel based analysis (Tournier *et al.*, 2019). Global intensity normalisation was then used across subjects to allow comparisons between participants (Raffelt *et al.*, 2017).

Next, fibre orientation distributions (FODs) were calculated for each participant via the Multi-Shell Multi-Tissue Constrained Spherical Deconvolution (MSMT-CSD) using the group average response function for each of the three tissue types (grey matter, white matter and CSF) (Hollander, T. *et al.*, 2016).

An unbiased, study-specific FOD template was created using FOD images from 30 randomly-selected subjects (20 Parkinson's disease, 10 healthy controls) in accordance with previous studies using fixel-based analysis (Mito *et al.*, 2018). Each subject's FOD image was then registered to the template using FOD-guided non-linear registration (Raffelt *et al.*, 2011). Fixel-based metrics (fibre density (FD), fibre cross-section (FC) and combined fibre density and cross-section (FDC)) were then calculated for each participant in template-space.

Functional images

Preprocessing of rsfMRI data was performed using fMRIPrep 1.5.0, which offers a standardised, automated processing pipeline (Esteban *et al.*, 2019). The first 4 volumes were discarded to allow for steady state equilibrium. Functional data was slice-time corrected using 3dTshift from AFNI (Cox, 1996) and motion corrected using mcflirt (Jenkinson *et al.*, 2002). Distortion correction was performed using a TOPUP implementation (Andersson *et al.*, 2003). This was followed by co-registration to the corresponding T1-weighted image using boundary-based registration with six degrees of freedom (Greve and Fischl, 2009). Motion correcting transformations, field distortion correcting warp, BOLD-to-T1w transformation and T1w-to-

template (MNI) warp were concatenated and applied in a single step using antsApplyTransforms (ANTs v2.1.0) using Lanczos interpolation. Physiological noise regressors were extracted applying CompCor (Behzadi *et al.*, 2007). Spurious sources of signal were removed through linear regression: six motion parameters, mean signal from white matter and cerebrospinal fluid. I did not regress global signal given the lack of consensus and potential to distort group differences (Saad *et al.*, 2012).

3. Quantifying the use of prior knowledge in Parkinson's associated hallucinations

3.1 Introduction

Dementia with Lewy Bodies and the related Parkinson's Disease Dementia are together the second most common cause of dementia in the elderly (Rahkonen *et al.*, 2003) accounting for approximately 15% of all dementia cases, with more than 130,000 people affected in the UK. Although they may differ in the sequence of onset of dementia and parkinsonism, but with disease progression, they produce a similar clinical phenotype and underlying pathological changes. These similarities have led to expert consensus that they are a continuum of Lewy Body disease (LBD: Dementia with Lewy Bodies and Parkinson's disease) rather than separate entities (Rahkonen *et al.*, 2003). Considering the two diseases together can provide useful insights into common mechanisms leading to the same symptom of hallucinations, an approach that has been advocated in recent years (Jellinger, 2012; Postuma *et al.*, 2016; Weil *et al.*, 2017).

One common symptom of LBD is visual hallucinations, which affect up to 70% of patients (Fénelon *et al.*, 2000; Hely *et al.*, 2008). Hallucinations are associated with worse outcomes in LBD: cognitive decline, increased mortality (Hobson and Meara, 2004), higher carer burden (Aarsland *et al.*, 2007), worse quality of life (McKinlay *et al.*, 2007) and higher likelihood of nursing home placement (Aarsland *et al.*, 2000). However, despite their importance for patients and carers, the neural mechanisms of visual hallucinations remain poorly understood and treatment options for visual hallucinations are limited (Fénelon *et al.*, 2000; Weil *et al.*, 2016).

A recent, useful framework for visual hallucinations suggests that they can be thought of as false inference, which arises due to impaired integration of sensory input and prior knowledge during visual perception (Fletcher and Frith, 2009; Adams *et al.*, 2013; Powers *et al.*, 2016; Corlett *et al.*, 2019). Indeed, recent evidence suggests that hallucinations occurring in healthy individuals or due to psychiatric disease are associated with an increased influence of prior knowledge and reduced influence of sensory evidence when viewing ambiguous visual or auditory stimuli (Teufel *et al.*, 2015; Alderson-Day *et al.*, 2017; Powers *et al.*, 2017; Davies *et al.*, 2018).

Visual hallucinations in LBD are associated with visual-processing deficits (Diederich *et al.*, 2005; Williams-Gray *et al.*, 2013; Fereshtehnejad *et al.*, 2019) and impaired accumulation of sensory evidence (O'Callaghan *et al.*, 2017). However, hallucinations are also experienced by patients without any visual deficits (Gallagher *et al.*, 2011; Weil *et al.*, 2016) making a solely bottom-up explanation for the occurrence of hallucinations less attractive.

The aim of the study presented in this chapter is to test the hypothesis that visual hallucinations in LBD are associated with an increased weighting of prior knowledge. To quantify the use of prior knowledge during visual perception, a visual learning paradigm was used where sensory evidence remained constant but prior knowledge was manipulated by supplying participants with information and comparing performance before and after information was provided.

I hypothesised that:

1) patients with LBD and visual hallucinations would show greater improvement in performance compared to patients with LBD who did not experience hallucinations after receiving prior knowledge

2) this performance benefit would be higher in those patients with more severe hallucinations.

3.2 Methods

Study Participants

A total of 57 participants were recruited to this study: 37 patients with LBD and 20 age-matched unaffected controls (*LBD cohort, Chapter 2.1*). All patients with LBD satisfied either the United Kingdom Parkinson's Disease Society Brain Bank criteria for Parkinson's disease, the Movement Disorder Society criteria for Parkinson's disease dementia or the Dementia with Lewy Bodies Consortium Criteria for DLB (Gibb and Lees, 1988; Emre *et al.*, 2007; McKeith *et al.*, 2017). Patients with LBD were further classified as habitual hallucinators (LBD-VH, n=17) if they scored ≥1 on question two of the Movement Disorder Society Unified Parkinson's Disease Rating Scale (UPDRS: "Over the past week have you seen, heard, smelled or felt things that were not really there?") (Goetz et al., 2008). All other participants were classified as LBD non VH. Details on the phenotype, frequency and severity of visual hallucinations were collected using the University of Miami Parkinson's Disease Hallucinations Questionnaire (UM-PDHQ) (Papapetropoulos et al., 2008).

All assessments and the experimental task were performed with patients in the ON state. The full list of clinical and neuropsychological assessments used in the LBD cohort are described in *Chapter 2.1* and in the relevant publication (Zarkali *et al.*, 2019). In brief, motor function was assessed using the UPDRS (Goetz *et al.*, 2008). General cognition using Mini-Mental State Examination (MMSE) and Montreal Cognitive Assessment (MoCA) (Dalrymple-Alford *et al.*, 2010; Creavin *et al.*, 2016). In addition two specific tasks were assessed per cognitive domain Attention: Digit span backwards (Wechsler, D, 2008), Stroop test: Naming subtest (Stroop, 1935), Executive function: Stroop Interference (Stroop, 1935), Category fluency (Rende *et al.*, 2002), Memory: Word Recognition Task (Warrington, 1984), Logical Memory (Wechsler, D,

2008), Language: Graded Naming Task (Warrington, 1997), Letter fluency (Rende *et al.*, 2002), Visuospatial: Benton's Judgment of Line (Benton *et al.*, 1978), Hooper Visual Organization Test (Hooper, 1983). Visual acuity was assessed using the 6-meter Snellen chart, colour vision using the D15 (Farnsworth, 1947) and contrast sensitivity using the Pelli-Robson (Pelli *et al.*, 1988).

Experimental design and procedure

A visual learning paradigm was used with two-tone images as stimuli. These appear when first seen as meaningless black and white patches (*Figure 3.1*) but after the template from which they were created is seen (therefore prior knowledge is given (*Figure 3.2, opposite*)) they generate a strong, coherent percept (Dolan *et al.*, 1997; Moore and Cavanagh, 1998; Hegdé and Kersten, 2010; Hsieh *et al.*, 2010; Cavanagh, 2011; Teufel *et al.*, 2015).

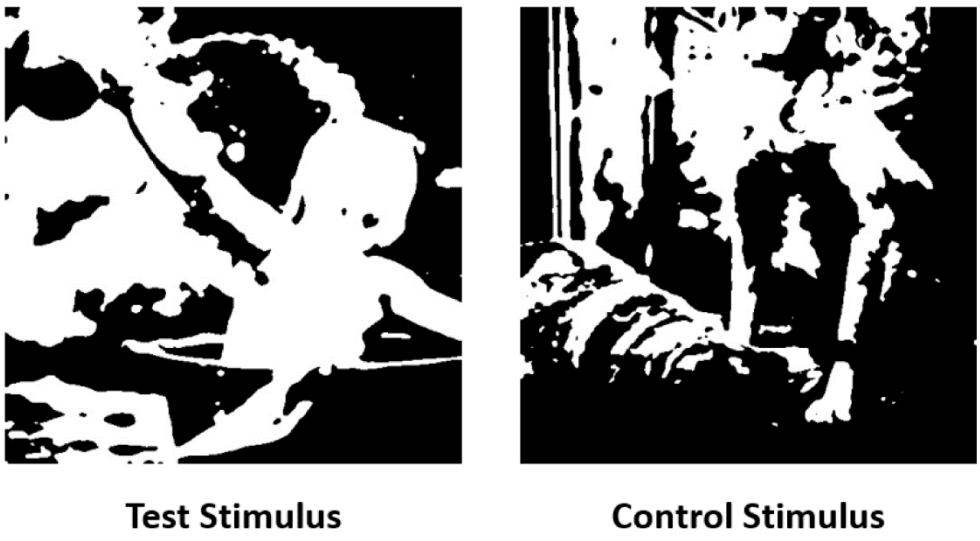

Figure 3.1 Two-tone stimuli.

Example of a test stimulus (Left) and control stimulus (Right). Both have similar characteristics, but the test images contain a person whilst the control images do not.

Figure 3.2 Example of a template image.

This image was used to create the test stimulus in Figure 3. 1.

Disambiguation of two-tone images after prior knowledge is provided is mediated primarily by top-down influences and therefore can be used as a proxy to quantify the effect that top-down influences have on visual perception (Dolan *et al.*, 1997; Hsieh *et al.*, 2010; Teufel *et al.*, 2015; Davies *et al.*, 2018). To do this, the performance of participants in disambiguating the two-tone images was assessed before and after prior knowledge was supplied using a block design (*Figure 3.3*).

The experiment consisted of 6 sessions, each with three trial blocks:

- ***Before block***: where participants were presented with 10 two-tone images (examples in *Figure 3.1*)

- ***Template block:*** participants presented with 20 coloured images (the templates for the 10 two-tone images of the Before block and 10 distractor images) in random order, and

- ***After block***: repetition of the 10 two-tone images of the Before block (their order was randomised).

This lead to a total of 60 ***Before*** and ***After*** trials per participant. The order of images presented within each block was randomised. On each trial participants were presented with an image (two-tone or colour) for 800ms. Then they were asked to indicate whether they saw a person or not in the image by keyboard press (*Figure 3.3*). There was no time limit on the response to account for expected prolonged reaction times of the LBD cohort. Participant responses during the ***Template*** blocks were not used in the analysis, but were recorded to ensure that participants were actively observing the template images thus receiving optimal prior information.

The experiment started with a practice session identical to the experimental sessions; only participants achieving >=65% discrimination sensitivity in the practice session proceeded to the experiment. All recruited participants passed this threshold, and therefore none were excluded from subsequent analyses. Each experimental session (comprised of a *Before, Template* and *After* block) lasted ~7 minutes with a total experiment time of ~45 minutes.

The experiment was conducted using a Dell XPS9570 15’ laptop with a 4k display at maximum brightness setting. The stimuli were presented with a custom application made on Unity (version 2018.3.0b4) with participants seated at distance ~60cm from the screen. The experimental procedure is described in *Figure 3.3*.

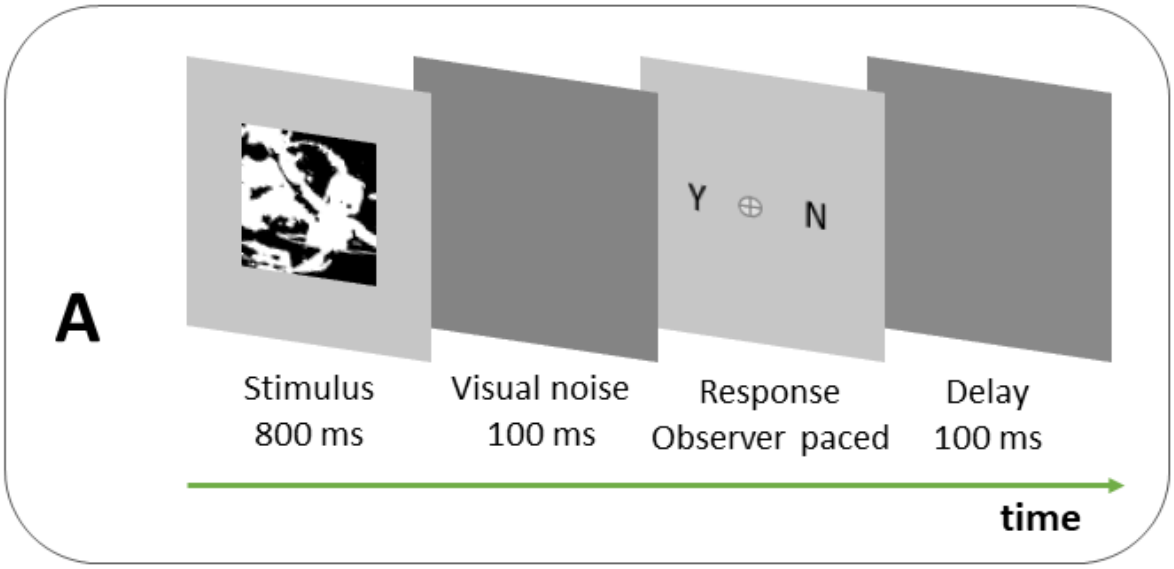
A
Y
N
Stimulus
800 ms
Visual noise
100 ms
Response
Observer paced
Delay
100 ms
time

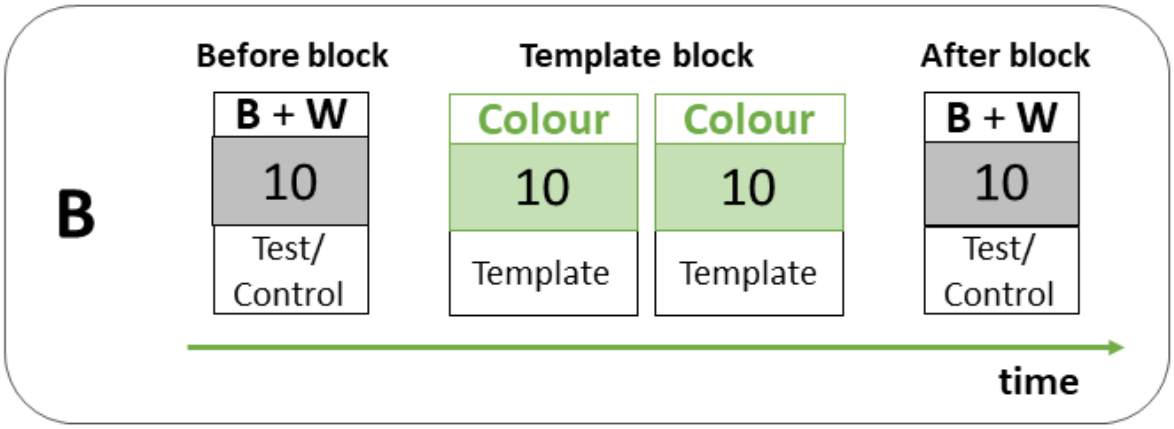
B
Before block
Template block
After block
B + W
10
Test/
Control
Colour
10
Template
Colour
10
Template
B + W
10
Test/
Control
time

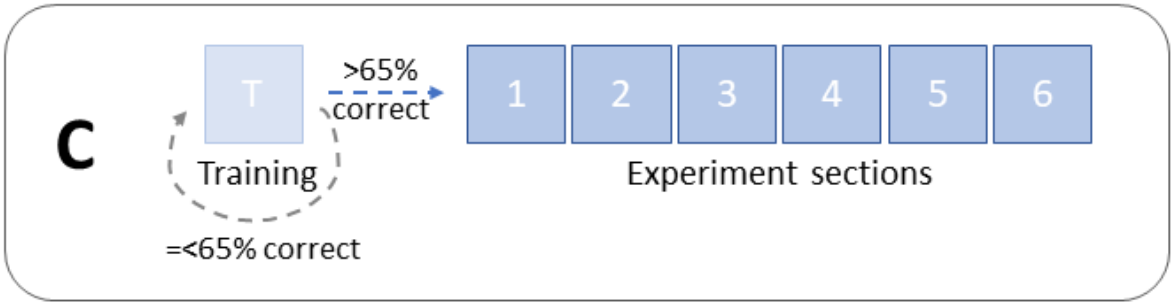
C
T
>65%
correct
Training
=<65% correct
1
2
3
4
5
6
Experiment sections

Figure 3.3. Illustration of the experimental procedure.
(Opposite)

A. Individual trial: *Participants are presented with an image and asked to indicate whether the image contains a person or not. Response was observer-paced without time limit to ensure capture from our clinical groups.*

B. Experiment Section: *First, in the Before Block, participants are presented with 10 two-tone images (5 test stimulus, 5 controls) in random order. Then, participants are presented with a Template block of 20 colour images in random order (including all templates for the two-tone stimuli shown in the Before Block). After each presented template image participants are asked again to indicate the presence of a person. This facilitates participant compliance by keeping the task simple and also ensures that participants actively observe the template images so optimal prior knowledge of the two-tone image content is provided. Finally, in the After Block, participants are presented with the same two-tone images as in Before Block in random order.*

C. Experiment: *The experiment consists of 6 sections and starts with a training section, identical to the experimental sections but with two-tone images that are easier to disambiguate. Only participants with >65% discrimination sensitivity proceed to the main experiment (all participants achieved this threshold).*

Stimulus generation procedure

A total of 150 two-tone images were created with a custom Python script using coloured high-definition template images of people and animals which were downloaded from https://stocksnap.io and https://www.pexels.com/ under the Creative Commons License. Template images were resized to 500x500 pixels using cubic interpolation and converted to grayscale. Image noise was cleared through opening (erosion followed by dilation) with a 1x1 kernel. A Gaussian blur was applied with a 9x9 kernel. Finally, a binary and Otsu threshold were applied (Sezgin and Sankur, 2004) (*Figure 3.4*).

The code used to generate the stimuli as well as the individual stimuli is available: https://github.com/AngelikaZa/Increased-weighting-on-prior-knowledge-in-Lewy-Body-associated-visual-hallucinations.-BrainComms2019

Figure 3.4. Illustration of the stimulus creation process.

Template images were resized to 500x500 pixels using cubic interpolation and converted to grayscale. Image noise was cleared through opening (erosion followed by dilation) using a 1x1 kernel. A Gaussian blur was applied with a 9x9 kernel. Finally, a binary and Otsu threshold were applied to each image (Sezgin and Sankur, 2004) resulting to the final Two-tone image.

The resulting two-tone images were piloted with 17 healthy volunteers to assess discrimination sensitivity before and after viewing the templates. Two-tone images that were too easy to disambiguate (≥75% of volunteers) before viewing the template or too difficult after seeing the template (≤25% of volunteers) were excluded. From the remaining two-tone images, 60 were randomly selected (30 of people and 30 of animals) for the main experiment. The presentation time of 800ms chosen in the experiment was also guided by reaction time data collected during pilot testing. Seventeen healthy volunteers were asked to indicate the presence of a person in the two-tone stimuli using a keyboard press without any prior information and without presentation time limit. A keyboard press triggered the next stimulus to be presented. Decision time was recorded and 800ms (mean + 2SD) was chosen for the main experiment.

Statistical analysis

Correct responses and reaction times for each participant and each trial were recorded in the ***Before*** and ***After*** blocks and analysed using signal detection theory (Tanner and Swets, 1954). In each experimental trial there are four possible outcomes: *hit* (person present in the presented stimulus and participant says "yes"), *miss* (person present and participant says "no"), *false alarm* (person absent and participant says "yes"), and *correct rejection* (person absent and participant says "no"). In this way, we can derive hit rates and false alarm rates from the collected responses; this was done separately for the ***Before*** and ***After*** Blocks.

I then derived *discrimination sensitivity (d')*: a measure of the observer's ability to distinguish 'signal' from 'noise' distributions (independent of any bias) from the following equation:

$$d' = z(h) - z(f)$$

where h: hit rate, f: false alarm rate.

Criterion (c) was also derived: a measure of the bias the observer has to detect a signal (Macmillan and Creelman, 1991), using:

$$c = -1/2[z(h) + z(f)]$$

where h: hit rate, f: false alarm rate.

Independent t-samples and ANOVAs were used to compared normally distributed continuous variables with Tukey post-hoc test and Mann-Whitney and Kruskall-Wallis for non-normally distributed ones, with Nemeyni post-hoc test (Shapiro-Wilk test and visual inspection used to test normality). In the main comparison of interest (LBD-VH vs LBD-non-VH) I also performed uncorrected t-tests and Kruskall-Wallis tests, to avoid missing small but potentially important differences between the two groups. The statistical significance threshold was set at $p<0.05$. All statistical analysis was performed in Python 3 (Jupyter Notebook 5.5.0).

3. 3. Results

57 participants were included: 17 patients with LBD and visual hallucinations (LBD-VH), 20 patients with LBD without hallucinations (LBD-non-VH) and 20 age-matched controls.

Demographics and results of clinical assessments

The three study groups did not significantly differ in demographics, education, low level vision, and general cognition (*Table 3.1*).

Of three measures of higher-level visuospatial perception, only one differed between groups: the Hooper test [Kruskal-Wallis: $H=86$, $p<0.001$] with post-hoc analysis attributing this difference to lower performance in LBD-VH compared to controls [$U=86$, $p=0.005$] whilst no difference in performance was seen between LBD-VH and LBD-non-VH [$U=141$, not

significant]; the other two visuo-perceptual measures (Judgement of Line orientation and Visual Object and Space Perception Battery) were not significantly different between any group. Depression scores in the Hospital Anxiety and Depression Scale were higher in LBD-VH [H=24.133, p<0.001] but were below the threshold for diagnosis of depression in this scale (Bjelland *et al.*, 2002; Mondolo *et al.*, 2006).

Of LBD-VH participants n=3 had a diagnosis of Dementia with Lewy Bodies and the remaining n=14 of Parkinson's disease, whilst n=2 of the LBD non VH patients had a diagnosis of Dementia with Lewy Bodies and n=16 had Parkinson's disease. Apart from diagnostic distinctions, there were no statistically significant differences between patients with a diagnosis of Dementia with Lewy Bodies and those with Parkinson's disease in disease duration, clinical or demographic measures (*Table 3.2*). Importantly, LBD-VH participants did not differ in any of the neuropsychology measures except for lower MOCA (U=7.0, p=0.043), worse Stroop interference time (U=7.0, p=0.044) and worse performance on Logical Memory Test in those with Dementia with Lewy Bodies (U=1.0, p=0.006).

Table 3. 1. Demographics and clinical characteristics, LBD cohort

Attribute		Controls n = 20	LBD non VH n = 20	LBD VH n = 17	p value*
Demographics	Age in years	69.7 (6.9)	68.9 (7.1)	68 (6.9)	0.457[b]
	Male (%)	11 (55)	13 (65)	7 (41.2)	0.079[b]
	Years in Education	15.9 (2.6)	15.9 (2.3)	15.4 (2.9)	0.567[a]
Mood (HADS)	Depression score	2.2 (2.2)	**2.5 (2.5)**	**4.5 (2.4)**	**0.017**[b]
	Anxiety score	4.3 (2.6)	4.5 (4.1)	5.2 (2.9)	0.212[b]
Vision	Visual acuity (bilateral)	1.1 (0.2)	1.1 (0.2)	1.0 (0.2)	0.216[b]
	Contrast sensitivity (Pelli Robson) (log units) (bilateral)	1.7 (0.2)	**1.7 (0.1)**	**1.5 (0.2)**	**0.017[b]**
	Colour vision (D15)	0.2 (0.4)	0.8 (1.3)	0.4 (1.3)	0.180[b]
Neuropsychology	MMSE	29.5 (0.7)	29 (1.5)	28 (2.1)	0.057[b]
	MOCA	27.8 (1.2)	26.8 (3.1)	25.5 (3.7)	0.131[b]
Attention	Digit span backwards	8.4 (2.4)	7.2 (2.6)	7.1 (2.2)	0.860[a]
	Stroop: Naming (sec)	38.1 (6.5)	**35.8 (8.5)**	**44.7 (14.5)**	**0.007[b]**
Executive function	Stroop: Interference (sec)	69.1 (14.2)	66.7 (22.9)	83 (27.2)	0.062[b]
	Category fluency	19.7 (4.4)	19.8 (4.3)	17.8 (5.6)	0.219[a]
Memory	Word Recognition Task	24.8 (0.4)	23.2 (1.9)	23.6 (2.0)	0.219[b]
	Logical Memory (delayed)	12.4 (4.3)	10.1 (3.9)	11.1 (2.8)	0.309[a]
Language	Graded Naming Task	24.4 (2.5)	23.8 (3.9)	22.3 (3.9)	0.079[b]
	Letter Fluency	16 (4.7)	14.6 (5.5)	12.8 (4.2)	0.297[a]
Visuospatial	VOSP	56.2 (2.0)	54.6 (3.3)	52.8 (5.4)	0.397[b]
	Benton's Judgement of Line Orientation	24.4 (4.3)	25.4 (4.1)	22.3 (4.4)	0.071[b]
	Hooper's Visual organisation test	25.6 (2.4)	23.2 (3.9)	21.7 (4.9)	0.187[b]
Disease specific	Age at diagnosis	-	64.4 (9.0)	63.4 (7.3)	0.719[a]
	Disease duration	-	4.5 (4.6)	4.6 (2.7)	0.944[a]
	RBDSQ	-	4.2 (2.5)	5.1 (3.0)	0.190[b]
	UPDRS Total	-	**38.7 (13.4)**	**52.8 (15.6)**	**0.003[b]**
	UPDRS Question 1.2	-	-	1.76 (0.73)	-
	Miami Hallucinations Questionnaire	-	-	5.2 (1.9)	-
	UPDRS part 3 (motor score)	-	24.7 (7.5)	30.5 (10.6)	0.136[b]
	LEDD (mg)	-	401.9 (288.3)	406 (244.8)	0.500
	Smell test	-	23.2 (3.9)	21.6 (4.9)	0.082[a]

LBD-VH: Patients with Lewy Body Disease and hallucinations; LBD-non-VH: patients without hallucinations.

*All data shown (except gender) are mean (SD). *Uncorrected P values shown are for comparison between LBD/VH and LBD/non-VH (comparison of interest), in bold statistically significant values (p<0.05).* [a] Student t test. [b]Mann-Whitney test. *HADS: Hospital anxiety and depression scale; MMSE: Mini-mental state examination; MOCA: Montreal cognitive assessment; VOSP: Visual Object and Space Perception Battery UPDRS: Unified Parkinson's disease rating scale; LEDD: Total Levodopa equivalent daily dose; RBDSQ: REM sleep behaviour disorder screening questionnaire.*

Table 3. 2. Comparison between participants with Parkinson's disease and patients with Dementia with Lewy bodies

Attribute		PD n = 32	DLB n = 5	p value*
Demographics	Age in years	69.3 (7.2)	67.8 (6.4)	0.817[a]
	Male (%)	17 (40.1)	3 (60)	0.398[b]
	Years in Education	15.6 (2.6)	16.0 (3.2)	0.730[a]
Mood (HADS)	Depression score	**3.2 (2.5)**	**5.3 (3.3)**	**0.033**[b]
	Anxiety score	**4.4 (3.7)**	**5.8 (2.1)**	**0.043**[b]
Vision	Visual acuity (bilateral)	1.1 (0.2)	1.0 (0.2)	0.339[b]
	Contrast sensitivity (Pelli Robson) (log units) (bilateral)	1.6 (0.2)	1.5 (0.2)	0.168[b]
	Colour vision (D15)	0.5 (1.2)	1.5 (1.9)	0.052[b]
Neuropsychology	MMSE	**28.9 (1.5)**	**26.4 (2.3)**	**0.005**[b]
	MOCA	**27.1 (2.4)**	**20.6 (3.8)**	**0.002**[b]
Attention	Digit span backwards	7.3 (2.3)	6.0 (2.9)	0.257[a]
	Stroop: Naming (sec)	**25.2 (7.9)**	**39.4 (12.1)**	**0.029**[b]
Executive function	Stroop: Interference (sec)	**69.6 (21.4)**	**118.8 (28.2)**	**0.002**[b]
	Category fluency	**19.8 (4.5)**	**13.0 (3.9)**	**0.003**[a]
Memory	Word Recognition Task	**23.7 (1.6)**	**21.4 (3.0)**	**0.036**[b]
	Logical Memory (delayed)	**11.6 (2.7)**	**6.8 (1.5)**	**0.001**[a]
Language	Graded Naming Task	**23.5 (3.7)**	**19.8 (4.1)**	**0.026**[b]
	Letter Fluency	**14.6 (4.6)**	**14 (3.6)**	**0.007**[a]
Visuospatial	VOSP	54.0 (4.3)	52.0 (4.9)	0.420[b]
	Benton's Judgement of Line Orientation	23.8 (3.9)	16.7 (2.3)	0.328[b]
	Hooper's Visual organisation test	22.9 (4.3)	19.9 (4.6)	0.073[b]
Disease specific	Hallucinations (%)	14 (33.3)	3 (60.0)	0.480[b]
	Miami Hallucinations Questionnaire	2.2 (2.8)	3.8 (3.8)	0.154
	Disease duration	4.8 (3.8)	2.4 (2.3)	0.168[a]
	RBDSQ	4.3 (2.7)	6.2 (3.0)	0.073[b]
	UPDRS Total	44.8 (16.0)	47.2 (16.9)	0.395[b]
	UPDRS part 3 (motor score)	27.4 (9.9)	28.4 (7.1)	0.420[b]
	LEDD (mg)	409.1 (257.8)	370.0 (343.4)	0.764[a]
	Smell test	7.5 (3.2)	6.0 (3.0)	0.258[a]

PD: Parkinson's Disease; DLB: Dementia with Lewy Bodies; VH: Visual hallucinations.
All data shown (except gender) are mean (SD).
[a] Student t test. [b]Mann-Whitney test.
HADS: Hospital anxiety and depression scale; MMSE: Mini-mental state examination; MOCA: Montreal cognitive assessment; VOSP: Visual Object and Space Perception Battery UPDRS: Unified Parkinson's disease rating scale; LEDD: Total Levodopa equivalent daily dose; RBDSQ: REM sleep behaviour disorder screening questionnaire.

Prior knowledge leads to greater performance improvement in patients who hallucinate.

All participants improved in performance in the ***After*** compared to the ***Before*** block, as expected by the experimental design. This was true both for absolute percentage correct [t=4.12, Hedge's g=0.77, p<0.001] and discrimination sensitivity, d' [t= 3.73, Hedge's g=0.69, p<0.001]. A between-groups ANOVA revealed that this improvement differed between the three study groups in percentage correct [F(2,54)=4.90, p=0.011] and d' [F(2,54)= 3.18, r2=0.11, p=0.049] (*Figure 3.5*). Post-hoc testing showed that this group difference was driven by a difference between patients with LBD with and without hallucinations [t=2.35, Hedge's g=0.75, p=0.025].

Hallucinators improved more than double the amount the non-hallucinators did after prior knowledge was provided (in the ***After*** block after the template images were seen): improvement in d' (d' diff) was mean ±SD = 0.20 ±0.46 in LBD-non-VH versus 0.54 ±0.41 in LBD-VH (*Figure 3.6*). To ensure that the observed difference in improvement was not secondary to a ceiling effect (LBD-non-VH or controls performing at ceiling in the ***Before*** block) I tested the variance of d' between the three groups using the Levene's test of variance: if an effect was due to ceiling performance in the ***Before*** block in a certain group, we would expect a lower variance in this group compared to other groups. Variance was not significantly different in LBD-VH compared to LBD-non-VH or controls in the ***Before*** block (Levene's test of variance W= 1.09, p=0.344) or the ***After*** block (W=0.77, p=0.469), suggesting that neither of the three groups was performing at ceiling in either block. Additionally, even participants with high performance in the ***Before*** block (higher d') were able to improve in the ***After*** block with higher d' in the ***Before*** block associated with higher improvement in d' (r^2=0.260, df=40, β=0.1376 p=0.001). Therefore, although a ceiling effect can not be excluded in LBD non VH, there is no evidence to suggest that this was driving group differences observed in this study.

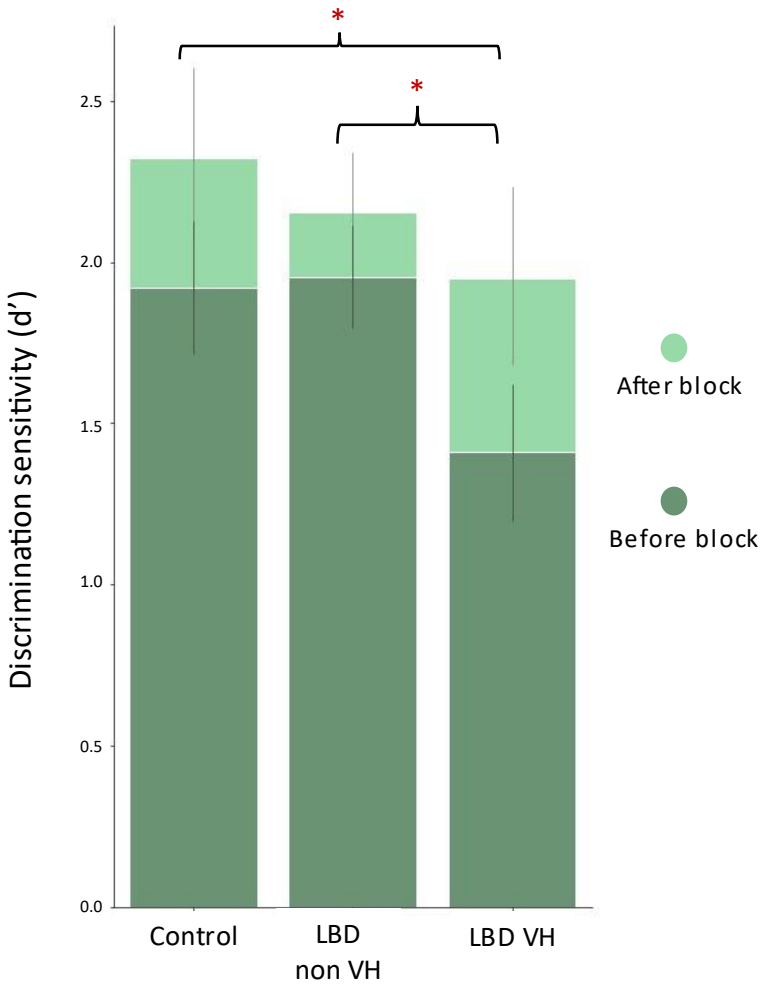

Figure 3.5. Improvement in performance in patients with LBD with and without hallucinations and controls.

*Discrimination sensitivity (d') in the Before block (dark green) and in the After blocks (light green) across the three study groups. Error bars depict standard deviation. * denote statistically significant differences across the specific groups in discrimination sensitivity improvement (d' improvement in the After block compared to the Before block).*

LBD non VH: patients with Lewy Body disease (LBD) without hallucinations, LBD VH: patients with LBD and habitual, at least weekly visual hallucinations

Of the 17 patients with LBD and VH, 4 (23.5%) had provoked, 3 (17.3%) formed, and 10 (58.8%) animate hallucinations; hallucination severity on the UM-PDHQ scale was mean ±SD = 5.2 ±1.9. Importantly, in those patients with habitual hallucinations, performance improvement (d-diff) was correlated with hallucination severity [r^2=0.617, df=16, p<0.001], with higher improvement in patients with more severe hallucinations. This correlation remained significant after correcting for the observed differences in contrast sensitivity, Stroop naming scores, depression scale scores and UPDRS as well as MMSE, levodopa equivalent dose and Hooper [df=7, t=2.549, p=0.038].

Improvement was driven by a reduction in false alarm rates.

The difference in performance improvement was primarily secondary to a greater reduction in false alarm rate in LBD-VH: -0.07 ±0.07 in LBD VH compared to -0.01 ±0.08 in LBD-non-VH [t=2.19, Hedge's g=0.70, p=0.035] (*Figure 3.6*). LBD-VH participants had higher false alarm rates in the ***Before*** block than LBD-non-VH [Mann-Whitney U=114, p=0.043] but did not differ in false alarm rates in the ***After*** block [U=150, p=0.269]. Hit rate did not significantly differ between LBD-VH and LBD-non-VH in either the ***Before*** [U=122, p=0.073] or ***After*** block [U=145, p=0.221]. Importantly, criterion also did not significantly differ between groups in either the ***Before*** [F(2,54)=0.902, p=0.412] or ***After*** blocks [F(2,54)=0.527, p=0.593], thus excluding a significant response bias difference between groups.

Figure 3.6 Improvement in performance in patients with LBD with and without hallucinations (Opposite)

A. False alarm rates in LBD with and without hallucination (VH).

B. Criterion (c). Lower values suggest a response bias to indicate the presence of a person independent of whether a test or control image is shown.

C. Discrimination sensitivity (d'): higher values suggest better ability to correctly disambiguate the two-tone images. In all panels confidence intervals 95% are shown.

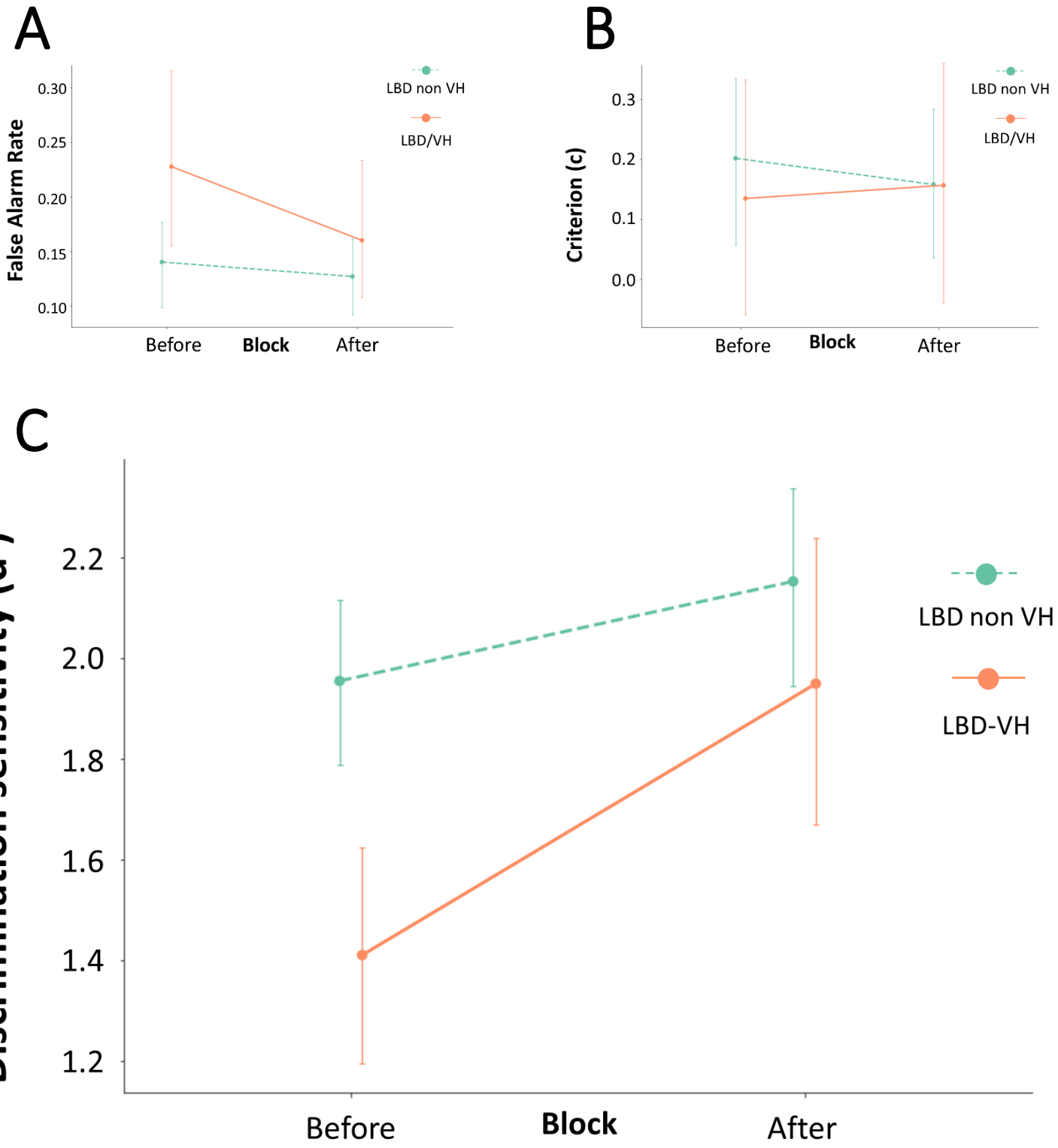
A
False Alarm Rate
0.30
0.25
0.20
0.15
0.10
Before
Block
After
LBD non VH
LBD/VH
B
Criterion (c)
0.3
0.2
0.1
0.0
Before
Block
After
LBD non VH
LBD/VH
C
Discrimination sensitivity (d')
2.2
2.0
1.8
1.6
1.4
1.2
Before
Block
After
LBD non VH
LBD-VH

3.4. Discussion

This is the first study showing that patients with LBD hallucinations place a relatively higher weighting on prior knowledge in perceptual inference: improvement in the visual disambiguation task following receipt of prior knowledge was more than double in LBD-VH compared to LBD-non-VH.

Hallucinations in LBD are usually progressive, often starting as illusions or misperceptions followed in time with the development of complex and vivid hallucinations (Mosimann *et al.*, 2004). Insight, although initially present is also often lost with disease progression and delusional ideas around hallucinations can also occur (Weil *et al.*, 2016). I found that severity of hallucinations, as assessed using a validated disease-specific questionnaire (UM-PDQH) was associated with greater improvement in performance and therefore an even higher effect of prior knowledge. This may provide some insights into how hallucinations progress during the disease. The whole visual system, as early as the retina, shows visual changes in LBD and evidence suggests that at least some of these changes happen early in the disease process (Williams-Gray *et al.*, 2013; Erskine *et al.*, 2019; Han *et al.*, 2020). Early damage in the low-level visual system could result in decreased sensory precision (a loss of signal/noise). This is supported by a decreased drift rate in an attentional task, implying slower evidence accumulation in patients with Parkinson's disease and hallucinations compared to those without hallucinations (O'Callaghan *et al.*, 2017).

In this study, I show an increase in false alarms and lower d' at baseline, implying closer 'signal' and 'noise' distributions in LBD-VH. Improvement in performance after prior information was given (viewing of coloured template images) in hallucinators was mostly realised as a reduction in false alarms rather than an increase in hits. This is in keeping with evidence that acquiring prior beliefs in this task sharpens basic sensory tuning curves

(Davies *et al.*, 2018): this effect may be even greater in those with least sensory precision. Whether hallucinations in LBD-VH are solely attributable to loss of sensory precision is unclear: it could also be that the precision of these patients' prior beliefs increases in absolute terms, alongside sensory precision loss. In this cohort, there was no strong evidence for sensory precision loss in hallucinators as their performance in low-level visual tasks was overall comparable to LBD-VH, but visuoperceptual deficits are described in LBD. A task specifically designed to measure the separately the relative contributions of priors and likelihoods could shed further light into the mechanisms of LBD-hallucinations (Karvelis *et al.*, 2018).

Interestingly, there was wide variability in performance improvement in those patients who did not experience habitual hallucinations. This, in addition with the correlation between performance improvement and hallucination severity, raises the question of whether patients with LBD and greater improvement in performance are on the cusp of developing hallucinations in the near future. Future prospective studies in LBD could shed further light on this question and evaluate tests of prior knowledge as potential markers of hallucination-susceptibility.

My findings are consistent with studies in psychiatric illness and hallucination-prone individuals. People at risk of or with early psychosis also show an overweighting of prior knowledge in a similar disambiguation task and have a perceptual advantage in disambiguating degraded visual or auditory stimuli (Teufel *et al.*, 2015; Alderson-Day *et al.*, 2017; Davies *et al.*, 2018). This suggests that irrespective of pathophysiological diagnosis, hallucinations may share a computational mechanism across diseases. This could have useful implications in translating advances and treatments across fields.

It is important to note, that in this study all patients were examined in the ON state. Levodopa equivalent doses did not differ between LBD-VH and LBD non VH, however higher levodopa doses are associated with a higher risk of hallucinations (Fénelon *et al.*, 2000; Gallagher *et al.*, 2011) and striatal dopamine release is linked to hallucinations (Cassidy *et al.*, 2018). Further studies specifically testing LBD patients both ON and OFF medications could provide further insights to the effect of dopamine on sensory integration.

Publication statement

The work included in this chapter has been published previously (Zarkali *et al.*, 2019) and is included here as per the publisher's policy with regards to thesis publications.

4. Imaging white matter in Parkinson's associated hallucinations

4.1 Introduction

In the previous chapter I showed that patients with Parkinson's disease (PD) and visual hallucinations show an increased weighting of prior knowledge relative to sensory evidence during visual perception (*Chapter 3*). As feedforward and feedback signals are communicated between regions via white matter connections, assessing the integrity of white matter in patients with PD and visual hallucinations could provide useful insights.

Although Parkinson's disease is classically thought of as a synucleinopathy (Spillantini *et al.*, 1997), patients with non-motor symptoms and particularly cognitive involvement usually show a combination of pathologies at post mortem, with fibrillary amyloid-beta, intraneuronal hyperphosphorylated tau as well as alpha-synuclein inclusions (Compta *et al.*, 2011). Occipital distribution of Lewy-related pathology is also linked to more rapid progression of Parkinson's dementia (Toledo *et al.*, 2016). Importantly, cognitive changes in Parkinson's disease appear to involve early axonal involvement. Dystrophic axonal changes are seen before any neuronal loss is evident, suggesting that alpha-synuclein accumulation starts in the axonal compartment (Chung *et al.*, 2009; Li *et al.*, 2009). Exogenous alpha-synuclein in neuronal cultures leads to formation of endogenous pathology that first starts in the axonal compartment (Volpicelli-Daley *et al.*, 2011).

Therefore, white matter changes, detected using diffusion-weighted MRI, may be more sensitive to early degenerative processes in PD than grey matter loss, as they reflect changes in axons rather than neuronal loss (Raffelt et al., 2017). Indeed, studies of diffusion weighted imaging (DWI)

analysed using the diffusion tensor model (DTI, see *Chapter 2* for details) have shown white matter changes in patients with PD even in the absence of significant grey matter atrophy (Hattori et al., 2013; Duncan et al., 2016). Changes in white matter are also more pronounced in those patients with PD with worse cognition (Agosta *et al.*, 2014; Duncan *et al.*, 2016) and those with established dementia (Deng *et al.*, 2013; Kamagata *et al.*, 2017). However, the white matter alterations of PD-associated hallucinations are not yet fully understood.

Fixel-based analysis (FBA) is an emerging framework that can quantify degenerative changes in fibre populations within a voxel ('fixels', see *Chapter 2* for details) and is more robust in modelling crossing fibres, a significant limitation of DTI techniques (Tournier *et al.*, 2007; Jeurissen *et al.*, 2013). FBA allows the measurement of:

1) macrostructural changes in the morphology of the fibre bundle, the fibre cross-section (FC)

2) microstructural changes in the density of fibres within a bundle the fibre density (FD), and

3) overall white matter integrity, represented as changes in both cross section and density in fibre bundles (FDC), which is a combination of both degenerative processes (Raffelt *et al.*, 2017).

This study aimed to investigate the microstructural and macrostructural white matter changes that accompany visual hallucinations in PD. I hypothesised that:

a) Higher tensor models such as fixel-based analysis would be able to identify white matter changes in Parkinson's associated hallucinations, outperforming DTI.

b) White matter connections between the thalamus and cortical structures as well as the posterior thalamic radiation would be preferentially affected in patients with PD and visual hallucinations.

4.2 Methods

Study Participants

Participants were recruited from the Vision in Parkinson's disease study (VIPD cohort, *Chapter 2: Study Cohorts*). 105 patients with PD were recruited of whom 19 had regular visual hallucinations (PD-VH) and 86 had no hallucinations (PD non VH); 35 unaffected controls were also recruited. All patients with PD satisfied the Queen Square Brain Bank criteria (Gibb and Lees, 1988).

The full study protocol is described in *Chapter 2*, with all participants undergoing the same clinical assessments. An overview of the study methodology is seen in *Figure 4.1*.

MRI data acquisition and preprocessing

The protocol for MRI acquisition is described in *Chapter 2.6.* Pre-processing of DWI images is described in *Chapter 2.7*. Following preprocessing, for each participant, fibre-orientation distributions (FODs) were computed using multi-shell 3-tissue constrained spherical-deconvolution with the group-average response function for each tissue type (Hollander, T. et al., 2016). A group-averaged fibre orientation distribution (FOD) template was created from baseline imaging data from 30 randomly-selected subjects (20 PD, 10 controls). Each participant's FOD was registered to the template (Raffelt et al., 2011) and fixel-based metrics were derived (FD, FC, and FDC).

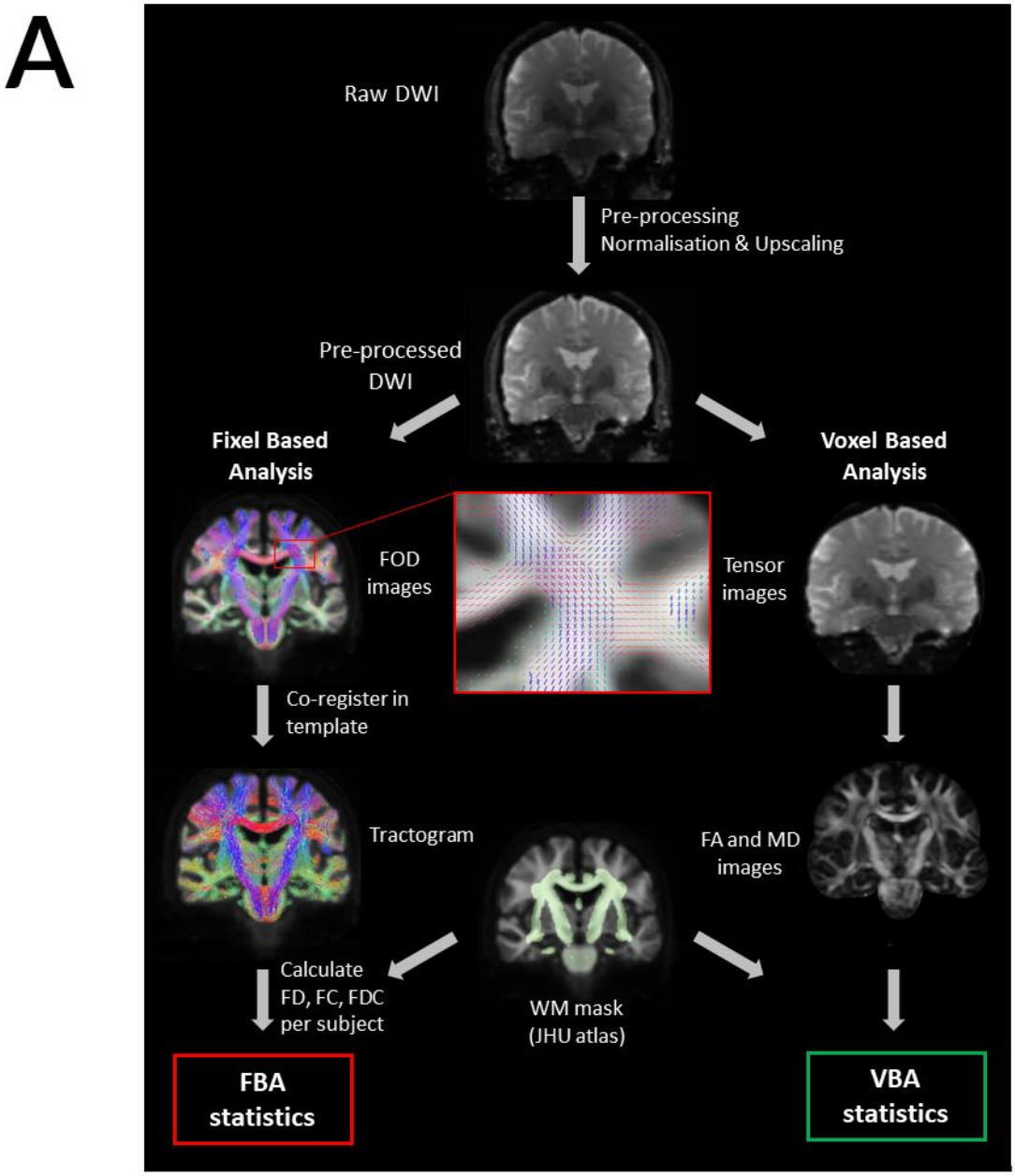
A
Raw DWI
Pre-processing
Normalisation & Upscaling
Pre-processed
DWI
Fixel Based
Analysis
Voxel Based
Analysis
FOD
images
Tensor
images
Co-register in
template
Tractogram
FA and MD
images
Calculate
FD, FC, FDC
per subject
WM mask
(JHU atlas)
FBA
statistics
VBA
statistics

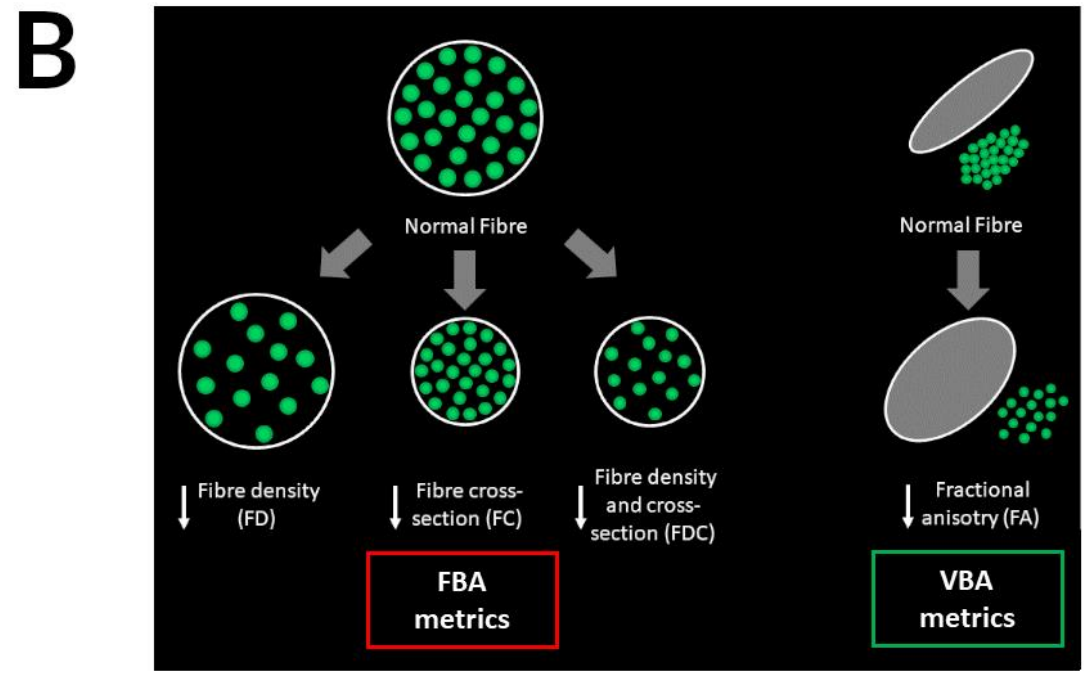
B
Normal Fibre
Normal Fibre
Fibre density
(FD)
Fibre cross-
section (FC)
Fibre density
and cross-
section (FDC)
Fractional
anisotry (FA)
FBA
metrics
VBA
metrics

Figure 4.1. Overview of the processing steps involved in fixel- (FBA) and voxel-based (VBA) whole-brain analyses.

(Opposite)

A. Processing steps specific to FBA are shown on the left, and those specific to VBA on the right.

B. Illustration of the derived FBA and VNA metrics.

FOD: fibre orientation distribution; FA: fractional anisotropy; MD: mean diffusivity; FD: fibre density; FC: fibre cross-section; FDC: fibre density and cross-section.

To compare the results of fibre-specific FBA with more commonly used measures of white matter integrity, I also performed a voxel-based analysis using the metrics of fractional anisotropy (FA) and mean diffusivity (MD). Following the DWI pre-processing steps, I derived the diffusion tensor from each participant's FOD image (Veraart et al., 2013) and calculated an FA and MD map in each participant's space. Each individual participant's FA and MD maps were then transformed to template space, using the same warp generated during the FBA registration step. I then performed voxel-wise analysis in template space (Figure 3.1A).

Statistical analysis

Group differences in clinical characteristics were assessed using independent t-samples and ANOVAs for normally distributed continuous variables, Mann-Whitney and Kruskall-Wallis for non-normally distributed variables and chi-square for categorical variables (with post-hoc Tukey test performed for ANOVA and Dunn test performed for Kruskal-Wallis) with a statistical significance threshold $p<0.05$. Normality was assessed both quantitatively using the Shapiro-Wilk test and through a visual assessment of the variable's distribution.

Whole brain Fixel-based analysis

To identify differences in fixel-based metrics I used whole brain FBA to identify regions with changes in FC, FD and FDC between 1) patients with PD and controls; 2) PD-VH and PD-non-VH. Whole brain FBA refers to the comparison of all white matter fixels within the brain, as is standard for this analysis (Mito *et al.*, 2018). Group comparisons of the three FBA-derived measures were performed at each fixel level using a General Linear Model with age and total intracranial volume included as nuisance covariates. I used connectivity-based fixel enhancement for statistical inference (Raffelt *et al.*, 2015): 2 million streamlines with default smoothing parameters (smoothing mm full-width at half-maximum, C=0.5, E=2, H=3), 5,000 permutations using non-parametric permutation testing and family-wise error (FWE) correction for multiple comparison (significance threshold $p < 0.05$).

Whole brain Voxel based analysis

Voxel-based analysis was performed using threshold-free cluster enhancement with the default parameters (dh =0.1, E =0.5, H =2) (Smith and Nichols, 2009) across the whole brain, as in the FBA, for the same comparator groups (FWE correction, $p < 0.05$).

Tract of interest analysis

To investigate potential degeneration of selective fibre pathways within the visual system in patients with PD-associated hallucinations, I performed further tract of interest analyses. I had strong a priori hypotheses that tracts from visual processing regions to the rest of the brain would be affected. I therefore selected 11 white matter tracts involved in visual processing, based on anatomical DTI atlases (Wakana *et al.*, 2007; Hua *et al.*, 2008; Mori *et al.*, 2008). These were: Posterior thalamic and optic radiations (Left and Right), Splenium, Body and Genu of the corpus callosum, Superior

longitudinal fasciculi (Left and Right), Inferior fronto-occipital fasciculi (Left and Right; the segmentation includes the inferior longitudinal fasciculus), and Superior fronto-occipital fasciculi (Left and Right). Mean FDC was calculated across each tract per participant and compared between PD-VH vs PD-non-VH; FDC was chosen as it is a combined metric and therefore would be most sensitive to both micro- and macro-structural changes. Statistical comparison was performed with a linear mixed model (age and intracranial volume included as nuisance covariates) in Python 3. A false discovery rate (FDR) correction was performed for the 11 tracts tested, using the Benjamini/Hochberg method. Results are displayed as as percentage difference from mean FDC (and 95% confidence interval) of the comparison group.

4. 3. Results

140 participants were included: 105 patients with Parkinson's disease (PD) and 35 controls. 86 patients with Parkinson's had no visual hallucinations (PD-non-VH) and 19 patients described recurrent visual hallucinations (PD-VH). PD-VH participants and PD-non-VH participants did not significantly differ in demographics or low-level vision. PD-VH had higher total UPDRS score [63.5 ± 35.6 compared to 43.2 ± 20.6 in PD non VH, ($U=481.5$, $p=0.003$)] but motor scores were not significantly different. PD-VH participants had higher anxiety scores [7.7 ± 4.9 compared to 5.6 ± 3.8 in PD non VH, ($U=566.5$, $p=0.037$)] but this was below the scale's threshold for the diagnosis of anxiety (Zigmond and Snaith, 1983). Of note, age, gender, intracranial volume and cognition did not significantly differ between hallucinators and non-hallucinators (*Table 4.1*). Demographics and results of clinical characteristics between PD and controls are seen in *Table 4.2*.

Table 4. 1. Demographic and clinical characteristics of participants with Parkinson's disease with and without hallucinations

Participants with Parkinson's with and without visual hallucinations				
Attribute		**PD / VH n=19**	**PD non VH n=86**	**Statistic**
Demographics	Age (y)	64.6 (8.2)	64.5 (7.9)	t=0.09 p=0.929
	Male (%)	6 (31.6)	49 (57.0)	x^2=3.07 p=0.079
	Years in Education	17.1 (3.5)	17.1 (2.6)	t=0.003 p=0.997
	Total Intracranial Volume	1409.9 (106.7)	1467.4 (134.8)	t=1.74 p=0.085
Mood (HADS)	Depression score	4.8 (3.2)	3.8 (2.9)	U=608.5 p=0.081
	Anxiety score	**7.7 (4.9)**	**5.6 (3.8)**	**U=566.5 p=0.037**
Vision	LogMAR (best)	-0.06 (0.1)	-0.09 (0.2)	U=656.5 p=0.181
	Pelli Robson (best)	1.70 (0.2)	1.79 (0.2)	U=1018.5 p=0.073
	D15 (total error score)	3.6 (4.9)	4.1 (12.3)	U=648 p=0.196
Cognition	MMSE	28.6 (1.8)	28.9 (1.1)	U=865.0 p=0.677
	MOCA	26.9 (3.1)	27.9 (2.1)	U=1014.5 p=0.094
Disease specific Measures	UPDRS	**63.5 (35.6)**	**43.2 (20.6)**	**U=481.5 p=0.005**
	UPDRS part 3 (motor score)	29.2 (20.8)	22.2 (11.5)	U=648.5 p=0.162
	UM-PDHQ	**4.8 (2.3)**	**0 (0)**	-
	LEDD (mg)	434.9 (210.3)	460.5 (267.8)	U=838 p=0.864
	Disease duration	4.8 (3.4)	4.1 (2.5)	t=1.12 p=0.263
	Sniffin' sticks	3.6 (3.4)	4.1 (3.1)	U=1003.5 p=0.119
	RBDSQ	**5.6 (2.5)**	**4.0 (2.4)**	**U=503 p=0.009**

All data shown are mean (SD) except gender.
In bold characteristics that differed between the two groups.
HADS: Hospital anxiety and depression scale; MMSE: Mini-mental state examination; MOCA: Montreal cognitive assessment; UPDRS: Unified Parkinson's disease rating scale; UM-PDHQ: University of Miami Hallucinations Questionnaire; LEDD: Total Levodopa equivalent dose; RBDSQ: REM sleep behaviour disorder screening questionnaire.

Table 4.2. Demographic and clinical characteristics in participants with Parkinson's disease and controls

Attribute		PD n=105	Controls n=35	Statistic
Demographics	Age (y)	64.5 (7.9)	66.7 (9.3)	t=1.4 p=0.169
	Male (%)	55 (52.4)	16 (45.8)	x^2=0.2 p=0.626
	Years in Education	17.1 (2.8)	17.7 (2.3)	t=1.2 p=0.231
	Total intracranial volume	**1456.9 (131.6)**	**1397.3 (104.8)**	**t=2.4 p=0.016**
Mood (HADS)	Depression score	**3.9 (2.9)**	**1.7 (2.0)**	**U=2758.5 p<0.001**
	Anxiety score	**5.9 (4.1)**	**3.7 (3.4)**	**U=2433.5 p=0.004**
Vision	LogMar*	-0.08 (0.2)	-0.08 (0.2)	U=2031.5 p=0.349
	Pelli Robson*	1.78 (0.2)	1.79 (0.2)	U=1762.5 p=0.702
	D15 (total error score)	3.9 (1.2)	2.3 (6.6)	U=2050 p=0.221
Cognition	MMSE	28.9 (1.3)	29.0 (1.0)	U=1792 p=0.819
	MOCA	**27.8 (2.3)**	**28.7 (1.4)**	**U=1439 p=0.050**
Disease specific	UPDRS	**46.9 (25.1)**	**9.3 (7.2)**	**U=3596 p<0.001**
	UPDRS part 3 (motor score)	**23.5 (13.8)**	**5.6 (4.8)**	**U=3473 p<0.001**
	LEDD (mg)	455.8 (257.6)	-	-
	Disease duration	4.2 (2.7)	-	-
	Sniffin' sticks	**7.6 (3.2)**	**12.3 (2.5)**	**U=450 p<0.001**
	RBDSQ	**4.3 (2.5)**	**1.8 (1.4)**	**U=2916.5 p<0.001**

All data shown are mean (SD) except gender.
** Best binocular score used; LogMAR: lower score implies better performance, Pelli Robson: higher score implies betterr performance.*
HADS: Hospital anxiety and depression scale; MMSE: Mini-mental state examination; MOCA: Montreal cognitive assessment; UPDRS: Unified Parkinson's disease rating scale; UM-PDHQ: University of Miami Hallucinations Questionnaire; LEDD: Total Levodopa equivalent dose; RBDSQ: REM sleep behaviour disorder screening questionnaire.

White matter changes in whole brain analysis

Patients with PD-associated hallucinations showed white matter macrostructural changes, with reductions in FC within the splenium of the corpus callosum and the left optic radiation, compared with non-hallucinators. The combined FDC metric that assesses micro- and macrostructural WM changes, showed large reductions (greater than 50% reduction) in PD-VH participants compared with PD-non-VH within the splenium of the corpus callosum. There were no significant changes in FD alone (*Figure 4.2*).

In contrast, conventional tensor-based analysis did not show any statistically significant differences between PD-VH versus PD-non-VH participants. Additionally, whole brain tensor-based analysis did not show any changes between PD versus control participants. Whole brain FBA comparing PD and controls showed macrostructural white matter changes with reduced fibre cross-section (FC) in several fixels within the left corticospinal tract (*Figure 4.3*). There were no differences at the microstructural level, measured as fibre density (FD) or the combined metric FDC between PD and control. Within the PD group, overall disease progression as assessed using the UPDRS total score was associated with decreased FC within the splenium of the corpus callosum (*Figure 4.3*).

Figure 4. 2. Fibre-specific reductions in PD-VH in whole-brain fixel-based analysis.

(Opposite)

A: *PD VH vs PD non VH. Parkinson's patients with hallucinations showed changes in white matter macrostructure (reduction in fibre cross-section (FC)) and overall ability to relay information (reduction in the combined FDC metric) compared to PD non VH. Colour bar reflects percentage reduction. (FWE-corrected $p<0.05$)*

B: *PD VH vs PD non VH, direction of fibres. Loss of fibre tracts in in PD-VH was particularly seen for left-right axons. (Colour bar reflects direction of fibre loss: (anterior-posterior: green; superior-inferior: blue; left-right: red). (FWE-corrected $p <0.05$)*

A

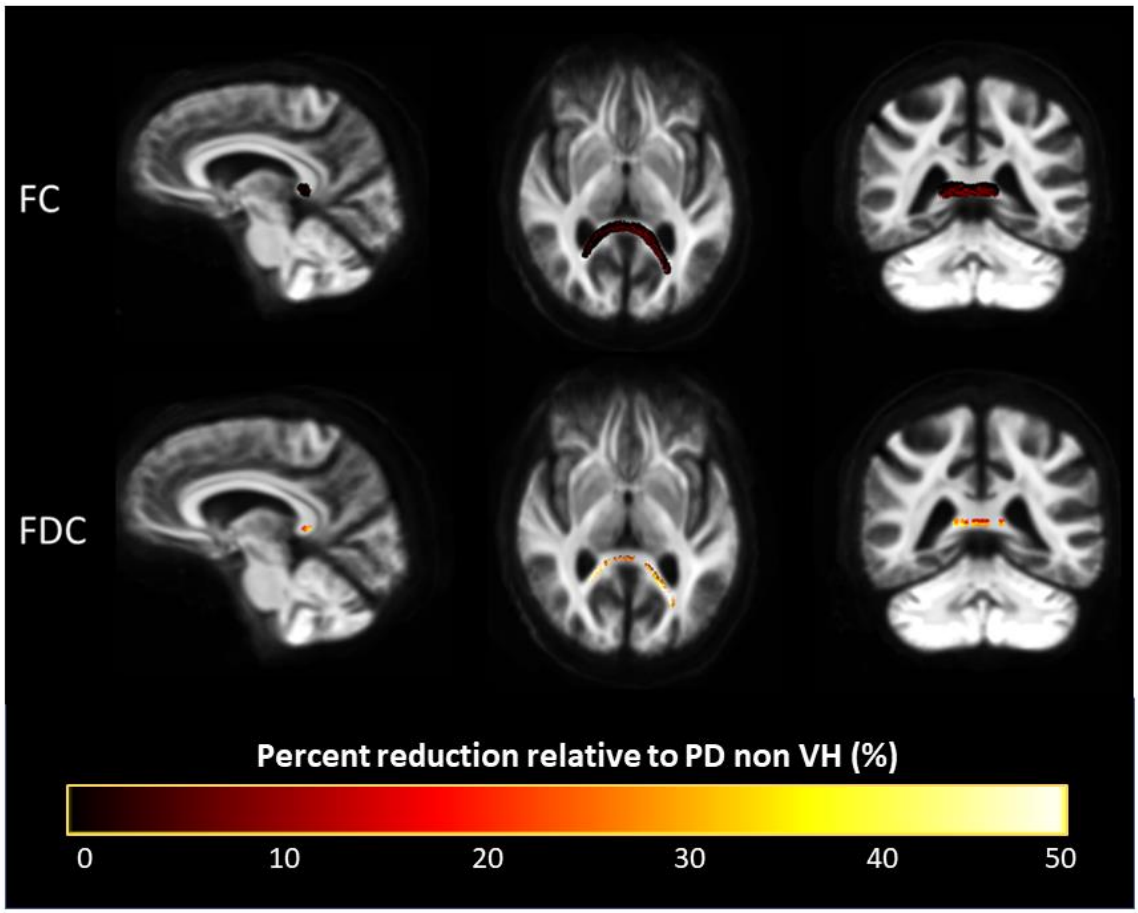
FC
FDC
Percent reduction relative to PD non VH (%)
0
10
20
30
40
50

B

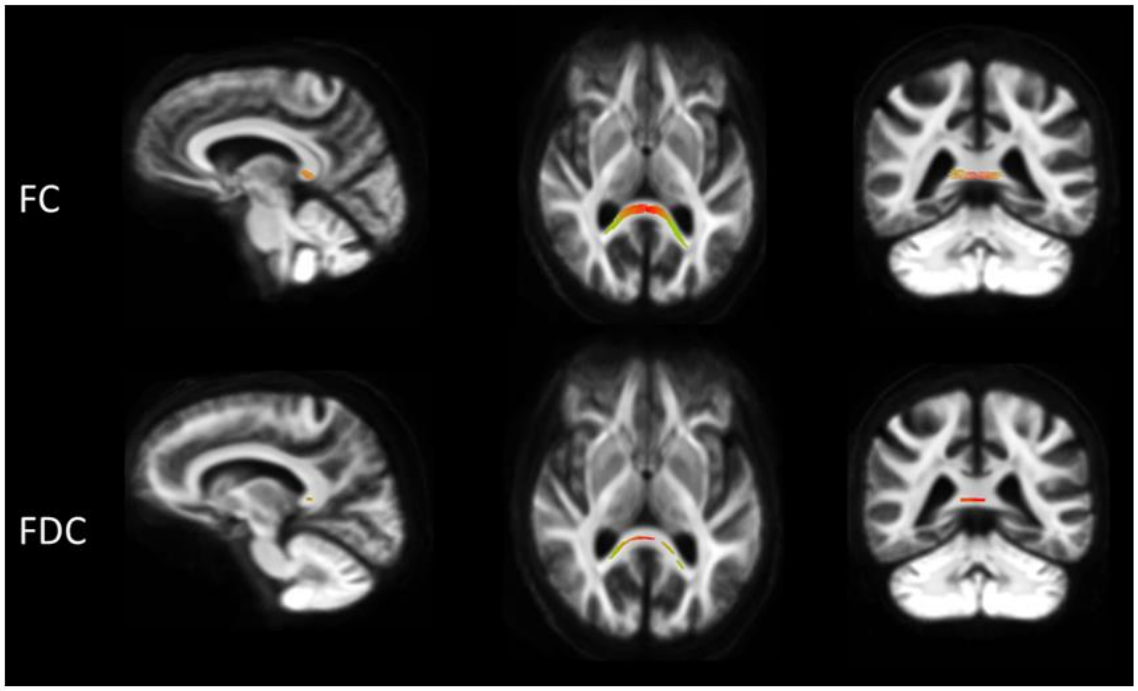
FC
FDC

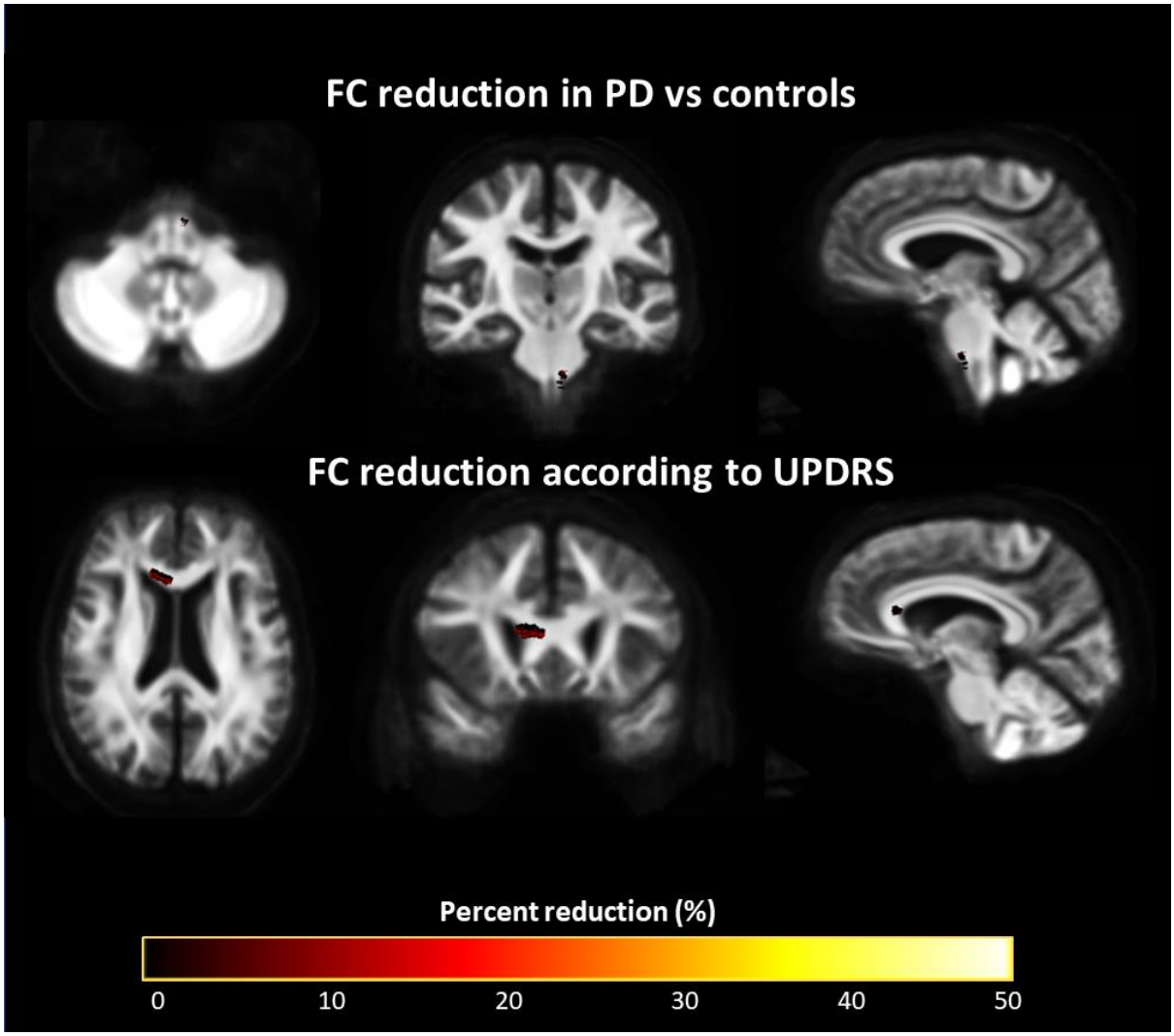

Figure 4. 3. FC reduction in PD compared to controls (top) and within participants with PD according to UPDRS scores (down).

Results are displayed as streamlines; streamline segments were cropped from the template tractogram to include only the points that correspond to fixels that significantly differed between participants with Parkinson's disease (PD) and controls (FWE-corrected p-value <0.05). Streamlines are coloured by percentage reduction in the PD group compared to controls for fiber bundle cross-section (FC).

Reduced FC was seen in multiple fixels within the left corticospinal tract. There were no differences at the microstructural level, measured as fibre density (FD) or the combined metric FDC between PD and control participants. Within the PD group, overall disease progression as assessed using the UPDRS total score was associated with decreased FC within the splenium of the corpus callosum.

White matter changes in tract of interest analysis

Widespread reductions in mean tract FDC were seen in PD-VH compared to PD-non-VH in a tract of interest analysis. Specifically, changes were seen in the splenium (t= -2.026, p=0.043), genu (t= -2.356, p=0.018), inferior fronto-occipital fasciculus bilaterally (left: t= -2.566, p=0.010, right: t= -2.506, p=0.012), posterior thalamic radiation bilaterally (left: t= -2.917, p=0.004, right= -2.331, p=0.020) and right superior longitudinal fasciculus (t=-2.640, p=0.008). The inferior fronto-occipital fasciculi bilaterally survived FDR correction for the 11 regions tested (right: p=0.033, left: p=0.033) and so did both posterior thalamic radiations (right: p=0.033, left: p=0.037), the genu (p=0.037) and right superior longitudinal fasciculus (p=0.033) (*Figure 4.4*).

Higher hallucination severity was associated with lower mean FDC within the left posterior thalamic radiation, accounting for age and total intracranial volume, although this was just above statistical significance levels (r^2=0.316, df=101, t=-1.955, p=0.053).

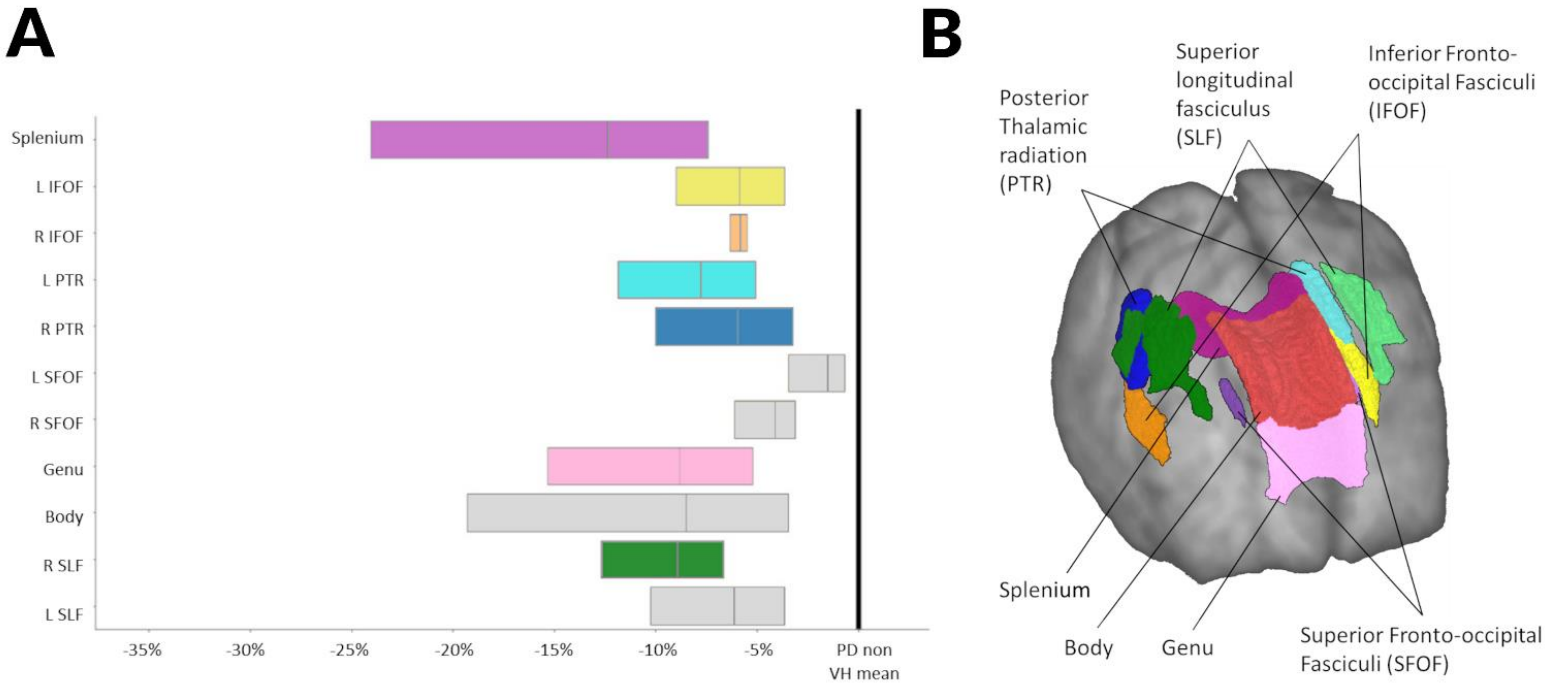

Figure 4. 4. Significant tracts in patients with Parkinson's hallucinations, tract of interest analysis.

Reduction (mean, 95% CI) in combined fibre density and cross-section (FDC) visualised as percentage reduction from the mean of patients with Parkinson's disease without hallucinations (PD non VH). Tracts with significantly reduced FDC (p-value <0.05) are shown in colour whilst tracts where there are no significant changes in FDC are plotted in grey.

The posterior thalamic radiations bilaterally, inferior fronto-occipital fasciculi bilaterally, genu and right superior longitudinal fasciculi survived FDR correction.

L: Left, R: Right.

4.4. Discussion

This study used fixel-based analysis to measure fibre-specific changes in patients with PD and visual hallucinations. Specifically, I have shown that:

1) Patients with PD-associated visual hallucinations exhibit white matter changes within the splenium and the left posterior thalamic radiation.
2) Widespread reductions in fibre cross section and the FDC metric (combining fibre density and cross section), suggesting that WM macrostructural changes occur in PD hallucinations together with changes that affect the ability to relay information between brain regions.

The finding of axonal changes in posterior tracts in PD-VH is consistent with previous work using tensor-derived metrics that showed reduced fractional anisotropy in the optic nerve and optic radiation in an analysis of five manually determined regions of interest (Lee *et al.*, 2016) and increased mean diffusivity within tracts from the nucleus basalis of Meynert to parietal and occipital regions in patients with Parkinson's-associated hallucinations (Hepp *et al.*, 2017*a*).

In contrast, past whole brain tensor-based analyses had not revealed any specific white matter changes between PD hallucinators and non-hallucinators (Lee *et al.*, 2017; Firbank *et al.*, 2018); whole brain voxel-based analysis also failed to reveal any changes in our cohort. Since tensor-based metrics are, by definition, averaged across a voxel, their results can be misleading particularly in the presence of crossing fibres (Jbabdi *et al.*, 2010). In contrast, the more sensitive and fibre-specific fixel-based analysis identified group differences in both fibre microstructure and macrostructure. This suggests that high-order diffusion models and specifically fixel-based

analysis may be a more sensitive and specific technique for examining white matter changes in the early stages of neurodegeneration.

The posterior thalamic radiation connects the posterior thalamus with the occipital and posterior parietal cortex, including key regions of the default mode network (DMN), such as the posterior cingulate. Several functional studies have highlighted the role of attentional networks in the development of visual hallucinations (Shine *et al.*, 2014, Yao *et al.*, 2014). The finding of reduced connectivity from the thalamus to posterior brain regions including the DMN provides a mechanistic model, whereby lack of inhibition between these brain regions leads to aberrant DMN activation (Shine *et al.*, 2014, Yao *et al.*, 2014).

In tract of interest analysis, I also saw FDC reductions within association fibres in PD hallucinators, specifically those connecting frontal and occipital lobes (inferior fronto-occipital fasciculi bilaterally and right superior longitudinal fasciculus). This highlights the importance of loss of fronto-occipital connectivity in the development of hallucinations.

There are a number of potential limitations to this study. I did not exclude participants with other pathologies that could influence white matter structure, such as white matter hyperintensities which could decrease fibre density. Although raw imaging data were visually inspected, and no clinically significant cerebrovascular disease was seen, the load of white matter hyperintensities was not systemically quantified or specifically controlled for. This is in keeping with other studies of fixel-based analysis in adults so far, none of which excluded participants with white matter hyperintensities (Grazioplene *et al.*, 2018; Mito *et al.*, 2018). Future studies could clarify the effect, if any, of white matter hyperintensities on fixel-based metrics. The patients with PD hallucinations had higher anxiety and RBDSQ scores than the non-hallucinators. However anxiety scores were

below clinical significant threshold for depression (Zigmond and Snaith, 1983) and the small observed changes in anxiety and RBD are unlikely to have resulted in white matter changes within tracts of the visual system. Participants underwent imaging acquisition while taking their usual dopaminergic medications. It seems unlikely that dopaminergic medications would directly affect structural integrity measures, and free water and corrected fractional anisotropy are not affected by levodopa (Chung *et al.*, 2017).

In conclusion, this study showed that patients with PD-associated visual hallucinations have a characteristic pattern of fibre tract degeneration, involving the splenium and posterior thalamic radiation; these findings provide mechanistic support for attentional network changes in PD hallucinations.

Publication statement

Some of the work included in this chapter has been published previously (Zarkali *et al.*, 2020) and is included here as per the publisher's policy with regards to thesis publications.

5. Longitudinal alterations in white and grey matter in Parkinson's associated hallucinations

5.1 Introduction

Visual hallucinations associated with Parkinson's disease (PD) are accompanied by large macroscale brain network imbalance: with aberrant activation of the default mode network (DMN) and reduced activity of other networks such as the dorsal attentional network (Shine et al., 2014; Yao et al., 2014). Network changes are thought to underlie the associated impaired accumulation of sensory evidence (O'Callaghan et al., 2017), and in a previous chapter (*Chapter 3*), I showed that PD hallucinators show an increased weighting of prior knowledge relative to sensory evidence during visual perception. Widespread changes in brain structure have also been shown in PD-associated hallucinations with changes in grey matter volume across many regions including the precuneus, cingulate and superior and inferior frontal gyri (Lenka et al., 2015) and white matter structure within posterior tracts as well as at whole network level (Hall *et al.*, 2019). However, our understanding of the drivers of these large-scale network changes remains unclear.

The thalamus is a connection-rich diencephalic hub critical for cortical sensory filtering (Cunningham et al., 2017; Wolff and Vann, 2019). It has been recently proposed as a potential key driver for unbalanced network activation (Esmaeeli et al., 2019; Onofrj et al., 2019; Russo et al., 2019). Thalamic hypometabolism and atrophy is seen in patients with PD and hallucinations (Nishio et al., 2017) and is also present in frontotemporal dementia associated with C9orf72 mutations where hallucinations are reported (Bocchetta et al., 2020). Reduced thalamic connectivity with the

prefrontal cortex is also seen in relation to hallucinations occurring in the context of psychosis (Anticevic et al., 2014). However, the thalamus is a heterogenous structure comprised of distinct nuclei with different cortical projections and functions (Wolff and Vann, 2019). Specific thalamic subnuclei may be implicated in visual hallucinations; changes at thalamic sub-nucleus level can now be assessed using a recently described probabilistic atlas (Iglesias *et al.*, 2018).

White matter changes, detected using diffusion-weighted MRI, may be more sensitive to early degenerative processes in PD than grey matter loss, as they reflect changes in axons rather than neuronal loss (Raffelt et al., 2017). White matter changes may occur at an earlier stage in PD (Chung et al., 2009): in whole brain studies of PD and cognition, white matter loss is seen before significant grey matter atrophy (Hattori et al., 2013; Duncan et al., 2016).

The study described in this chapter aims to clarify the timeline of grey and white matter changes underlying visual hallucinations in PD and assess the relative involvement of the different thalamic nuclei. Specifically, I will:

1) describe changes in whole brain cortical thickness and white matter micro- and macrostructural integrity at baseline and after 15 months in PD patients with (PD-VH) and without hallucinations (PD non VH).

2) I will describe changes in the grey matter volume of 50 thalamic sub-nuclei and macrostructural white matter integrity of their respective cortico-thalamic white matter projections at baseline and longitudinally.

I hypothesise that cortico-thalamic connection loss will precede volume loss in PD-VH and that sub-regions of the thalamus will show differential vulnerability to degeneration in PD-VH compared to PD non VH.

5.2 Methods

Study Participants

Participants were recruited from the Vision in Parkinson's disease study (VIPD cohort, *Chapter 2: Study Cohorts*). Only participants who had both grey matter structural and diffusion-weighted imaging satisfying pre-determined quality control criteria at both study visits were included. A total of 140 participants were imaged at baseline. At Visit 2, 4 patients withdrew, 11 were unable to be scanned due to evolving contra-indications, 3 were excluded due to a subsequent revision of their PD diagnosis, 19 were unable to participate due to COVID-19 imposed restrictions and 2 failed quality control for Visit 2 diffusion-weighted imaging. Therefore 101 participants were included in the study: 76 patients with PD and 25 controls. All patients with PD satisfied the Queen Square Brain Bank criteria (Gibb and Lees, 1988).

Participants with PD were classified as PD with visual hallucinations (PD-VH, n=22) if they scored equal to or more than 1 for Question 2 of the UPDRS: "Over the past week have you seen, heard, smelled or felt things that were not really there?" in either study visit. All other participants with PD were classified as PD non VH (n=54). Further information on the frequency and severity of hallucinations was collected using the University of Miami Parkinson's Disease Hallucinations Questionnaire (UM-PDHQ) (Papapetropoulos et al., 2008).

The full study protocol is described in *Chapter 2*. Clinical assessments and imaging was undertaken at baseline and again at follow up (between 14 and 20 months later (mean=15.4 months).

MRI data acquisition and preprocessing

The protocol for MRI acquisition is described in *Chapter 2.6.* Preprocessing of structural images was performed using Freesurfer v6.0 longitudinal pipeline (for details see *Chapter 2.8*).

In addition to whole grey matter segmentations, I derived thalamic sub-nuclei volumes from each longitudinal Freesurfer reconstruction using a recently described Bayesian segmentation method based on a probabilistic atlas derived from histology (Iglesias et al., 2018). Volumes were derived for 25 sub-nuclei for each thalamus: anteroventral (AV), laterodorsal (LD), lateral posterior (LP), ventral anterior (VA), ventral anterior magnocellular (VAmc), ventral lateral anterior (VLa), ventral lateral posterior (VLp), ventral posterolateral (VPL), ventromedial (VM), central medial (CeM), central lateral (CL), paracentral (Pc), Centromedian (CM), parafascicular (Pf), paratenial (Pt), Reuniens medial ventral (MV-re), mediodorsal medial magnocellular (MDm), mediodorsal medial parvocellular (MDl), lateral geniculate (LGN), medial geniculate (MGN), limitans (L-Sg), pulvinar anterior (PuA), pulvinar medial (PuM), pulvinar lateral (PuL) and pulvinar inferior (PuI) (*Figure. 5.1*).

Pre-processing of DWI images is described in *Chapter 2.7*. Following preprocessing, for each participant, fibre-orientation distributions (FODs) were computed using multi-shell 3-tissue constrained spherical-deconvolution with the group-average response function for each tissue type (Hollander, T. et al., 2016). A group-averaged FOD template was created from baseline imaging data from 30 randomly-selected participants (20 PD, 10 controls). Each participant's FOD was registered to the template (Raffelt et al., 2011) and fixel-based metrics were derived.

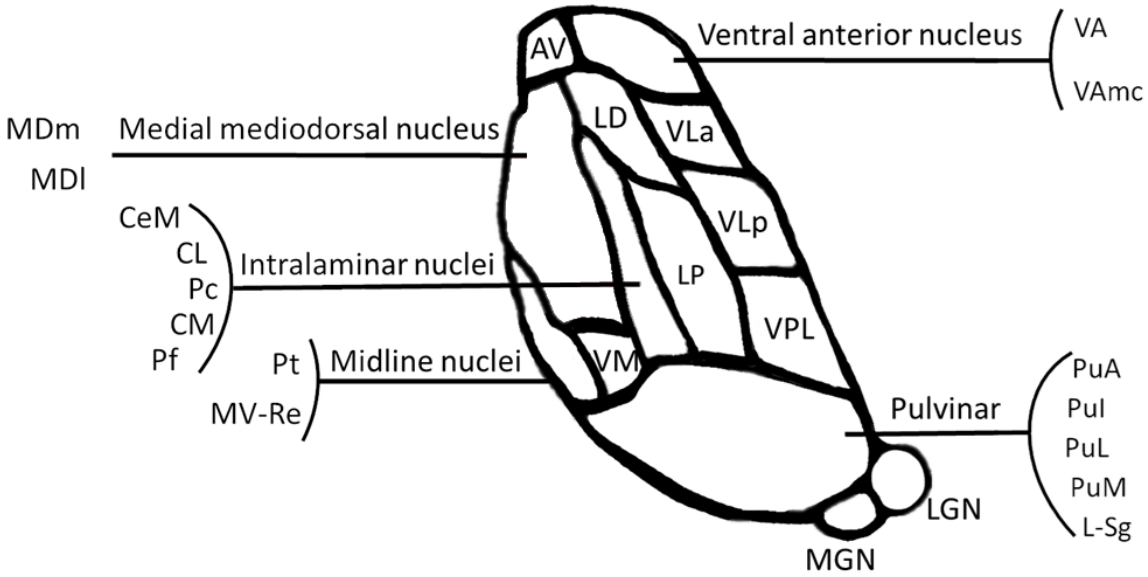

Figure 5. 1. Schematic representation of the Thalamic subnuclei, view from above

AV: anteroventral, CeM: central medial, CM: centromedian, L_Sg: limitans, LD: laterodorsal, LGN: lateral geniculate, LP: lateral posterior, MDl: mediodorsal medial parvocellular, MDm: mediodorsal medial magnocellular, MGN: medial geniculate, MVRe: Reuniens medial ventral, Pf: parafascicular, PuA: pulvinar anterior, PuI: pulvinar inferior, PuL: pulvinar lateral, PuM: pulvinar medial, VA: ventral anterior, VAmc: ventral anterior magnocellular, VLa: ventral lateral anterior, VLp: ventral lateral posterior, VPL: ventral posterolateral, VM: ventromedial, CL: central lateral, Pc: paracentral, Pt: paratenial.

Fixel based metrics are described in detail in *Chapter 2.4*; briefly the following were calculated:

1. **Fibre density (FD):** a measure of microstructural changes within the tracts. (Raffelt *et al.*, 2012).
2. **Fibre cross-section (FC):** a measure of macrostructural white matter change, as it provides morphological information about relative sizes of fibre bundles (Raffelt *et al.*, 2017).

3. **Combined measure of fibre density and cross-section (FDC):** an overall measure of ability to relay information (Raffelt *et al.*, 2017).

To specifically assess the integrity of thalamic connections, I generated specific tracts of interest for each of the 50 thalamic subnuclei to the ipsilateral hemisphere. To achieve this, each thalamic subnucleus was registered to the population template using linear registration with NiftyReg (Modat et al., 2010). A tractogram for each thalamic sub-nucleus was then generated using probabilistic tractography on the population template in MRtrix3 (Tournier et al., 2019). Streamlines were initiated in each thalamic sub-nucleus to the ipsilateral hemisphere, with the rest of the thalamus excluded to minimise overlap between the different thalamic tracts. This resulted in a single fibre tract-of-interest from each thalamic sub-nucleus to the ipsilateral cortex. Mean FC was calculated across each of these tracts per participant; for the tract-based analysis, FC was chosen as prior work described in *Chapter 3* and by other groups (Rau *et al.*, 2019) showed that it may be the most sensitive fibre-specific metric in PD.

Statistical analysis

Group differences in demographics and clinical characteristics were assessed using independent t-samples and ANOVAs for normally distributed continuous data, Mann-Whitney and Kruskall-Wallis for non-normally distributed data and chi-square for categorical data (post-hoc Tukey for ANOVA and Dunn for Kruskal-Wallis); statistical significance was set at $p<0.05$. Normality was assessed using the Shapiro-Wilk test and visual assessment of the variable's distribution.

Whole brain Fixel-based analysis

To identify differences in fixel-based metrics I used whole brain fixel based analysis using non-parametric permutation testing and connectivity-based fixel enhancement (CFE) (Raffelt et al., 2015). A tractogram (20 million

streamlines) was generated with whole-brain probabilistic tractography on the population FOD template and filtered to 2 million streamlines using SIFT (spherical-deconvolution informed filtering of tractograms) (Smith et al., 2013). CFE was performed on the resulting streamlines with default parameters (C=0.5, E=2, H=3), 5,000 permutations and family-wise error correction (FWE) for multiple comparisons. Statistical significance was set at FWE-corrected $p<0.05$ with cluster-extent-based threshold of 10 voxels. To identify white matter fixels for subsequent statistical comparisons, I used the John Hopkins University atlas, similar to previous studies (Mito *et al.*, 2018; Rau *et al.*, 2019). Using this atlas as a mask of white-matter fixels only, whole-white-matter comparisons were performed at baseline between PD-VH and PD-non-VH, using age, gender and total intracranial volume as covariates. As longitudinal fixel based analyses are not currently available, to allow comparisons at Visit 2, I subtracted each baseline image from the Visit 2 image, as previously described (Genc et al., 2018) and performed whole-white-matter statistical analyses on these difference images with baseline age, gender, total intracranial volume and time between scans included as covariates.

Whole brain cortical thickness analysis

Differences in cortical thickness trajectories over time between PD-VH and PD non VH were assessed using Linear Mixed Effect models in MATLAB (The MathWorks, Inc) designed for longitudinal FreeSurfer data (Bernal-Rusiel et al., 2013b, a). A spatiotemporal novel mass-univariate analysis was performed with cortical thickness as the dependent variable and a random intercept defining subject as a random factor. Additional regressors included the time between scans in years (baseline imaging was marked as 0), age at baseline, gender, group (PD-VH vs PD non VH), and group-by-time interaction (variable of interest). Significance maps for group-by-time interactions were corrected for multiple comparisons using FDR-correction

combined over both hemispheres. Significance maps were saved for later visualization in freeview.

Thalamic sub-nucleus and Tract-of-interest analysis

Thalamic volumes and mean tract FC at baseline were compared between PD-VH and PD non VH using a linear mixed model with age, gender and total intracranial volumes as covariates. To assess differences in longitudinal rate of change for each thalamic sub-nucleus and each tract-of-interest respectively , I used a linear mixed model with group-by-time interaction as the variable of interest and group (PD-VH vs PD non VH), age, gender, and time between scans as regressors and a random intercept (corrected for multiple comparisons using FDR correction across 50 sub-nuclei/tracts). Correlational analyses of subnucleus volumes or mean tract FC with UM-PDHQ scores (indicating hallucination severity) were performed using Spearman correlation coefficient.

All statistical analyses were performed in Python3 using Jupyter Lab v1.2.6. The code used to perform these statistical analyses is available at: https://github.com/AngelikaZa/ThalamicSubnuclei.

5. 3. Results

This study included 101 participants: 22 PD-VH, 54 PD non VH, and 25 controls. Groups were well-matched in terms of age, gender and years in education and there was no significant difference between PD-VH and PD non VH in terms of global cognition, disease duration, motor severity or levodopa-equivalent daily dose. Demographics and results of clinical assessments at baseline are shown in *Table 5.1*. At longitudinal follow up, PD-VH showed greater deterioration in cognitive performance than PD non VH (*Table 5.2).*

Table 5.1. Demographics and results of baseline clinical assessments

Characteristic	Controls n= 25	PD non VH n= 54	PD VH n= 22	Statistic
Age (years)	67.4 (8.2)	64.6 (8.1)	64.5 (8.0)	r^2=0.004, p=0.308
Male (%)	12 (48.0)	36 (59.0)	6 (40%)	x^2=2.393. p=0.302
Years of education	17.9 (2.2)	17.3 (2.6)	16.9 (3.8)	H=0.755. p=0.686
Vision				
Contrast sensitivity (Pelli Robson) *	1.8 (0.2)	1.8 (0.2)	1.7 (0.2)	H=3.991. p=0.136
Visual Acuity (LogMar) *	-0.08 (0.2)	-0.07 (0.2)	-0.08 (0.1)	H=1.761. p=0.136
Colour vision (D15) *	1.2 (1.0)	1.2 (1.0)	1.6 (1.8)	H=0.151. p=0.927
General cognition				
MOCA	29 (1.2)	28.0 (2.3)	27.6 (1.8)	H=6.009. p=0.050[c]
MMSE	29.2 (0.9)	29.0 (1.2)	28.9 (1.3)	H=0.332. p=0.847
Mood				
HADS anxiety	**3.5 (3.5)**	**5.1 (3.5)**	**8.0 (4.2)**	**H=12.428 p=0.002[a,b,c]**
HADS depression	**1.2 (1.5)**	**3.7 (3.1)**	**4.8 (3.3)**	**H=23.010 p<0.001[b,c]**
Detailed neuropsychology				
Attention				
Digit span backwards	6.9 (2.4)	7.3 (2.2)	7.6 (2.4)	r^2=-0.021. p=0.748
Stroop: Colour (sec)	**31.9 (7.6)**	**32.6 (6.4)**	**38.3 (8.5)**	**r^2=0.068. p=0.012[a,c]**
Executive function				
Stroop: Interference (sec)	**56.2 (14.3)**	**40.3 (20.1)**	**72.9 (26.6)**	**H=7.025. p=0.029 [a,c]**
Category fluency	21.9 (4.8)	22.1 (6.0)	20.1 (4.0)	H=1.380. p=0.502
Memory				
Word Recognition Task	24.5 (1.0)	24.3 (2.3)	23.8 (1.2)	H=5.130. p=0.077
Logical Memory	12.8 (3.5)	13.3 (4.6)	13.5 (4.5)	r^2=-0.027. p=0.928
Language				
Graded Naming Task	23.6 (1.0)	24.3 (2.5)	23.5 (3.1)	H=0.899, p=0.638
Letter Fluency	17.8 (5.1)	17.3 (5.3)	16.1 (4.9)	H=0.682, p=0.711
Visuospatial				
JLO	26 (3.4)	25.3 (3.7)	23.1 (4.8)	H=4.019, P=0.134
Hooper	25.9 (2.1)	25.0 (2.9)	23.9 (3.1)	H=5.010, p=0.082
Disease specific measures				
Years from diagnosis	-	4.0 (2.5)	4.5 (2.7)	U=403, p=0.238

UPDRS total score	-	**42.9 (19.4)**	**57.8 (24.3)**	**U=289, p=0.014**
UPDRS motor score	-	22.7 (11.7)	26.2 (15.2)	U=395, p=0.052
Right side affected at onset	-	28 (45.9)	4 (26.7)	x^2=3.358, p=0.187
RBDSQ	-	**3.8 (2.1)**	**5.7 (2.4)**	**U=247, p=0.003**
Sniffin sticks	-	**7.6 (2.9)**	**6.9 (3.4)**	**U=421.5, p=0.003**
LEDD	-	427.1 (220.1)	431.0 (233.1)	t=-0.061, p=0.951

All data shown are mean (SD) except gender and affected size.
In bold characteristics that significantly differed between groups.
[a] Statistically significant difference between PD VH and PD non VH, [b] Statistically significant difference between PD non VH and controls, [c] Statistically significant difference between PD VH and controls
** Best binocular score used; LogMAR and D15: lower score implies better performance, Pelli-Robson: higher score implies better performance.*
[+] Higher values imply worse image quality, [-] Higher values imply better image quality
HADS: Hospital anxiety and depression scale; MMSE: Mini-mental state examination; MOCA: Montreal cognitive assessment; JLO: Benton's Judgement of Line Orientation, UPDRS: Unified Parkinson's Disease Rating Scale; MCI: Mild Cognitive Impairment; RBDSQ: REM sleep behaviour disorder scale; LEDD: Levodopa Equivalent Dose.

Table 5.2. Longitudinal changes in patients with Parkinson's disease

Cognitive test	**PD non VH n= 54**	**PD VH n= 22**	**PD non VH n= 54**	**PD VH n= 22**	**Statistic**
General cognition	**Baseline visit**		**Follow up visit (18 months)**		**p-value***
MOCA	**28.0 (2.3)**	**27.6 (1.8)**	**28.1 (2.1)**	**25.5 (5.2)**	**t=2.93, p=0.005**
MMSE	**29.0 (1.2)**	**28.9 (1.3)**	**29.1 (1.0)**	**27.7 (3.2)**	**U=317.5, p=0.030**
Attention					
Digit span backwards	7.3 (2.2)	7.6 (2.4)	7.9 (2.3)	7.6 (2.6)	t=0.923, p=0.359
Stroop: Colour (sec)	32.6 (6.4)	38.3 (8.5)	33.6 (8.7)	40.2 (3.8)	U=394, p=0.362
Executive function					
Stroop: Interference (sec)	40.3 (20.1)	72.9 (26.6)	59.1 (22.5)	70.7 (19.7)	U=373, p=0.406
Category fluency	22.1 (6.0)	20.1 (4.0)	20.4 (5.5)	18.8 (7.1)	t=0.269, p=0.789
Memory					
Word Recognition Task	24.3 (2.3)	23.8 (1.2)	24.1 (1.4)	24.0 (1.0)	U=347.5, p=0.131
Logical Memory (delayed)	13.3 (4.6)	13.5 (4.5)	12.7 (3.6)	13.0 (4.6)	t=0.293, p=0.770
Language					
Graded Naming Task	24.3 (2.5)	23.5 (3.1)	24.8 (2.9)	23.3 (4.1)	U=437, p=0.395
Letter Fluency	17.3 (5.3)	16.1 (4.9)	16.7 (4.4)	16.2 (6.1)	t=-0.590, p=0.557
Visuospatial					
JLO	25.3 (3.7)	23.1 (4.8)	25.3 (3.7)	21.9 (4.8)	U=265, p=0.066
Hooper	25.0 (2.9)	23.9 (3.1)	25.2 (3.2)	23.2 (5.0)	U=424, p=0.333
Motor Symptoms					
UPDRS total score	42.9 (19.4)	57.8 (24.3)	41.8 (6.3)	58.4 (17.2)	t=0.345, p=0.731
UPDRS motor score	22.7 (11.7)	26.2 (15.2)	21.7 (10.2)	26.1 (10.2)	t=0.244, p=0.808
LEDD	427.1 (220.1)	431.0 (233.1)	427.1 (220.1)	431.0 (233.1)	-

All data shown are mean (SD).
** Statistical comparison of individual performance change (Performance in Follow up visit – Performance in Baseline visit) for each metric; using t test for normally distributed variables and Mann-Whitney for non-normally distributed variables. In bold characteristics that significantly differed in terms of change between Visit 2 and baseline between groups.*
JLO: Judgement of Line Orientation.

Cortical gray matter is relatively preserved in patients with PD and visual hallucinations despite widespread white matter changes

At baseline, no statistically significant changes in cortical thickness were seen between PD-VH and PD non VH. Cortical thickness for both groups decreased at follow up, with significantly higher reductions longitudinally in PD-VH compared to PD non VH, in clusters including the left precuneus, bilateral precentral and postcentral gyrus, bilateral superior frontal and anterior cingulate gyrus, bilateral insula, right superior temporal gyrus, right supramarginal gyrus, and right lateral occipital gyrus (*Figure 5.2, Table 5.3*).

In contrast, PD-VH showed significant changes in white matter macro- and micro-structure compared to PD without hallucinations already at baseline (*Figure 5.3*): macrostructural changes (reduction in FC) and microstructural changes (reduction in FD) within the splenium of the corpus callosum and the left posterior thalamic radiation. Reductions were also seen in the combined FDC metric across the same regions, particularly within the splenium of the corpus callosum which showed over 30% reductions in FDC in PD-VH compared to PD non VH.

White matter changes continued to develop longitudinally (*Figure 5.4)* with additional extensive macrostructural changes (FC reductions) in PD-VH compared to PD non VH within the splenium, bilateral posterior internal capsules, bilateral posterior thalamic radiations, bilateral tapetum, the left inferior and left superior fronto-occipital fasciculus (*Figure 5.4*). No changes were seen between PD with and without hallucinations in the longitudinal reduction of FD or FDC.

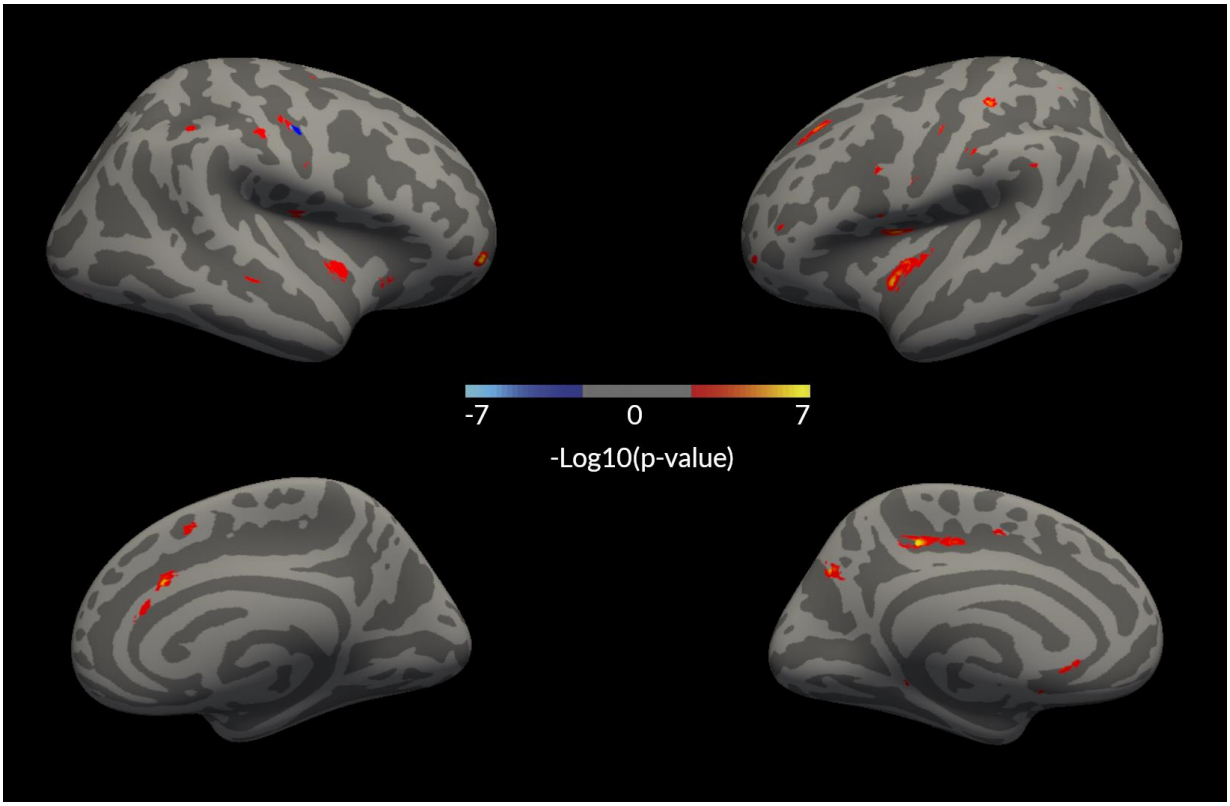

Figure 5. 2. Longitudinal whole-brain grey matter changes in PD with hallucinations.

Changes in cortical thickness seen in patients with Parkinson's disease with hallucinations (PD-VH) compared to those without hallucinations (PD non VH) at Visit 2 rendered on the surface.

No statistically significant changes were seen in cortical thickness at baseline imaging.

Colour coding indicates cluster significance for group-by-time interactions, on a logarithmic scale of p values (−log10) FDR corrected across both hemispheres. Positive values indicate PD-VH cortical thickness < PD non VH; negative values indicate PD-VH > PD non VH.

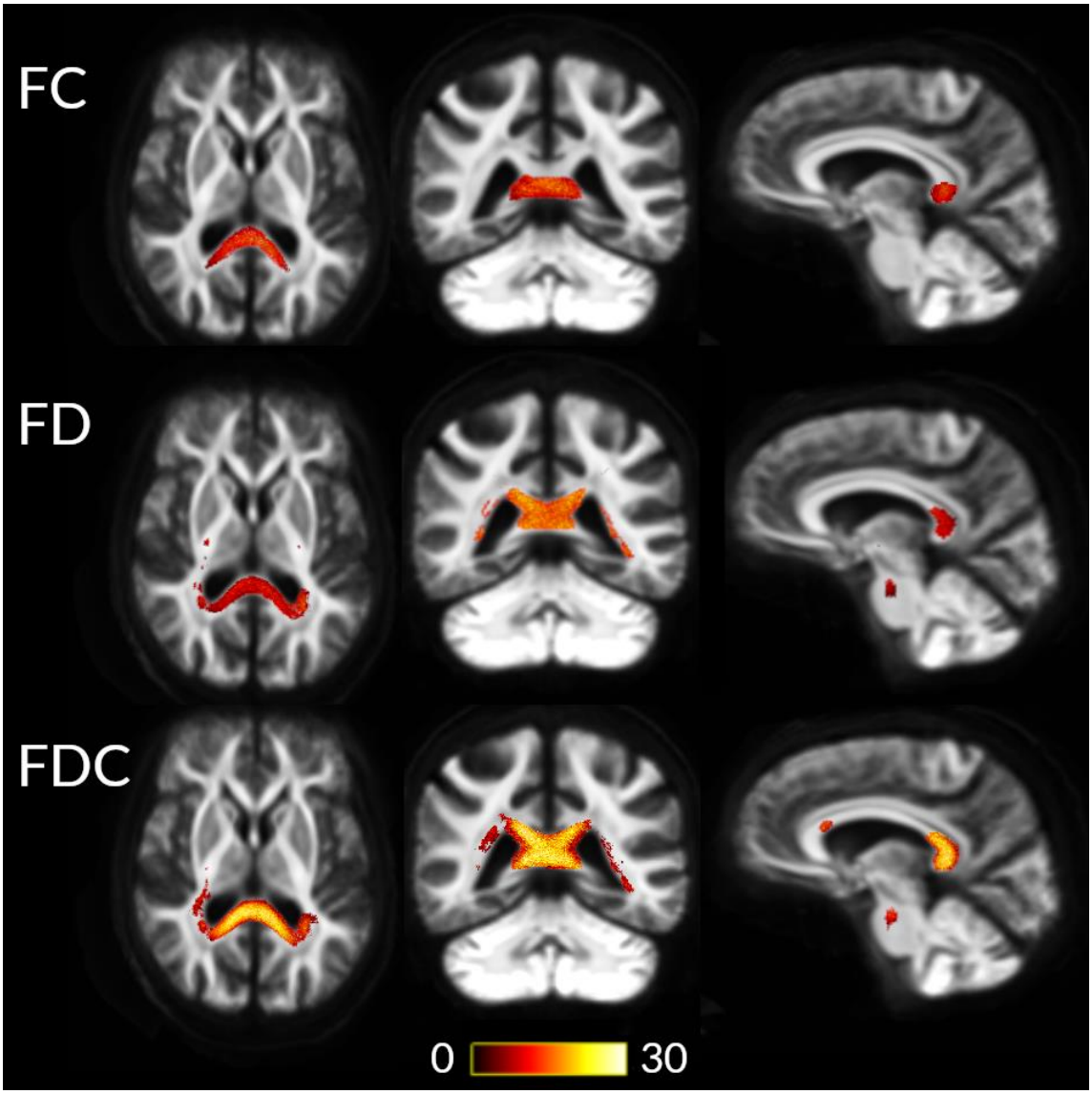

Figure 5. 3 Fibre tract-specific reductions at baseline in PD with hallucinations.

PD-VH showed macrostructural changes (fibre cross-section (FC)) within the splenium of the corpus callosum and bilateral posterior thalamic radiations. Microstructural changes (reductions in fibre density (FD)) were also seen at baseline imaging, with FD reductions in PD-VH in the splenium of the corpus callosum, bilateral posterior thalamic radiations and the right corticospinal tract. Changes in the combined FDC metric were seen within the body and splenium of the corpus callosum, posterior thalamic radiations bilaterally, and the right corticospinal tract.

Results are displayed as streamlines (FWE-corrected p <0.05). Streamlines are coloured by percentage reduction (colourbars) in PD-VH compared to PD non VH.

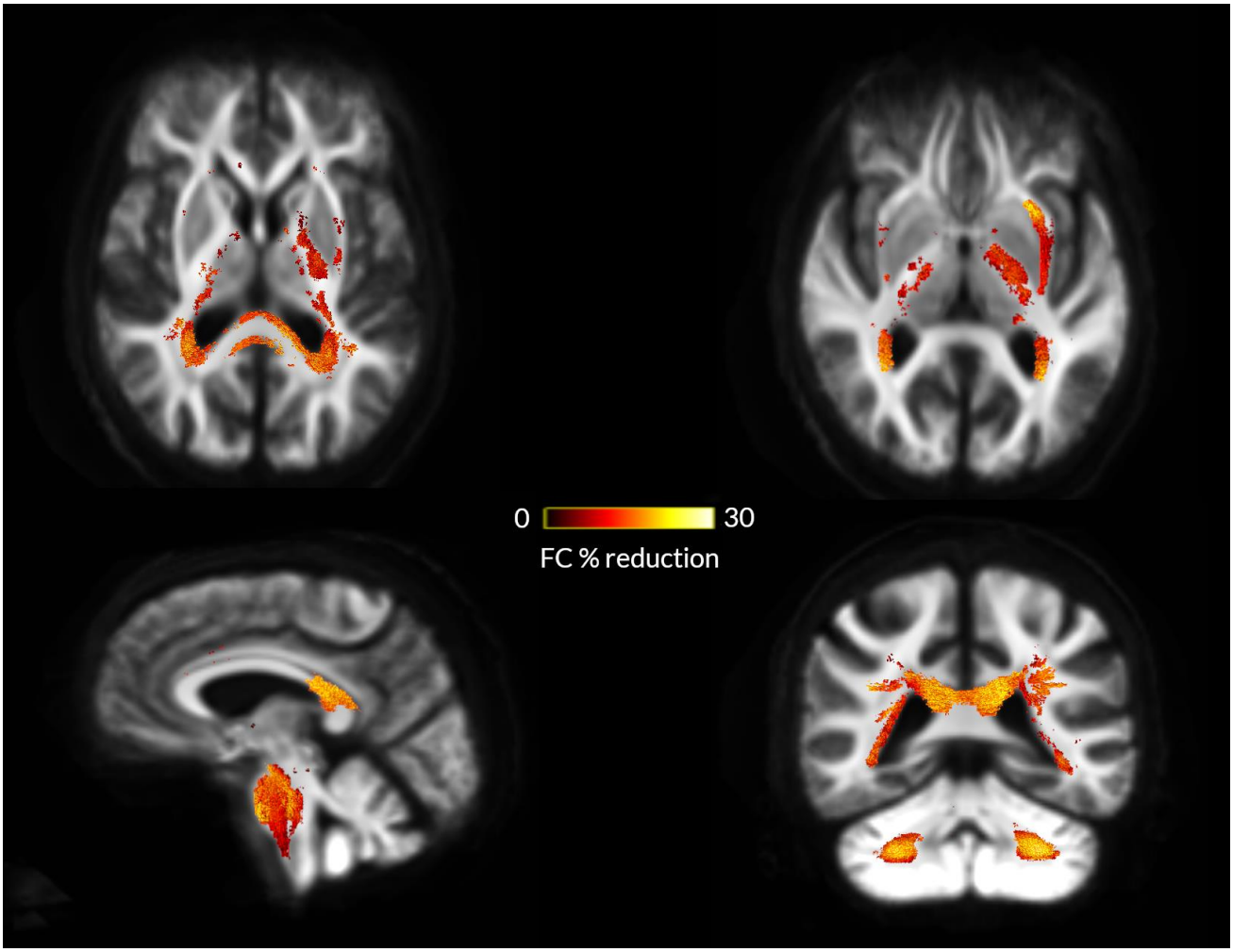

Figure 5. 4 Changes in white matter macrostructure in PD with hallucinations at longitudinal follow up.

FC: Fibre cross-section. Results are displayed as streamlines; these correspond to fixels that significantly differed between PD low and high visual performers (FWE-corrected p <0.05). Streamlines are coloured by percentage reduction (colourbars) in PD-VH compared to PD non VH.

Table 5.3. Gray matter clusters showing significant longitudinal differences in cortical thickness between PD patients with and without hallucinations

Changes in Cortical Thickness							
Tailarach Coordinates			**Hemisphere**	**Anatomical location**	**Number of vertices**	**Size (mm^2)**	**Zmax**
x	**y**	**z**					
28.1	-20.8	37.8	L	Precuneus	368	140.54	7.5
-32.7	55.4	14.2	R	Caudal anterior cingulate	136	56.87	7.4
29	13.8	27.1	R	Precentral	143	39.47	7.4
3.5	92.5	-31	R	Rostral middle frontal	115	57.25	7.3
27.7	-66.5	28.8	L	Superior frontal	134	55.16	7.2
-16	29.5	-12.3	L	Insula	184	45.62	7.1
-20.4	-11	42.5	L	Postcentral	113	29.17	7.1
-15.8	28.4	-31.5	L	Insula	343	136.58	7
5.7	67.6	30.9	L	Superior frontal	196	98.74	6.9
22.8	12.3	-5.5	R	Postcentral	126	31.91	6.7
-30.2	42.5	41.1	R	Superior frontal	53	27.29	6.7
38.1	48.9	-28.4	L	Rostral anterior cingulate	50	29.98	6.6
16.7	25.3	-27.5	R	Insula	152	57.93	6.6
28.3	-29.1	31.3	R	Supramarginal	91	24.73	6.6
35.8	0.5	25.4	R	Postcentral	84	22.18	6.4
3.5	-86.9	-28.8	R	Lateral occipital	19	9.09	6.3
30.2	24.7	38.3	L	Superior frontal	50	15.03	6.1
-33.5	62.6	4.4	R	Caudal anterior cingulate	50	29.73	6.1
39.4	-7	-29.4	R	Superior temporal	29	9.06	6.1
-4	93.4	-27.3	L	Rostral middle frontal	41	21.08	6
-27.7	36.1	11.5	L	Precentral	25	9.54	5.9

Anatomical locations extracted from aparc freesurfer annotation.
Zmax indicates the -log10(pvalue) for the cluster, a threshold of 5.613 was calculated to represent FDR corrected values for both hemispheres.
R: Right, L: Left hemispheres.
No statistically changes were seen at baseline imaging between PD-VH and PD non VH participants.

Specific volume loss of the right mediodorsal thalamic nucleus is seen in PD-VH longitudinally and is preceded by respective white matter thalamic connection loss

Thalamic volumes (for the whole of the thalamus as well as for the 50 derived sub-nuclei) showed no significant difference between PD-VH and PD non VH at baseline, correcting for age, gender and total intracranial volume. However, when assessing differences in longitudinal thalamic sub-nuclei volumes, PD-VH showed significantly higher reductions in grey matter volume of the right medial mediodorsal magnocellular nucleus (MDm: t=-3.018, FDR-corrected p-value, q<0.001) and the left paracentral thalamic nucleus (Pc: t=-3.490, q<0.001) compared to PD non VH (*Figure 5.5*). Thalamic sub-nucleus volume loss was significantly correlated with hallucination severity for both the right MDm (rho=-0.362, p=0.001) and the left Pc nucleus (rho =-0.339, p=0.003).

White matter tracts-of-interest from thalamic sub-nuclei to the ipsilateral hemisphere showed significant reductions in mean FC in PD-VH already at baseline; specifically in the right MDm and the right centromedial nucleus. Longitudinally, tracts-of-interest from 44 out of 50 thalamic subnuclei showed significant reductions in mean FC in PD-VH compared to PD non VH, adjusting for age, gender, total intracranial volume and time between scans and FDR-corrected across 50 tracts (*Table 5.4*). Longitudinal reduction in mean FC of these tracts was significantly correlated with hallucination severity (rho=-0.212, q<0.001).

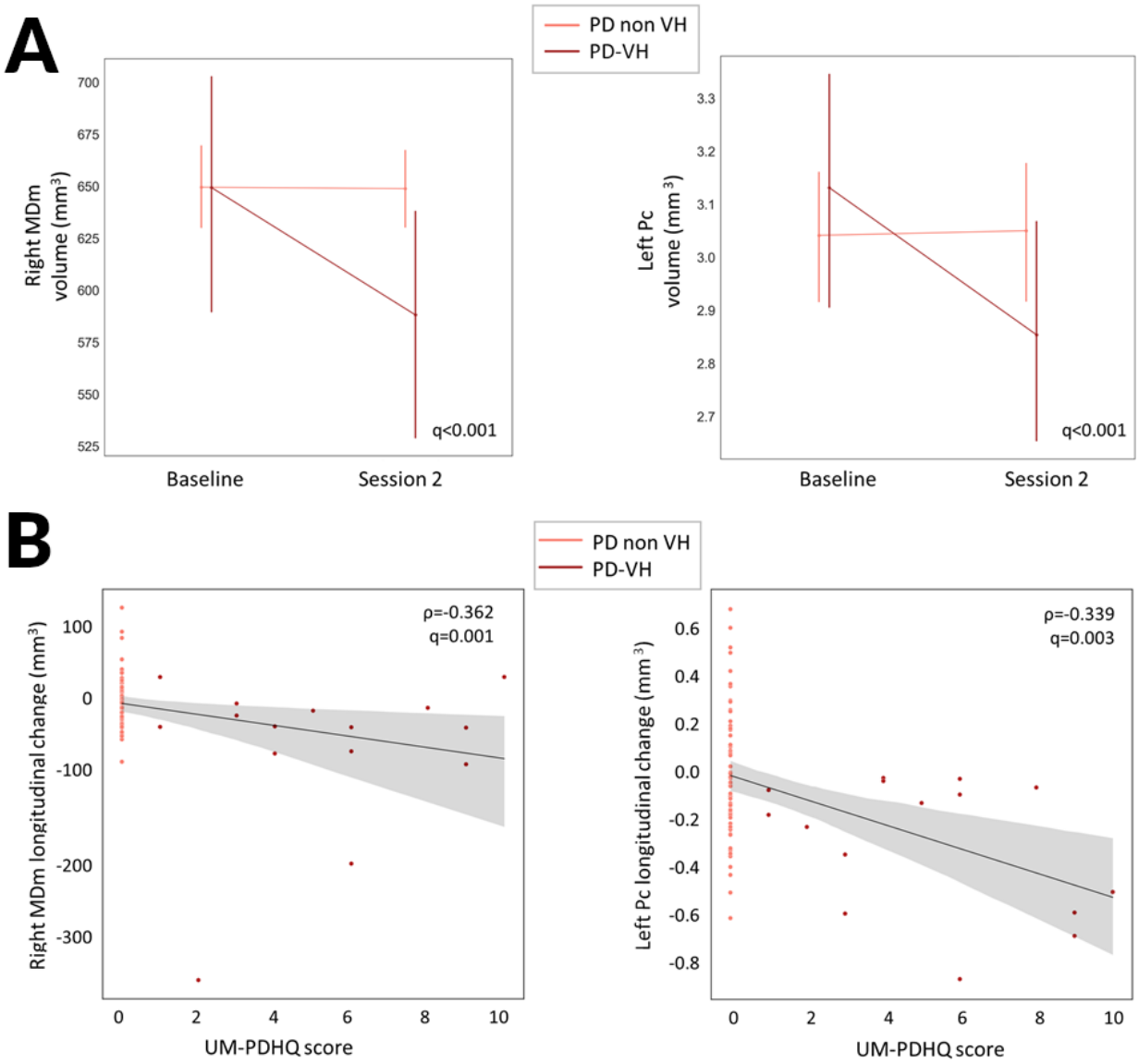

Figure 5.5 Thalamic subnucleus changes in PD with hallucinations

A. Longitudinal change in thalamic nuclei volumes for the right MDm (mediodorsal medial magnocellular) and the left Pc (paracentral subnucleus) in PD-VH, PD non VH in mm2. Corrected for age, gender, total intracranial volume and time between scan. P-value presented for the group-by-time interaction comparison between PD-VH and PD non VH participants. Error bars represent standard deviation.

B. Change in thalamic nuclei volumes for the right MDm and the left Pc in PD participants was correlated with severity of visual hallucinations, assessed using the University of Miami Parkinson's disease Hallucinations Questionnaire (UM-PDHQ).

Table 5.4. White matter thalamic tract differences in mean FC between patients with Parkinson's disease and visual hallucinations (PD-VH) and without hallucinations (PD non VH).

Tract	Changes at Baseline			Visit 2 (18 months follow up)		
	beta	p-value	q-value	beta	p-value	q-value
Left AV	-0.0167	0.073575	0.176	**-0.159**	**0.005**	**0.006098**
Left CeM	-0.01496	0.106572	0.176	**-0.168**	**0.004**	**0.006098**
Left CM	-0.01536	0.087835	0.176	**-0.167**	**0.004**	**0.006098**
Left L_Sg	-0.0143	0.151725	0.217	**-0.157**	**0.005**	**0.006098**
Left LD	-0.01729	0.078379	0.176	**-0.162**	**0.005**	**0.006098**
Left LGN	-0.01614	0.100528	0.176	**-0.158**	**0.007**	**0.007609**
Left LP	-0.00259	0.825082	0.855	**-0.174**	**0.001**	**0.006098**
Left MDl	-0.00856	0.442954	0.481	**-0.146**	**0.002**	**0.006098**
Left MDm	-0.01157	0.261344	0.297	**-0.148**	**0.004**	**0.006098**
Left MGN	-0.01538	0.092495	0.176	**-0.165**	**0.004**	**0.006098**
Left MVRe	-0.01651	0.064117	0.176	**-0.167**	**0.004**	**0.006098**
Left Pf	-0.01552	0.065164	0.176	**-0.167**	**0.004**	**0.006098**
Left PuA	-0.00886	0.838129	0.855	**-0.131**	**0.027**	**0.028125**
Left PuI	-0.01694	0.076763	0.176	**-0.164**	**0.005**	**0.006098**
Left PuL	-0.0134	0.160321	0.217	**-0.166**	**0.005**	**0.006098**
Left PuM	-0.01653	0.106226	0.176	**-0.16**	**0.006**	**0.006818**
Left VA	-0.01349	0.190176	0.241	**-0.162**	**0.005**	**0.006098**
Left VAmc	-0.01667	0.070042	0.176	**-0.166**	**0.004**	**0.006098**
Left VLa	-0.01213	0.197567	0.241	**-0.168**	**0.004**	**0.006098**
Left VLp	-0.012	0.217166	0.253	**-0.165**	**0.004**	**0.006098**
Left VPL	-0.01255	0.15604	0.217	**-0.17**	**0.004**	**0.006098**
Left VM	0.054166	0.167992	0.221	**0.683**	**0.004**	**0.006098**
Left CL	-0.01582	0.104575	0.176	**-0.158**	**0.005**	**0.006098**
Left Pc	0.046429	0.071154	0.176	0.493	0.041	0.060981
Left Pt	0.046429	0.071154	0.176	0.072	0.086	0.087755
Right AV	-0.02101	0.020802	0.176	**-0.158**	**0.005**	**0.006098**
Right CeM	**-0.01569**	**9.85E-06**	**<0.001**	**-0.169**	**0.003**	**0.006098**
Right CM	-0.01791	0.041074	0.176	**-0.166**	**0.004**	**0.006098**
Right L_S	-0.02014	0.051005	0.176	**-0.159**	**0.006**	**0.006818**
Right LD	-0.02256	0.016982	0.176	**-0.16**	**0.005**	**0.006098**

Right LGN	-0.01993	0.107471	0.176	**-0.154**	**0.007**	**0.007609**
Right LP	-0.01586	0.110677	0.176	**-0.158**	**0.005**	**0.006098**
Right MDl	0.013326	0.432889	0.481	**-0.128**	**0.005**	**0.006098**
Right MDm	-0.03742	0.002003	0.05	**-0.152**	**0.004**	**0.006098**
Right MGN	-0.02135	0.112517	0.176	**-0.16**	**0.005**	**0.006098**
Right MVRe	-0.01951	0.032731	0.176	**-0.163**	**0.004**	**0.006098**
Right Pf	-0.015	0.088	0.176	**-0.169**	**0.003**	**0.006098**
Right PuA	-0.0088	0.520089	0.553	**-0.154**	**0.005**	**0.006098**
Right PuI	-0.02137	0.043955	0.176	**-0.162**	**0.005**	**0.006098**
Right PuL	-0.01752	0.061791	0.176	**-0.165**	**0.004**	**0.006098**
Right PuM	-0.02221	0.020873	0.176	**-0.158**	**0.006**	**0.006818**
Right VA	-0.01884	0.062591	0.176	**-0.161**	**0.005**	**0.006098**
Right VAmc	-0.02079	0.032996	0.176	**-0.161**	**0.005**	**0.006098**
Right VLa	-0.01488	0.11635	0.176	**-0.167**	**0.004**	**0.006098**
Right VLp	-0.01399	0.12015	0.177	**-0.169**	**0.003**	**0.006098**
Right VPL	-0.01395	0.079667	0.176	**-0.17**	**0.003**	**0.006098**
Right VM	0.063079	0.090592	0.176	**0.676**	**0.004**	**0.006098**
Right CL	-0.00386	0.86107	0.861	**-0.167**	**0.008**	**0.008511**
Right Pc	0.037085	0.202579	0.241	0.503	0.050	0.06098
Right Pt	0.037085	0.202579	0.241	0.052	0.119	0.119

AV*: anteroventral, CeM: central medial, CM: centromedian, L_Sg: limitans, LD: laterodorsal, LGN: lateral geniculate, LP: lateral posterior, MDl: mediodorsal medial parvocellular, MDm: mediodorsal medial magnocellular, MGN: medial geniculate, MVRe: Reuniens medial ventral, Pf: parafascicular, PuA: pulvinar anterior, PuI: pulvinar inferior, PuL: pulvinar lateral, PuM: pulvinar medial, VA: ventral anterior, VAmc: ventral anterior magnocellular, VLa: ventral lateral anterior, VLp: ventral lateral posterior, VPL: ventral posterolateral, VM: ventromedial, CL: central lateral, Pc: paracentral, Pt: paratenial.*

In bold tracts showing FDR-corrected statistically significant differences between PD-VH and PD non VH participants.

Assessing a potential effect of anxiety and depression

Given the observed differences in anxiety and depression between PD-VH PD non VH, I performed additional analyses to ensure the observed structural white and grey matter changes were not directly influenced by anxiety and depression scores. There was no statistically significant correlation between HADS depression and anxiety scores and the main structural grey and white matter changes seen in PD-VH: specifically the mean volume of the medial mediodorsal magnocellular thalamic subnucleus (MDm) or mean fibre cross section (FC) of thalamic white matter tracts, either at baseline or longitudinally (*Table 5.5*).

Table 5.5. Relationship between anxiety and depression scores and thalamic volumes and white matter tract integrity

	Relationship with MDm volume		**Relationship with mean tract FC**	
	Baseline	**Longitudinal difference**	**Baseline**	**Longitudinal difference**
HADS anxiety	rho=0.009 p=0.939	rho=0.036 p=0.758	rho = -0.111 p=0.338	rho = -0.100 p=0.388
HADS depression	rho=-0.102 p=0.381	rho=0.003 p=0983	rho=0.020 p=0.863	rho=-0.172 p=0.138

HADS: Hospital anxiety and depression questionnaire, higher scores indicate higher severity of anxiety or depression respectively. MDm: medial mediodorsal magnocellular thalamic subnucleus. FC: fibre cross section

Since HADS anxiety and depression scores were not correlated with the main outcome measures (MDm volume and tract FC) and they were inherently different in our compared groups (PD-VH versus PD non VH) they were not included as covariates, as this would reduce the sensitivity of the model to detect a true effect without improving specificity (Miller and Chapman, 2001; Rohrer, 2018).

4.4. Discussion

This study sheds light on the timeline and spatial profile of structural brain changes in patients with Parkinson's disease and visual hallucinations across the grey matter, white matter and thalamus. Specifically, I showed that:

a. the right mediodorsal medial thalamus is affected in PD with hallucinations, with white matter tracts originating from the right mediodorsal thalamus showing macrostructural changes (reduced mean FC) at baseline followed by volume loss within the nucleus after longitudinal follow-up,
b. widespread white matter micro- and macrostructural changes are present in PD with hallucinations already at baseline, in the absence of grey matter changes (cortical thickness)
c. macrostructural white matter changes continue in PD with visual hallucinations over time involving many cortical-cortical connections and the majority of thalamo-cortical white matter
d. differences in cortical thickness only evolve after follow up and are relatively mild in PD with compared to those without hallucinations.

By using a recently described probabilistic atlas derived from ex vivo imaging and histology (Iglesias et al., 2018), I was able to detect differences in volumes within the right mediodorsal medial thalamic sub-nucleus in PD with visual hallucinations. The mediodorsal medial nucleus is a higher order, associative thalamic nucleus with multiple reciprocal connections with the prefrontal and anterior cingulate cortex (Mitchell and Chakraborty, 2013). It plays an establised role in cognition, particularly in sustaining prefrontal cortex (PFC) activity during working and spatial memory (Parnaudeau et al., 2018) and monitoring and updating mental representations (Wolff and Vann, 2019). It has also been implicated in

psychiatric disease; patients with schizophrenia show reduced functional activation within the mediodorsal medial thalamus and reduced functional connectivity to the PFC during executive tasks (Minzenberg et al., 2009); they also show grey matter atrophy in the mediodorsal thalamus (Cobia et al., 2017; Pergola et al., 2017). Reduced functional connectivity of the mediodorsal thalamus with the paracingulate and posterior cingulate has also been described in patients with Parkinson's disease and cognitive impairment (Owens-Walton et al., 2019). The complex way that the mediodorsal medial thalamic sub-nucleus interacts with the PFC is not fully understood, however there is evidence to suggest that it may act as a regulator of PFC function (Pergola et al., 2018): reduced input from the mediodorsal medial nucleus, due to white matter degeneration and neuronal loss within the nucleus could result in subsequent unregulated PFC activity.

In whole brain fixel-based analysis, there was a significant posterior predominance of white matter structural changes in PD-VH: changes in the splenium of the corpus callosum and posterior thalamic radiations were seen at baseline imaging and progressed further during follow up to involve multiple posterior tracts such as the tapetum and posterior internal capsules but frontal connections remained relatively preserved. Reduced connectivity between subcortical regions and visuo-spatial regions when combined with unregulated PFC activity (due to reduced control from the mediodorsal medial thalamic nucleus) which retains its other cortical white matter projections may partly explain the over-weighting of prior knowledge seen in Parkinson's hallucinations (*Chapter 3*).

Both in whole-brain and in thalamic sub-nucleus analyses, white matter macrostructural changes were detectable in PD-VH before any changes in cortical thickness or thalamic volume loss were evident. PD-VH showed significant macrostructural (reduced FC) and microstructural changes

(reduced FD) within posterior white matter tracts already at baseline, in the absence of any cortical thickness changes. In addition, the right mediodorsal medial thalamus which showed reduced volume in PD-VH compared to PD non-VH at follow up, showed macrostructural changes in its connections with the ipsilateral hemisphere at baseline.

This result could be due to different sensitivity of the imaging modalities used to assess grey and white matter, however it does provides further support for the important role that white matter degeneration plays in PD. Axonal pathology has been demonstrated prior to dopaminergic neuronal loss in animal (Tofaris et al., 2006; Chung et al., 2009; Li et al., 2009) and in cell models (Volpicelli-Daley et al., 2011). Alpha-synuclein affects axonal growth with higher density, thinner axons seen in the brain of patients with early Parkinson's disease (Schechter et al., 2020). Imaging biomarkers that assess white matter integrity such as fixel-based analysis might be more sensitive at picking up anatomical abnormalities at the earliest stages of PD; this is supported by our findings.

Our finding of changes in thalamic grey and white matter in PD patients with hallucinations could underlie the more widespread network differences found in PD hallucinators (Shine *et al.*, 2014; Yao *et al.*, 2014; Hall *et al.*, 2019) The medial mediodorsal nucleus, which showed volume reduction in PD-hallucinators is a feasible target for deep brain stimulation which has been performed in small numbers of patients with severe obsessive compulsive disorder (Maarouf et al., 2016). Given the changes in white matter connectivity from the medial mediodorsal nucleus to the cortex that we found in PD with hallucinations, further work in the connectivity between this subnucleus and the frontal cortex in particular could yield other possible connectomic targets for deep brain stimulation (Li et al., 2020) to treat hallucinations in PD.

Several methodological considerations need to be taken into account. Study participants underwent imaging acquisition whilst continuing their usual dopaminergic medications. Given that structural metrics were assessed it is unlikely that these will be affected by medication; additionally, levodopa equivalent doses did not differ between PD groups. Raw imaging data were visually inspected and no clinically significant cerebrovascular disease was seen, but due to the imaging acquisition protocols in the study, the presence of white matter hyperintensities could not be formally assessed and controlled for. No studies using fixel-based analysis so far have specifically controlled for white matter hyperintensities (Grazioplene *et al.*, 2018; Mito *et al.*, 2018; Rau *et al.*, 2019), but these could decrease fibre density if they were present (Dhollander et al., 2017). It is not clear if white matter hyperintensities could have an effect on fibre cross-section which was the primary white matter metric particularly longitudinally, but this could be clarified in future studies.

In conclusion, this study showed that patients with Parkinson's disease and visual hallucinations show both white matter and grey matter degeneration longitudinally but white matter changes are detectable before any loss of cortical thickness can be seen. In addition, thalamic-cortical connectivity is affected in Parkinson's-associated hallucinations, particularly within the mediodorsal nucleus. These findings provide mechanistic support for the role of the thalamus as a driver of network imbalance in Parkinson's hallucinations, and support the use of imaging techniques aimed at white rather than grey matter in assessing early stages of Parkinson's disease.

Publication statement

Some of the work included in this chapter (baseline white matter imaging) has been published previously (Zarkali *et al.*, 2020) and is included here as

per the publisher's policy with regards to thesis publications. Work describing longitudinal grey and white matter imaging (including thalamic subnuclei) has been submitted for publication and is currently under review.

6. Uncovering the biological processes driving white matter vulnerability in Parkinson's hallucinations

6.1 Introduction

An attractive theoretical model for visual hallucinations in Parkinson's disease (PD) is that they arise due to a shift in the balance of different networks, particularly those involved in attention and conscious perception, with overactivity of the Default Mode Network (DMN) and failure to engage the dorsal attention network (Muller *et al.*, 2014, Shine *et al.*, 2014*b*; Onofrj *et al.*, 2019). Indeed, aberrant default mode network (DMN) activation has been repeatedly described in patients with PD and hallucinations (Shine *et al.*, 2014*a*, 2015; Yao *et al.*, 2014; Franciotti *et al.*, 2015). In addition to changes in the relative effects of functional brain networks, there is evidence of a failure to integrate sensory input and prior knowledge during visual perception in patients with PD and visual hallucinations: PD with hallucinations show impaired sensory evidence accumulation (O'Callaghan *et al.*, 2017), visual-perceptual deficits (Weil *et al.*, 2016) and in a previous chapter (*Chapter 3*) I showed that they also exhibit an over-reliance on prior knowledge. This imbalance in sensory integration and the functional activation of brain regions are likely to be mediated or influenced by changes in underlying structural connectivity.

In previous chapters (*Chapters 4 and 5*) I showed that white matter shows macrostructural and microstructural changes in PD with hallucinations, with changes within the splenium of the corpus callosum and the left posterior thalamic radiation at baseline but subsequent widespread changes at 15 months follow up. Changes at the network level have also been reported in PD with hallucinations, primarily affecting regions of the "diverse club"

which are thought to be crucial for integration across specialist modules (Hall *et al.*, 2019). It is difficult however to infer from these studies what impact structural connectivity loss will have on functional dynamics, nor what factors make specific brain regions more vulnerable to connectivity loss.

Network control theory is an emerging framework that tries to bridge structural network with functional dynamics (Gu *et al.*, 2015). Specifically, using structural connectivity estimates and linear estimates of local dynamics, network control theory can be used to derive a measure of the extent of the influence one region (or node) of the network has over other parts of the brain and in facilitating the transitioning between brain states; this is called average controllability (Gu *et al.*, 2015). Given the importance that relative shifts in activation between brain networks seem to play in PD hallucinations (Muller *et al.*, 2014), controllability is likely to provide important insights into how hallucinations arise in PD.

In this chapter I aim to clarify the structural connectivity changes in patients with PD and habitual visual hallucinations (PD-VH) at a network level. I will use network control theory to assess the average controllability in PD-VH compared to those with PD without hallucinations at whole-network and subnetwork level; this will assess the effect structural changes will have on brain function. Finally, I will aim to shed light on the pathological processes that drive regional selective vulnerability to connectivity loss by assessing differences in regional gene expression between affected and unaffected regions. Regional gene expression in health has been shown to predict white matter connectivity loss in Huntington's disease (McColgan *et al.*, 2018) and schizophrenia (Romme *et al.*, 2017) and expression of candidate genes has been associated with cortical atrophy in PD (Freeze *et al.*, 2018, 2019). Characterising potential changes in regional gene

expression linked to connectivity loss in PD VH may provide important mechanistic insights.

6.2 Methods

Study Participants

Participants were recruited from the Vision in Parkinson's disease study (VIPD cohort, *Chapter 2: Study Cohorts*). All participants with baseline diffusion weighted imaging (DWI) and structural brain imaging scans passing predetermined quality control criteria were included in the study leading to 100 participants with PD and 34 unaffected controls included in this study. Patients with PD satisfied the Queen Square Brain Bank Criteria for PD (Emre *et al.*, 2007).

Participants with PD were classified as PD with visual hallucinations (PD-VH, n=19) if they scored more than 1 for Question 2 of the UPDRS: "Over the past week have you seen, heard, smelled or felt things that were not really there?". All other participants with PD were classified as PD non VH (n=81). Further information on the frequency and severity of hallucinations was collected using the University of Miami Parkinson's Disease Hallucinations Questionnaire (UM-PDHQ) (Papapetropoulos et al., 2008). The full study protocol is described in *Chapter 2*.

MRI data acquisition and preprocessing

An overview of the study methodology is seen in *Figure 6.1*. The study protocol and preprocessing steps are described in *Chapter 2* in detail. After DWI pre-processing, diffusion tensor metrics were calculated and constrained spherical deconvolution (CSD) performed, as implemented in MRtrix (Hollander, T. *et al.*, 2016).

360 cortical regions of interest (ROIs) were generated by segmenting a structural T1-weighted image according to the Glasser segmentation which is based on a large number of participants (210), precisely aligned to each other (Glasser *et al.*, 2016) and 19 subcortical ROIs were generated from the automatic Freesurfer parcellation (Fischl *et al.*, 2002). ROIs were warped into DWI space by registering the structural image to the DWI image using FLIRT (Greve and Fischl, 2009). Anatomically constrained tractography was performed with 10 million streamlines (Smith *et al.*, 2012) and then tractograms were reduced using the spherical deconvolution informed filtering of tractograms (SIFT2) algorithm (Smith *et al.*, 2015) to reduce biases. The resulting set of streamlines was used to construct the structural brain network.

For each participant, a structural connectivity matrix was then generated by determining whether each pair of ROIs were connected by a streamline; connections were weighted by streamline count and a cross-sectional area multiplier (Smith *et al.*, 2015) and combined into 379 × 379 undirected and weighted connectivity matrices. As recommended by the authors of SIFT2, no threshold was applied to the connectivity matrices (Smith *et al.*, 2015).

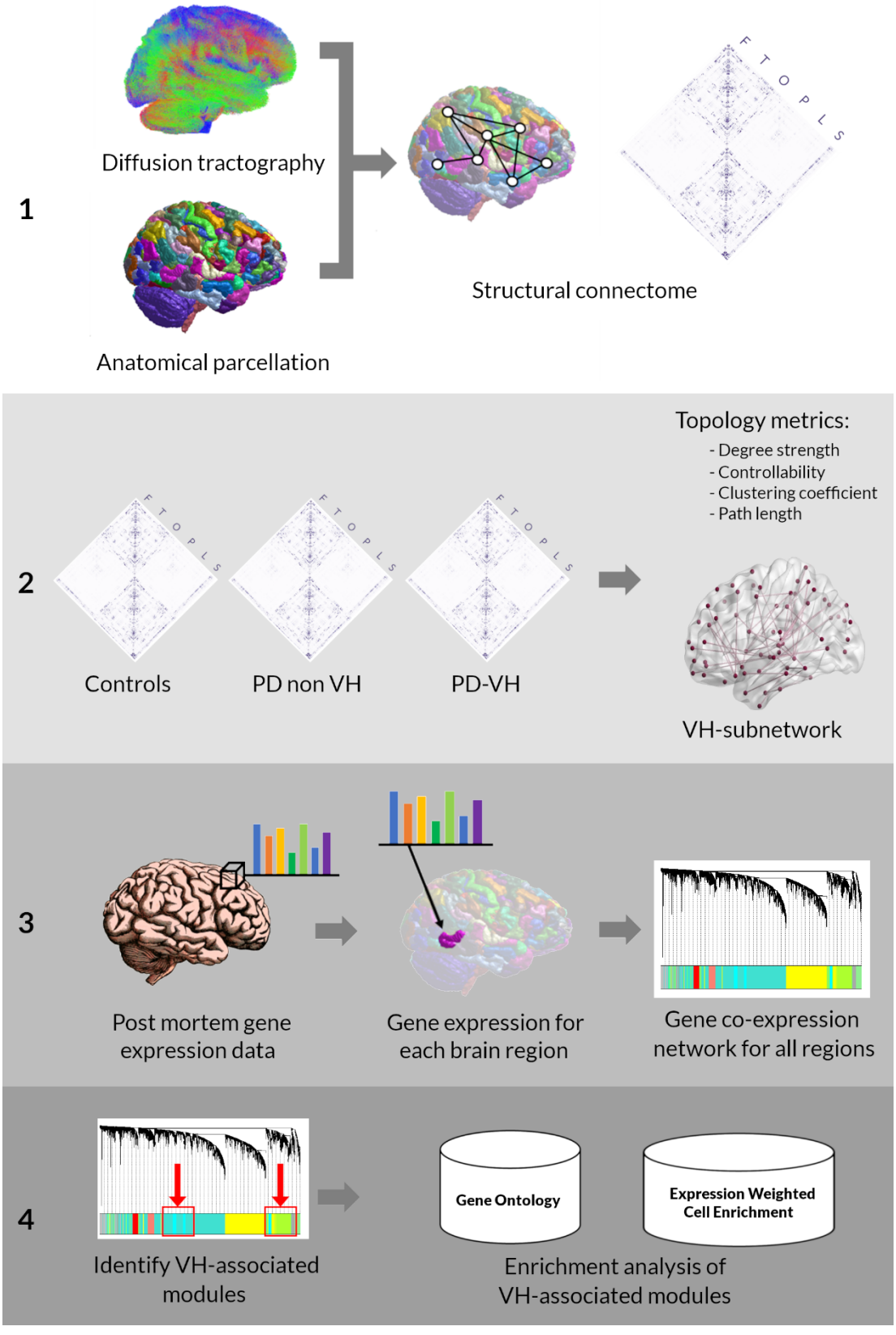
1
Diffusion tractography
Anatomical parcellation
Structural connectome
2
Topology metrics:
- Degree strength
- Controllability
- Clustering coefficient
- Path length
Controls
PD non VH
PD-VH
VH-subnetwork
3
Post mortem gene expression data
Gene expression for each brain region
Gene co-expression network for all regions
4
Identify VH-associated modules
Gene Ontology
Expression Weighted Cell Enrichment
Enrichment analysis of VH-associated modules

Figure 6. 1. Overview of the study methodology

(Opposite)

1. *Anatomically constrained tractography was used to determine white matter streamlines from diffusion weighted imaging (DWI) data for each participant. DWI were combined with an anatomical parcellation of 379 brain regions (360 cortical/19 subcortical) to generate a connectivity matrix for each participant.*

2. *Structural connectomes were compared between groups. Global topology metrics (degree strength, path length, clustering coefficient) and controllability were calculated for each participant and compared between PD vs controls, and PD with hallucinations (PD-VH) vs PD without hallucinations (PD-non-VH). Network-based statistics was then performed (contrasts: PD vs controls and PD-VH vs PD-non-VH, age and total intracranial volume as covariates) resulting to the identification of a VH-subnetwork of reduced connectivity strength.*

3. *Gene expression data were extracted from the Allen Brain atlas and mapped into the 180 cortical regions from the left hemisphere. An average regional gene expression level was calculated for each gene for each cortical region. Gene co-expression network analysis was then performed for the 180 regions resulting to a network of 27 modules.*

4. *The resulting gene co-expression network was examined to identify the modules associated with the VH-subnetwork: the summary profile (eigengene) for each module was correlated with presence in the VH-subnetwork. Two modules were significantly associated after correction for multiple comparison's, one downweighted (cyan module) and one upweighted (greenyellow module). Gene significance (the absolute value) of correlation between the gene and the trait (region's presence in the VH subnetwork) was then calculated for each gene of the two VH-associated module. Enrichment analyses were performed using the gene lists for these two modules, ranked by gene significance.*

F: Frontal, T: Temporal, O: Occipital, L: Limbic, P: Parietal, S: Subcortical

Network topology and controllability

Network control theory provides mathematically-derived predictions on the impact that structural connectivity has on brain function (Gu *et al.*, 2015; Betzel *et al.*, 2016). It models the role of a specific brain region in regulating whole-brain network function, in contrast to static graph theory metrics (Gu *et al.*, 2015). According to this framework a brain network with k nodes, can be described as a collection of neural states; these can be mathematically described as simulated states (x) of the network over time steps t using the following equation:

$$x_{t+1} = Ax_t + Bu_t$$

where x_t is a vector of all simulated states of all nodes k at time t, t are discrete time steps (t=1, 2, …), A_{ke} is the network's structural connectivity matrix (k number of nodes and e number of edges), B is a matrix of the control nodes in the network and u_t is the energy applied to the control nodes B at time t.

Using this framework, the influence that each brain region has on whole-brain function can be quantified using the metric of average controllability. Average controllability for a brain region (node) is a measure of the node's ability to influence other brain regions, specifically its ability to drive the whole brain network into all possible states. Average controllability is calculated as the average input energy required to be applied to a control node to reach all possible target states of the network. Regions with high average controllability can therefore drive the brain network to many easily reachable states. Mathematically average controllability is defined as the trace of the controllability gramian (Trace(W_k)) (Tang *et al.*, 2017) which is calculated as:

$$W_k = \sum_{T=0}^{\infty} A^T B_k B_k^T A^T$$

where A is the structural connectivity matrix, B is the control node matrix with k nodes and T is the control horizon. As previously described, I calculated average controllability for each node separately, therefore the matrix B was reduced to a one-dimensional vector $B_k = (1\ 0\ 0\ 0\ \ldots)^T$ where the first brain regions is the control node for which controllability is calculated. In this case k simply denotes this specific control node rather than all the nodes of the network.

Average controllability at node- and network-level was calculated for each participant using: https://complexsystemsupenn.com/s/controllability_code-smb8.zip. Then I compared average controllability between groups (PD-VH, PD non VH and controls).

Finally, global network metrics were calculated for each participant's structural connectome (*Figure 6.1, Step 2*): connectome density, clustering coefficient (metric of segregation), and characteristic path length (metric of integration) using the Brain Connectivity Toolbox (Bullmore and Sporns, 2009).

Network based statistics (NBS)

I performed network-based statistic (NBS) to investigate whether visual hallucinations were associated with altered connectivity strength (Zalesky et al., 2010). A general linear model was used with contrasts of interest: 1) PD-VH versus PD non VH and 2) PD versus controls. Age and total intracranial volume were included as nuisance covariates. Permutation testing with unpaired t-tests was performed with 5000 permutations, calculating a test statistic for each connection. A predetermined threshold of t = 3.1 was used (critical t-statistic for the study sample size) and family-wise error rate (FWE) of $p<0.05$ for multiple comparisons (*Figure 6.1, Step 2*).

Regional Gene Expression Analysis

Gene expression microarray data were extracted from the Allen Institute for Brain Science transcriptome atlas (Hawrylycz *et al.*, 2015). This was constructed postmortem from the brains of 6 human donors (aged 24-57 years) with no prior history of psychiatric or neurological disease. The atlas contains a database of expression levels for 20,737 genes represented by 58,692 probes across the cortical mantle and is available freely here: http://human.brain-map.org/static/download. Data from all six donors are available for the left hemisphere but only data from two donors are available for the right hemisphere; therefore, only left cortical regions (180 regions) were included in gene expression analyses similar to other studies (Romme *et al.*, 2017; McColgan *et al.*, 2018). The rigorous method of preprocessing by Arnatkevičiūtė et al. (Arnatkeviciūtė *et al.*, 2019) was used to extract gene expression data and map them to the 180 left cortical ROIs of the Glasser atlas. Each tissue sample was assigned to a ROI using the MRI data for each donor. Distances between samples were evaluated on the cortical surface, with a 2 mm threshold. Probe-to-gene annotations were then updated using the Re-Annotator package (Arloth *et al.*, 2015). Probes whose expression measures were above a background threshold in more than 50% of samples were selected and then a representative probe for each gene was chosen based on highest intensity. Expression data were normalised using scaled, outlier-robust sigmoid normalisation and then compiled to form a 180 × 15745 regional transcription matrix (Arnatkeviciūtė *et al.*, 2019). This process was performed using code from: https://github.com/BMHLab/AHBAprocessing. (*Figure 5.1, Step 3*).

Different genes are not expressed in isolation in the brain but modules of genes which are part of the same functional subsystem tend to get expressed together (Carpenter and Sabatini, 2004; Oldham *et al.*, 2008). I therefore used gene co-expression analysis to identify modules of highly co-expressed genes

that form a co-expression network. To construct gene co-expression networks I used weighted gene co-expression network analysis (WGCNA), one of the most widely used and validated methods (Langfelder and Horvath, 2008; Langfelder *et al.*, 2011; Botía *et al.*, 2017) using the WGCNA package in R (Zhang and Horvath, 2005; Langfelder and Horvath, 2008) and post-processing with k-means (Botía *et al.*, 2017). WGCNA uses measures of gene co-expression similarity to construct a network of gene-to-gene co-expression; this can be represented as a NxN matrix for N number of genes, where each connection between two genes represents the interaction strength between them. This matrix is then transformed using topological overlap into a proximity matrix where a pair of genes has a high proximity if it is closely interconnected; this way clusters or modules of highly interconnected genes that are co-expressed can be identified.

180 cortical ROIs of the left hemisphere were used in this analysis. Each region or node represented a different sample to construct a gene co-expression network of the healthy brain for the specific parcellation. The nodes/samples that participated in the VH-subnetwork were classified as nodes/samples that had the trait of visual hallucinations (VH) whilst the others were classified as non-VH nodes/samples. As suggested by the WGCNA authors (Langfelder and Horvath, 2008) outliers were assessed using distance-based networks (Zhang and Horvath, 2005) and I excluded nodes which had more than 50% missing entries (3 nodes were excluded as a result).

After the co-expression network was constructed and modules of highly-co-expressed genes were identified, the module membership for each gene within a given module was calculated as the Pearson's correlation coefficient between gene expression values and the module eigengene. Genes with

higher module memberships are more representative of the module's overall function and more likely to be critical components (*Figure 6.1, Step 3*).

The summary profile (eigengene) for each module was correlated to the VH trait using biweight midcorrelation; this way modules that were significantly associated (following FDR-correction) with the VH-subnetwork were identified: VH-associated modules. For each VH-associated module, gene significance for the VH trait was calculated for each gene. Gene significance is defined as the absolute value of the correlation between the gene and the trait and can be considered as the association of individual genes with specific clinical information. In this study this clinical information reflects reduced structural connectivity seen in the brains of PD-VH participants.

Enrichment Analyses

Enrichment analysis of the VH-associated modules was performed by ranking the genes of these modules according to their gene significance (*Figure 5.1, Step 4*). Gene Ontology (GO) and KEGG pathway terms were analysed on g:Profiler using FDR correction for multiple comparisons and $p<0.01$ as the statistical significance threshold (Raudvere et al., 2019). The reduce and visualize gene ontology tool (REVIGO) was used to visualise significant GO terms using semantic similarity (Supek *et al.*, 2011).

Expression-weighted Cell-type Enrichment Analysis (EWCE) was also performed to assess whether the VH-associated modules contained genes which where enriched more than expected by chance within a particular cell type (Skene and Grant, 2016). Target lists were the genes of the VH-associated modules which were significantly ($q<0.05$) associated with VH trait, ranked according to their gene significance. Single-cell transcription data were used from AIBS (https://portal.brain-map.org/atlases-and-data/rnaseq) containing data from the middle temporal gyrus (Hawrylycz *et al.*, 2015) and replicated in a different human-derived dataset (Habib *et al.*,

2017). EWCE was then performed with 100,000 bootstrap lists, controlling for transcript length and content and FDR-corrected for multiple comparisons. The EWCE package is available here: https://github.com/NathanSkene/EWCE.

Statistical Analysis

Demographics, clinical characteristics and network metrics were compared between the three groups using ANOVA (post-hoc Tukey) for normally distributed and Kruskal-Wallis (post-hoc Dunn) for non-normally distributed variables. Normality was assessed using the Shapiro-Wilk test and visual inspection of the variable's distribution. For comparisons between PD-VH and PD-non-VH, t-tests for normally distributed, and Mann-Whitney for non-normally distributed variables were used. Statistical significance was defined as $p<0.05$. All analyses were performed using Python 3 (Jupyter Lab v1.0.2).

6. 3. Results

134 participants were included in the study: 19 had PD and habitual, at least weekly, visual hallucinations (PD-VH), 81 had PD without hallucinations (PD non VH, and 34 unaffected age-matched controls. Demographics and results of clinical assessments at baseline are shown in *Table 6.1*. Importantly there was no significant difference between PD-VH and PD non VH participants in terms of demographics, motor severity or levodopa equivalent doses. No participants were receiving antipsychotic medications, acetylcholinesterase inhibitors or anticholinergics at the time of the study. Details on the experienced hallucinatory phenomena by PD-VH participants are seen in *Table 6.2.*

Table 6.1. Demographics and results of baseline clinical assessments

Attribute		Controls n = 34	PD non VH n=81	PD-VH n=19	Statistic	p value
Demographics	**Age (y)**	66.4 (9.3)	64.4 (7.8)	64.6 (8.2)	r^2=0.003	0.459
	Male (%)	16 (47.1)	47 (58.0)	6 (31.6)	r^2=0.022	0.086
	Years in Education	17.6 (2.3)	16.9 (2.7)	17.1 (3.5)	r^2=0.004	0.490
	Total Intracranial Volume (ml)	**1397.3 (106.4)**	**1476.4 (130.8)**	**1409.9 (106.7)**	**r^2=0.070**	**0.003[a,c]**
Mood (HADS)	**Depression score**	1.6 (2.0)	3.8 (2.9)	4.8 (3.2)	r^2=0.120	<0.001[c]
	Anxiety score	**3.8 (3.5)**	**5.6 (3.8)**	**7.7 (4.9)**	r^2=**0.071**	**0.0031[a,b,c]**
Vision	**LogMAR (best) ***	-0.08 (0.23)	-0.08 (0.16)	-0.06 (0.15)	r^2=0.013	0.854
	Pelli Robson (best) *	1.79 (0.2)	1.79 (0.2)	1.70 (0.2)	r^2=0.016	0.127
	D15 (total error score)	1.29 (1.2)	1.28 (1.1)	1.56 (1.6)	r^2=0.010	0.689
Cognition	**MMSE**	29.0 (1.0)	28.9 (1.1)	28.6 (1.8)	r^2=0.004	0.485
	MOCA	28.8 (1.3)	28.0 (2.1)	26.9 (3.1)	r^2=0.051	0.011[c]
Disease specific Measures	**UPDRS**	**-**	**42.4 (20.2)**	**63.5 (35.6)**	**U=444**	**0.004**
	UPDRS part 3 (motor score)	-	21.8 (11.2)	29.2 (20.8)	U=604	0.129
	UM-PDHQ (hallucination severity score)	**-**	**0**	**4.4 (2.3)**	**-**	**-**
	LEDD (mg)	-	456.9 (265.0)	434.9 (210.3)	U=787	0.948
	Dopamine agonist use (%)	-	48 (59.3)	9 (47.4)	x^2=39.59	0.999
	Amantadine use (%)	-	8 (9.8)	1 (5.3)	x^2=57.09	0.998
	Disease duration	-	4.0 (2.5)	4.8 (3.4)	U=669.5	0.339
	Sniffin' sticks	-	7.8 (3.1)	6.1 (3.4)	U=940.5	0.159
	RBDSQ	-	**4.0 (2.5)**	**5.6 (2.5)**	**U=486**	**0.010**

All data shown are mean (SD) except gender.
In bold characteristics that significantly differed between the PD-VH and PD-non-VH.
[a]: significant difference between PD-VH and PD-non-VH; [b]: significant difference between PD-non-VH and controls; [c]: significant difference between PD-VH and controls.
** Best binocular score used; LogMAR: lower score implies better performance, Pelli Robson: higher score implies betterr performance.*
HADS: Hospital anxiety and depression scale; MMSE: Mini-mental state examination; MOCA: Montreal cognitive assessment; UPDRS: Unified Parkinson's disease rating scale; UM-PDHQ: University of Miami Hallucinations Questionnaire (max score: 14); LEDD: Total Levodopa equivalent dose; RBDSQ: REM sleep behaviour disorder screening questionnaire.

Table 6.2. Characteristics of hallucinations experienced by patients with Parkinson's disease (PD-VH).

Hallucinations Characteristics		PD-VH (n=19)
Phenotype	Complex hallucinations	11 (57.9%)
	Minor hallucinations	8 (42.1%)
Frequency	Less than once a week	11 (57.9%)
	More than once a week	8 (42.1%)
Duration	Less than 1 seconds	8 (42.1%)
	Less than 10 seconds	6 (31.6%)
	More than 10 seconds	5 (26.3%)
Insight	Always preserved	13 (68.4%)
	Sometimes preserved	4 (21.1%)
	No insight	2 (10.5%)
Number of experienced images mean (sd)		1 (0.67)
Distress	No distress	14 (73.7%)
	Mild to moderate distress	5 (26.3%)

Participants were asked to reflect on all hallucinatory phenomena experienced within the previous month.
Complex hallucinations included well form imagery (people, animals, etc), stationary or animate
Minor hallucinations included passage hallucinations as well as non formed images (shadows etc)

Patients with PD and visual hallucinations exhibited a subnetwork of reduced connectivity strength.

PD-VH participants showed a subnetwork of reduced structural connectivity strength compared to PD-non-VH participants (VH-subnetwork, using NBS controlling for age and total intracranial volume), comprised of 92 edges and 82 nodes (*Figure 6.2*). A list of all significant connections within the subnetwork is seen in *Appendix 2*.

No significant subnetwork was identified in the opposite direction (meaning that the presence of hallucinations was not correlated with any increase in connectivity strength). Importantly, no significant subnetwork was identified in PD compared to controls, nor in PD participants in relation to disease severity (total UPDRS score, motor UPDRS score) or general cognition (MoCA or MMSE), therefore these findings seem to be specific to hallucinations.

Global network topology across (clustering coefficient and characteristic path length, and density) did not significantly differ between PD and controls, or PD-VH and PD-non-VH.

PD with visual hallucinations showed reduced average controllability.

As previously described (Bernhardt *et al.*, 2019), average controllability in healthy controls was highest in the thalamus and temporal and prefrontal regions bilaterally (*Figure 6.3*, the full list of ranking is seen in A*ppendix 3*). Average controllability was significantly correlated with degree strength for each node ($U=568$, $p<0.001$), similar to previous work (Gu *et al.*, 2015; Bernhardt *et al.*, 2019).

Next, I compared average controllability between PD-VH, PD non VH and controls. Within the VH-subnetwork, average controllability was significantly reduced in PD-VH compared to controls (Mann-Whitney:

U=176.5, p=0.003) and compared to PD-non-VH (U=526, p=0.014) (*Figure 6.3*).

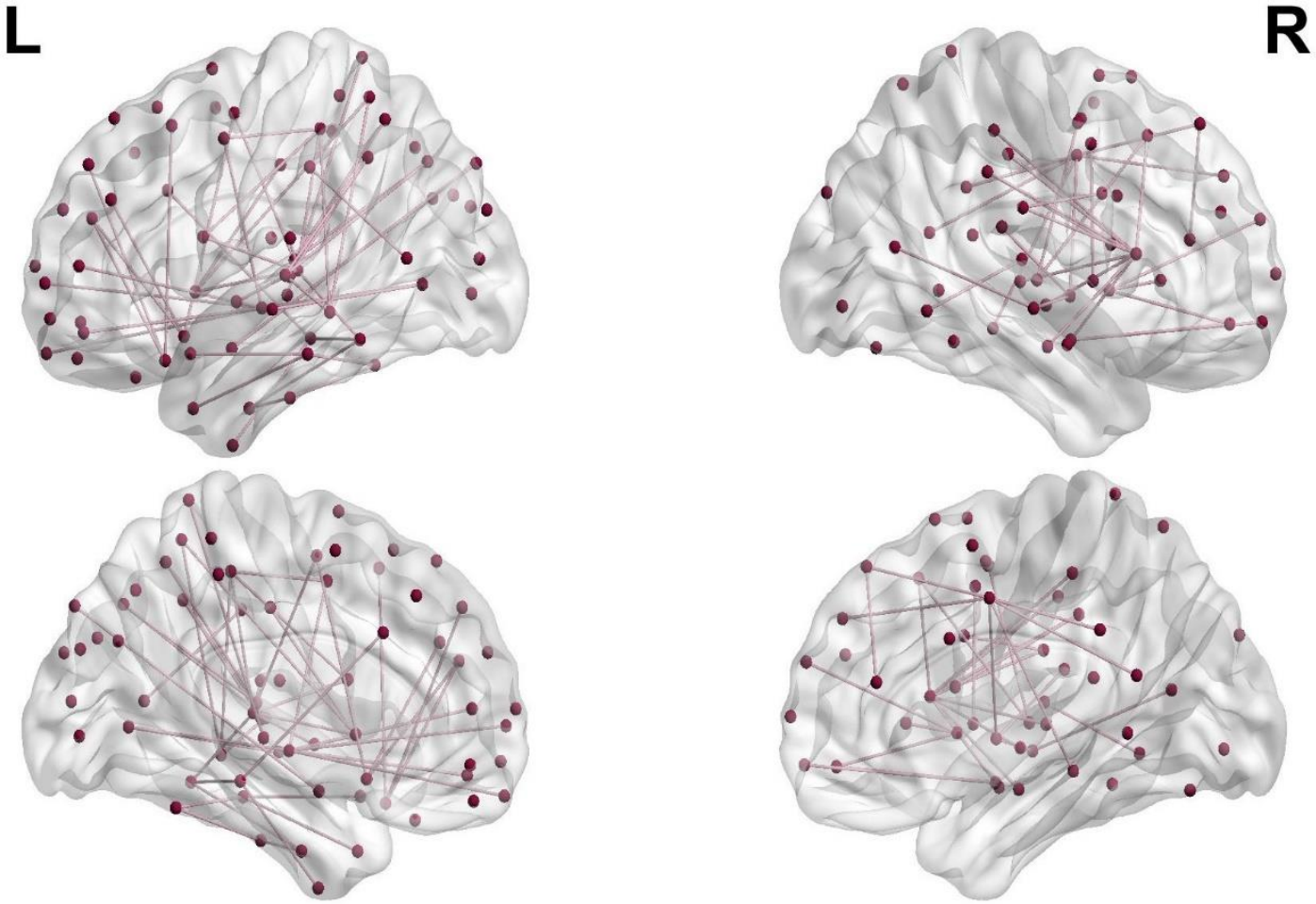

Figure 6. 2. The VH – subnetwork

Network based statistical analysis revealed a subnetwork of reduced structural connectivity strength in patients with Parkinson's and visual hallucinations (PD-VH), FDR corrected for multiple comparisons, controlling for age and total intracranial volume. The subnetwork comprised of 92 edges and 82 nodes. The subnetwork was visualised using BrainNetViewer (Xia et al., 2013)

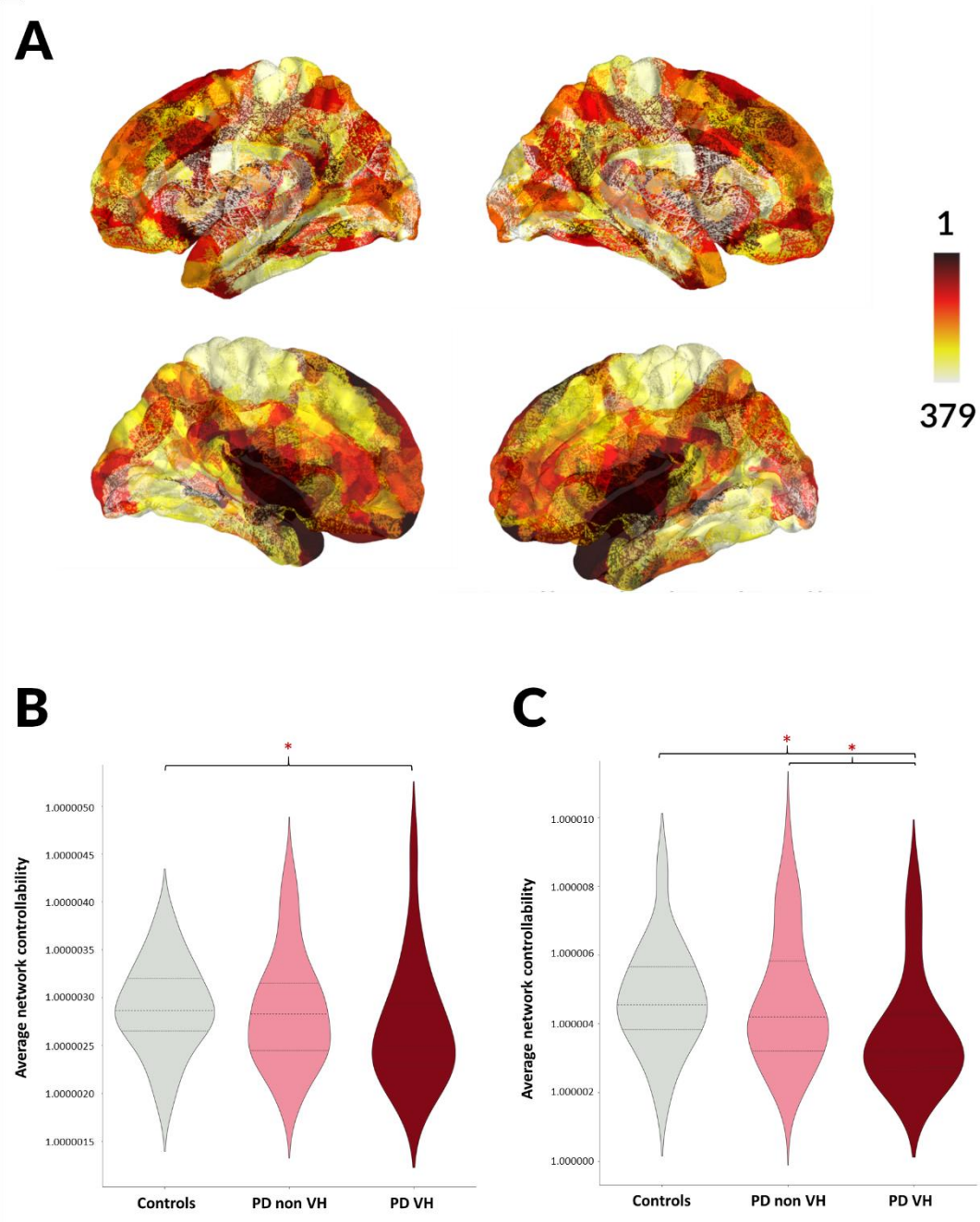

Figure 6. 3 Reduced controllability in PD-VH

A. Controllability ranking in controls, visualised using PySurfer.
B. Average controllability in the whole brain in controls, patients with Parkinson's without (PD-non-VH) and with hallucinations (PD-VH).
C. Average controllability in the VH-subnetwork in controls, PD-non-VH and PD-VH.
** denotes statistically significant differences between the specific groups.*

In contrast, differences in average controllability across the whole brain network were less pronounced (PD-VH versus controls U=233.5, p=0.049; PD-VH versus PD-non-VH (U=625, p=0.091) (*Figure 5.3*). Finally, the subnetwork of reduced connectivity strength seemed to preferentially affect regions of high controllability: nodes with higher average controllability in controls were more likely to participate within the VH subnetwork (U=572.5, p<0.001) (*Figure 6.4*).

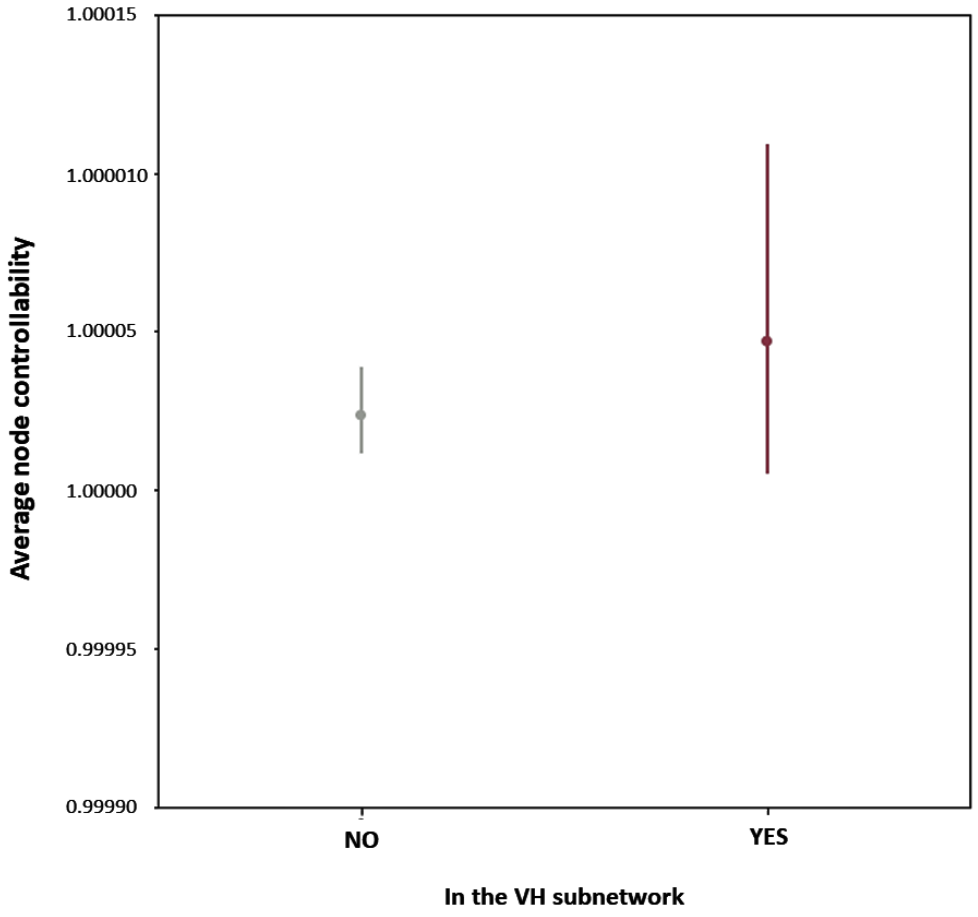

Figure 6. 4. Regions of higher average controllability within the VH-subnetwork.

Nodes with higher average controllability in healthy control participants were more likely to be within the subnetwork.

Specific gene co-expression patterns are linked with presence of visual hallucinations in PD.

Next, I examined whether the brain regions (nodes) of the VH-subnetwork which showed structural connectivity loss in PD-VH, differed in terms of gene co-expression from the rest of the brain. Gene co-expression networks of the left hemisphere of the healthy adult brain were constructed using gene expression data from the Allen atlas (Hawrylycz *et al.*, 2015) resulting in a gene co-expression network of 27 modules, each of gene size ranging between 56-1735 genes (mean=583, standard deviation =564). Each module of the gene network was assessed on whether it was significantly associated with the presence of the brain region/node in the VH-subnetwork. Two modules of the network were significantly correlated (VH-associated modules): one had a negative correlation with the VH-subnetwork or was less expressed in regions that participated in the VH-subnetwork ("downweighted", r= -0.183, FDR corrected p-value: q=0.014) and one had a positive correlation or was more expressed in regions of the VH-subnetwork ("upweighted", r=0.161, q=0.032). The two modules had a gene size of 284 and 601 respectively.

For both of the VH-associated modules, gene module membership was highly correlated with gene significance for the VH-subnetwork which allowed the ranking of the genes of the two modules according to gene module memberships in subsequent enrichment analyses.

Functional properties and cell types of the VH-associated modules.

Gene ontology analysis was then performed for genes within the two VH-associated modules. Most significant GO terms for the "downweighted" module included mRNA processing and metabolism, chromosome organisation, and histone lysine methylation. In contrast, for the "upweighted" module, the most significant GO terms included protein

localisation to membrane and organelle, protein targeting, mRNA catabolism and viral transcription (*Figure 6.5, Table 6.3*). Enrichment analysis using the KEGG database showed that the "upweighted" module was significantly enriched in terms related to ribosome (KEGG:03010, q<0.000, B=134, N=522, b=27); there were no statistically significant KEGG terms for the "downweighted" module. The full GO terms for the "upweighted" module are seen in *Appendix 4* and for the "downweighted" module in *Appendix 5*. I then examined whether the VH-associated modules (genes ranked by gene significance) were enriched in specific cell types. The "downweighted" module was enriched in oligodendrocytes whilst the "upweighted" module was enriched in glutamatergic neurons and GABAergic interneurons (*Figure 6.6*). To ensure that these cell type enrichment results were not influenced by the chosen single-cell dataset, these findings were replicated in a separate dataset (Habib, 2017). A similar enrichment pattern was seen: the "downweighted" module was again enriched for oligodendrocyte markers and the "upweighted" module for neuronal cells and GABAergic interneurons (*Figure 6.6*).

Figure 6. 5 Functional processes of VH-associated modules.

(Opposite)

Significant gene ontology (GO) terms for biological processes plotted in semantic space, where similar terms are clustered together. The top five most significant GO terms are labelled for each analysis. Redundant GO terms have been excluded. Markers are scaled based on the log10 q value for the significance of each GO term.

Large blue circles are highly significant, while red circles are less significant (see colour bar).

mRNA: messenger RNA.

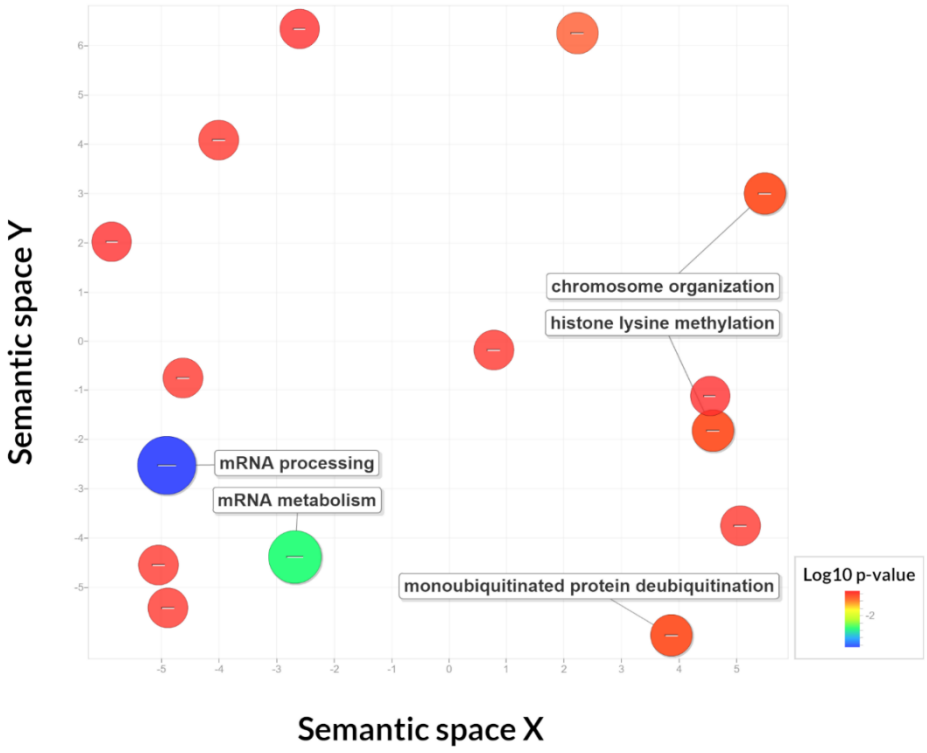

Downweighted

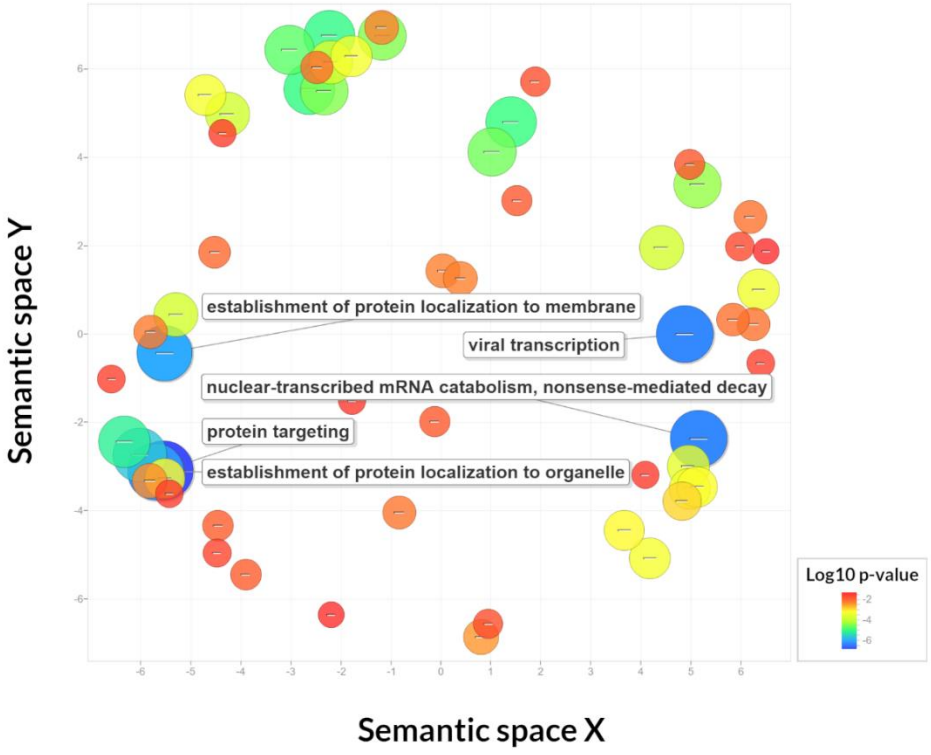

Upweighted

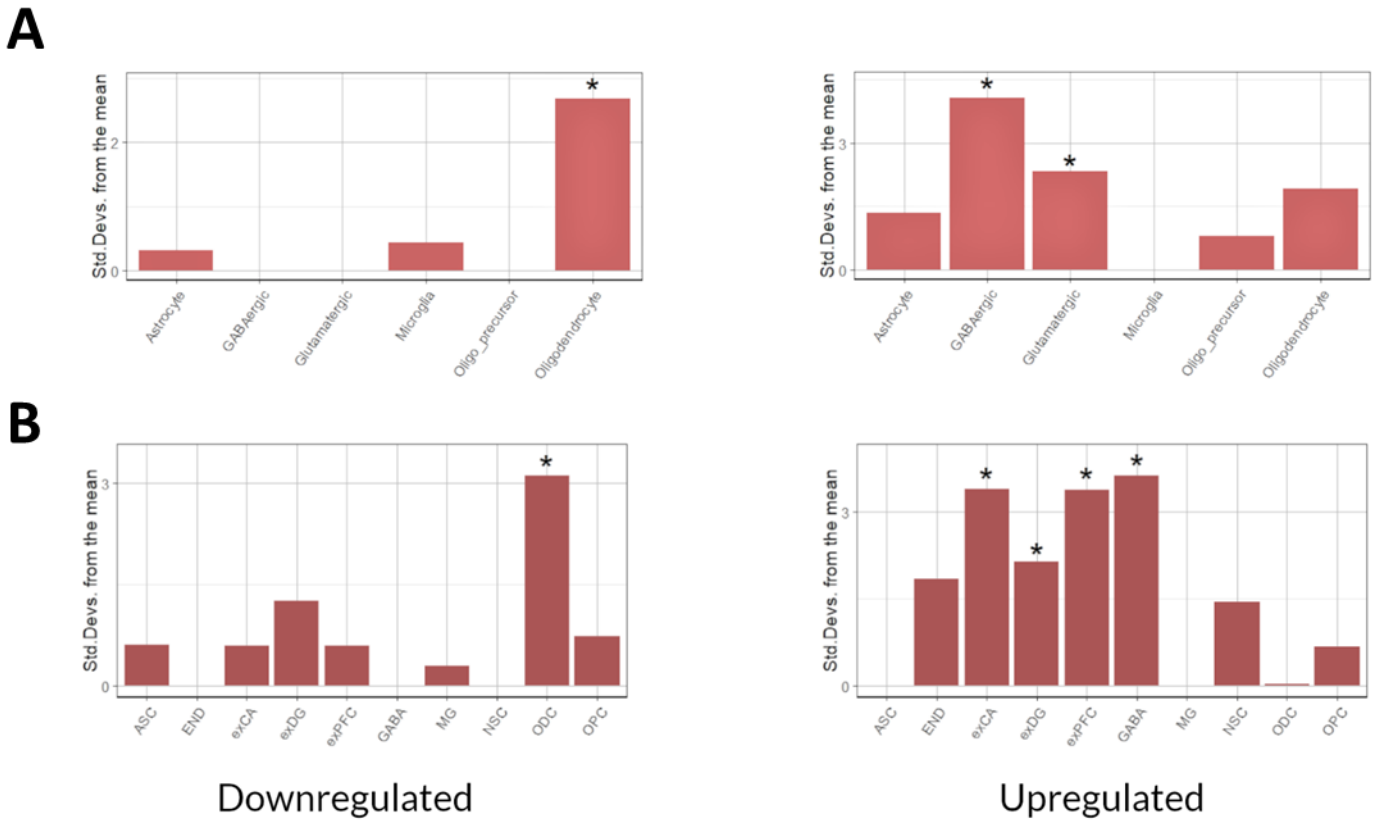

Figure 6. 6 Cell type enrichment for the downweighted and upweighted VH-associated module.

A. *Expression-weighted cell-type enrichment analysis (EWCE) for the VH associated modules using the AIBS dataset.*

B. *Replication of EWCE results on a separate dataset (Habib, 2017).*

*Data are presented as standard deviations from the mean. Marked with * are statistically significant (FDR corrected) results.*

ASC: astrocytes, END: endothelial cells, NSC: neuronal stem cells, OPC: Oligodendrocyte Precursor cells, MC: Microglia, exCA: Pyramidal CA, exPFC: Pyramidal prefrontal cortex, exDG: Granule neurons, hippocampus dentate gyrus, GABA: GABAergic interneurons, ODC: Oligodendrocytes.

Table 6. 3. Gene Ontology (GO) terms for biological processes associated with VH-associated modules.

Downweighted Module					
GO term	**Description**	**q value**	**B**	**N**	**b**
GO:0006397	mRNA processing	0.001	517	272	25
GO:0016071	mRNA metabolic process	0.005	860	272	32
GO:0034968	histone lysine methylation	0.035	119	221	8
GO:0035520	monoubiquitinated protein deubiquitination	0.035	10	161	3
GO:0051276	chromosome organization	0.035	1238	180	28
Upweighted Module					
GO term	**Description**	**q value**	**B**	**N**	**b**
GO:0006605	protein targeting	1.38E-07	428	523	41
GO:0019083	viral transcription	5.06E-07	178	519	24
GO:0000184	nuclear-transcribed mRNA catabolic process, nonsense-mediated decay	5.06E-07	122	519	20
GO:0072594	establishment of protein localization to organelle	6.61E-07	565	534	46
GO:0090150	establishment of protein localization to membrane	1.07E-06	330	535	33

The top five most significant GO terms are displayed for each connection type. Redundant GO terms have been removed.
q value: log10 of the FDR adjusted p value; B: Total number of genes associated with a specific GO term;
b:Number of genes in the intersection ; N: Number of genes in the target set (query size).

6.4. Discussion

This study sheds light on network-level structural connectivity changes underlying visual hallucinations in Parkinson's disease and sheds light on the underlying biological processes and cell types that may be contributing to regional selective vulnerability. Specifically, I showed that:

a. PD-VH exhibit a subnetwork of reduced structural connectivity strength compared to PD non VH
b. this subnetwork is crucial for brain integration normally, as regions that have high average controllability in healthy controls (are important for switching the brain between different states) preferentially participate in the VH-subnetwork
c. regions of the VH-subnetwork show distinct gene expression patterns with "downweighted" genes related to mRNA metabolism, chromosome organisation and histone lysine methylation and "upweighted" genes related to protein targeting and localisation
d. distinct cell-types seemed to be differentially expressed in regions of the VH-subnetwork with "downweighted" genes enriched in oligodendrocyte markers and "upweighted" genes enriched in glutamatergic and GABAergic neurons.

Recent theoretical models of visual hallucinations in PD implicate an imbalance in relevant effects of different brain networks, particularly attentional brain networks with aberrant DMN activation (Shine *et al.*, 2014*a*, 2015; Yao *et al.*, 2014; Baggio *et al.*, 2015). This study provides further evidence for these models by showing loss of structural connectivity within a subnetwork of normally high controllability; regions of this subnetwork are, in healthy controls, crucial for switching the brain between easily accessible states. Therefore, structural changes within these regions may explain the observed functional network changes as an inability to

switch between functional networks, for example inability to deactivate the DMN or activate the dorsal attention network.

Other theoretical models strongly implicate thalamic regions as drivers of shifts in network control (Onofrj *et al.*, 2017, 2019). Indeed there is growing evidence of thalamic involvement in PD hallucinations: lateral geniculate networks were identified as key regions in the development of hallucinations using network localisation techniques (Kim *et al.*, 2019; Weil *et al.*, 2019) and in the previous chapter (*Chapter 4*), I showed longitudinal changes within the mediodorsal thalamic subnucleus in patients with PD and visual hallucinations. Both the right and left thalamus participated in the VH-subnetwork of reduced structural connectivity strength seen in PD-VH; the thalamus was also amongst the brain regions of highest controllability ranking in healthy controls, implying significant influence over whole-brain function.

Importantly, this study showed that white matter connectivity loss in PD-VH is associated with distinct regional gene expression patterns. Regions participating in the VH-subnetwork showed a pattern of "downweighted" genes related to histone lysine methylation and mRNA processing. Histone methylation is crucial for transcriptional control (Greer and Shi, 2012) and closely related to DNA methylation (Cedar and Bergman, 2009) a hallmark of aging (Hannum *et al.*, 2013; Marioni *et al.*, 2015; Michalak *et al.*, 2019). RNA segments also accumulate in aging neurons (Sudmant *et al.*, 2018; Butler *et al.*, 2019) and, recently, impaired repair of nucleic acids has been implicated as an age-related modifier of PD (Sepe *et al.*, 2016). Brain regions which normally express lower levels of genes related to histone methylation and RNA processing could be more vulnerable to these age-related changes.

Regions of the VH-subnetwork, which are vulnerable to structural connectivity loss, also showed "upweighted" genes related to protein localisation. Dysfunction of the autophagy-lysosome pathway, particularly chaperone-mediated autophagy, is thought to be an important mechanism of neurodegeneration in PD (Pan *et al.*, 2008; Alvarez-Erviti *et al.*, 2011), with lysosomal malfunction contributing to the accumulation of alpha-synuclein (Cuervo *et al.*, 2010; Lawrence and Zoncu, 2019). Glucocerebrosidase activity is decreased in Parkinson's disease, with associated impaired chaperone-mediated autophagy (Murphy *et al.*, 2014). *GBA* mutations are linked with a higher PD risk and higher rate of hallucinations (Neumann *et al.*, 2009; Brockmann *et al.*, 2011), whilst the most common *GBA*-mutations associated with PD (N370S and L44P (Velayati *et al.*, 2010)) are thought to induce endoplasmic reticulum stress through activation of the unfolded protein response (Mu *et al.*, 2008; Doyle *et al.*, 2011; Sanchez-Martinez *et al.*, 2016). Upweighting of genes related to membrane and organelle localisation in affected regions, as well as the presence of macro-autophagy amongst significantly enriched GO-terms of the upweighted module (*Appendix 4*) provide further support to the key role of the autophagy-lysosome pathway in PD, particularly in relation to hallucinations.

Differential cell-type enrichment was also seen in regions of the VH-subnetwork. Specifically, regions of the VH-subnetwork downweighted genes enriched in oligodendrocytes and upweighted genes enriched in neuronal cells. Oligodendrocytes have recently been implicated in PD, with heritability for PD enriched in oligodendrocyte-specific genes (Bryois *et al.*, 2019) and genetic alterations of oligodendrocyte populations within the putamen in the brain of patients with PD (Teeple *et al.*, 2021). The structural connectivity changes we saw in PD-VH involved many connections between spatially remote areas. These longer connections are likely to rely more on myelination for signal transfer and oligodendrocytes

play a key role in myelination, remodelling of myelin and metabolic support of axons (Young *et al.*, 2013; Pepper *et al.*, 2018). Brain regions which normally are less rich in oligodendrocytes could be more vulnerable to losing these longer range connections in the presence of disease.

Several limitations need to be taken into account. Structural connectivity estimates were derived from diffusion tractography which can be limited particularly in modelling crossing fibres. Our diffusion-weighted imaging data was multi-shell and underwent robust post-processing (Smith *et al.*, 2015) to provide the best possible estimate of underlying structural connectivity. Study participants underwent imaging whilst continuing their usual medications; however structural metrics were assessed, which are unlikely to be affected by medication, and levodopa equivalent doses did not differ between PD groups. Regional gene expression analyses used data from healthy human brains and should be interpreted with caution as transcription in PD in the cortex could differ from healthy controls. Clarifying potential transcriptome changes in PD using brain tissue of patients with and without hallucinations could be an area of future research.

In conclusion, this study showed that PD-hallucinations are associated with a subnetwork of reduced structural connectivity strength. This subnetwork exerts control over distributed brain regions and is crucial for switching the brain between states. In addition, this subnetwork exhibits distinct gene expression patterns and cellular subtypes which may contribute to selective vulnerability to connectivity loss. These findings provide new insights into how hallucinations develop in PD and indicate potential therapeutic targets.

Publication statement

Work included in this chapter has been published previously (Zarkali *et al.*, 2020) and is included here as per the publisher's policy with regards to thesis publications.

7. Bridging the gap between structural and functional connectivity

7.1 Introduction

Resting state functional MRI (rsfMRI) studies demonstrate significant network-level changes in functional connectivity of attentional brain networks in patients with PD-hallucinations (Muller *et al.*, 2014), with overactivity of the Default Mode Network and impaired dorsal attention network involvement (Shine *et al.*, 2014, 2015; Yao *et al.*, 2014; Baggio *et al.*, 2015). Although functional connectivity analyses of rsfMRI data has provided useful insights about altered patterns of between-regions interactions in PD-hallucinations, it provides a "static" image of functional connectivity, calculated over an entire scanning period.

Functional connectivity however is not static but shows spontaneous, dynamic fluctuations over time where the brain switches between different dynamic states (Hutchison *et al.*, 2013; Allen *et al.*, 2014; Shine *et al.*, 2016); in fact dynamic functional connectivity may be more representative of behaviour than static approaches (Liégeois *et al.*, 2019). Changes in dynamic functional connectivity have been described in PD early in the disease process (Cordes *et al.*, 2018) and are associated with progression of motor symptoms as well as the development of cognitive impairment and dementia (Kim *et al.*, 2017; Díez-Cirarda *et al.*, 2018; Fiorenzato *et al.*, 2019). Changes in temporal functional dynamics have also been seen in schizophrenia and other psychiatric conditions (Sakoğlu *et al.*, 2010; Kaiser *et al.*, 2016; Rashid *et al.*, 2016; Jin *et al.*, 2017), and recent work showed imbalance of the temporal dynamics of integrated and segregated sub-states in disorders of consciousness (Luppi *et al.*, 2019) and after administration of

the psychedelic LSD (Luppi *et al.*, 2021). However, whether PD-hallucinations are also associated with an imbalance between primarily integrated and segregated sub-states is not yet known.

In the previous chapter I showed that PD patients with visual hallucinations show widespread changes in structural connectivity between brain regions, particularly affecting highly connected brain regions that are important for switching the brain between different states (*Chapter 6*). Structural connectivity guides the temporal progression between brain sub-states (Stiso *et al.*, 2019; Cornblath *et al.*, 2020) and the transitions between sub-states can be modelled using the framework of network control theory (Gu *et al.*, 2015, 2017; Betzel *et al.*, 2016). Specifically, the optimal energy cost needed to move the brain from one sub-state to another can be calculated based on the structural network (Gu *et al.*, 2015, 2017; Betzel *et al.*, 2016). A substate that is less energy-demanding to maintain or requires significantly lower energy to transition to may be preferred. Therefore this framework can provide important insights to why a specific sub-state is predominantly seen in health and how the balance between sub-states may change in the presence of disease.

This study will aim to clarify the pattern of temporal dynamics in PD-associated visual hallucinations using rsfMRI; specifically, whether the balance between primarily integrated and primarily segregated sub-states is preserved in patients with PD and visual hallucinations compared to those without hallucinations and controls. I will show that patients with Parkinson's and hallucinations show impaired temporal dynamics, with a predisposition towards a more segregated sub-state of functional connectivity. I will then used network control theory to calculate each individual's required energy cost to transition from the integrated-to-the-segregated substate and vice versa, as well as the cost to maintain each sub-state. I predict that patients with Parkinson's and visual hallucinations will

require less energy to transition from the integrated-to-segregated substate than those without hallucinations and controls. Finally, I will clarify the brain regions that mostly contribute to the transition from integrated-to-segregated state; I will then relate the regional contribution to this state transition to neurotransmitter systems using PET-derived regional density profiles and regional gene expression data for neurotransmitter receptors from healthy human brains.

7.2 Methods

Study Participants

Participants were recruited from the Vision in Parkinson's disease study (VIPD cohort, *Chapter 2: Study Cohorts*). All participants with baseline diffusion weighted imaging (DWI), structural brain imaging and rsfMRI scans passing predetermined quality control criteria were included in the study leading to 123 included participants: 91 patients with PD and 32 unaffected controls. Patients with PD satisfied the Queen Square Brain Bank Criteria for PD (Emre *et al.*, 2007).

As in previous studies, participants with PD were classified as PD with visual hallucinations (PD-VH, n=16) if they scored more than 1 for Question 2 of the UPDRS: "Over the past week have you seen, heard, smelled or felt things that were not really there?". All other participants with PD were classified as PD non VH (n=75). Data on the frequency and severity of hallucinations was collected with the University of Miami Parkinson's Disease Hallucinations Questionnaire (UM-PDHQ) (Papapetropoulos et al., 2008). The full study protocol is described in *Chapter 2*.

MRI data acquisition and pre-processing

An overview of the study methodology is seen in *Figure 7.1*.

The study protocol and quality control as well as pre-processing steps for diffusion-weighted imaging (DWI) and resting state functional MRI (rsfMRI) data is presented in detail in *Chapter 2*.

Briefly, the MRI quality control tool (MRIQC) was used to assess the quality of resting state functional MRI (rsfMRI) data (Esteban *et al.*, 2017). Participants were excluded if any of the following was met: 1) mean frame-wise displacement (FD) >0.3mm, 2) any FD >5mm, or 3) outliers >30% of the whole sample. This led to 12 participants being excluded (11 PD, of whom 5 low visual performers, and 1 control). This resulted to the total of 91 patients with PD (16 with visual hallucinations PD-VH and 75 without hallucinations, PD non VH) and 32 unaffected controls being included in our study. In addition, all volumes of raw DWI datasets were visually inspected and each volume evaluated for the presence of artefact; only scans with <15 volumes containing artefacts (Roalf *et al.*, 2016) were included to subsequent structural analyses. As a result, 5 PD and 2 control participants were excluded from our structural analyses.

To construct functional and structural connectivity matrices, each participant's T1-weighted image was parcellated into 200 cortical and 32 subcortical regions of interest (ROIs) using the Schaefer (Schaefer *et al.*, 2018) and Tian parcellations (Tian *et al.*, 2020) respectively. Parcellations in the order of 200 regions result in connectomes with highest representativeness (Messé, 2020; Luppi and Stamatakis, 2021) and specifically the combined Schaefer-232 parcellation used here is one of the best performing across structural and functional connectomes (Luppi and Stamatakis, 2021). The same parcellation was used to construct functional and structural connectivity matrices for each participant. All analyses were

replicated using the more fine-grained version of the Schaefer and Tian parcellations with 400 cortical and 54 subcortical ROIs respectively.

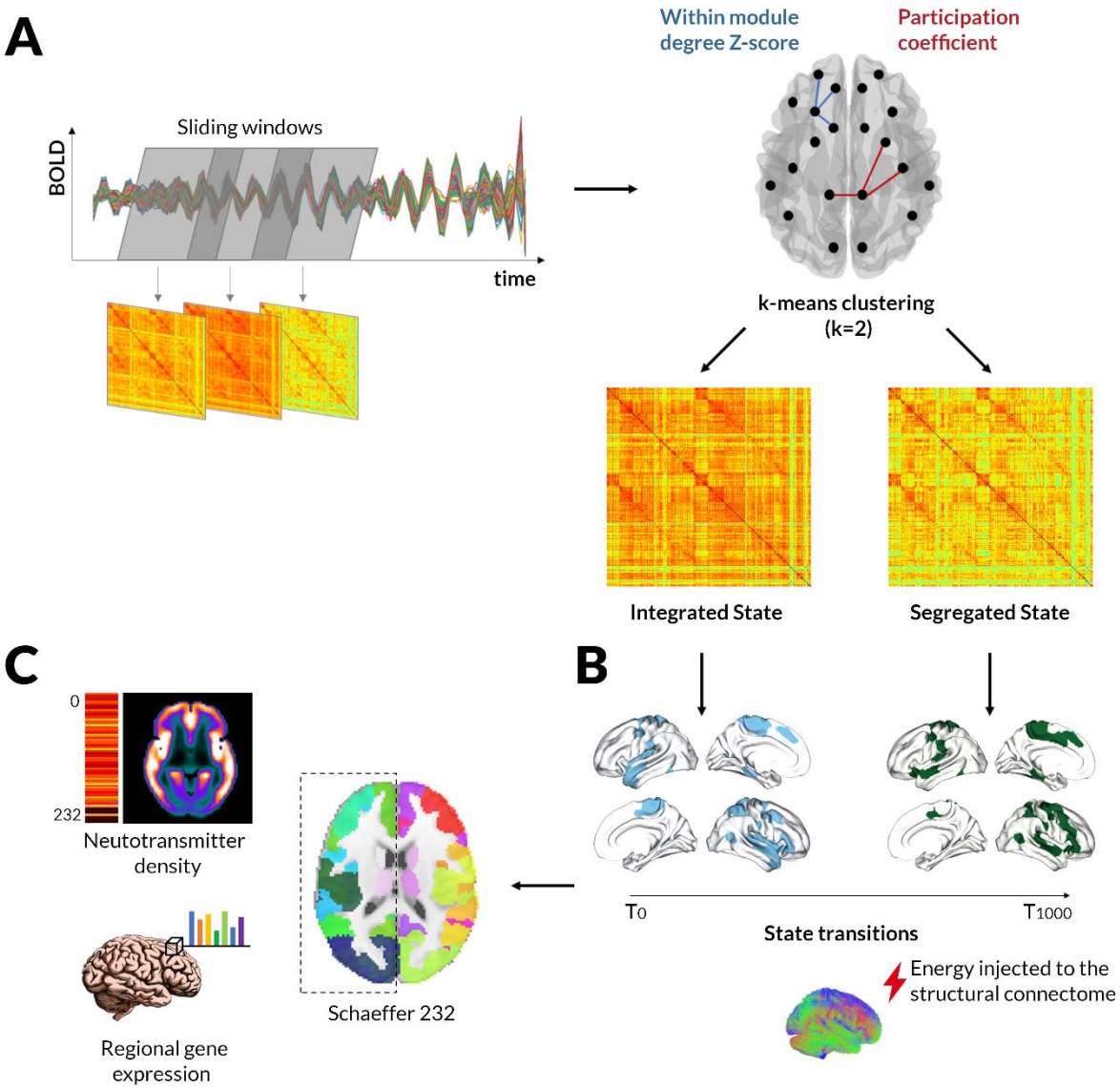

Figure 7. 1. Overview of the study methodology

(Opposite)

A. Deriving predominantly integrated and segregated sub-states of dynamic functional connectivity. After obtaining sliding-windows (each 44s duration) of dynamic functional connectivity for each participant, the joint histogram of participation coefficient and within-module degree Z-score was used for k-means clustering (k = 2). The cluster with highest average participation coefficient is then identified as the predominantly Integrated dynamic sub-state and the cluster with the lowest participation coefficient as the predominantly Segregated sub-state. Note that this is done for each participant separately leading to individually-defined Integrated and Segregated sub-states.

B. Modelling state transitions. After deriving each individual's Integrated and Segregated sub-states I used an optimal control framework to calculate the minimal control energy that needs to be applied to each node of the network to transition from a baseline state at time T0 to a target state at time T1000. Here, as an example, we illustrate the transition from the Integrated substate (in blue) to the Segregated state (in green) but minimal energies were also calculated for Segregated-to-Integrated transition as well as to maintain the integrated state (Integrated-to-integrated) and segregated state (segregated-to-segregated) using the same model. Minimal control energies were calculated for each subject based on their structural brain network, which was estimated using diffusion imaging and probabilistic tractography. Both sub-states were represented to the model as a vector of the sum connectivity strength for each node (1*232); here shown the top 20% of the nodes for the Integrated state (blue) and Segregated state (green).

C. Linking with neurotransmitter systems. Minimal control energies to transition between and maintain functional sub-states were compared between patients with PD with (PD-VH) and without hallucinations (PD non VH). Transitions that differed between groups were then further explored to examine whether contributing nodes (requiring mode control energy) were associated with specific neurotransmitter systems. To do this, we calculated for each of the 232 regions of interest of our parcellation (Schaeffer 232: 200 cortical and 32 subcortical regions) 1) mean neurotransmitter density profiles derived from PET data (serotonin (5HT1a, 5HT2a and 5HT1b), dopamine (D1 and D2) and GABAA receptors) and 2) gene expression profiles for each of 31 pre-selected genes encoding receptors for norepinephrine, acetylcholine, dopamine and serotonin.

Dynamic functional connectivity

Following rsfMRI pre-processing, mean regional BOLD signal was calculated for all voxels belonging to each ROI. Functional connectivity between any two ROIs was quantified as the Pearson correlation coefficient between mean regional BOLD time-series. Dynamic connectivity matrices were derived using an overlapping sliding-window approach (Allen *et al.*, 2014): resting state data were divided into windows of 44s duration (63*TR) in steps of 1 repetition size (*Figure 7. 1*). The selected window was chosen to be within the recommended range (30-60s) for capturing functional connectivity fluctuations and overlapping windows were chosen as they minimise error from outliers and spurious correlations (Allen *et al.*, 2014; Preti *et al.*, 2017). This resulted to 63 windows of 44s duration. Within each temporal window, we calculated a 232*232 weighted adjacency matrix representing the functional connectome for that timepoint.

We then identified sub-states of higher integration or segregation using a "cartographic profile" based on the module assignments of each ROI (Shine *et al.*, 2016; Fukushima *et al.*, 2018; Luppi *et al.*, 2019, 2021). At each time point , the asymmetric algorithm of Rubinov and Sporns (Rubinov and Sporns, 2011) was used to identify network modules by applying the community Louvain algorithm, which iteratively evaluates different ways of assigning nodes to modules, in order to maximise the resulting modularity function Q:

$$Q = \frac{1}{\upsilon^{+}} \sum_{ij} ({w_{ij}}^{+} - {e_{ij}}^{+}) \delta_{M_i M_j} - \frac{1}{\upsilon^{+} + \upsilon^{-}} ({w_{ij}}^{-} - {e_{ij}}^{-}) \delta_{M_i M_j}$$

where υ is the total weight of the graph (sum of all the graph's edges), w_{ij} is the signed weight of the edge between nodes i and j, e_{ij} is the weight of an edge divided by the total weight of the graph (superscripts denote + positive and - negative edges), and δ_{MiMj} is set to 1 when nodes i and j are in the

same module and 0 otherwise. We performed 100 iterations for each time-resolved networks with module size resolution parameter γ set at the default γ=1.

We then calculated participation coefficient and within-degree Z-score for each node using the Brain Connectivity Toolbox in MATLAB version 2018b (https://www.mathworks.com/products/matlab.html). Participation coefficient was calculated as:

$$P_i = 1 - \sum_{s=1}^{M} \left(\frac{\kappa_{is}}{k_i}\right)^2$$

where κ_{is} is the strength of positive connections between node i and other nodes in module s, k_i is the strength of all its positive connections, and M is the number of modules in the network, as identified by the modularity detection algorithm. The participation coefficient ranges between zero (no connections with other modules) and one (equal connections to all other modules). High mean participation coefficient within a network implies higher levels of integration between-modules.

The within module degree Z-score Z*i* was calculated as:

$$z_i = \frac{\kappa_{is} - \bar{\kappa}_{is}}{\sigma_{\kappa_{is}}}$$

where κ_{is} is the strength of connections between node *i* and other nodes in module *s*, and $\bar{\kappa}_{is}$ and $\sigma_{\kappa is}$ are respectively the average and the standard deviation of κ_{is} over all nodes belonging to module *s*.

Joint histograms of participation coefficient and within-module Z-score were then derived for each timepoint (Shine *et al.*, 2016) and for each participant, these were used to assign each timepoint to one of two clusters, using k-means clustering (k = 2). In addition to our a-priori hypothesis of two sub-states, k=2 was the optimal number of clusters overall in our cohort

using the Calinski-Harabasz score (*Figure 7.2*). Finally, the cluster with higher mean participation coefficient was labelled as the *Integrated* state, while the cluster with lower average participation coefficient was considered to be the *Segregated* state. For each subject, a centroid matrix of functional connectivity was computed for each state, as the element-wise median of the timepoint-specific FC matrices assigned to the cluster corresponding to that state.

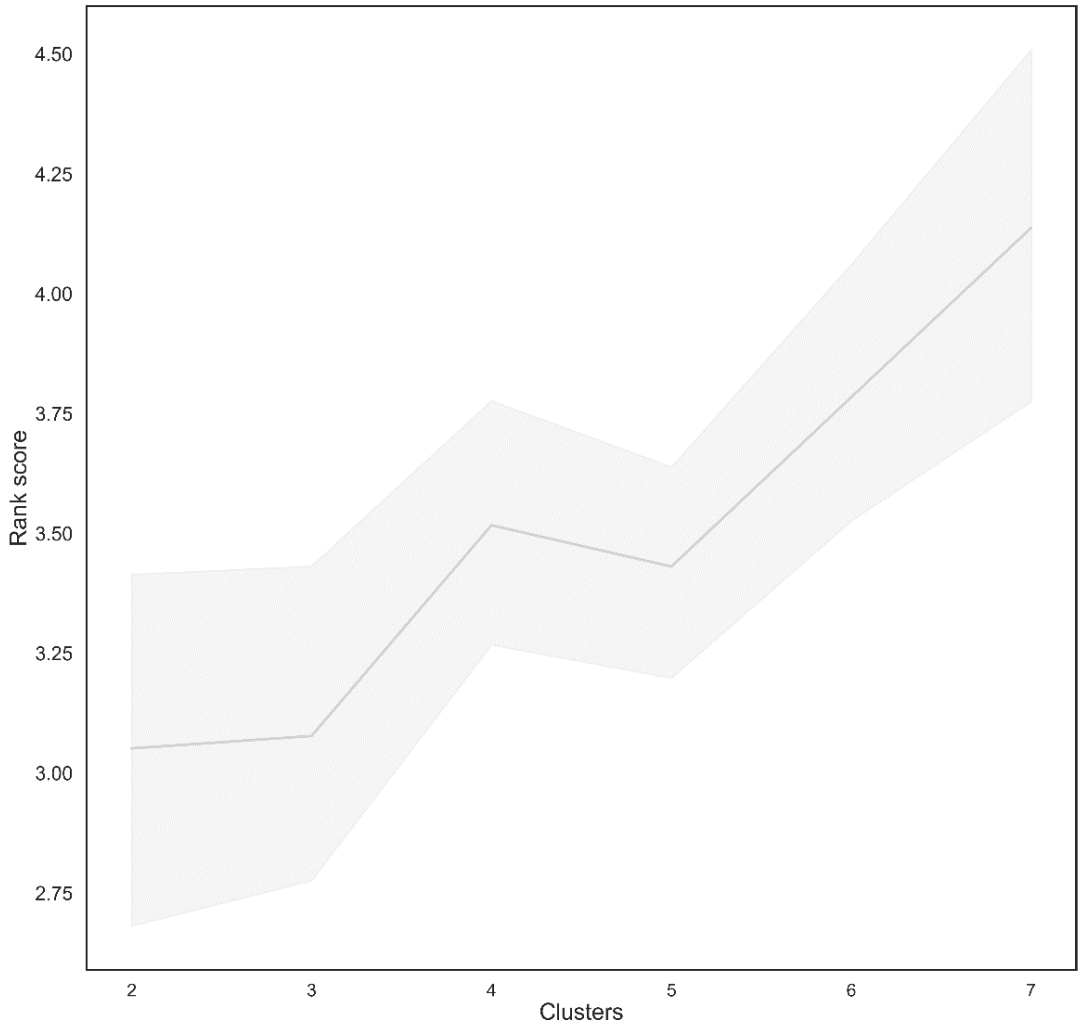

Figure 7. 2 Optimal number of clusters

For all participants the Calinski-Harabasz score was calculated for 2-7 clusters. Cluster scores were ranked with best score (highest) ranked 1 and worse (lowest) score ranked 6 per participant. Line: mean, Shaded area: 95% confidence intervals)

I then calculated the *proportion of time spent in each sub-state* as the number of timepoints assigned to the sub-state divided by number of total timepoints (Luppi *et al.*, 2021). Average *dwell time* spent in each sub-state was calculated as the number of consecutive windows/timepoints belonging to each sub-state and the *number of transitions* as the number of transitioning from one sub-state to the other; transitions were further divided into transitions from integrated-to-segregated and segregated-to-integrated sub-states.

Network control analysis

I examined how the structural brain network of each participant, composed of white matter tracts, constrains the brain in transitioning from one sub-state of functional connectivity (*Integrated* and *Segregated* states) to the other.

First a structural connectome was constructed. After DWI-image pre-processing, diffusion tensor metrics were calculated for each participant and constrained spherical deconvolution performed (Hollander, T. *et al.*, 2016). The raw T1-weighted images were registered to the diffusion-weighted image and five-tissue anatomical segmentation performed followed by anatomically constrained tractography with 10 million streamlines (Smith *et al.*, 2012) and subsequent informed filtering of the tractograms using the spherical deconvolution informed filtering of tractograms (SIFT2) algorithm (Smith *et al.*, 2015). The resulting set of streamlines was used to construct the structural brain network; connections, weighted by streamline count were combined to a 232*232 undirected weighted connectivity matrix.

Then I used a linear time-invariance network model, as previously detailed (Gu *et al.*, 2015; Betzel *et al.*, 2016; Kim *et al.*, 2018). In brief, this can

describe neural states as simulated states (x) of a network with n number of nodes over time steps t using:

$$x(t+1) = Ax(t) + Bu(t)$$

where x(t) is a vector (1*N nodes) that represents the brain state a given time t, n is the number of nodes (232 ROIs), matrix A represents the structural connectome n*n (normalised to ensure stability (Betzel *et al.*, 2016; Gu *et al.*, 2017)), matrix B is the matrix of control nodes for the network with n*n dimensions and u(t) is the control energy applied for each node at a given time t. For all analyses presented, we chosen to not constrain the number of nodes that could be controlled, therefore B is an identity matrix, as all 232 ROIs were included as control nodes.

This model can be used to derive the structural control energy necessary to transition from an initial state x(0) to a target state x(T) where T=1 is the control horizon (Betzel *et al.*, 2016; Zöller *et al.*, 2021) using the following equation:

$$min_u \int_0^T \left(x_T - x(t)\right)' S \left(x_T - x(t)\right) + \rho u(t)'\, t(t)\, dt$$

where x_T is the target state (1*n vector where n is the number of nodes), S is the diagonal n*n matrix that selects a subset of states to constrain (here the identify matrix), ρ is the importance of the input penalty to the state penalty (here ρ=1) and T is the control horizon.

As in this model, states are represented as a 1*232 vector, I represented the integrated and segregated sub-states by their sum connectivity profiles, comprised of the sum of the connection weights (pearson correlation coefficient) for each node to all other nodes; this was calculated separately for the integrated and segregated state.

I then used this equation to calculate the control energy needed to be applied to each node of the network to: 1) transition from the integrated-to-segregated state, using as the baseline state of the model x_0 the sum connectivity vector of the integrated state and as the target state x_T, the sum connectivity vector of the segregated state, 2) transition from the segregated-to-integrated state, using as x_0 the sum connectivity vector of the segregated state and state x_T, the sum connectivity vector of the integrated state, and 3) persist within the integrated or within the segregated state, using the sum connectivity vector for that sub-state for both x_0 and x_T (*Figure 6.1*). A sum of the control energies that need to be applied across all nodes of the network represents the minimal energy for the specific transition. In this way, minimal transition and persistence energies were calculated for each individual's own *Integrated* and *Segregated* functional sub-state using each individual's own structural connectivity matrix.

Statistical analyses

Demographics and clinical characteristics were compared between the three groups using ANOVA with post-hoc Tukey for normally distributed and Kruskal-Wallis for non-normally distributed variables (normality assessed using Shapiro-Wilk test and visual inspection). For comparisons between PD-VH and PD-non-VH we performed t-tests for normally distributed, and Mann-Whitney for non-normally distributed variables. Statistical significance was defined as $p<0.05$.

Temporal properties of the two dynamic sub-states were assessed by comparing mean dwell time in each sub-state, proportion spent in integrated vs segregated sub-state and number of transitions between PD-VH vs PD non VH and PD vs controls. As these measures were not normally distributed group-differences were tested using Kruskal Wallis (post hoc

Dunn, statistical significance $p<0.05$). Differences in transition and persistence energy between PD-VH and PD non VH were performed using repeated measures ANOVA ($p<0.05$, post-hoc Tukey).

Additionally I investigated whether each of the two sub-states significantly differed amongst control, PD non VH and PD-VH using network-based statistics (NBS) (Zalesky *et al.*, 2010). A general linear model was used with contrast of interest including PD-VH versus PD non VH and PD versus controls; age and total intracranial volume were included as covariates. Permutation testing with unpaired t-tests was performed with 5000 permutations, calculating a test statistic for each connection. An a-priori threshold of $t = 2.7$ based on our sample size as well as family-wise error rate (FWE) of $p<0.05$ was applied.

Correlation with Neurotransmitter systems.

Finally, I aimed to identify whether the temporal changes in functional connectivity seen in PD-VH were associated with specific neurotransmitter systems (*Figure 6.1*). To do this I first calculated the regional control energy needed to transition towards and persist within a sub-state that was found to be more predominant in PD-VH. This metric was expressed as a vector 1*232 with one control energy value per node. Neurotransmitter density profiles were then extracted for each of the 232 regions of interest (ROIs) of the parcellation using JuSpace (Dukart *et al.*, 2021) using the included PET maps. Mean values for each ROI were extracted from JuSpace for:

- Serotonin receptors 5-HT1A, 5-HT1B, 5-HT2A based on carbonyl-(11)C]WAY-100635, [(11)C]P943, [(18)F]altanseri templates (Savli *et al.*, 2012)
- D1 receptors from the D1R-selective [11C]SCH23390 template (Kaller *et al.*, 2017)

- D2/3 receptors from [(11)C]raclopride template (Alakurtti *et al.*, 2015)
- and GABAa receptors from (11C)flumazenil template (Dukart *et al.*, 2018)

Each of the templates was registered to MNl space and parcellated with the Schaefer 232 atlas and mean values of binding potential were extracted from each ROI using the built-in JuSpace function (Dukart *et al.*, 2021).

Expression profiles for genes of noradrenergic, cholinergic (nicotinic and muscarinic), dopaminergic and serotoninergic receptors were obtained using data from the Allen Human Brain Atlas (AHBA) (Hawrylycz *et al.*, 2015). A recently described rigorous method of preprocessing (Arnatkevic Iūtė *et al.*, 2019) was used to extract gene expression data from AHBA and map them to the 232 ROIs of our parcellation, in abagen (Markello *et al.*, 2020). Each tissue sample was assigned to an ROI, using the AHBA MRI data for each donor. Data was pooled between homologous cortical regions to ensure adequate coverage of both the left (data from 6 donors) and right hemisphere (data from 2 donors). Distances between samples were evaluated on the cortical surface with a 2mm distance threshold. Probe-to-gene annotations were updated in Re-Annotator (Arloth *et al.*, 2015). Only probes where expression measures were above a background threshold in more than 50% of samples were selected. A representative probe for a gene was selected based on highest intensity. Gene expression data were normalised across the cortex using scaled, outlier-robust sigmoid normalisation. 15745 genes (of 20,737 initially included in the Allen atlas gene expression data) survived these quality assurance steps. Expression profiles for 31 pre-selected genes (*Table 7.1*) encoding neurotransmitter receptors were extracted for each cortical region of the parcellation.

Table 7.1. List of selected genes encoding neurotransmitter receptors.

Gene symbol	Receptor (subunit) name
Norepinephrine	
ADRA1A	Alpha-1A adrenergic receptor
ADRA1B	Alpha-1B adrenergic receptor
ADRA1D	Alpha-1D adrenergic receptor
ADRA2A	Alpha-2A adrenergic receptor
ADRA2C	Alpha-2C adrenergic receptor
Acetylcholine	
CHRM1	Muscarinic Acetylcholine Receptor M1
CHRM2	Muscarinic Acetylcholine Receptor M2
CHRM3	Muscarinic Acetylcholine Receptor M3
CHRM4	Muscarinic Acetylcholine Receptor M4
CHRM5	Muscarinic Acetylcholine Receptor M5
CHRNA2	Nicotinic Cholinergic Receptor (Alpha 2)
CHRNA3	Nicotinic Cholinergic Receptor (Alpha 3)
CHRNA4	Nicotinic Cholinergic Receptor (Alpha 4)
CHRNA6	Nicotinic Cholinergic Receptor (Alpha 6)
CHRNA7	Nicotinic Cholinergic Receptor (Alpha 7)
CHRNA10	Nicotinic Cholinergic Receptor (Alpha 10)
CHRNB1	Nicotinic Cholinergic Receptor (Beta 1)
CHRNB2	Nicotinic Cholinergic Receptor (Beta 2)
Dopamine	
DRD1	Dopamine Receptor D1
DRD2	Dopamine Receptor D2
DRD4	Dopamine Receptor D4
Serotonin	
HTR1A	5-Hydroxytryptamine Receptor 1A, G protein-coupled
HTR1E	5-Hydroxytryptamine Receptor 1E, G protein-coupled
HTR1F	5-Hydroxytryptamine Receptor 1F, G protein-coupled
HTR2A	5-Hydroxytryptamine Receptor 2A, G protein-coupled
HTR2C	5-Hydroxytryptamine Receptor 2C, G protein-coupled
HTR3B	5-Hydroxytryptamine Receptor 3B, ionotropic
HTR3C	5-Hydroxytryptamine Receptor 3C, ionotropic
HTR4	5-Hydroxytryptamine Receptor 4, G protein-coupled
HTR5A	5-Hydroxytryptamine Receptor 5A, G protein-coupled
HTR7	5-Hydroxytryptamine Receptor 7, G protein-coupled

ADRA2B, CHRNA1, CHRNA5, CHRNA9, CHRNB3, CHRND, CHRNE, DRD3, DRD5, HTR1B, HTR1D, HTR3D, HTR3E, HTR5BP, HTR6 were not included in the analysis as they failed preprocessing steps.

Table 7.2. Demographics and clinical assessments in the study cohort.

Attribute		Controls n = 32	PD non VH n = 75	PD-VH n = 16	p value
Demographics	Age (years)	66.1 (9.4)	64.4 (7.8)	64.8 (8.6)	0.653
	Male (%)	13 (40.6)	41 (54.7)	5 (31.3)	0.029
	Years in Education	17.8 (2.5)	16.9 (2.6)	17.5 (3.6)	0.279
	Total Intracranial Volume (ml)	1390.7 (96.6)	1479.0 (132.6)	1407.3 (114.8)	0.002[c]
Mood (HADS)	Depression score	**1.7 (1.9)**	**3.9 (3.0)**	**4.7 (3.4)**	**0.032[a,b,c]**
	Anxiety score	4.0 (3.5)	5.6 (3.8)	7.0 (4.4)	<0.001[c]
Vision	Visual acuity (LogMAR) *	-0.08 (0.23)	-0.08 (0.16)	-0.07	0.351
	Contrast sensitivity (Pelli Robson) *	1.78 (0.2)	1.79 (0.2)	1.70 (0.2)	0.106
	Colour vision (D15 total error score)	2.4 (6.9)	3.4 (8.7)	2.7 (4.6)	0.681
Cognition	MMSE	29.0 (1.0)	28.9 (1.2)	28.6 (1.9)	0.883
	MOCA	29.0 (1.3)	28.2 (2.1)	26.9 (3.4)	0.047[c]
Attention	Digit span backwards	7.2 (2.1)	7.1 (2.3)	7.9 (2.3)	0.601
	Stroop: colour (sec)	32.1 (6.7)	33.5 (7.6)	38.1 (9.1)	0.089
Executive function	Stroop: interference (sec)	55.4 (11.6)	60.2 (19.2)	69.6 (23.9)	0.051
	Category fluency	22.5 (5.1)	21.7 (5.9)	19.8 (7.4)	0.339
Memory	Word Recognition Task	24.3 (1.2)	24.3 (1.2)	23.8 (0.9)	0.056
	Logical Memory	14.1 (4.1)	13.5 (4.3)	12.5 (4.6)	0.617
Language	Graded Naming Task	22.5 (6.2)	23.9 (2.9)	23.7 (2.3)	0.802
	Letter Fluency	16.4 (5.4)	16.7 (5.4)	17.7 (5.3)	0.509
Visuospatial	Benton's Judgement of Line Orientation	24.9 (5.6)	24.5 (3.7)	23.1 (5.3)	0.338
	Hooper	25.7 (2.1)	24.7 (2.8)	23.3 (4.3)	0.074
Disease specific Measures	Disease duration	-	**3.9 (2.3)**	**5.3 (3.4)**	**0.044**
	UPDRS total Score	-	**42.7 (20.8)**	**62.1 (38.5)**	**0.014**
	UPDRS part 3 (motor)	-	21.2 (11.3)	29.8 (22.6)	0.129
	UM-PDHQ (hallucination severity score)	-	-	4.6 (2.4)	-
	LEDD (mg)	-	437.0 (255.1)	450.0 (221.2)	0.295
	Sniffin' sticks	-			0.113
	RBDSQ	-	4.0 (2.4)	5.1 (2.5)	0.055
Image Quality metrics	Mean framewise displacement	0.17 (0.09)	0.18 (0.12)	0.23 (0.15)	0.177
	Coefficient of joint variation	0.69 (0.26)	0.67 (0.20)	0.68 (0.26)	0.921
	Entropy focus criterion	0.59 (0.02)	0.60 (0.02)	0.59 (0.02)	0.045[±]

Total signal to noise ratio	1.89 (0.17)	1.85 (0.18)	1.82 (0.11)	0.338

All data shown are mean (SD) except gender.
In bold characteristics that significantly differed between the PD-VH and PD-non-VH.
[a]: significant difference between PD-VH and PD-non-VH; [b]: significant difference between PD-non-VH and controls; [c]: significant difference between PD-VH and controls.
[±] No significant difference found between any comparison's in post-hoc testing (Tukey)
** Best binocular score used; LogMAR: lower score implies better performance, Pelli Robson: higher score implies beter performance. HADS: Hospital anxiety and depression scale; MMSE: Mini-mental state examination; MOCA: Montreal cognitive assessment; UPDRS: Unified Parkinson's disease rating scale; UM-PDHQ: University of Miami Hallucination Questionnaire (max score: 14); LEDD: Total Levodopa equivalent dose; RBDSQ: REM sleep behaviour disorder screening questionnaire.*

7. 3. Results

A total of 123 participants were included; 16 with PD and visual hallucinations (PD-VH), 75 with PD without hallucinations (PD non VH) and 32 controls. Demographics and clinical assessment results are seen in Table 7.2.

Preserved topology but impaired temporal properties of dynamic functional connectivity substates

To examine the dynamic changes in functional connectivity underlying PD hallucinations, an a-priori clustering of dynamic functional connectivity into two sub-states was used, an *Integrated* and a *Segregated* state. No significant differences were seen in the two sub-states between PD versus controls or PD-VH versus PD non VH when comparing connectivity strength using network-based statistics.

In contrast, there were significant changes in the temporal properties of the sub-states. PD-VH spent a significantly smaller proportion of time in the *Integrated* state (therefore higher proportion of time in the *Segregated* state) than PD non VH (β=-0.113, p=0.032) and controls (β=-0.128, p=0.026) (*Figure 7.3*). Within PD participants, the proportion of time spent in the *Integrated* state was signifinantly correlated with hallucination severity,

measured by the UM-PDHQ (ρ=-0.259, p=0.013) (*Figure 7.3*). Mean dwell time in the *Segregated* state was higher in PD-VH than PD non VH (19.1 ± 16.9 in PD-VH vs 9.5 ± 9.1 in PD non VH H=4.058, p=0.044), with no difference between the two groups in mean dwell time of the *Integrated* state (H = 2.166, p=0.141). No differences were seen in dwell time of either state between PD and controls. Finally, the total number of transitions were lower in PD-VH than PD non VH (5.7 ± 5.3 in PD-VH vs 8.5 ± 6.2 in PD non VH, H=3.87, p=0.049) but there was no difference when between the two groups when the number of transitions from integrated-to-segregated state and segregated-to-integrated state were examined separately.

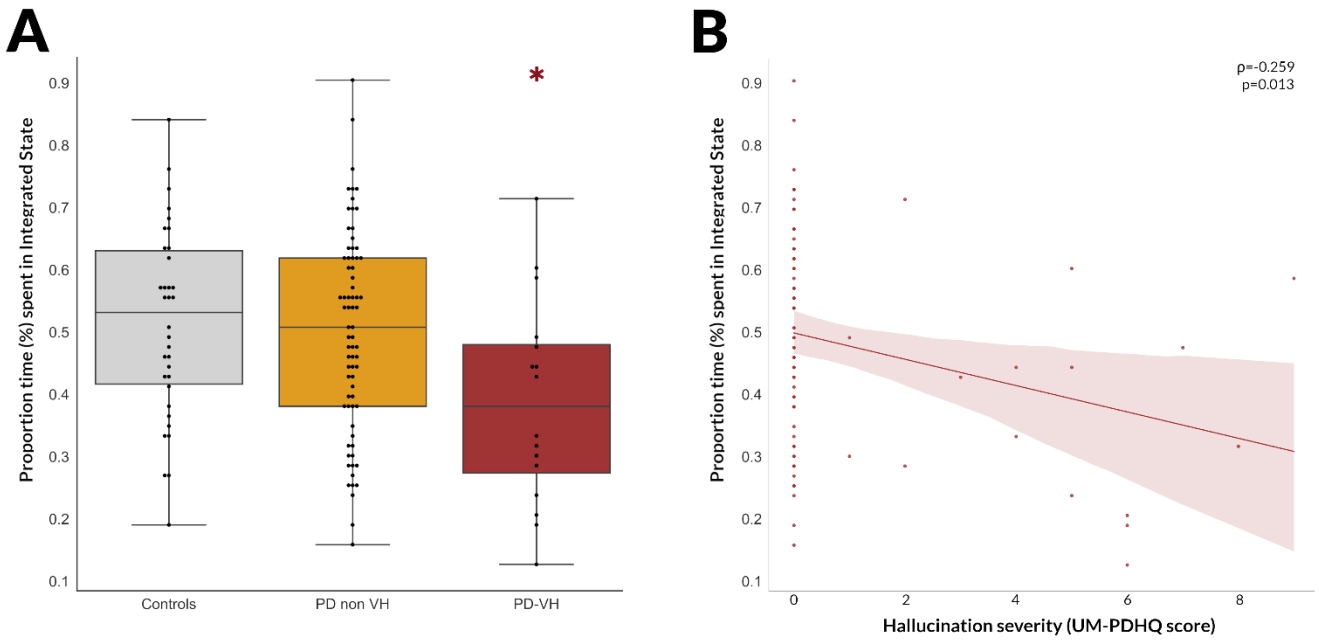

Figure 7. 3. Altered temporal properties of dynamic functional connectivity in PD-VH.

A. *PD-VH spent significantly less time in the Integrated sub-state of dynamic functional connectivity than patients without hallucinations (p=0.032) and controls (p=0.0262). Box shows the quartiles and whiskers extend to cover the whole distribution.*

B. *The proportion of time spent in the integrated State was significantly correlated with hallucination severity in PD participants (Spearman's correlation coefficient ρ=-0.259, p=0.013): participants with more severe hallucinations spent less time in the integrated sub-state. Shaded area represents 95% confidence intervals.*

Overall, these findings suggest that PD-VH spend more time overall in the *Segregated* state than PD non VH, with fewer total number of transitions and longer dwelling time within the *Segregated* state (*Figure 7.3*).

Reduced energy costs to transition from the integrated to the segregated sub-state in PD-VH

I next aimed to investigate whether the *Segregated* state predominance observed in PD-VH participants could be explained by differences in the ease of transition from the integrated-to-segregated state or vice versa or a difference in ease of maintaining the segregated state in PD-VH compared to PD non VH participants. To do this, I calculated the minimal control energy that needs to be applied to the structural network of each participant to 1) transition from integrated-to-segregated state 2) transition from segregated-to-integrated state 3) maintain the integrated, and 4) maintain the segregated state. I then examined whether transition and persistence energies in each sub-state differed between PD-VH and PD non VH.

As previously described (Braun *et al.*, 2019), persistence energy for the computationally more demanding *Integrated* state was higher than the *Segregated* state (repeated measures ANOVA main effect of *Integrated* to *Segregated* state persistence energy $F(1,113) = 12.432$, $p<0.001$) (*Figure 7.4*). Similarly the minimal energy needed to transition from the less connected *Segregated* to the more interconnected *Integrated* state was higher ($F(1,113)= 6.722$, $p=0.011$).

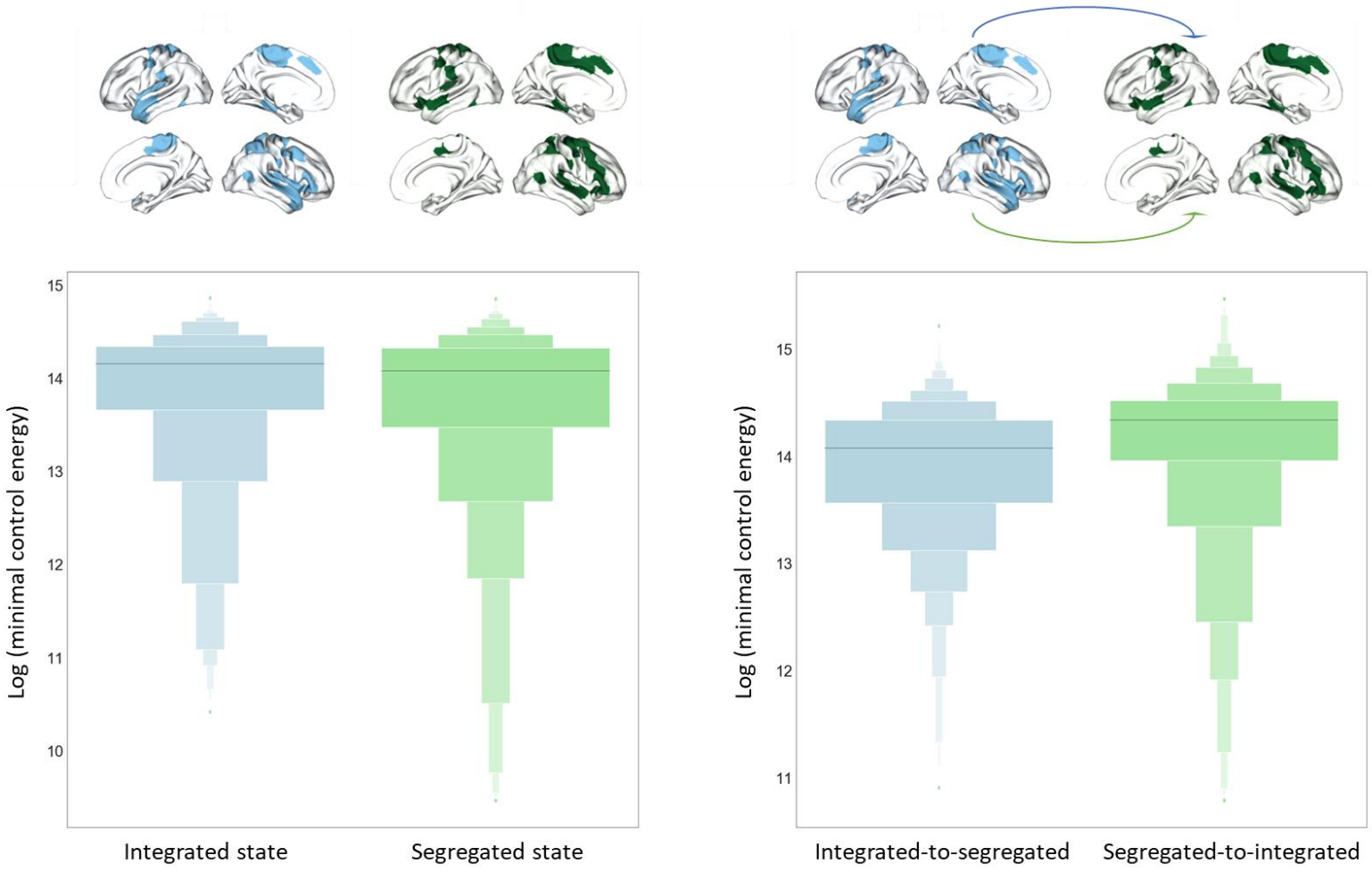

Figure 7. 4. Mean minimal control energy to maintain and transition between sub-states

LEFT: The minimal control energy that is required across the whole of the brain network (232 regions of interest) to maintain the Integrated substate (blue) was significantly higher than the energy needed to maintain the Segregated sub-state (green): repeated measures ANOVA main effect of integrated to segregated state persistence energy $F(1,113) = 12.432$, $p<0.001$).

RIGHT: The minimal energy needed to transition from the less connected segregated to the more interconnected integrated state (green) was higher than that to transition from the segregated to the integrated state (blue, ($F(1,113)= 6.722$, $p=0.011$))

PD-VH needed significantly lower control energy to transition from the integrated-to-segregated state than PD non VH (effect size Hedge's g= 0.922, t= 2.376, p=0.029) (*Figure 7.5*). The minimal control energy to transition from an integrated-to-segregated state was significantly correlated with the severity of hallucinations, with lower energy needed the higher the hallucination severity (ρ= -0.283, p=0.008) (*Figure 7.5*). There were no statistically significant differences between PD-VH and PD non VH in the minimal control energy needed to transition from segregated-to-integrated state (t= 1.346, p=0.195), or to persist within the *Integrated* (t=1.041, p=0.312) or *Segregated* sub-state (t=1.079, p=0.295).

Transition from the integrated to the segregated state is driven by subcortical and more multimodal brain regions

Next, I aimed to identify which brain regions contribute more to the transition from the integrated-to-segregated state (which nodes need more energy to be applied to make the transition). As expected, subcortical regions heavily contributed to the transition from the integrated to the segregated state with 25 subcortical nodes being amongst the top 20% of contributors (25 of 47 or 53.2%). Amongst the cortical nodes the top contributors included primarily right hemispheric regions (20 of 22 cortical nodes) including the cingulum, precuneus, inferior and superior temporal regions and medial frontal regions (*Table 7.3, Figure 7.4*). There was a significant correlation between the minimal transition energy from integrated-to-segregated state that was needed to be applied to each node and the node's position in the cortical hierarchy, with higher amount of energy needed for more transmodal regions (ρ= 0.526, p<0.001) (*Figure 7.4*).

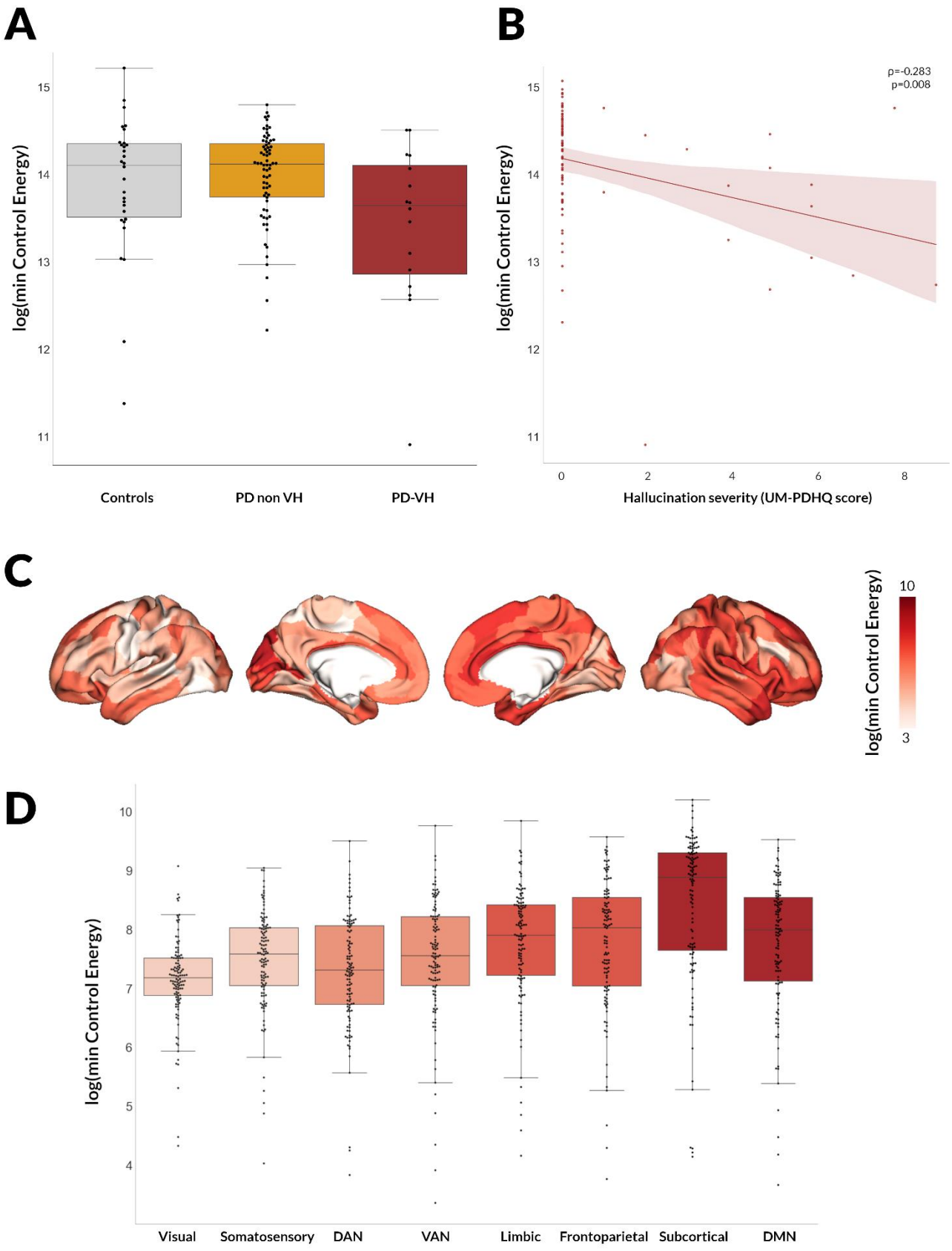
A
log(min Control Energy)
15
14
13
12
11
Controls
PD non VH
PD-VH
B
log(min Control Energy)
ρ=-0.283
p=0.008
0
2
4
6
8
Hallucination severity (UM-PDHQ score)
C
log(min Control Energy)
10
3
D
log(min Control Energy)
10
9
8
7
6
5
4
Visual
Somatosensory
DAN
VAN
Limbic
Frontoparietal
Subcortical
DMN

Figure 7. 5. Changes in control energy to transition from the Integrated to the Segregated substate in PD-VH.

(Opposite)

A. *Less minimal control energy is needed to transition from the Integrated to the Segregated substate for patients with Parkinson's and visual hallucinations (PD-VH) than those without hallucinations (PD non VH). Log-transformed minimal control energy is presented.*

B. *The log-transformed minimal control energy required across the whole of the network to transition from the Integrated to the Segregated substate was significantly correlated with severity in participants with Parkinson's disease (Spearman's correlation coefficient ρ=-0.283, p=0.008): participants with more severe hallucinations needed less energy to transition.*

C. *There was regional variation in log-transformed minimal control energy needed to transition from the Integrated to the Segregated substate; darker colours denote higher amounts of energy required. Note that only cortical regions are plotted.*

D. *The mean minimal control energy to transition from the Integrated to the Segregated substate across all nodes of the seven cortical and one subcortical resting state networks is plotted. Darker colours denote higher levels of the cortical hierarchy; also left to right: unimodal to transmodal regions. There was a significant correlation between the minimal transition energy from integrated-to-segregated state that was needed to be applied to each node and the nodes position in the cortical hierarchy, with higher amount of energy needed for more transmodal regions (ρ= 0.526, p<0.001).*

Table 7.3. Top 20% of nodes that contribute to the transition from the integrated to the segregated state of dynamic functional connectivity

Region	Coordinates in MNI space			Log(Energy) mean (std)	Network
	x	y	z		
Cortical					
Occipital_Mid_L	-22	-96	6	9.66 (8.49)	Visual
Cuneus_L	-12	-72	22	9.65 (8.49)	Visual
Temporal_Sup_R	64	-24	8	9.70 (8.35)	Somatosensory
Temporal_Sup_R	44	-28	18	9.72 (8.81)	Somatosensory
Rolandic_Oper_R	60	0	10	9.59 (8.60)	Somatosensory
Postcentral_R	58	-4	30	9.63 (8.54)	Somatosensory
Paracentral_Lobule_R	6	-22	68	9.94 (8.62)	Somatosensory
Cingulum_Mid_R	10	-36	46	9.38 (8.48)	VAN
Temporal_Inf_R	46	-12	-34	9.79 (8.38)	Limbic
ParaHippocampal_R	26	-10	-32	9.59 (8.38)	Limbic
SupraMarginal_R	62	-38	36	8.73 (8.76)	Frontoparietal
Temporal_Inf_R	62	-42	-12	9.38 (8.60)	Frontoparietal
Cuneus_R	14	-70	36	9.39 (8.60)	Frontoparietal
Cingulum_Mid_R	6	-24	30	8.99 (8.78)	Frontoparietal
Cingulum_Mid_R	4	2	30	7.97 (7.90)	Frontoparietal
Cingulum_Ant_R	8	30	28	7.64 (7.77)	Frontoparietal
Angular_R	50	-58	44	9.49 (8.50)	DMN
Rectus_R	4	36	-14	9.59 (8.38)	DMN
Cingulum_Ant_R	8	42	4	8.74 (8.94)	DMN
Frontal_Sup_Medial_R	8	58	18	5.07 (5.50)	DMN
Frontal_Mid_R	28	30	42	7.92 (8.18)	DMN
Precuneus_R	6	-58	44	9.24 (8.41)	DMN
Subcortical					
Antrerior hippocampus R	26	-14	-20	9.55 (8.57)	Subcortical
Posterior hippocampus R	28	-32	-8	9.68 (8.87)	Subcortical
Lateral amygdala R	28	-2	-22	9.83 (8.30)	Subcortical
Medial amygdala R	22	-6	-16	5.49 (5.59)	Subcortical

Dorsoposterior thalamus R	16	-30	2	9.86 (8.64)	Subcortical
Ventroanterior thalamus R	8.0	-10.0	6.0	9.22 (8.67)	Subcortical
Dorsoanterior thalamus R	12.0	-22.0	12.0	8.57 (8.19)	Subcortical
Nucleus accumbens, shell R	12.0	10.0	-6.0	9.61 (8.68)	Subcortical
Nucleus accumbens, core R	14.0	18.0	-2.0	9.05 (8.53)	Subcortical
Posterior globus pallidus R	24.0	-8.0	-2.0	7.55 (8.16)	Subcortical
Posterior Putamen R	30.0	-6.0	4.0	5.15 (5.45)	Subcortical
Anterior Caudate R	14.0	14.0	6.0	8.05 (7.60)	Subcortical
Posterior Caudate R	14.0	4.0	16.0	9.89 (9.13)	Subcortical
Antrerior hippocampus L	-24.0	-14.0	-20.0	8.15 (8.26)	Subcortical
Posterior hippocampus L	-26.0	-32.0	-8.0	9.32 (8.23)	Subcortical
Lateral amygdala L	-26.0	-2.0	-22.0	8.36 (8.29)	Subcortical
Medial amygdala L	-20.0	-6.0	-16.0	9.67 (8.64)	Subcortical
Dorsoposterior thalamus L	-14.0	-30.0	2.0	9.74 (8.39)	Subcortical
Ventroanterior thalamus L	-6.0	-10.0	6.0	8.22 (8.06)	Subcortical
Dorsoanterior thalamus L	-10.0	-22.0	12.0	7.47 (6.76)	Subcortical
Nucleus accumbens, shell L	-10.0	10.0	-6.0	7.66 (7.69)	Subcortical
Nucleus accumbens, core L	-12.0	18.0	-2.0	9.30 (8.50)	Subcortical
Posterior globus pallidus L	-22.0	-8.0	-2.0	7.30 (7.50)	Subcortical
Anterior Caudate L	-12.0	14.0	6.0	9.87 (8.63)	Subcortical
Posterior Caudate L	-12.0	4.0	16.0	6.89 (7.14)	Subcortical

L: Left, R: Right hemisphere

Correlation with neurotransmitter systems

Finally, I examined whether the transition from the integrated-to-segregated state, which was less costly for PD-VH participants is associated with specific neurotransmitter systems in the healthy brain. To do this, I correlated the mean regional control energy that is needed to be applied to each node to transition from the integrated-to-segregated state with mean regional expression values of neurotransmitter density (derived from PET data) and neurotransmitter receptor gene expression levels (derived from the Allen Brain atlas (Hawrylycz *et al.*, 2015) in health; I tested this against spatially correlated null models through sphere permutations, then FDR-corrected for multiple comparisons.

There was a significant correlation between regional log(Energy) and density of *5-HT1b* (ρ=-0.274, q_{spin}=0.009), *5-HT2a* (ρ=-0.347, q_{spin}<0.001) and *GABA$_A$* receptors (ρ=-0.317, q_{spin}=0.022). Regional energy and regional expression levels of 5-HT2a receptors were also significantly correlated (ρ=-0.1438, q_{spin}=0.044) as well as two $GABA_A$ receptors [GABRA1 (ρ=-0.2437, q_{spin}=0.020) and *GABRA2* (ρ=0.128, q_{spin}=0.023)]; gene expression data for 5-HT1b receptors were not available. Although noradrenergic and acetylcholinergic PET data were not available, genetic expression of noradrenergic (*ADRA1B* and *ADRA2A*), muscarinic (*CHRM1*, *CHRM2*, *CHRM3*, *CHRM4*) and nicotinic receptors (*CHRNA3*, *CHRNA4*, *CHRNA7*, *CHRNB2*). Gene expression of DRD2 was also correlated with regional control energy for the integrated-to-segregated state transition (ρ=0.318, q_{spin}=0.013) but this was not replicated using density data derived from PET (ρ=0.056, q_{spin}=0.800). *Table 7.4* and *Figure 7.6* show the correlation between regional control energy and transmitter density and regional gene expression.

Table 7.4. Neurotransmitter receptors showing density and gene expression correlations with regional control energy required to transition from the integrated to the segregated state.

Receptor density			
Receptor	**Ligand**	**Correlation coefficient**	**q value**
5-HT1B	Serotonin	-0.274	0.009
5-HT2A	Serotonin	-0.347	0.000
GABA	GABA	-0.317	0.022
Receptor gene expression			
Gene symbol	**Ligand**	**Correlation coefficient**	**q value**
ADRA1B	Norepinephrine	-0.154	0.018
ADRA2A	Norepinephrine	-0.210	0.013
CHRM1	Acetylcholine	-0.279	0.018
CHRM2	Acetylcholine	-0.265	0.028
CHRM3	Acetylcholine	-0.223	0.018
CHRM4	Acetylcholine	0.202	0.018
CHRNA3	Acetylcholine	0.416	0.013
CHRNA4	Acetylcholine	-0.158	0.033
CHNRA7	Acetylcholine	-0.244	0.023
CHNRB2	Acetylcholine	0.207	0.028
DRD2	Dopamine	0.318	0.013
HTR1E	Serotonin	-0.207	0.013
HTR1F	Serotonin	-0.3301	0.013
HTR2A	Serotonin	-0.144	0.044
HTR5A	Serotonin	-0.311	<0.001
GABRA1	GABA	-0.244	0.020
GABRA2	GABA	0.128	0.023
GABRAB2	GABA	0.433	0.018
GABRAD	GABA	-0.289	0.013
GABRG1	GABA	0.227	0.023
GABRG2	GABA	-0.337	0.023
GABRG3	GABA	-0.217	0.044

CHRNA: Nicotinic Cholinergic Receptor (Alpha), DRD: Dopamine Receptor D, HTR: 5-Hydroxytryptamine Receptor, ADRA: Alpha-1A adrenergic receptor, GABR: GABA Receptor
Note that correlation coefficients of absolute values between 0.1 and 0.4 represent moderate correlation in our dataset. Q values are FDR-corrected p-values from spatial permutation testing (q-spin).

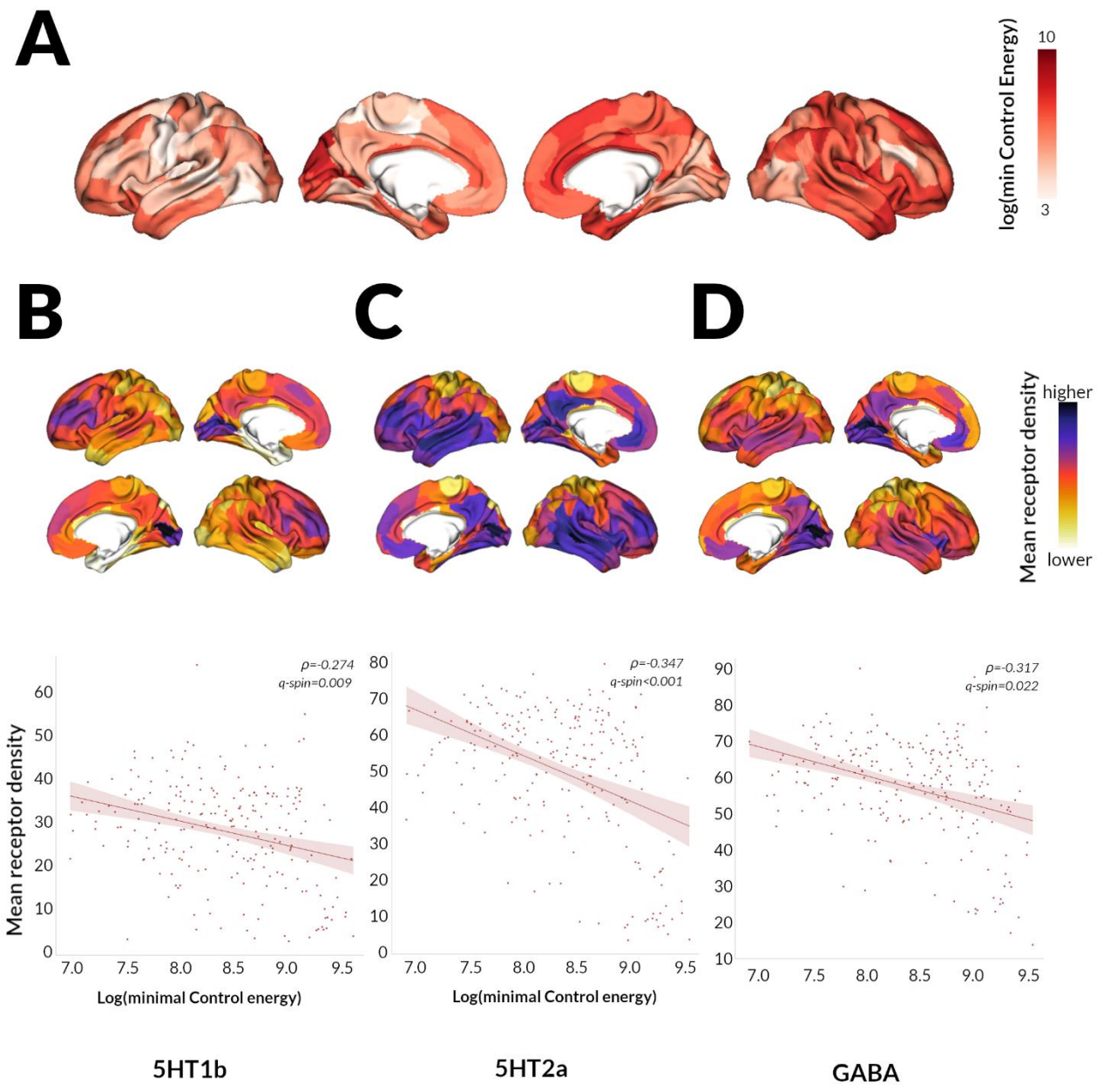

Figure 7. 6. Neurotransmitter correlates of Integrated-to-Segregated state transition.

The log-transformed minimal control energy that needs to be applied to each node (A) was correlated with the mean regional receptor density of 5HT1b receptors (B), 5HT2a receptors (C) and GABA receptors (D).

In all cases ρ is the Spearman correlation coefficient and q-spin is the FDR corrected p-value derived following spatial permutations (p-spin, 1000 permutations).

7.4. Discussion

This study sheds light on the alterations in temporal functional dynamics underlying visual hallucinations in Parkinson's disease and examines how these specific patterns of temporal dynamics can be explained through brain structure. Specifically, I showed that:

a. PD-VH spend more time in a *Segregated* sub-state of functional connectivity than those without hallucinations, with fewer total number of transitions and longer dwelling time within the *Segregated* state
b. the transition from the *Integrated* to the *Segregated* state is less energy demanding in PD-VH than PD non VH, therefore may be preferential
c. the transition from the *Integrated* to the *Segregated* state is mediated primarily by transmodal brain regions and modulated by specific neurotransmitter systems, including serotoninergic and GABAergic receptors.

The predisposition for a *Segregated* state in PD with hallucinations is in keeping with other studies in PD where patients with PD and cognitive impairment showed increased dwell time in a more segregated state and reduced transitions compared to those with intact cognition and healthy controls (Díez-Cirarda *et al.*, 2018; Fiorenzato *et al.*, 2019). No difference in terms of cognitive performance was seen between PD with and without hallucinations in our cohort, but visual hallucinations are associated with the development of subsequent dementia in PD (Aarsland *et al.*, 2007). In schizophrenia, where hallucinations are also a core feature, similar findings of altered dwell time have been seen (Sakoğlu *et al.*, 2010; Damaraju *et al.*, 2014) and this correlated with measures of hallucination severity (Weber *et al.*, 2020). I similarly saw a correlation with hallucination severity with

patients with more severe hallucinations spending less time in the *Integrated* state (and more time in the *Segregated* state) suggesting that this finding is specific to hallucinations.

Only the temporal dynamics of functional connectivity were altered in PD with hallucinations: we found no differences in the *Integrated* or *Segregated* sub-states themselves between groups. This indicates that a change in the temporal balance between normal/preserved sub-states rather than a change in the sub-states themselves underly PD-hallucinations. Using a similar methodology, studies in loss of consciousness and LSD have shown within-state changes particularly within the *Integrated* state(Luppi *et al.*, 2019, 2021), which is more linked to cognitive performance and alertness(Shine *et al.*, 2016). As I examined the trait rather than the state of PD-hallucinations (participants were not actively experiencing visual hallucinations during scanning) it is possible that additional within-state changes could underly visual hallucinations in PD. In addition, although hallucinations in our participants were frequent (at least weekly) they were not universally complex and severe. However, LSD-induced visual hallucinations are primarily driven by serotoninergic system activation alone, and are associated with changes in other sensory modalities as well as ego-dissolution, depersonalisation and time/space dysperceptions(Carhart-Harris *et al.*, 2016), which are not seen in PD-associated hallucinations; the underlying changes in temporal dynamics may also be different.

As temporal transition between functional sub-states is constrained by structural connectivity (Betzel *et al.*, 2016; Stiso *et al.*, 2019; Cornblath *et al.*, 2020), I examined the energy cost of transitioning between and maintaining the *Integrated* and *Segregated* sub-state. PD-VH needed significantly low energy cost to transition from the integrated-to-segregated state than PD non VH, suggesting that this transition may be easier to achieve in hallucinators. This transition is mediated primarily by subcortical

and multimodal brain regions of the DMN, further highlighting the importance of the DMN in the development of visual hallucinations in PD (Shine *et al.*, 2014).

Interestingly, the brain regions contributing most to this transition from integrated-to-segregated state showed a correlation with specific neurotransmitter systems in health. Although directionality of the relationship is difficult to interpret as data on regional neurotransmitter density and gene expression were derived from healthy individuals, regional density of *5HT2A* receptors was significantly correlated with the regional control energy needed to transition from integrated-to-segregated state; this was replicated using regional expression data for the *5HT2A* receptor gene. Activation of 5HT2A receptors is a key mechanism for drug-induced hallucinations from LSD, psilocybin and ayahuasca(Geyer and Vollenweider, 2008) and both post mortem and in vivo studies have shown higher density of 5-HT2A receptors within frontal, temporal and occipital regions in patients with Parkinson's disease and visual hallucinations(Cheng *et al.*, 1991; Huot *et al.*, 2010). Pimavanserin, an inverse agonist of 5-HT2A receptors, improves hallucinations in Parkinson's (Cummings *et al.*, 2014) and another anti-serotoninergic medication, Ondansetron, targeting 5HT3 receptors, is currently being trialled (University College, London, 2019). Unfortunately, no receptor density or gene expression data were available for 5HT3 receptors but other serotoninergic receptors were also important for the integrated-to-segregated state transition including: *5HT1B* (receptor density, no genetic expression data), *5HT1E*, *5HT1F* and *5HT5A* (all genetic expression data only). This highlights the complexity of the serotoninergic system's role in PD-hallucinations and suggests that anti-serotoninergic medications targeting multiple receptors could be potential therapeutic targets of PD-hallucinations.

Regional receptor density and gene expression for GABAergic receptors were also significantly correlated with regional transition energy. GABA concentration is reduced in the visual cortex of PD patients with visual hallucinations (Khundakar *et al.*, 2016; Firbank *et al.*, 2018), this may be a compensatory mechanism in PD-VH to increase stability in the presence of poor visual sensory evidence (van Loon *et al.*, 2013; O'Callaghan *et al.*, 2017). Interestingly, the regional gene expression of noradrenergic (ADRA1B, ADRA2A) and cholinergic (muscarinic and nicotinic) receptors was also significantly correlated with the integrated-to-segregated state transmission although PET-derived density data was not available to replicate this finding. In contrast there was no correlation with dopaminergic receptors (DRD2 regional gene expression was correlated with regional control energy but this was not replicated when assessed regional density profiles). This highlights the role of transmitters other than dopamine in the development of PD-hallucinations. Convergent evidence have recently highlighted the importance of the noradrenergic system in non-motor symptoms of PD (Vazey and Aston-Jones, 2012; Iwaki *et al.*, 2019; O'Callaghan *et al.*, 2021) and noradrenaline plays a key role in modulating selective attention (Dahl *et al.*, 2020); changes within the noradrenergic system may be involved in altered state transitions in PD-hallucinations.

Several limitations need to be considered. Functional data, including time-varying estimates, are susceptible to motion artefact; strict exclusion criteria were adopted to mitigate for this (Power *et al.*, 2014). Global signal regression has been proposed as an additional tool to counteract residual artifacts from head motion (Power *et al.*, 2014) however it could contain behaviourally-relevant information and affect group results (Saad *et al.*, 2012; Power *et al.*, 2017), therefore we did not regress global signal in this study similar to prior work (Luppi *et al.*, 2019, 2021). All participants were scanned receiving their usual dopaminergic medications and the same time

of day and levodopa equivalent doses did not significantly differ between PD-VH and PD non VH; however time and medication usage can influence rsfMRI (Orban *et al.*, 2020) and further studies assessing PD patients ON and OFF levodopa might provide additional information. Similarly, differences in arousal can influence dynamic functional connectivity estimates (Tagliazucchi and Laufs, 2014); all participants were asked to remain awake during scanning with their eyes open, however differences in arousal could not be quantified between participants. Although brain networks are non-linear, I used a linear optimal control model. However linear models have been shown to provide important insight on non-linear dynamics (Honey *et al.*, 2009). Finally, it is important to know that data on regional neurotransmitter density and gene expression profiles were derived from healthy human brains; therefore results relating to neurotransmitter receptor gene expression should be interpreted with caution.

In conclusion, this study describes, for the first time, that temporal functional dynamics are altered in PD-hallucinations, with a predisposition towards a *Segregated* sub-state of functional connectivity. This *Segregated* state predominance can be explained by a reduced energy cost to transition from the integrated-to-segregated state in PD with hallucinations compared to those without hallucinations. This study quantified the brain regions that contribute most to this transition and clarified the neuromodulatory correlates of the integrated-to-segregated state transition in the healthy brain. Altogether, these findings provide mechanistic insights into visual hallucinations in PD and highlight potential therapeutic targets.

8. Summary and Conclusions

8.1 Introduction

In this thesis, I aimed to better clarify the neural correlates of visual hallucinations in Parkinson's disease (PD). I began by quantifying the use of prior knowledge in PD (*Chapter 3*): I showed for the first time that, in addition to visuospatial deficits (implying less precise feedforward signals), patients with PD and visual hallucinations also overweight they prior knowledge when viewing ambiguous visual stimuli.

To understand the structural correlates of PD-hallucinations, I then revealed how white matter micro- and macro-structure degenerates in PD patients with hallucinations (*Chapter 4*), particularly affected posterior tracts like the splenium and posterior thalamic radiations.

I then examined the longitudinal changes in white matter and gray matter in PD-hallucinators (*Chapter 5*): I showed widespread white matter changes longitudinally in Parkinson's hallucinators compared with non-hallucinators, in the absence of cortical atrophy, as well as particular involvement of the mediodorsal medial thalamus.

I clarified the structural connectivity changes at network level and showed that Parkinson's-hallucinators exhibit a subnetwork of reduced connectivity strength (*Chapter 6*). Within this subnetwork, hallucinators showed reduced controllability (influence over other brain regions). I then linked these changes in white matter connectivity to reduced expression of genes associated with related to mRNA metabolism (enrichment in oligodendrocytes) and upweighted genes relate to protein localisation (enrichment in neuronal cells) (*Chapter 6*).

Finally, I clarified the temporal dynamical changes in functional connectivity underlying PD-hallucinations showing that patients with hallucinations spend more time in a more segregated, less inter-connected functional state (*Chapter 7*). I used network control theory to understand how changes in the structural brain network may lead to these altered functional dynamics and showed that the transition to this segregated functional state required less energy in PD-hallucinators, therefore may be preferential. Finally I linked the regional contribution to this transition to specific neurotransmitter receptors including *5HT2A, 5HT1B, GABA* and cholinergic receptors using density profiles and gene expression data from healthy human brains (*Chapter 7*).

In this chapter, I will review the main findings of experimental chapters, discuss their implications and the new questions and hypotheses that they have generated and describe future work.

8.2 Network imbalance in Parkinson's associated visual hallucinations

This thesis has aided our understanding of network imbalance in PD hallucinations across scales: computational, structural and temporally dynamic functional networks.

In *Chapter 3* I used a visual learning paradigm to show that PD patients with hallucinations over-rely on feedback signals, with overweighting of prior knowledge when viewing ambiguous stimuli. This overweighting of prior knowledge was positively correlated to the severity of visual hallucinations: patients with more severe hallucinations improved even more in performance in the visual task after receiving prior knowledge. Changes in the balance between feedback and feedforward signals has been

postulated as a key mechanism leading to hallucinations (Powers *et al.*, 2016) and PD-hallucinations have been associated with deficits in visual processing (McKinlay *et al.*, 2007; O'Callaghan *et al.*, 2017); this was the first time that overweighting of prior knowledge was demonstrated in PD-associated hallucinations. This finding clarifies the computational mechanisms of visual hallucinations in PD providing evidence of strong priors and weak sensory evidence both contributing to the development of hallucinations.

In addition, in *Chapters 4, 5 and 6* I clarified the alterations in structural connectivity in PD-hallucinations both at the white matter tract and network level. Structural connectivity constrains and predicts functional connectivity (Honey *et al.*, 2009). Preserved or even increased brain activity measured during task or resting state fMRI may also occur in the presence of neurodegeneration despite underlying structural changes due to compensatory mechanisms. Structural changes could be more reliable and more representative of underlying pathology.

Prior work has shown significant changes in functional brain networks in PD with hallucinations (Muller *et al.*, 2014), however most structural studies so far focused on gray matter (Pezzoli *et al.*, 2017). In *Chapter 5* I showed that white matter changes are evident using diffusion-weighted imaging in PD with hallucinations in the absence of significant changes in cortical thickness; this is in keeping with animal and cell-level data (Chung *et al.*, 2009; Volpicelli-Daley *et al.*, 2011) and highlights the importance of neuroimaging methods assessing white matter in the study of PD hallucinations. Given the widespread white matter macrostructural changes that were seen longitudinally, diffusion-weighted imaging (analysed using higher tensor models such as fixel based analysis) could represent an attractive measure of impact on disease progression for future clinical trials assessing treatments of PD-associated visual hallucinations.

Finally, in *Chapter 5* I showed that the mediodorsal medial thalamus is particularly affected in PD with hallucinations, with white matter tracts affected before gray matter volume loss occurs. The thalamus has been postulated as a potential driver of network changes in PD-hallucinations (Onofrj *et al.*, 2019; Russo *et al.*, 2019), but this has not been previously demonstrated. The mediodorsal thalamus specifically, plays a crucial role in directing attention via its connection to the superficial layers of the prefrontal cortex which in turn regulates areas further down the cortical hierarchy via feedback connections (Ouhaz *et al.*, 2018; Anastasiades *et al.*, 2021). Gray matter loss or reduced connectivity of the mediodorsal and subsequent aberrant, unregulated prefrontal cortex activity could explain the increased feedback signals, or overweighting of prior knowledge seen in PD-hallucinators. Finally, the mediodorsal thalamus could be a potential therapeutic target for hallucinations as it is a region where deep brain stimulation can be applied; indeed this has been performed in patients with obsessive compulsive disorders (Maarouf *et al.*, 2016).

Unanswered questions and next steps

Although this thesis has helped clarify the changes seen in brain networks in PD with hallucinations at different scales, the specific level in the hierarchy that changes in feedforward and feedback signals are seen still remains unclear. Feedback and feedforward circuits in health are arranged into distinct layers of grey matter close to the surface of the brain, with feedforward circuits in middle layers and feedback circuits in superficial and deeper layers (Muckli *et al.*, 2015). Until now, the changes in brain circuits have not been shown in living patients, as conventional 3 Tesla MRI lacks the resolution to examine cortical layers. In future work I plan to leverage the greater anatomical detail and increased accuracy of 7 Tesla (7T) MRI to identify structural and functional changes within cortical layers.

As hallucinations are transient and unpredictable, they are challenging to directly elicit in the scanner. Instead, I will use a visual task to evoke Pareidolias, the perception of a face that is not there. Pareidolias occur more in patients with the related Demential with Lewy Bodies (DLB) and visual hallucinations (Uchiyama *et al.*, 2012), correlate with hallucination severity (Uchiyama *et al.*, 2012) and can distinguish DLB from Alzheimer's disease (Inagawa *et al.*, 2020).

I have already adjusted the pareidolia task to make it suitable for in-scanner use and piloted this in 35 PD patients (17 hallucinators). Participants with hallucinations experienced significantly more pareidolias than non-hallucinators and the number of pareidolias correlated with the severity of their hallucinations (*Figure 8.1*). Using this task during ultra-high field MRI will allow me to examine functional changes during pareidolias within cortical layers in LBD-hallucinators. Given the findings of increased weighting of prior knowledge in PD-hallucinators (*Chapter 3*), I predict that BOLD signal during the experience of pareidolias will be increased in deep and superficial layers (representing feedback connections) but not in middle layers (representing feedforward connections) in patients with PD and habitual visual hallucinations compared with non-hallucinators.

Identifying layer specific changes associated with PD-hallucinations will provide new insights to the complex changes in circuitry that give rise to hallucinations. As different cortical layers have different cell populations and inputs from different neutrotransmitter systems, this could also open potential avenues for treatments for this distressing symptom.

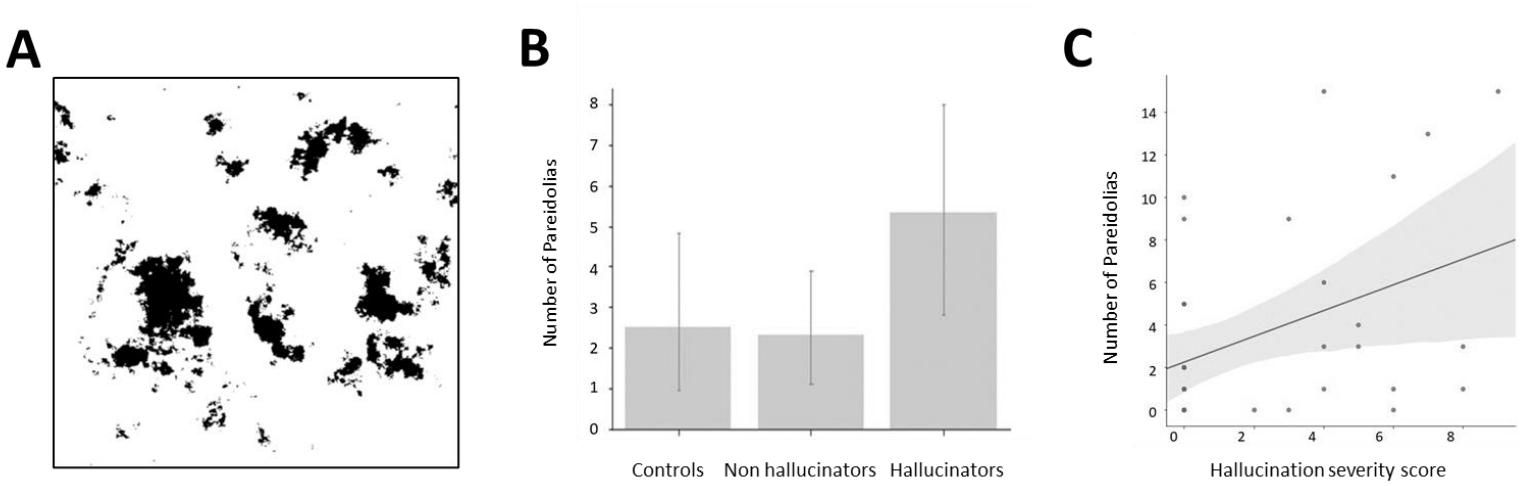

Figure 8. 1. The Pareidolia Task: Pilot data

A. *Example of an image in the Pareidolia task. This black and white image is perceived as containing a face in the absence of one (Pareidolia) by people with Lewy Body Dementia (LBD) and habitual hallucinations*

B. *Pareidolias were significantly more common in patients with hallucinations (mean ± standard deviation= 5.3 ± 5.9) compared to non hallucinators (2.3 ± 3.0) and controls (2.5 ± 4.6); p=0.011.*

C. *Hallucination severity (using the Miami Hallucinations Questionnaire) was associated with higher number of perceived pareidolias (F=23.65, df=34, r2=0.400, p<0.001).*

8.3. Bridging structure and function

In contrast with previous "static" characterisation of functional changes, in *Chapter 7* I examined how dynamic patterns of functional connectivity change in PD with hallucinations. PD-hallucinators showed changes affecting primarily regions of high controllability, which are important for switching the brain between states. PD-hallucinators spent more time in a more segregated functional sub-state; this is in keeping with prior work in PD with cognitive impairment (Fiorenzato *et al.*, 2019). Time spent in this segregated state was correlated with hallucination severity suggesting that this finding is specific to presence of hallucinations.

To provide a link on how structural changes may lead to changes in brain function, in *Chapter 6*, I showed that PD patients with visual hallucinations show widespread changes in structural connectivity between brain regions, particularly affecting highly connected brain regions that are important for switching the brain between different states. Building further on this on *Chapter 7*, I modelled the transition of the structural connectome between specific states of functional connectivity. I showed that the observed changes in dynamic functional connectivity seen in patients with PD could be potentially explained by changes in the structural connectome as PD with hallucinations needed less energy to transition to a segregated connectivity state and therefore this transition may be preferred.

By linking the regions most important for this transition to regional differences in neurotransmitter density profiles and receptor gene expression, I was able in *Chapter 7*, to identify specific neurotransmitters that may be important in modulating hallucinations in PD: *5HT2A* has a established role in visual hallucinations (Cheng *et al.*, 1991; Huot *et al.*, 2010) but other receptors identified such as *5HT1B* and *GABA*, as well as noradrenergic receptors (*ADRA1B* and *ADRA2A*) have not been clearly

linked to PD-hallucinations previously. This finding could inform future research into the role of these receptors in PD-hallucinations which could be potential novel therapeutic targets.

Finally, whilst assessing changes in dynamic functional states and modelling the structural connectome's transition between these states has provided useful insights in the healthy brain (Braun *et al.*, 2019; Cornblath *et al.*, 2020), this was the first application of these methods in disease. Similar methods could provide important insights into other symptoms, particularly transient and unpredictable symptoms, such as visual hallucinations, where dynamic approaches are more suitable. I plan to apply this framework to better understand the temporal dynamics of cognitive fluctuations in Dementia with Lewy Bodies (DLB).

Cognitive fluctuations are particularly common and distressing in DLB (Walker *et al.*, 2015) and are thought to be secondary to changes in attentional circuitry and the ability of switching the brain between states (Matar *et al.*, 2020). Changes in temporal functional dynamics have been described in DLB (Schumacher *et al.*, 2019) and Parkinson's dementia (Fiorenzato *et al.*, 2019), but their relationship with cognitive fluctuations and underlying structural changes are unclear. Identifying key regions for these temporal alterations and their neurotransmitter, gene expression and cyto-architectural profiles could provide important new insights to cognitive fluctuations.

The methodology described in *Chapter 7*, investigating the temporal dynamic changes associated with visual hallucinations in PD, has significant potential to shed lights into cognitive fluctuations as well, given that these are similarly transient and unpredictable. In future work, I plan to use established measures of cognitive fluctuations in DLB, such as the Clinician Assessment of Fluctuation (CAF) (Walker *et al.*, 2000) and Dementia

Cognitive Fluctuation Scales (DCFS) (Lee *et al.*, 2014) to assess how changes in brain structure and connectivity lead to altered functional state dynamics in DLB. As described in *Chapter 7*, I plan to link these findings with neurotransmitter systems using: 1) neurotransmitter density profiles from PET-derived atlases using JuSpace (Dukart *et al.*, 2021) and2) regional gene expression data from the Allen Institute Brain Atlas (Hawrylycz *et al.*, 2015),This will shed light onto the neurotransmitter systems that drive cognitive fluctuations in DLB.

8.4. Understanding drivers of regional vulnerability

In a cross-sectional analysis in *Chapter 6*, I showed that brain regions which are vulnerable to white matter connectivity loss in PD with visual hallucinations, show specific gene expression profiles with downweighting of genes related to mRNA metabolism and enriched in oligodendrocyte markers and upweighting of genes related to protein localisation and enriched in neuronal markers. This provides important insights to biological processes and cell types driving regional vulnerability.

Using similar methodology, I was able to assess regional white matter vulnerability in patients with PD who are at high risk of dementia (Zarkali *et al.*, 2020) (*Figure 8.3*). I found that connection type and gene expression profiles affected regional vulnerability with interhemispheric connections and regions with higher expression of genes related to metabolic processes and neuronal markers being most affected (Zarkali *et al.*, 2020). Subsequently, other work in our group has applied this to iron deposition in the same population (Thomas *et al.*, 2021).

Building further on these findings, I plan to link changes in cortical layers identified using 7T imaging (*see Chapter 8.1 Next Steps*) to understand the

neurotransmitter systems, cell types and molecular processes that drive regional vulnerability at the cortical layer level. To do this I will use layer specific data on cellular composition and neurotransmitter receptor maps from healthy human brains using BigBrain (Xiao *et al.*, 2019). By correlating this rich dataset with cortical layer changes underlying PD-hallucinations I will be able to provide insights on the drivers of regional vulnerability and potential modulating neurotransmitter systems at a finer grained level than our current understanding.

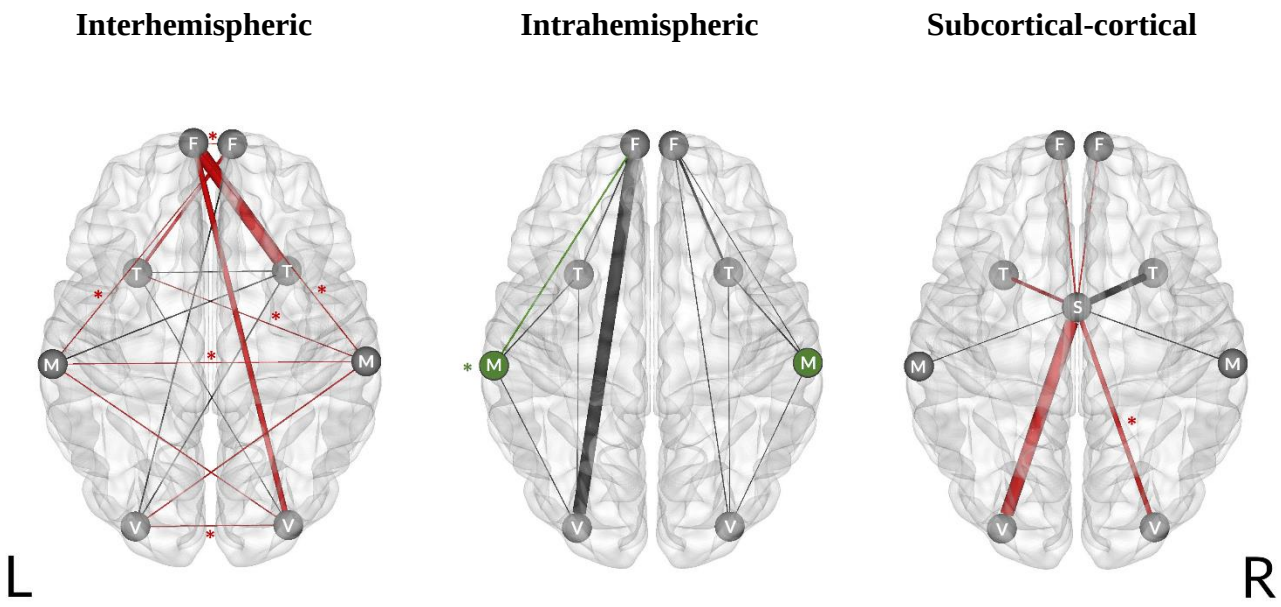

Figure 8. 2. Hierarchy of connection vulnerability in PD with low visual performance (higher risk of dementia).

Figure illustrates the individual connections showing changes in connectivity strength in PD low visual performers. Interhemispheric connections are most affected, followed by subcortical-cortical connections, with intrahemispheric and intramodular connections showing preserved connectivity strength. The thickness of the line represents absolute effect size (difference in connectivity strength in PD low visual performers compared to those with intact vision).

Red: Reduced connectivity strength, Green: Increased connectivity strength, Grey: No significant difference in connectivity strength. F: frontal, T: temporal; M: motor-parietal; V: occipital, B: Subcortical.

8.5. Conclusions

The work described in this thesis showed, for the first time, that patients with Parkinson's disease and visual hallucinations over-rely on feedback signals, with overweighting of prior knowledge when viewing ambiguous visual stimuli. In addition, it shed light in the underlying changes in white matter structure at the tract and network level, and longitudinally, linking the imbalance of feedforward and feedback signals to underlying structural connectivity changes. This furthers our understanding on the neural mechanisms of visual hallucinations in Parkinson's disease and will have implications for other disorders where hallucinations are prominent (Corlett *et al.*, 2019; Haarsma *et al.*, 2020).

In addition, this thesis has provided further support to the important role white matter changes play in Parkinson's hallucinations and in neurodegeneration in Parkinson's disease in general. Whilst gray matter remained relatively preserved longitudinally, white matter showed significant macrostructural changes. This finding, will have implications to future neuroimaging studies as it highlights the increased sensitivity of diffusion weighted imaging compared to imaging techniques assessing grey matter in Parkinson's. Indeed other groups have also described white matter changes in PD using fixel based analysis (Rau *et al.*, 2019).

In this thesis I was able to apply emerging frameworks such as network control theory to directly examine the effect structural connectivity changes have on brain function. Whilst this has been applied in health previously (Braun *et al.*, 2019; Cornblath *et al.*, 2020; Cui *et al.*, 2020), this was the first time that it was used in the context of neurodegeneration. This methodology could be applied to other neurological and psychiatric diseases in order to better understand the interplay between structural changes caused by brain pathology and functional activation patterns.

Finally this thesis could inform potential therapeutic targets for Parkinson's hallucinations. The medial mediodorsal thalamic subnucleus which was identified as a region showing white and, later, gray matter changes in Parkinson's patients with hallucinations (with changes correlating with hallucination severity), could be targeted with deep brain stimulation. Specific neurotransmitter receptors that were found to play an important role in state transitions in PD with hallucinations, such as 5HT2A, $GABA_A$, and noradrenergic receptors could also be potential therapeutic targets.

8.6. Future directions

This thesis aimed to shed light to the neural correlates of visual hallucinations in Parkinson's disease and clarify the changes in large scale brain networks that lead to the development of hallucinations. In doing so, several important questions have evolved. These were discussed in part in this Chapter but are summarised here:

1. At which level of the cortical hierarchy does the imbalance between structural and functional connectivity occur?

2. Could the network level changes (computational, structural and functional) precede the onset of visual hallucinations, therefore enabling their use as a potential biomarker?

3. Are the mechanisms of visual hallucinations transdiagnostic or disease specific?

4. Do similar changes underly other transient symptoms in Lewy Body disorders, such as cognitive fluctuations?

5. What is the underlying cause of white matter loss in Parkinson's hallucinations: axonal degeneration or demyelination?

Answering these questions will have important implications for our mechanistic understanding of visual hallucinations and neurodegeneration in Parkinson's disease and potential future therapies for this distressing symptom of Parkinson's disease as well as other conditions.

9. Bibliography

Aarsland D, Brønnick K, Ehrt U, De Deyn PP, Tekin S, Emre M, et al. Neuropsychiatric symptoms in patients with Parkinson's disease and dementia: frequency, profile and associated care giver stress. J Neurol Neurosurg Psychiatry 2007; 78: 36–42.

Aarsland D, Larsen JP, Tandberg E, Laake K. Predictors of nursing home placement in Parkinson's disease: a population-based, prospective study. J Am Geriatr Soc 2000; 48: 938–42.

Abós A, Baggio HC, Segura B, García-Díaz AI, Compta Y, Martí MJ, et al. Discriminating cognitive status in Parkinson's disease through functional connectomics and machine learning. Sci Rep 2017; 7: 45347.

Adams RA, Stephan KE, Brown HR, Frith CD, Friston KJ. The computational anatomy of psychosis. Front Psychiatry 2013; 4: 47.

Agosta F, Canu E, Stefanova E, Sarro L, Tomić A, Špica V, et al. Mild cognitive impairment in Parkinson's disease is associated with a distributed pattern of brain white matter damage. Hum Brain Mapp 2014; 35: 1921–9.

Alakurtti K, Johansson JJ, Joutsa J, Laine M, Bäckman L, Nyberg L, et al. Long-term test-retest reliability of striatal and extrastriatal dopamine D2/3 receptor binding: study with [(11)C]raclopride and high-resolution PET. J Cereb Blood Flow Metab Off J Int Soc Cereb Blood Flow Metab 2015; 35: 1199–205.

Alderson-Day B, Lima CF, Evans S, Krishnan S, Shanmugalingam P, Fernyhough C, et al. Distinct processing of ambiguous speech in people with non-clinical auditory verbal hallucinations. Brain J Neurol 2017; 140: 2475–89.

Allen EA, Damaraju E, Plis SM, Erhardt EB, Eichele T, Calhoun VD. Tracking Whole-Brain Connectivity Dynamics in the Resting State. Cereb Cortex 2014; 24: 663–76.

Alvarez-Erviti L, Seow Y, Schapira AH, Gardiner C, Sargent IL, Wood MJA, et al. Lysosomal dysfunction increases exosome-mediated alpha-synuclein release and transmission. Neurobiol Dis 2011; 42: 360–7.

Anastasiades PG, Collins DP, Carter AG. Mediodorsal and Ventromedial Thalamus Engage Distinct L1 Circuits in the Prefrontal Cortex. Neuron 2021; 109: 314-330.e4.

Andersson JLR, Skare S, Ashburner J. How to correct susceptibility distortions in spin-echo echo-planar images: application to diffusion tensor imaging. NeuroImage 2003; 20: 870–88.

Andersson JLR, Sotiropoulos SN. An integrated approach to correction for off-resonance effects and subject movement in diffusion MR imaging. NeuroImage 2016; 125: 1063–78.

Anticevic A, Cole MW, Repovs G, Murray JD, Brumbaugh MS, Winkler AM, et al. Characterizing Thalamo-Cortical Disturbances in Schizophrenia and Bipolar Illness. Cereb Cortex 2014; 24: 3116–30.

Arloth J, Bader DM, Röh S, Altmann A. Re-Annotator: Annotation Pipeline for Microarray Probe Sequences. PLOS ONE 2015; 10: e0139516.

Arnatkevic Iūtė A, Fulcher BD, Fornito A. A practical guide to linking brain-wide gene expression and neuroimaging data. NeuroImage 2019; 189: 353–67.

Arnulf I, Bonnet AM, Damier P, Bejjani BP, Seilhean D, Derenne JP, et al. Hallucinations, REM sleep, and Parkinson's disease: a medical hypothesis. Neurology 2000; 55: 281–8.

Atkinson D, Hill DL, Stoyle PN, Summers PE, Keevil SF. Automatic correction of motion artifacts in magnetic resonance images using an entropy focus criterion. IEEE Trans Med Imaging 1997; 16: 903–10.

Baggio HC, Segura B, Junque C. Resting-state functional brain networks in Parkinson's disease. CNS Neurosci Ther 2015; 21: 793–801.

Barnes J, Boubert L, Harris J, Lee A, David AS. Reality monitoring and visual hallucinations in Parkinson's disease. Neuropsychologia 2003; 41: 565–74.

Barnes J, David AS. Visual hallucinations in Parkinson's disease: a review and phenomenological survey. J Neurol Neurosurg Psychiatry 2001; 70: 727–33.

Bastos AM, Vezoli J, Bosman CA, Schoffelen J-M, Oostenveld R, Dowdall JR, et al. Visual areas exert feedforward and feedback influences through distinct frequency channels. Neuron 2015; 85: 390–401.

Baum GL, Cui Z, Roalf DR, Ciric R, Betzel RF, Larsen B, et al. Development of structure–function coupling in human brain networks during youth. Proc Natl Acad Sci U S A 2020; 117: 771–8.

Behzadi Y, Restom K, Liau J, Liu TT. A component based noise correction method (CompCor) for BOLD and perfusion based fMRI. NeuroImage 2007; 37: 90–101.

Bejr-Kasem H, Pagonabarraga J, Martínez-Horta S, Sampedro F, Marín-Lahoz J, Horta-Barba A, et al. Disruption of the default mode network and its intrinsic functional connectivity underlies minor hallucinations in Parkinson's disease. Mov Disord Off J Mov Disord Soc 2019; 34: 78–86.

Benton AL, Varney NR, Hamsher K deS. Visuospatial Judgment: A Clinical Test. Arch Neurol 1978; 35: 364–7.

Bernhardt BC, Fadaie F, Liu M, Caldairou B, Gu S, Jefferies E, et al. Temporal lobe epilepsy: Hippocampal pathology modulates connectome topology and controllability. Neurology 2019; 92: e2209–20.

Bernard A, Lubbers LS, Tanis KQ, Luo R, Podtelezhnikov AA, Finney EM, et al. Transcriptional Architecture of the Primate Neocortex. Neuron 2012; 73: 1083–99.

Bernasconi F, Blondiaux E, Potheegadoo J, Stripeikyte G, Pagonabarraga J, Bejr-Kasem H, et al. Robot-induced hallucinations in Parkinson's disease depend on altered sensorimotor processing in fronto-temporal network [Internet]. Sci Transl Med 2021; 13[cited 2021 Jun 14] Available from: https://stm.sciencemag.org/content/13/591/eabc8362

Betzel RF, Byrge L, He Y, Goñi J, Zuo X-N, Sporns O. Changes in structural and functional connectivity among resting-state networks across the human lifespan. NeuroImage 2014; 102 Pt 2: 345–57.

Betzel RF, Gu S, Medaglia JD, Pasqualetti F, Bassett DS. Optimally controlling the human connectome: the role of network topology. Sci Rep 2016; 6: 30770.

Bjelland I, Dahl AA, Haug TT, Neckelmann D. The validity of the Hospital Anxiety and Depression Scale. An updated literature review. J Psychosom Res 2002; 52: 69–77.

Biglan KM, Holloway RG, McDermott MP, Richard IH, Parkinson Study Group CALM-PD Investigators. Risk factors for somnolence, edema, and hallucinations in early Parkinson disease. Neurology 2007; 69: 187–95.

Biswal B, Yetkin FZ, Haughton VM, Hyde JS. Functional connectivity in the motor cortex of resting human brain using echo-planar MRI. Magn Reson Med 1995; 34: 537–41.

Boes AD, Prasad S, Liu H, Liu Q, Pascual-Leone A, Caviness VS, et al. Network localization of neurological symptoms from focal brain lesions. Brain 2015; 138: 3061–75.

Bonanni L, Thomas A, Tiraboschi P, Perfetti B, Varanese S, Onofrj M. EEG comparisons in early Alzheimer's disease, dementia with Lewy bodies and Parkinson's disease with dementia patients with a 2-year follow-up. Brain J Neurol 2008; 131: 690–705.

Botía JA, Vandrovcova J, Forabosco P, Guelfi S, D'Sa K, United Kingdom Brain Expression Consortium, et al. An additional k-means clustering step improves the biological features of WGCNA gene co-expression networks. BMC Syst Biol 2017; 11: 47.

Braun U, Harneit A, Pergola G, Menara T, Schaefer A, Betzel RF, et al. Brain state stability during working memory is explained by network control theory, modulated by dopamine D1/D2 receptor function, and diminished in schizophrenia. bioRxiv 2019: 679670.

Brockmann K, Srulijes K, Hauser AK, Schulte C, Csoti I, Gasser T, et al. GBA-associated PD presents with nonmotor characteristics. Neurology 2011; 77: 276–80.

Bryois J, Skene NG, Hansen TF, Kogelman L, Watson HJ, Consortium EDWG of the PG, et al. Genetic Identification of Cell Types Underlying Brain Complex Traits Yields Novel Insights Into the Etiology of Parkinson's Disease. bioRxiv 2019: 528463.

Bullmore E, Sporns O. Complex brain networks: graph theoretical analysis of structural and functional systems. Nat Rev Neurosci 2009; 10: 186–98.

Butler AA, Johnston DR, Kaur S, Lubin FD. Long noncoding RNA NEAT1 mediates neuronal histone methylation and age-related memory impairment [Internet]. Sci Signal 2019; 12[cited 2019 Nov 11] Available from: https://stke.sciencemag.org/content/12/588/eaaw9277

Callard F, Margulies DS. What we talk about when we talk about the default mode network [Internet]. Front Hum Neurosci 2014; 8[cited 2021 Jun 14] Available from: https://www.frontiersin.org/articles/10.3389/fnhum.2014.00619/full

Carhart-Harris RL, Muthukumaraswamy S, Roseman L, Kaelen M, Droog W, Murphy K, et al. Neural correlates of the LSD experience revealed by multimodal neuroimaging. Proc Natl Acad Sci 2016; 113: 4853–8.

Carpenter AE, Sabatini DM. Systematic genome-wide screens of gene function. Nat Rev Genet 2004; 5: 11–22.

Cassidy CM, Balsam PD, Weinstein JJ, Rosengard RJ, Slifstein M, Daw ND, et al. A Perceptual Inference Mechanism for Hallucinations Linked to Striatal Dopamine. Curr Biol 2018; 28: 503-514.e4.

Cavanagh P. Visual cognition. Vision Res 2011; 51: 1538–51.

Cedar H, Bergman Y. Linking DNA methylation and histone modification: patterns and paradigms. Nat Rev Genet 2009; 10: 295–304.

Chang C, Glover GH. Time–frequency dynamics of resting-state brain connectivity measured with fMRI. NeuroImage 2010; 50: 81–98.

Cheng AV, Ferrier IN, Morris CM, Jabeen S, Sahgal A, McKeith IG, et al. Cortical serotonin-S2 receptor binding in Lewy body dementia, Alzheimer's and Parkinson's diseases. J Neurol Sci 1991; 106: 50–5.

Chung CY, Koprich JB, Siddiqi H, Isacson O. Dynamic changes in presynaptic and axonal transport proteins combined with striatal neuroinflammation precede dopaminergic neuronal loss in a rat model of AAV alpha-synucleinopathy. J Neurosci Off J Soc Neurosci 2009; 29: 3365–73.

Chung JW, Burciu RG, Ofori E, Shukla P, Okun MS, Hess CW, et al. Parkinson's disease diffusion MRI is not affected by acute antiparkinsonian medication. NeuroImage Clin 2017; 14: 417–21.

Clegg BJ, Duncan GW, Khoo TK, Barker RA, Burn DJ, Yarnall AJ, et al. Categorising Visual Hallucinations in Early Parkinson's Disease. J Park Dis 2018; 8: 447–53.

Cocchi L, Harding IH, Lord A, Pantelis C, Yucel M, Zalesky A. Disruption of structure–function coupling in the schizophrenia connectome. NeuroImage Clin 2014; 4: 779–87.

Compta Y, Parkkinen L, O'Sullivan SS, Vandrovcova J, Holton JL, Collins C, et al. Lewy- and Alzheimer-type pathologies in Parkinson's disease dementia: which is more important? Brain J Neurol 2011; 134: 1493–505.

Corlett PR, Horga G, Fletcher PC, Alderson-Day B, Schmack K, Powers AR. Hallucinations and Strong Priors. Trends Cogn Sci 2019; 23: 114–27.

Cordes D, Zhuang X, Kaleem M, Sreenivasan K, Yang Z, Mishra V, et al. Advances in functional magnetic resonance imaging data analysis methods

using Empirical Mode Decomposition to investigate temporal changes in early Parkinson's disease. Alzheimers Dement Transl Res Clin Interv 2018; 4: 372–86.

Cornblath EJ, Ashourvan A, Kim JZ, Betzel RF, Ciric R, Adebimpe A, et al. Temporal sequences of brain activity at rest are constrained by white matter structure and modulated by cognitive demands. Commun Biol 2020; 3: 1–12.

Corlett PR, Horga G, Fletcher PC, Alderson-Day B, Schmack K, Powers AR. Hallucinations and Strong Priors. Trends Cogn Sci 2019; 23: 114–27.

Cox RW. AFNI: Software for Analysis and Visualization of Functional Magnetic Resonance Neuroimages. Comput Biomed Res 1996; 29: 162–73.

Creavin ST, Wisniewski S, Noel-Storr AH, Trevelyan CM, Hampton T, Rayment D, et al. Mini-Mental State Examination (MMSE) for the detection of dementia in clinically unevaluated people aged 65 and over in community and primary care populations [Internet]. Cochrane Database Syst Rev 2016[cited 2019 Feb 15] Available from: https://www.cochranelibrary.com/cdsr/doi/10.1002/14651858.CD011145.pub2/abstract

Cuervo AM, Wong ESP, Martinez-Vicente M. Protein degradation, aggregation, and misfolding. Mov Disord Off J Mov Disord Soc 2010; 25 Suppl 1: S49-54.

Cui Z, Stiso J, Baum GL, Kim JZ, Roalf DR, Betzel RF, et al. Optimization of energy state transition trajectory supports the development of executive function during youth. eLife 2020; 9: e53060.

Cummings J, Isaacson S, Mills R, Williams H, Chi-Burris K, Corbett A, et al. Pimavanserin for patients with Parkinson's disease psychosis: a randomised, placebo-controlled phase 3 trial. Lancet Lond Engl 2014; 383: 533–40.

Currie S, Hoggard N, Craven IJ, Hadjivassiliou M, Wilkinson ID. Understanding MRI: basic MR physics for physicians. Postgrad Med J 2013; 89: 209–23.

Dahl MJ, Mather M, Sander MC, Werkle-Bergner M. Noradrenergic Responsiveness Supports Selective Attention across the Adult Lifespan. J Neurosci 2020; 40: 4372–90.

Dalrymple-Alford JC, MacAskill MR, Nakas CT, Livingston L, Graham C, Crucian GP, et al. The MoCA: well-suited screen for cognitive impairment in Parkinson disease. Neurology 2010; 75: 1717–25.

Dauwan M, Hoff JI, Vriens EM, Hillebrand A, Stam CJ, Sommer IE. Aberrant resting-state oscillatory brain activity in Parkinson's disease patients with visual hallucinations: An MEG source-space study. NeuroImage Clin 2019; 22: 101752.

Davidsdottir S, Cronin-Golomb A, Lee A. Visual and spatial symptoms in Parkinson's disease. Vision Res 2005; 45: 1285–96.

Davies DJ, Teufel C, Fletcher PC. Anomalous Perceptions and Beliefs Are Associated With Shifts Toward Different Types of Prior Knowledge in Perceptual Inference. Schizophr Bull 2018; 44: 1245–53.

Damaraju E, Allen EA, Belger A, Ford JM, McEwen S, Mathalon DH, et al. Dynamic functional connectivity analysis reveals transient states of dysconnectivity in schizophrenia. NeuroImage Clin 2014; 5: 298–308.

Dell'Acqua F, Tournier J-D. Modelling white matter with spherical deconvolution: How and why? NMR Biomed 2019; 32: e3945.

Deng B, Zhang Y, Wang L, Peng K, Han L, Nie K, et al. Diffusion tensor imaging reveals white matter changes associated with cognitive status in patients with Parkinson's disease. Am J Alzheimers Dis Other Demen 2013; 28: 154–64.

Diederich NJ, Goetz CG, Stebbins GT. Repeated visual hallucinations in Parkinson's disease as disturbed external/internal perceptions: focused review and a new integrative model. Mov Disord Off J Mov Disord Soc 2005; 20: 130–40.

Díez-Cirarda M, Strafella AP, Kim J, Peña J, Ojeda N, Cabrera-Zubizarreta A, et al. Dynamic functional connectivity in Parkinson's disease patients with mild cognitive impairment and normal cognition. NeuroImage Clin 2018; 17: 847–55.

Dolan RJ, Fink GR, Rolls E, Booth M, Holmes A, Frackowiak RS, et al. How the brain learns to see objects and faces in an impoverished context. Nature 1997; 389: 596–9.

Doyle KM, Kennedy D, Gorman AM, Gupta S, Healy SJM, Samali A. Unfolded proteins and endoplasmic reticulum stress in neurodegenerative disorders. J Cell Mol Med 2011; 15: 2025–39.

Dukart J, Holiga Š, Chatham C, Hawkins P, Forsyth A, McMillan R, et al. Cerebral blood flow predicts differential neurotransmitter activity. Sci Rep 2018; 8: 4074.

Dukart J, Holiga S, Rullmann M, Lanzenberger R, Hawkins PCT, Mehta MA, et al. JuSpace: A tool for spatial correlation analyses of magnetic resonance imaging data with nuclear imaging derived neurotransmitter maps. Hum Brain Mapp 2021; 42: 555–66.

Duncan GW, Firbank MJ, Yarnall AJ, Khoo TK, Brooks DJ, Barker RA, et al. Gray and white matter imaging: A biomarker for cognitive impairment in early Parkinson's disease? Mov Disord 2016; 31: 103–10.

Emre M, Aarsland D, Brown R, Burn DJ, Duyckaerts C, Mizuno Y, et al. Clinical diagnostic criteria for dementia associated with Parkinson's disease. Mov Disord Off J Mov Disord Soc 2007; 22: 1689–707; quiz 1837.

Erskine D, Taylor J-P, Thomas A, Collerton D, McKeith I, Khundakar A, et al. Pathological Changes to the Subcortical Visual System and its Relationship to Visual Hallucinations in Dementia with Lewy Bodies. Neurosci Bull 2019

Esteban O, Birman D, Schaer M, Koyejo OO, Poldrack RA, Gorgolewski KJ. MRIQC: Advancing the automatic prediction of image quality in MRI from unseen sites. PloS One 2017; 12: e0184661.

Esteban O, Markiewicz CJ, Blair RW, Moodie CA, Isik AI, Erramuzpe A, et al. fMRIPrep: a robust preprocessing pipeline for functional MRI. Nat Methods 2019; 16: 111–6.

Farnsworth Dean. The Farnsworth dichotomous test for color blindness, panel D-15: manual [Internet]. New York: Psychological Corp.; 1947[cited 2019 Jan 23] Available from: https://catalog.hathitrust.org/Record/102201930

Feldman H, Friston KJ. Attention, uncertainty, and free-energy. Front Hum Neurosci 2010; 4: 215.

Fénelon G, Mahieux F, Huon R, Ziégler M. Hallucinations in Parkinson's disease: prevalence, phenomenology and risk factors. Brain J Neurol 2000; 123 (Pt 4): 733–45.

Fénelon G, Soulas T, Cleret de Langavant L, Trinkler I, Bachoud-Lévi A-C. Feeling of presence in Parkinson's disease. J Neurol Neurosurg Psychiatry 2011; 82: 1219–24.

Fereshtehnejad S-M, Yao C, Pelletier A, Montplaisir JY, Gagnon J-F, Postuma RB. Evolution of prodromal Parkinson's disease and dementia with Lewy bodies: a prospective study [Internet]. Brain 2019[cited 2019 May 28] Available from: https://academic.oup.com/brain/advance-article/doi/10.1093/brain/awz111/5492352

ffytche DH, Creese B, Politis M, Chaudhuri KR, Weintraub D, Ballard C, et al. The psychosis spectrum in Parkinson disease. Nat Rev Neurol 2017; 13: 81–95.

Ffytche DH, Pereira JB, Ballard C, Chaudhuri KR, Weintraub D, Aarsland D. Risk factors for early psychosis in PD: insights from the Parkinson's Progression Markers Initiative. J Neurol Neurosurg Psychiatry 2017; 88: 325–31.

Fischl B, Sereno MI, Dale AM. Cortical surface-based analysis. II: Inflation, flattening, and a surface-based coordinate system. NeuroImage 1999; 9: 195–207.

Fiorenzato E, Strafella AP, Kim J, Schifano R, Weis L, Antonini A, et al. Dynamic functional connectivity changes associated with dementia in Parkinson's disease. Brain 2019; 142: 2860–72.

Firbank MJ, Parikh J, Murphy N, Killen A, Allan CL, Collerton D, et al. Reduced occipital GABA in Parkinson disease with visual hallucinations. Neurology 2018; 91: e675–85.

Fischl B, Salat DH, Busa E, Albert M, Dieterich M, Haselgrove C, et al. Whole brain segmentation: automated labeling of neuroanatomical structures in the human brain. Neuron 2002; 33: 341–55.

Fletcher PC, Frith CD. Perceiving is believing: a Bayesian approach to explaining the positive symptoms of schizophrenia. Nat Rev Neurosci 2009; 10: 48–58.

Fornito A, Arnatkevičiūtė A, Fulcher BD. Bridging the Gap between Connectome and Transcriptome. Trends Cogn Sci 2019; 23: 34–50.

Franciotti R, Delli Pizzi S, Perfetti B, Tartaro A, Bonanni L, Thomas A, et al. Default mode network links to visual hallucinations: A comparison between Parkinson's disease and multiple system atrophy. Mov Disord Off J Mov Disord Soc 2015; 30: 1237–47.

Freeze B, Acosta D, Pandya S, Zhao Y, Raj A. Regional expression of genes mediating trans-synaptic alpha-synuclein transfer predicts regional atrophy in Parkinson disease. NeuroImage Clin 2018; 18: 456–66.

Freeze B, Pandya S, Zeighami Y, Raj A. Regional transcriptional architecture of Parkinson's disease pathogenesis and network spread. Brain 2019; 142: 3072–85.

Friston K, Kiebel S. Predictive coding under the free-energy principle. Philos Trans R Soc Lond B Biol Sci 2009; 364: 1211–21.

Fukushima M, Betzel RF, He Y, van den Heuvel MP, Zuo X-N, Sporns O. Structure-function relationships during segregated and integrated network states of human brain functional connectivity. Brain Struct Funct 2018; 223: 1091–106.

Gallagher DA, Parkkinen L, O'Sullivan SS, Spratt A, Shah A, Davey CC, et al. Testing an aetiological model of visual hallucinations in Parkinson's disease. Brain J Neurol 2011; 134: 3299–309.

Galvin JE, Pollack J, Morris JC. Clinical phenotype of Parkinson disease dementia. Neurology 2006; 67: 1605–11.

Ganzetti M, Wenderoth N, Mantini D. Intensity Inhomogeneity Correction of Structural MR Images: A Data-Driven Approach to Define Input Algorithm Parameters [Internet]. Front Neuroinformatics 2016; 10[cited 2019 Dec 19] Available from: https://www.frontiersin.org/articles/10.3389/fninf.2016.00010/full

Geyer MA, Vollenweider FX. Serotonin research: contributions to understanding psychoses. Trends Pharmacol Sci 2008; 29: 445–53.

Gibb WR, Lees AJ. The relevance of the Lewy body to the pathogenesis of idiopathic Parkinson's disease. J Neurol Neurosurg Psychiatry 1988; 51: 745–52.

Gispert JD, Reig S, Pascau J, Vaquero JJ, García-Barreno P, Desco M. Method for bias field correction of brain T1-weighted magnetic resonance images minimizing segmentation error. Hum Brain Mapp 2004; 22: 133–44.

Glasser MF, Coalson TS, Robinson EC, Hacker CD, Harwell J, Yacoub E, et al. A multi-modal parcellation of human cerebral cortex. Nature 2016; 536: 171–8.

Goetz CG, Stebbins GT. Mortality and hallucinations in nursing home patients with advanced Parkinson's disease. Neurology 1995; 45: 669–71.

Goldman JG, Stebbins GT, Dinh V, Bernard B, Merkitch D, deToledo-Morrell L, et al. Visuoperceptive region atrophy independent of cognitive

status in patients with Parkinson’s disease with hallucinations. Brain 2014; 137: 849–59.

Goetz CG, Tilley BC, Shaftman SR, Stebbins GT, Fahn S, Martinez-Martin P, et al. Movement Disorder Society-sponsored revision of the Unified Parkinson’s Disease Rating Scale (MDS-UPDRS): scale presentation and clinimetric testing results. Mov Disord Off J Mov Disord Soc 2008; 23: 2129–70.

Graham MS, Drobnjak I, Zhang H. Realistic simulation of artefacts in diffusion MRI for validating post-processing correction techniques. NeuroImage 2016; 125: 1079–94.

Grazioplene RG, Bearden CE, Subotnik KL, Ventura J, Haut K, Nuechterlein KH, et al. Connectivity-enhanced diffusion analysis reveals white matter density disruptions in first episode and chronic schizophrenia. NeuroImage Clin 2018; 18: 608–16.

Greer EL, Shi Y. Histone methylation: a dynamic mark in health, disease and inheritance. Nat Rev Genet 2012; 13: 343–57.

Greve DN, Fischl B. Accurate and robust brain image alignment using boundary-based registration. NeuroImage 2009; 48: 63–72.

Goñi J, Heuvel MP van den, Avena-Koenigsberger A, Mendizabal NV de, Betzel RF, Griffa A, et al. Resting-brain functional connectivity predicted by analytic measures of network communication. Proc Natl Acad Sci 2014; 111: 833–8.

Gu S, Betzel RF, Mattar MG, Cieslak M, Delio PR, Grafton ST, et al. Optimal trajectories of brain state transitions. NeuroImage 2017; 148: 305–17.

Gu S, Pasqualetti F, Cieslak M, Telesford QK, Yu AB, Kahn AE, et al. Controllability of structural brain networks. Nat Commun 2015; 6: 1–10.

Habib N, Avraham-Davidi I, Basu A, Burks T, Shekhar K, Hofree M, et al. Massively parallel single-nucleus RNA-seq with DroNc-seq. Nat Methods 2017; 14: 955–8.

Hagmann P, Jonasson L, Maeder P, Thiran J-P, Wedeen VJ, Meuli R. Understanding diffusion MR imaging techniques: from scalar diffusion-weighted imaging to diffusion tensor imaging and beyond. Radiogr Rev Publ Radiol Soc N Am Inc 2006; 26 Suppl 1: S205-223.

Hagmann P, Sporns O, Madan N, Cammoun L, Pienaar R, Wedeen VJ, et al. White matter maturation reshapes structural connectivity in the late developing human brain. Proc Natl Acad Sci 2010; 107: 19067–72.

Hall JM, O'Callaghan C, Muller AJ, Ehgoetz Martens KA, Phillips JR, Moustafa AA, et al. Changes in structural network topology correlate with severity of hallucinatory behavior in Parkinson's disease. Netw Neurosci 2019; 3: 521–38.

Halliday GM. Thalamic changes in Parkinson's disease. Parkinsonism Relat Disord 2009; 15: S152–5.

Hamedani AG, Abraham DS, Maguire MG, Willis AW. Visual Impairment Is More Common in Parkinson's Disease and Is a Risk Factor for Poor Health Outcomes. Mov Disord Off J Mov Disord Soc 2020

Han G, Han J, Han K, Youn J, Chung T-Y, Lim DH. Visual Acuity and Development of Parkinson's Disease: A Nationwide Cohort Study. Mov Disord 2020; 35: 1532–41.

Hannum G, Guinney J, Zhao L, Zhang L, Hughes G, Sadda S, et al. Genome-wide methylation profiles reveal quantitative views of human aging rates. Mol Cell 2013; 49: 359–67.

Hansson M, Chotai J, Nordstöm A, Bodlund O. Comparison of two self-rating scales to detect depression: HADS and PHQ-9. Br J Gen Pract 2009; 59: e283–8.

Harding AJ, Broe GA, Halliday GM. Visual hallucinations in Lewy body disease relate to Lewy bodies in the temporal lobe. Brain J Neurol 2002; 125: 391–403.

Hattori N, Yabe I, Hirata K, Shiga T, Sakushima K, Tsuji-Akimoto S, et al. Brain regions associated with cognitive impairment in patients with Parkinson disease: quantitative analysis of cerebral blood flow using 123I iodoamphetamine SPECT. Clin Nucl Med 2013; 38: 315–20.

Hawrylycz M, Miller JA, Menon V, Feng D, Dolbeare T, Guillozet-Bongaarts AL, et al. Canonical genetic signatures of the adult human brain. Nat Neurosci 2015; 18: 1832–44.

Heeger DJ, Ress D. What does fMRI tell us about neuronal activity? Nat Rev Neurosci 2002; 3: 142–51.

Hegdé J, Kersten D. A Link between Visual Disambiguation and Visual Memory. J Neurosci Off J Soc Neurosci 2010; 30: 15124–33.

Hely MA, Reid WGJ, Adena MA, Halliday GM, Morris JGL. The Sydney multicenter study of Parkinson's disease: the inevitability of dementia at 20 years. Mov Disord Off J Mov Disord Soc 2008; 23: 837–44.

Hepp DH, Foncke EMJ, Berendse HW, Wassenaar TM, Dubbelink KTEO, Groenewegen HJ, et al. Damaged fiber tracts of the nucleus basalis of Meynert in Parkinson's disease patients with visual hallucinations. Sci Rep 2017; 7: 10112.

Hepp DH, Foncke EMJ, Olde Dubbelink KTE, van de Berg WDJ, Berendse HW, Schoonheim MM. Loss of Functional Connectivity in Patients with Parkinson Disease and Visual Hallucinations. Radiology 2017; 285: 896–903.

Hillman EMC. Coupling Mechanism and Significance of the BOLD Signal: A Status Report. Annu Rev Neurosci 2014; 37: 161–81.

Hobson P, Meara J. Risk and incidence of dementia in a cohort of older subjects with Parkinson's disease in the United Kingdom. Mov Disord Off J Mov Disord Soc 2004; 19: 1043–9.

Holland D, Kuperman JM, Dale AM. Efficient correction of inhomogeneous static magnetic field-induced distortion in Echo Planar Imaging. NeuroImage 2010; 50: 175–83.

Hollander, T., Raffelt D, Connelly A. Unsupervised 3-tissue response function estimation from single-shell or multi-shell diffusion MR data without a co-registered T1 image. ISMRM Workshop Break Barriers Diffus MRI 2016: 5.

Honey CJ, Sporns O, Cammoun L, Gigandet X, Thiran JP, Meuli R, et al. Predicting human resting-state functional connectivity from structural connectivity. Proc Natl Acad Sci U S A 2009; 106: 2035–40.

Hooper H. Hooper Visual Organization Test (VOT) Manual. Los Angeles: CA: Western Psychological Services; 1983

Hsieh P-J, Vul E, Kanwisher N. Recognition alters the spatial pattern of FMRI activation in early retinotopic cortex. J Neurophysiol 2010; 103: 1501–7.

Hua K, Zhang J, Wakana S, Jiang H, Li X, Reich DS, et al. Tract Probability Maps in Stereotaxic Spaces: Analyses of White Matter Anatomy and Tract-Specific Quantification. NeuroImage 2008; 39: 336–47.

Hummel T, Sekinger B, Wolf SR, Pauli E, Kobal G. 'Sniffin' sticks': olfactory performance assessed by the combined testing of odor identification, odor discrimination and olfactory threshold. Chem Senses 1997; 22: 39–52.

Huot P, Johnston TH, Darr T, Hazrati L-N, Visanji NP, Pires D, et al. Increased 5-HT2A receptors in the temporal cortex of parkinsonian patients with visual hallucinations. Mov Disord Off J Mov Disord Soc 2010; 25: 1399–408.

Hutchison RM, Womelsdorf T, Allen EA, Bandettini PA, Calhoun VD, Corbetta M, et al. Dynamic functional connectivity: promise, issues, and interpretations. NeuroImage 2013; 80: 360–78.

Ibarretxe-Bilbao N, Ramirez-Ruiz B, Junque C, Marti MJ, Valldeoriola F, Bargallo N, et al. Differential progression of brain atrophy in Parkinson's disease with and without visual hallucinations. J Neurol Neurosurg Psychiatry 2010; 81: 650–7.

Ibarretxe-Bilbao N, Ramírez-Ruiz B, Tolosa E, Martí MJ, Valldeoriola F, Bargalló N, et al. Hippocampal head atrophy predominance in Parkinson's disease with hallucinations and with dementia. J Neurol 2008; 255: 1324.

Inagawa Y, Kanetaka H, Tsugawa A, Sakurai S, Serisawa S, Shimizu S, et al. Efficacy of Olfactory and Pareidolia Tests Compared With That of Indicative Biomarkers in Diagnosis of Dementia With Lewy Bodies. Front Neurol 2020; 11: 540291.

Iwaki H, Blauwendraat C, Leonard HL, Kim JJ, Liu G, Maple-Grødem J, et al. Genomewide association study of Parkinson's disease clinical biomarkers in 12 longitudinal patients' cohorts. Mov Disord Off J Mov Disord Soc 2019; 34: 1839–50.

Jacobson SA, Morshed T, Dugger BN, Beach TG, Hentz JG, Adler CH, et al. Plaques and tangles as well as Lewy-type alpha synucleinopathy are associated with formed visual hallucinations. Parkinsonism Relat Disord 2014; 20: 1009–14.

Janzen J, van 't Ent D, Lemstra AW, Berendse HW, Barkhof F, Foncke EMJ. The pedunculopontine nucleus is related to visual hallucinations in Parkinson's disease: preliminary results of a voxel-based morphometry study. J Neurol 2012; 259: 147–54.

Jaywant A, Shiffrar M, Roy S, Cronin-Golomb A. Impaired perception of biological motion in Parkinson's disease. Neuropsychology 2016; 30: 720–30.

Jbabdi S, Behrens TEJ, Smith SM. Crossing fibres in tract-based spatial statistics. NeuroImage 2010; 49: 249–56.

Jellinger KA. Neurobiology of cognitive impairment in Parkinson's disease. Expert Rev Neurother 2012; 12: 1451–66.

Jenkinson M, Bannister P, Brady M, Smith S. Improved Optimization for the Robust and Accurate Linear Registration and Motion Correction of Brain Images. NeuroImage 2002; 17: 825–41.

Jeurissen B, Leemans A, Tournier J-D, Jones DK, Sijbers J. Investigating the prevalence of complex fiber configurations in white matter tissue with diffusion magnetic resonance imaging. Hum Brain Mapp 2013; 34: 2747–66.

Jeurissen B, Tournier J-D, Dhollander T, Connelly A, Sijbers J. Multi-tissue constrained spherical deconvolution for improved analysis of multi-shell diffusion MRI data. NeuroImage 2014; 103: 411–26.

Jin C, Jia H, Lanka P, Rangaprakash D, Li L, Liu T, et al. Dynamic brain connectivity is a better predictor of PTSD than static connectivity. Hum Brain Mapp 2017; 38: 4479–96.

Jones DK, Knösche TR, Turner R. White matter integrity, fiber count, and other fallacies: the do's and don'ts of diffusion MRI. NeuroImage 2013; 73: 239–54.

Kaiser RH, Whitfield-Gabrieli S, Dillon DG, Goer F, Beltzer M, Minkel J, et al. Dynamic Resting-State Functional Connectivity in Major Depression. Neuropsychopharmacol Off Publ Am Coll Neuropsychopharmacol 2016; 41: 1822–30.

Kaller S, Rullmann M, Patt M, Becker G-A, Luthardt J, Girbardt J, et al. Test-retest measurements of dopamine D1-type receptors using simultaneous PET/MRI imaging. Eur J Nucl Med Mol Imaging 2017; 44: 1025–32.

Kamagata K, Zalesky A, Hatano T, Ueda R, Di Biase MA, Okuzumi A, et al. Gray Matter Abnormalities in Idiopathic Parkinson's Disease: Evaluation by Diffusional Kurtosis Imaging and Neurite Orientation Dispersion and Density Imaging. Hum Brain Mapp 2017

Karvelis P, Seitz AR, Lawrie SM, Seriès P. Autistic traits, but not schizotypy, predict increased weighting of sensory information in Bayesian visual integration. eLife 2018; 7

Kellner E, Dhital B, Kiselev VG, Reisert M. Gibbs-ringing artifact removal based on local subvoxel-shifts. Magn Reson Med 2016; 76: 1574–81.

Khundakar AA, Hanson PS, Erskine D, Lax NZ, Roscamp J, Karyka E, et al. Analysis of primary visual cortex in dementia with Lewy bodies indicates GABAergic involvement associated with recurrent complex visual hallucinations. Acta Neuropathol Commun 2016; 4: 66.

Kim J, Criaud M, Cho SS, Díez-Cirarda M, Mihaescu A, Coakeley S, et al. Abnormal intrinsic brain functional network dynamics in Parkinson's disease. Brain J Neurol 2017; 140: 2955–67.

Kim NY, Hsu J, Talmasov D, Joutsa J, Soussand L, Wu O, et al. Lesions causing hallucinations localize to one common brain network. Mol Psychiatry 2019: 1–11.

Kim JZ, Soffer JM, Kahn AE, Vettel JM, Pasqualetti F, Bassett DS. Role of graph architecture in controlling dynamical networks with applications to neural systems. Nat Phys 2018; 14: 91–8.

Kok P, Bains LJ, van Mourik T, Norris DG, de Lange FP. Selective Activation of the Deep Layers of the Human Primary Visual Cortex by Top-Down Feedback. Curr Biol CB 2016; 26: 371–6.

Koubiyr I, Besson P, Deloire M, Charre-Morin J, Saubusse A, Tourdias T, et al. Dynamic modular-level alterations of structural-functional coupling in clinically isolated syndrome. Brain 2019; 142: 3428–39.

Krienen FM, Yeo BTT, Ge T, Buckner RL, Sherwood CC. Transcriptional profiles of supragranular-enriched genes associate with corticocortical network architecture in the human brain. Proc Natl Acad Sci 2016; 113: E469–78.

de Lange FP, Heilbron M, Kok P. How Do Expectations Shape Perception? Trends Cogn Sci 2018; 22: 764–79.

Langfelder P, Horvath S. WGCNA: an R package for weighted correlation network analysis. BMC Bioinformatics 2008; 9: 559.

Langfelder P, Luo R, Oldham MC, Horvath S. Is My Network Module Preserved and Reproducible? [Internet]. PLoS Comput Biol 2011; 7[cited

2020 Apr 24] Available from: https://www.ncbi.nlm.nih.gov/pmc/articles/PMC3024255/

Lawrence RE, Zoncu R. The lysosome as a cellular centre for signalling, metabolism and quality control. Nat Cell Biol 2019; 21: 133–42.

Le Bihan D, Mangin JF, Poupon C, Clark CA, Pappata S, Molko N, et al. Diffusion tensor imaging: concepts and applications. J Magn Reson Imaging JMRI 2001; 13: 534–46.

Lee AH, Weintraub D. Psychosis in Parkinson's disease without dementia: common and comorbid with other non-motor symptoms. Mov Disord Off J Mov Disord Soc 2012; 27: 858–63.

Lee DR, McKeith I, Mosimann U, Ghosh-Nodial A, Grayson L, Wilson B, et al. The dementia cognitive fluctuation scale, a new psychometric test for clinicians to identify cognitive fluctuations in people with dementia. Am J Geriatr Psychiatry Off J Am Assoc Geriatr Psychiatry 2014; 22: 926–35.

Lee J-Y, Yoon EJ, Lee WW, Kim YK, Lee J-Y, Jeon B. Lateral geniculate atrophy in Parkinson's with visual hallucination: A trans-synaptic degeneration? Mov Disord 2016; 31: 547–54.

Lee W-W, Yoon EJ, Lee J-Y, Park S-W, Kim YK. Visual Hallucination and Pattern of Brain Degeneration in Parkinson's Disease. Neurodegener Dis 2017; 17: 63–72.

Lenka A, Jhunjhunwala KR, Saini J, Pal PK. Structural and functional neuroimaging in patients with Parkinson's disease and visual hallucinations: A critical review. Parkinsonism Relat Disord 2015; 21: 683–91.

Lenka A, Pagonabarraga J, Pal PK, Bejr-Kasem H, Kulisvesky J. Minor hallucinations in Parkinson disease: A subtle symptom with major clinical implications. Neurology 2019; 93: 259–66.

Li Y, Liu W, Oo TF, Wang L, Tang Y, Jackson-Lewis V, et al. Mutant LRRK2(R1441G) BAC transgenic mice recapitulate cardinal features of Parkinson's disease. Nat Neurosci 2009; 12: 826–8.

Liégeois R, Li J, Kong R, Orban C, Van De Ville D, Ge T, et al. Resting brain dynamics at different timescales capture distinct aspects of human behavior. Nat Commun 2019; 10: 2317.

Lindauer U, Dirnagl U, Füchtemeier M, Böttiger C, Offenhauser N, Leithner C, et al. Pathophysiological Interference with Neurovascular Coupling – When Imaging Based on Hemoglobin Might Go Blind

[Internet]. Front Neuroenergetics 2010; 2[cited 2021 Jun 10] Available from: https://www.ncbi.nlm.nih.gov/pmc/articles/PMC2955428/

Litvan I, Goldman JG, Tröster AI, Schmand BA, Weintraub D, Petersen RC, et al. Diagnostic Criteria for Mild Cognitive Impairment in Parkinson's Disease: Movement Disorder Society Task Force Guidelines. Mov Disord Off J Mov Disord Soc 2012; 27: 349–56.

Logothetis NK, Pauls J, Augath M, Trinath T, Oeltermann A. Neurophysiological investigation of the basis of the fMRI signal. Nature 2001; 412: 150–7.

Luppi AI, Carhart-Harris RL, Roseman L, Pappas I, Menon DK, Stamatakis EA. LSD alters dynamic integration and segregation in the human brain. NeuroImage 2021; 227: 117653.

Luppi AI, Craig MM, Pappas I, Finoia P, Williams GB, Allanson J, et al. Consciousness-specific dynamic interactions of brain integration and functional diversity. Nat Commun 2019; 10: 4616.

Luppi AI, Stamatakis EA. Combining network topology and information theory to construct representative brain networks. Netw Neurosci 2021; 5: 96–124.

Maarouf M, Neudorfer C, El Majdoub F, Lenartz D, Kuhn J, Sturm V. Deep Brain Stimulation of Medial Dorsal and Ventral Anterior Nucleus of the Thalamus in OCD: A Retrospective Case Series [Internet]. PLoS ONE 2016; 11[cited 2021 Jan 11] Available from: https://www.ncbi.nlm.nih.gov/pmc/articles/PMC4978440/

Mack J, Rabins P, Anderson K, Goldstein S, Grill S, Hirsch ES, et al. Prevalence of psychotic symptoms in a community-based Parkinson disease sample. Am J Geriatr Psychiatry Off J Am Assoc Geriatr Psychiatry 2012; 20: 123–32.

Magnotta VA, Friedman L, FIRST BIRN. Measurement of Signal-to-Noise and Contrast-to-Noise in the fBIRN Multicenter Imaging Study. J Digit Imaging 2006; 19: 140–7.

Maiti B, Koller JM, Snyder AZ, Tanenbaum AB, Norris SA, Campbell MC, et al. Cognitive correlates of cerebellar resting-state functional connectivity in Parkinson disease. Neurology 2020; 94: e384–96.

Manni R, Pacchetti C, Terzaghi M, Sartori I, Mancini F, Nappi G. Hallucinations and sleep-wake cycle in PD: a 24-hour continuous polysomnographic study. Neurology 2002; 59: 1979–81.

Mansfield P. Multi-planar image formation using NMR spin echoes. J Phys C Solid State Phys 1977; 10: L55–8.

Mao J, Huang X, Yu J, et al. Association Between REM Sleep Behavior Disorder and Cognitive Dysfunctions in Parkinson's Disease: A Systematic Review and Meta-Analysis of Observational Studies. *Front Neurol*. 2020;0. doi:10.3389/fneur.2020.577874

Marioni RE, Shah S, McRae AF, Chen BH, Colicino E, Harris SE, et al. DNA methylation age of blood predicts all-cause mortality in later life. Genome Biol 2015; 16: 25.

Markello R, Shafiei G, Zheng Y-Q, Mišić B. abagen: A toolbox for the Allen Brain Atlas genetics data. Zenodo 2020

Markov NT, Vezoli J, Chameau P, Falchier A, Quilodran R, Huissoud C, et al. Anatomy of hierarchy: feedforward and feedback pathways in macaque visual cortex. J Comp Neurol 2014; 522: 225–59.

Matar E, Phillips JR, Martens KAE, Halliday GM, Lewis SJG. Impaired Color Discrimination—A Specific Marker of Hallucinations in Lewy Body Disorders. J Geriatr Psychiatry Neurol 2019; 32: 257–64.

Matar E, Shine JM, Halliday GM, Lewis SJG. Cognitive fluctuations in Lewy body dementia: towards a pathophysiological framework. Brain 2020; 143: 31–46.

McColgan P, Gregory S, Razi A, Seunarine KK, Gargouri F, Durr A, et al. White matter predicts functional connectivity in premanifest Huntington's disease. Ann Clin Transl Neurol 2017; 4: 106–18.

McColgan P, Gregory S, Seunarine KK, Razi A, Papoutsi M, Johnson E, et al. Brain Regions Showing White Matter Loss in Huntington's Disease Are Enriched for Synaptic and Metabolic Genes. Biol Psychiatry 2018; 83: 456–65.

McKeith IG, Boeve BF, Dickson DW, Halliday G, Taylor J-P, Weintraub D, et al. Diagnosis and management of dementia with Lewy bodies. Neurology 2017; 89: 88–100.

McKinlay A, Grace RC, Dalrymple-Alford JC, Anderson T, Fink J, Roger D. A Profile of Neuropsychiatric Problems and Their Relationship to Quality of Life for Parkinson's Disease Patients Without Dementia. Park Relat Disord 2007; 14 (1): 37–42.

Meppelink AM, de Jong BM, Teune LK, van Laar T. Regional cortical grey matter loss in Parkinson's disease without dementia is independent from visual hallucinations. Mov Disord Off J Mov Disord Soc 2011; 26: 142–7.

Messé A. Parcellation influence on the connectivity-based structure–function relationship in the human brain. Hum Brain Mapp 2020; 41: 1167–80.

Michalak EM, Burr ML, Bannister AJ, Dawson MA. The roles of DNA, RNA and histone methylation in ageing and cancer. Nat Rev Mol Cell Biol 2019; 20: 573–89.

Mišić B, Sporns O. From regions to connections and networks: new bridges between brain and behavior. Curr Opin Neurobiol 2016; 40: 1–7.

Mitchell AS. The mediodorsal thalamus as a higher order thalamic relay nucleus important for learning and decision-making. Neurosci Biobehav Rev 2015; 54: 76–88.

Mito R, Raffelt D, Dhollander T, Vaughan DN, Tournier J-D, Salvado O, et al. Fibre-specific white matter reductions in Alzheimer's disease and mild cognitive impairment. Brain 2018; 141: 888–902.

Mondolo F, Jahanshahi M, Granà A, Biasutti E, Cacciatori E, Di Benedetto P. The Validity of the Hospital Anxiety and Depression Scale and the Geriatric Depression Scale in Parkinson's Disease [Internet]. Behav Neurol 2006[cited 2019 Jan 23] Available from: https://www.hindawi.com/journals/bn/2006/136945/abs/

Moore C, Cavanagh P. Recovery of 3D volume from 2-tone images of novel objects. Cognition 1998; 67: 45–71.

Mori S, Oishi K, Jiang H, Jiang L, Li X, Akhter K, et al. Stereotaxic White Matter Atlas Based on Diffusion Tensor Imaging in an ICBM Template. NeuroImage 2008; 40: 570–82.

Mosimann UP, Mather G, Wesnes KA, O'Brien JT, Burn DJ, McKeith IG. Visual perception in Parkinson disease dementia and dementia with Lewy bodies. Neurology 2004; 63: 2091–6.

Moskovitz C, Moses H, Klawans HL. Levodopa-induced psychosis: a kindling phenomenon. Am J Psychiatry 1978; 135: 669–75.

Mu T-W, Ong DST, Wang Y-J, Balch WE, Yates JR, Segatori L, et al. Chemical and biological approaches synergize to ameliorate protein-folding diseases. Cell 2008; 134: 769–81.

Muckli L, De Martino F, Vizioli L, Petro LS, Smith FW, Ugurbil K, et al. Contextual Feedback to Superficial Layers of V1. Curr Biol CB 2015; 25: 2690–5.

Muller AJ, Shine JM, Halliday GM, Lewis SJG. Visual hallucinations in Parkinson's disease: theoretical models. Mov Disord Off J Mov Disord Soc 2014; 29: 1591–8.

Murphy KE, Gysbers AM, Abbott SK, Tayebi N, Kim WS, Sidransky E, et al. Reduced glucocerebrosidase is associated with increased α-synuclein in sporadic Parkinson's disease. Brain J Neurol 2014; 137: 834–48.

Murphy N, Killen A, Gupta RK, Graziadio S, Rochester L, Firbank M, et al. Exploring Bottom-Up Visual Processing and Visual Hallucinations in Parkinson's Disease With Dementia. Front Neurol 2020; 11: 579113.

Neher PF, Descoteaux M, Houde J-C, Stieltjes B, Maier-Hein KH. Strengths and weaknesses of state of the art fiber tractography pipelines – A comprehensive in-vivo and phantom evaluation study using Tractometer. Med Image Anal 2015; 26: 287–305.

Neumann J, Bras J, Deas E, O'Sullivan SS, Parkkinen L, Lachmann RH, et al. Glucocerebrosidase mutations in clinical and pathologically proven Parkinson's disease. Brain J Neurol 2009; 132: 1783–94.

Nishio Y, Yokoi K, Uchiyama M, Mamiya Y, Watanabe H, Gang M, et al. Deconstructing psychosis and misperception symptoms in Parkinson's disease. J Neurol Neurosurg Psychiatry 2017; 88: 722–9.

Norton DJ, Jaywant A, Gallart-Palau X, Cronin-Golomb A. Normal discrimination of spatial frequency and contrast across visual hemifields in left-onset Parkinson's disease: Evidence against perceptual hemifield biases. Vision Res 2015; 107: 94–100.

O'Callaghan C, Hall JM, Tomassini A, Muller AJ, Walpola IC, Moustafa AA, et al. Visual Hallucinations Are Characterized by Impaired Sensory Evidence Accumulation: Insights From Hierarchical Drift Diffusion Modeling in Parkinson's Disease. Biol Psychiatry Cogn Neurosci Neuroimaging 2017; 2: 680–8.

O'Callaghan C, Hezemans FH, Ye R, Rua C, Jones PS, Murley AG, et al. Locus coeruleus integrity and the effect of atomoxetine on response inhibition in Parkinson's disease [Internet]. Brain 2021[cited 2021 May 19] Available from: https://doi.org/10.1093/brain/awab142

O’Callaghan C, Kveraga K, Shine JM, Adams RB, Bar M. Predictions penetrate perception: Converging insights from brain, behaviour and disorder. Conscious Cogn 2017; 47: 63–74.

Ogawa S, Lee TM, Kay AR, Tank DW. Brain magnetic resonance imaging with contrast dependent on blood oxygenation. Proc Natl Acad Sci U S A 1990; 87: 9868–72.

Ogawa S, Tank DW, Menon R, Ellermann JM, Kim SG, Merkle H, et al. Intrinsic signal changes accompanying sensory stimulation: functional brain mapping with magnetic resonance imaging. Proc Natl Acad Sci 1992; 89: 5951–5.

Oldham MC, Konopka G, Iwamoto K, Langfelder P, Kato T, Horvath S, et al. Functional organization of the transcriptome in human brain. Nat Neurosci 2008; 11: 1271–82.

Onofrj M, Carrozzino D, D’Amico A, Di Giacomo R, Delli Pizzi S, Thomas A, et al. Psychosis in parkinsonism: an unorthodox approach. Neuropsychiatr Dis Treat 2017; 13: 1313–30.

Onofrj M, Espay AJ, Bonanni L, Pizzi SD, Sensi SL. Hallucinations, somatic-functional disorders of PD-DLB as expressions of thalamic dysfunction. Mov Disord 2019; 34: 1100–11.

Orban C, Kong R, Li J, Chee MWL, Yeo BTT. Time of day is associated with paradoxical reductions in global signal fluctuation and functional connectivity. PLoS Biol 2020; 18: e3000602.

Ouhaz Z, Fleming H, Mitchell AS. Cognitive Functions and Neurodevelopmental Disorders Involving the Prefrontal Cortex and Mediodorsal Thalamus [Internet]. Front Neurosci 2018; 12[cited 2021 May 20] Available from: https://www.frontiersin.org/articles/10.3389/fnins.2018.00033/full

Pagonabarraga J, Soriano-Mas C, Llebaria G, López-Solà M, Pujol J, Kulisevsky J. Neural correlates of minor hallucinations in non-demented patients with Parkinson’s disease. Parkinsonism Relat Disord 2014; 20: 290–6.

Pan T, Kondo S, Le W, Jankovic J. The role of autophagy-lysosome pathway in neurodegeneration associated with Parkinson’s disease. Brain J Neurol 2008; 131: 1969–78.

Papapetropoulos S, McCorquodale DS, Gonzalez J, Jean-Gilles L, Mash DC. Cortical and amygdalar Lewy body burden in Parkinson’s disease

patients with visual hallucinations. Parkinsonism Relat Disord 2006; 12: 253–6.

Papapetropoulos S, Katzen H, Schrag A, Singer C, Scanlon BK, Nation D, et al. A questionnaire-based (UM-PDHQ) study of hallucinations in Parkinson's disease. BMC Neurol 2008; 8: 21.

Paquola C, Wael RVD, Wagstyl K, Bethlehem RAI, Hong S-J, Seidlitz J, et al. Microstructural and functional gradients are increasingly dissociated in transmodal cortices. PLOS Biol 2019; 17: e3000284.

Parkes L, Fulcher B, Yücel M, Fornito A. An evaluation of the efficacy, reliability, and sensitivity of motion correction strategies for resting-state functional MRI. NeuroImage 2018; 171: 415–36.

Parr T, Rees G, Friston KJ. Computational Neuropsychology and Bayesian Inference [Internet]. Front Hum Neurosci 2018; 12[cited 2019 Jan 28] Available from: https://www.ncbi.nlm.nih.gov/pmc/articles/PMC5829460/

Pauling L, Coryell CD. The Magnetic Properties and Structure of Hemoglobin, Oxyhemoglobin and Carbonmonoxyhemoglobin. Proc Natl Acad Sci U S A 1936; 22: 210–6.

Pelli D, Robson JG, Wilkins AJ. The design of a new letter chart for measuring contrast sensitivity. Clin Vis Sci 1988; 2: 187–99.

Pepper RE, Pitman KA, Cullen CL, Young KM. How Do Cells of the Oligodendrocyte Lineage Affect Neuronal Circuits to Influence Motor Function, Memory and Mood? [Internet]. Front Cell Neurosci 2018; 12[cited 2019 Nov 4] Available from: https://www.ncbi.nlm.nih.gov/pmc/articles/PMC6262292/

Pezzoli S, Cagnin A, Bandmann O, Venneri A. Structural and Functional Neuroimaging of Visual Hallucinations in Lewy Body Disease: A Systematic Literature Review [Internet]. Brain Sci 2017; 7[cited 2019 Feb 19] Available from: https://www.ncbi.nlm.nih.gov/pmc/articles/PMC5532597/

Poewe W. Psychosis in Parkinson's disease. Mov Disord 2003; 18: 80–7.

Postuma RB, Berg D, Stern M, Poewe W, Olanow CW, Oertel W, et al. Abolishing the 1-year rule: How much evidence will be enough? Mov Disord Off J Mov Disord Soc 2016; 31: 1623–7.

Poustchi-Amin M, Mirowitz SA, Brown JJ, McKinstry RC, Li T. Principles and Applications of Echo-planar Imaging: A Review for the General Radiologist. RadioGraphics 2001; 21: 767–79.

Poustchi-Amin M, Mirowitz SA, Brown JJ, McKinstry RC, Li T. Principles and Applications of Echo-planar Imaging: A Review for the General Radiologist. RadioGraphics 2001; 21: 767–79.

Power JD, Laumann TO, Plitt M, Martin A, Petersen SE. On Global fMRI Signals and Simulations. Trends Cogn Sci 2017; 21: 911–3.

Power JD, Mitra A, Laumann TO, Snyder AZ, Schlaggar BL, Petersen SE. Methods to detect, characterize, and remove motion artifact in resting state fMRI. NeuroImage 2014; 84: 320–41.

Powers AR, Kelley M, Corlett PR. Hallucinations as top-down effects on perception. Biol Psychiatry Cogn Neurosci Neuroimaging 2016; 1: 393–400.

Powers AR, Mathys C, Corlett PR. Pavlovian conditioning-induced hallucinations result from overweighting of perceptual priors. Science 2017; 357: 596–600.

Preti MG, Bolton TA, Van De Ville D. The dynamic functional connectome: State-of-the-art and perspectives. NeuroImage 2017; 160: 41–54.

Rahkonen T, Eloniemi-Sulkava U, Rissanen S, Vatanen A, Viramo P, Sulkava R. Dementia with Lewy bodies according to the consensus criteria in a general population aged 75 years or older. J Neurol Neurosurg Psychiatry 2003; 74: 720–4.

Raffelt D, Tournier J-D, Fripp J, Crozier S, Connelly A, Salvado O. Symmetric diffeomorphic registration of fibre orientation distributions. NeuroImage 2011; 56: 1171–80.

Raffelt D, Tournier J-D, Rose S, Ridgway GR, Henderson R, Crozier S, et al. Apparent Fibre Density: a novel measure for the analysis of diffusion-weighted magnetic resonance images. NeuroImage 2012; 59: 3976–94.

Raffelt DA, Tournier J-D, Smith RE, Vaughan DN, Jackson G, Ridgway GR, et al. Investigating white matter fibre density and morphology using fixel-based analysis. NeuroImage 2017; 144: 58–73.

Raffelt DA, Smith RE, Ridgway GR, Tournier J-D, Vaughan DN, Rose S, et al. Connectivity-based fixel enhancement: Whole-brain statistical analysis

of diffusion MRI measures in the presence of crossing fibres. NeuroImage 2015; 117: 40–55.

Ramírez-Ruiz B, Martí M-J, Tolosa E, Giménez M, Bargalló N, Valldeoriola F, et al. Cerebral atrophy in Parkinson's disease patients with visual hallucinations. Eur J Neurol 2007; 14: 750–6.

Rashid B, Arbabshirani MR, Damaraju E, Cetin MS, Miller R, Pearlson GD, et al. Classification of schizophrenia and bipolar patients using static and dynamic resting-state fMRI brain connectivity. NeuroImage 2016; 134: 645–57.

Rau Y-A, Wang S-M, Tournier J-D, Lin S-H, Lu C-S, Weng Y-H, et al. A longitudinal fixel-based analysis of white matter alterations in patients with Parkinson's disease [Internet]. NeuroImage Clin 2019; 24[cited 2020 Jul 17] Available from: https://www.ncbi.nlm.nih.gov/pmc/articles/PMC6889638/

Raudvere U, Kolberg L, Kuzmin I, Arak T, Adler P, Peterson H, et al. g:Profiler: a web server for functional enrichment analysis and conversions of gene lists (2019 update). Nucleic Acids Res 2019; 47: W191–8.

Rende B, Ramsberger G, Miyake A. Commonalities and differences in the working memory components underlying letter and category fluency tasks: a dual-task investigation. Neuropsychology 2002; 16: 309–21.

Reuter M, Schmansky NJ, Rosas HD, Fischl B. Within-subject template estimation for unbiased longitudinal image analysis. NeuroImage 2012; 61: 1402–18.

Richiardi J, Altmann A, Milazzo A-C, Chang C, Chakravarty MM, Banaschewski T, et al. Correlated gene expression supports synchronous activity in brain networks. Science 2015; 348: 1241–4.

Rittman T, Rubinov M, Vértes PE, Patel AX, Ginestet CE, Ghosh BCP, et al. Regional expression of the MAPT gene is associated with loss of hubs in brain networks and cognitive impairment in Parkinson disease and progressive supranuclear palsy. Neurobiol Aging 2016; 48: 153–60.

Roalf DR, Quarmley M, Elliott MA, Satterthwaite TD, Vandekar SN, Ruparel K, et al. The impact of quality assurance assessment on diffusion tensor imaging outcomes in a large-scale population-based cohort. NeuroImage 2016; 125: 903–19.

Romero-Garcia R, Warrier V, Bullmore ET, Baron-Cohen S, Bethlehem RAI. Synaptic and transcriptionally downregulated genes are associated

with cortical thickness differences in autism. Mol Psychiatry 2019; 24: 1053–64.

Romme IAC, de Reus MA, Ophoff RA, Kahn RS, van den Heuvel MP. Connectome Disconnectivity and Cortical Gene Expression in Patients With Schizophrenia. Biol Psychiatry 2017; 81: 495–502.

Roalf DR, Quarmley M, Elliott MA, Satterthwaite TD, Vandekar SN, Ruparel K, et al. The impact of quality assurance assessment on diffusion tensor imaging outcomes in a large-scale population-based cohort. NeuroImage 2016; 125: 903–19.

Rosazza C, Minati L. Resting-state brain networks: literature review and clinical applications. Neurol Sci Off J Ital Neurol Soc Ital Soc Clin Neurophysiol 2011; 32: 773–85.

Rubinov M, Sporns O. Weight-conserving characterization of complex functional brain networks. NeuroImage 2011; 56: 2068–79.

Russo M, Carrarini C, Dono F, Rispoli MG, Di Pietro M, Di Stefano V, et al. The Pharmacology of Visual Hallucinations in Synucleinopathies [Internet]. Front Pharmacol 2019; 10[cited 2020 Dec 16] Available from: https://www.frontiersin.org/articles/10.3389/fphar.2019.01379/full

Saad ZS, Gotts SJ, Murphy K, Chen G, Jo HJ, Martin A, et al. Trouble at Rest: How Correlation Patterns and Group Differences Become Distorted After Global Signal Regression. Brain Connect 2012; 2: 25–32.

Sakoğlu U, Pearlson GD, Kiehl KA, Wang YM, Michael AM, Calhoun VD. A method for evaluating dynamic functional network connectivity and task-modulation: application to schizophrenia. Magma N Y N 2010; 23: 351–66.

Sanchez-Martinez A, Beavan M, Gegg ME, Chau K-Y, Whitworth AJ, Schapira AHV. Parkinson disease-linked GBA mutation effects reversed by molecular chaperones in human cell and fly models [Internet]. Sci Rep 2016; 6[cited 2020 Apr 24] Available from: https://www.ncbi.nlm.nih.gov/pmc/articles/PMC4990939/

Savli M, Bauer A, Mitterhauser M, Ding Y-S, Hahn A, Kroll T, et al. Normative database of the serotonergic system in healthy subjects using multi-tracer PET. NeuroImage 2012; 63: 447–59.

Schaefer A, Kong R, Gordon EM, Laumann TO, Zuo X-N, Holmes AJ, et al. Local-Global Parcellation of the Human Cerebral Cortex from Intrinsic Functional Connectivity MRI. Cereb Cortex N Y N 1991 2018; 28: 3095–114.

Schumacher J, Peraza LR, Firbank M, Thomas AJ, Kaiser M, Gallagher P, et al. Dynamic functional connectivity changes in dementia with Lewy bodies and Alzheimer's disease. NeuroImage Clin 2019; 22: 101812.

Schumacher J, Peraza LR, Firbank M, Thomas AJ, Kaiser M, Gallagher P, et al. Functional connectivity in dementia with Lewy bodies: A within- and between-network analysis. Hum Brain Mapp 2018; 39: 1118–29.

Shine JM, Bissett PG, Bell PT, Koyejo O, Balsters JH, Gorgolewski KJ, et al. The Dynamics of Functional Brain Networks: Integrated Network States during Cognitive Task Performance. Neuron 2016; 92: 544–54.

Shine JM, Halliday GM, Gilat M, Matar E, Bolitho SJ, Carlos M, et al. The role of dysfunctional attentional control networks in visual misperceptions in Parkinson's disease. Hum Brain Mapp 2014; 35: 2206–19.

Shine JM, Keogh R, O'Callaghan C, Muller AJ, Lewis SJG, Pearson J. Imagine that: elevated sensory strength of mental imagery in individuals with Parkinson's disease and visual hallucinations. Proc Biol Sci 2015; 282: 20142047.

Shine JM, O'Callaghan C, Halliday GM, Lewis SJG. Tricks of the mind: Visual hallucinations as disorders of attention. Prog Neurobiol 2014; 116: 58–65.

Shmuel A, Leopold DA. Neuronal correlates of spontaneous fluctuations in fMRI signals in monkey visual cortex: Implications for functional connectivity at rest. Hum Brain Mapp 2008; 29: 751–61.

Sepe S, Milanese C, Gabriels S, Derks KWJ, Payan-Gomez C, van IJcken WFJ, et al. Inefficient DNA Repair Is an Aging-Related Modifier of Parkinson's Disease. Cell Rep 2016; 15: 1866–75.

Sezgin M, Sankur B. Survey over image thresholding techniques and quantitative performance evaluation. J Electron Imaging 2004; 13: 146–66.

Silva MF, Faria P, Regateiro FS, Forjaz V, Januário C, Freire A, et al. Independent patterns of damage within magno-, parvo- and koniocellular pathways in Parkinson's disease. Brain J Neurol 2005; 128: 2260–71.

Skene NG, Grant SGN. Identification of Vulnerable Cell Types in Major Brain Disorders Using Single Cell Transcriptomes and Expression Weighted Cell Type Enrichment [Internet]. Front Neurosci 2016; 10[cited 2019 Nov 6] Available from: https://www.frontiersin.org/articles/10.3389/fnins.2016.00016/full

Sloan LL. New test Charts for the Measurement of Visual Acuity at far and Near Distances *. Am J Ophthalmol 1959; 48: 807–13.

Smith SM, Nichols TE. Threshold-free cluster enhancement: addressing problems of smoothing, threshold dependence and localisation in cluster inference. NeuroImage 2009; 44: 83–98.

Smith RE, Tournier J-D, Calamante F, Connelly A. Anatomically-constrained tractography: improved diffusion MRI streamlines tractography through effective use of anatomical information. NeuroImage 2012; 62: 1924–38.

Smith RE, Tournier J-D, Calamante F, Connelly A. SIFT2: Enabling dense quantitative assessment of brain white matter connectivity using streamlines tractography. NeuroImage 2015; 119: 338–51.

Smith SM, Fox PT, Miller KL, Glahn DC, Fox PM, Mackay CE, et al. Correspondence of the brain's functional architecture during activation and rest. Proc Natl Acad Sci 2009; 106: 13040–5.

Spillantini MG, Schmidt ML, Lee VM, Trojanowski JQ, Jakes R, Goedert M. Alpha-synuclein in Lewy bodies. Nature 1997; 388: 839–40.

Stejskal EO, Tanner JE. Spin Diffusion Measurements: Spin Echoes in the Presence of a Time-Dependent Field Gradient. J Chem Phys 1965; 42: 288–92.

Stiso J, Khambhati AN, Menara T, Kahn AE, Stein JM, Das SR, et al. White Matter Network Architecture Guides Direct Electrical Stimulation through Optimal State Transitions. Cell Rep 2019; 28: 2554-2566.e7.

Stroop JR. Studies of interference in serial verbal reactions. J Exp Psychol 1935; 18: 643–62.

Stuke H, Kress E, Weilnhammer VA, Sterzer P, Schmack K. Overly Strong Priors for Socially Meaningful Visual Signals Are Linked to Psychosis Proneness in Healthy Individuals [Internet]. Front Psychol 2021; 12[cited 2021 Jun 14] Available from: https://www.frontiersin.org/articles/10.3389/fpsyg.2021.583637/full

Sudmant PH, Lee H, Dominguez D, Heiman M, Burge CB. Widespread Accumulation of Ribosome-Associated Isolated 3′ UTRs in Neuronal Cell Populations of the Aging Brain. Cell Rep 2018; 25: 2447-2456.e4.

Supek F, Bošnjak M, Škunca N, Šmuc T. REVIGO Summarizes and Visualizes Long Lists of Gene Ontology Terms. PLOS ONE 2011; 6: e21800.

Tailarach J. Co-Planar Stereotaxic Atlas of the Human Brain-3-Dimensional Proportional System [Internet]. Approach Cereb Imaging 1988[cited 2021 Jun 10] Available from: https://ci.nii.ac.jp/naid/10008533708/

Tanner WP, Swets JA. A decision-making theory of visual detection. Psychol Rev 1954; 61: 401–9.

Tagliazucchi E, Laufs H. Decoding wakefulness levels from typical fMRI resting-state data reveals reliable drifts between wakefulness and sleep. Neuron 2014; 82: 695–708.

Tang E, Giusti C, Baum GL, Gu S, Pollock E, Kahn AE, et al. Developmental increases in white matter network controllability support a growing diversity of brain dynamics. Nat Commun 2017; 8: 1–16.

Teeple E, Joshi P, Pande R, Huang Y, Karambe A, Latta-Mahieu M, et al. Single Nuclei Sequencing of Human Putamen Oligodendrocytes Reveals Altered Heterogeneity and Disease-Associated Changes in Parkinson's Disease and Multiple System Atrophy. bioRxiv 2021: 2021.05.06.442967.

Teufel C, Subramaniam N, Dobler V, Perez J, Finnemann J, Mehta PR, et al. Shift toward prior knowledge confers a perceptual advantage in early psychosis and psychosis-prone healthy individuals. Proc Natl Acad Sci 2015; 112: 13401–6.

Teufel C, Subramaniam N, Fletcher PC. The role of priors in Bayesian models of perception. Front Comput Neurosci 2013; 7: 25.

Thomas, George, Zarkali, Angeliki, Ryten, Mina, Shmueli, Karin, Gill Martinez, Ana Luisa, Leyland, Louise-Ann, et al. Regional brain iron and gene expression provide insights into neurodegeneration in Parkinson's disease. Brain 2021

Tian Y, Margulies DS, Breakspear M, Zalesky A. Topographic organization of the human subcortex unveiled with functional connectivity gradients. Nat Neurosci 2020; 23: 1421–32.

Toledo JB, Gopal P, Raible K, Irwin DJ, Brettschneider J, Sedor S, et al. Pathological α-synuclein distribution in subjects with coincident Alzheimer's and Lewy body pathology. Acta Neuropathol (Berl) 2016; 131: 393–409.

Tomlinson CL, Stowe R, Patel S, Rick C, Gray R, Clarke CE. Systematic review of levodopa dose equivalency reporting in Parkinson's disease. Mov Disord 2010; 25: 2649–53.

Tournier J-D, Calamante F, Connelly A. Robust determination of the fibre orientation distribution in diffusion MRI: non-negativity constrained super-resolved spherical deconvolution. NeuroImage 2007; 35: 1459–72.

Tournier J-D, Calamante F, Connelly A. Determination of the appropriate b value and number of gradient directions for high-angular-resolution diffusion-weighted imaging. NMR Biomed 2013; 26: 1775–86.

Tournier J-D, Mori S, Leemans A. Diffusion tensor imaging and beyond. Magn Reson Med 2011; 65: 1532–56.

Tournier J-D, Smith R, Raffelt D, Tabbara R, Dhollander T, Pietsch M, et al. MRtrix3: A fast, flexible and open software framework for medical image processing and visualisation. NeuroImage 2019; 202: 116137.

Turner R, Le Bihan D, Moonen CT, Despres D, Frank J. Echo-planar time course MRI of cat brain oxygenation changes. Magn Reson Med 1991; 22: 159–66.

Tustison NJ, Avants BB, Cook PA, Zheng Y, Egan A, Yushkevich PA, et al. N4ITK: improved N3 bias correction. IEEE Trans Med Imaging 2010; 29: 1310–20.

Uchiyama M, Nishio Y, Yokoi K, Hirayama K, Imamura T, Shimomura T, et al. Pareidolias: complex visual illusions in dementia with Lewy bodies. Brain J Neurol 2012; 135: 2458–69.

University College, London. Trial of Ondansetron as a Parkinson's HAllucinations Treatment [Internet]. clinicaltrials.gov; 2019[cited 2021 May 18] Available from: https://clinicaltrials.gov/ct2/show/NCT04167813

Van Dijk KRA, Sabuncu MR, Buckner RL. The influence of head motion on intrinsic functional connectivity MRI. NeuroImage 2012; 59: 431–8.

van Loon AM, Knapen T, Scholte HS, St. John-Saaltink E, Donner TH, Lamme VAF. GABA Shapes the Dynamics of Bistable Perception. Curr Biol 2013; 23: 823–7.

Vázquez-Rodríguez B, Suárez LE, Markello RD, Shafiei G, Paquola C, Hagmann P, et al. Gradients of structure–function tethering across neocortex. Proc Natl Acad Sci 2019; 116: 21219–27.

Vazey E, Aston-Jones G. The emerging role of norepinephrine in cognitive dysfunctions of Parkinson's disease [Internet]. Front Behav Neurosci 2012; 6[cited 2021 May 19] Available from: https://www.frontiersin.org/articles/10.3389/fnbeh.2012.00048/full

Velayati A, Yu WH, Sidransky E. The role of glucocerebrosidase mutations in Parkinson disease and Lewy body disorders. Curr Neurol Neurosci Rep 2010; 10: 190–8.

Veraart J, Fieremans E, Novikov DS. Diffusion MRI noise mapping using random matrix theory. Magn Reson Med 2016; 76: 1582–93.

Volpicelli-Daley LA, Luk KC, Patel TP, Tanik SA, Riddle DM, Stieber A, et al. Exogenous α-Synuclein Fibrils Induce Lewy Body Pathology Leading to Synaptic Dysfunction and Neuron Death. Neuron 2011; 72: 57–71.

Walker MP, Ayre GA, Cummings JL, Wesnes K, McKeith IG, O'Brien JT, et al. The Clinician Assessment of Fluctuation and the One Day Fluctuation Assessment Scale. Two methods to assess fluctuating confusion in dementia. Br J Psychiatry J Ment Sci 2000; 177: 252–6.

Walker Z, Possin KL, Boeve BF, Aarsland D. Lewy body dementias. Lancet Lond Engl 2015; 386: 1683–97.

Walsh KS, McGovern DP, Clark A, O'Connell RG. Evaluating the neurophysiological evidence for predictive processing as a model of perception. Ann N Y Acad Sci 2020; 1464: 242–68.

Wakana S, Caprihan A, Panzenboeck MM, Fallon JH, Perry M, Gollub RL, et al. Reproducibility of quantitative tractography methods applied to cerebral white matter. NeuroImage 2007; 36: 630–44.

Warrington EK. Recognition Memory Test: Manual. Berkshire: UKNFER-Nelson; 1984

Warrington EK. The Graded Naming Test: A Restandardisation. Neuropsychol Rehabil 1997; 7: 143–6.

Watanabe H, Senda J, Kato S, Ito M, Atsuta N, Hara K, et al. Cortical and subcortical brain atrophy in Parkinson's disease with visual hallucination. Mov Disord Off J Mov Disord Soc 2013; 28: 1732–6.

Weber S, Johnsen E, Kroken RA, Løberg E-M, Kandilarova S, Stoyanov D, et al. Dynamic Functional Connectivity Patterns in Schizophrenia and the Relationship With Hallucinations [Internet]. Front Psychiatry 2020; 11[cited

2021 May 19] Available from: https://www.ncbi.nlm.nih.gov/pmc/articles/PMC7145395/

Wechsler, D. Wechsler Adult Intelligence Scale-Fourth Edition [Internet]. Fourth. San Antonio, TX: NCS Pearson; 2008[cited 2019 Feb 6] Available from: https://www.pearsonclinical.com/psychology/products/100000392/wechsler-adult-intelligence-scalefourth-edition-wais-iv.html

Weil RS, Lashley TL, Bras J, Schrag AE, Schott JM. Current concepts and controversies in the pathogenesis of Parkinson's disease dementia and Dementia with Lewy Bodies [Internet]. F1000Research 2017; 6[cited 2019 Apr 5] Available from: https://www.ncbi.nlm.nih.gov/pmc/articles/PMC5580419/

Weil RS, Hsu JK, Darby RR, Soussand L, Fox MD. Neuroimaging in Parkinson's disease dementia: connecting the dots [Internet]. Brain Commun 2019; 1[cited 2019 Nov 1] Available from: https://academic.oup.com/braincomms/article/1/1/fcz006/5529671

Weil RS, Pappa K, Schade RN, Schrag AE, Bahrami B, Schwarzkopf DS, et al. The Cats-and-Dogs test: A tool to identify visuoperceptual deficits in Parkinson's disease. Mov Disord 2017; 32: 1789–90.

Weil RS, Schrag AE, Warren JD, Crutch SJ, Lees AJ, Morris HR. Visual dysfunction in Parkinson's disease. Brain J Neurol 2016.

White NS, Dale AM. Optimal diffusion MRI acquisition for fiber orientation density estimation: an analytic approach. Hum Brain Mapp 2009; 30: 3696–703.

Whitwell JL, Graff-Radford J, Singh TD, Drubach DA, Senjem ML, Spychalla AJ, et al. 18F-FDG PET in Posterior Cortical Atrophy and Dementia with Lewy Bodies. J Nucl Med Off Publ Soc Nucl Med 2017; 58: 632–8.

Williams DR, Warren JD, Lees AJ. Using the presence of visual hallucinations to differentiate Parkinson's disease from atypical parkinsonism. J Neurol Neurosurg Psychiatry 2008; 79: 652–5.

Williams-Gray CH, Mason SL, Evans JR, Foltynie T, Brayne C, Robbins TW, et al. The CamPaIGN study of Parkinson's disease: 10-year outlook in an incident population-based cohort. J Neurol Neurosurg Psychiatry 2013; 84: 1258–64.

Wolf T, Lindauer U, Villringer A, Dirnagl U. Excessive oxygen or glucose supply does not alter the blood flow response to somatosensory stimulation or spreading depression in rats. Brain Res 1997; 761: 290–9.

Yao N, Shek-Kwan Chang R, Cheung C, Pang S, Lau KK, Suckling J, et al. The default mode network is disrupted in Parkinson's disease with visual hallucinations. Hum Brain Mapp 2014; 35: 5658–66.

Young KM, Psachoulia K, Tripathi RB, Dunn S-J, Cossell L, Attwell D, et al. Oligodendrocyte dynamics in the healthy adult CNS: evidence for myelin remodeling. Neuron 2013; 77: 873–85.

Xiao Y, Lau JC, Anderson T, DeKraker J, Collins DL, Peters T, et al. An accurate registration of the BigBrain dataset with the MNI PD25 and ICBM152 atlases. Sci Data 2019; 6: 210.

Zalesky A, Fornito A, Bullmore ET. Network-based statistic: Identifying differences in brain networks. NeuroImage 2010; 53: 1197–207.

Zarkali A, Adams RA, Psarras S, Leyland L-A, Rees G, Weil RS. Increased weighting on prior knowledge in Lewy body-associated visual hallucinations. Brain Commun 2019; 1 Available from: https://academic.oup.com/braincomms/article/1/1/fcz007/5532510

Zarkali A, McColgan P, Leyland L-A, Lees AJ, Rees G, Weil RS. Fiber-specific white matter reductions in Parkinson hallucinations and visual dysfunction. Neurology 2020

Zarkali A, McColgan P, Ryten M, Reynolds RH, Leyland L-A, Lees AJ, et al. Dementia risk in Parkinson's disease is associated with interhemispheric connectivity loss and determined by regional gene expression. NeuroImage Clin 2020; 28: 102470.

Zarkali A, McColgan P, Ryten M, Reynolds R, Leyland L-A, Lees AJ, et al. Differences in network controllability and regional gene expression underlie hallucinations in Parkinson's disease. Brain 2020; 143: 3435–48.

Zhang B, Horvath S. A general framework for weighted gene co-expression network analysis. Stat Appl Genet Mol Biol 2005; 4: Article17.

Zhang Z, Liao W, Chen H, Mantini D, Ding J-R, Xu Q, et al. Altered functional-structural coupling of large-scale brain networks in idiopathic generalized epilepsy. Brain J Neurol 2011; 134: 2912–28.

Zigmond AS, Snaith RP. The hospital anxiety and depression scale. Acta Psychiatr Scand 1983; 67: 361–70.

Zöller D, Sandini C, Schaer M, Eliez S, Bassett DS, Ville DVD. Structural control energy of resting-state functional brain states reveals less cost-effective brain dynamics in psychosis vulnerability. Hum Brain Mapp 2021; 42: 2181–200.

10. List of Tables

11. List of Figures

12. Data and Code availability

The code that was used to generate data and perform analyses described in this dissertation is freely available in the below repositories.

Chapter 3:

- https://github.com/AngelikaZa/Increased-weighting-on-prior-knowledge-in-Lewy-Body-associated-visual-hallucinations.-BrainComms2019
- Two-tone stimulus creation ("Mooney Converter")
- Collection of the stimuli used in the main experiment
- Analysis code used to derive discrimination sensitivity (d') and criterion (c) and code to perform comparisons between groups

Chapter 5:

- https://github.com/AngelikaZa/ThalamicSubnuclei
- Analysis code used in all statistical analyses and figure generation described in this chapter

Chapter 7:

- https://github.com/AngelikaZa/TVFC.
- Group-level data and all code used for analyses described in this chapter

Additional repositories containing code used for analyses as well as useful functions and tools used throughout this thesis are included in https://github.com/AngelikaZa/.

13. Glossary

ANOVA – Analysis of variance

BOLD – Blood oxygen level dependent

CSD – Constrained spherical deconvolution

CSF – Cerebrospinal fluid

DLB – Dementia with Lewy Bodies

DTI – Diffusion tensor imaging

DWI – Diffusion weighted imaging

EPI – Echo planar imaging

FC – Fibre cross section

FA – Fractional anisotropy

FD – Fibre density

FDC – Combined fibre density and cross-section

FDR – False discovery rate

FOD – Fibre orientation distribution

FWE – Family wise error

GM – Grey Matter

GO – Gene Ontology

HADS – Hospital Anxiety and Depression Scale

LBD – Lewy Body Disease (Dementia with Lewy Bodies and Parkinson's disease)

MD – Mean Diffusivity

MMSE – Mini Mental State Examination

MOCA – Montreal cognitive assessment

MNI – Montreal Neurological Institute (MNI152 2009 version space)

MRI – Magnetic resonance imaging

NBS – Network based statistics

PD – Parkinson's disease

PET – Positron emission tomography

PLS – Partial least squares

QC – Quality control

REM – Rapid eye movement sleep

RF – Radiofrequency

ROI – Region of interest

rsfMRI – Resting state functional MRI

SD – Standard deviation

TE – Echo time

TR – Repetition time

TIV – Total intracranial volume

UCL – University College London

UM-PDHQ – University of Miami Parkinson's disease hallucinations questionnaire

VH – Visual hallucinations

WM – White matter

14. Appendix

Appendix 1. The University of Miami Hallucinations Questionnaire (Chapter 2).

Question	Score reference	Score
1. Do you experience hallucinations? (Have you ever see/hear/feel/smell/taste things that are not really there or that other people do not see?)	0. No hallucinations (skip to Annex) 1. One type only 2. Combination C: Not within the past month, but it has happened in the past	
Type: (mark appropriate): *a. Visual* *b. Auditory* *c. Somatic/Cutaneous* *d. Gustatory* *e. Olfactory (assess each separately)*		
2. How often do you experience hallucinations?	0 = Only a few times 1 = Occasionally (less than once a week, but continuously) 2 = Often (about once per week) 3 = Frequently (several times per week but < than once per day) 4 = Very frequently (≥once per day)	
3. On average, how long do the experiences last?	0 = Short Duration (< 1sec) 1 = Medium Duration (< 10secs) 2 = Prolonged Duration (> 10secs)	
4. Do you think what you are seeing/experiencing is real?	0 = Not real 1 = Sometimes real 2 = Always real	
5. How many types of images/sensations do you experience?	1 = One 2 = Few (2 or 3) 3 = Several (more than 3)	

6. How severe/emotionally distressing do you find these images/sensations or visions?	0 = No effect/Friendly 1 = Mildly – produce little distress 2 = Moderately – produce distress and are disturbing and disruptive 3 = Severely – very disturbing (medications may be required)	
7. What do you normally see/feel/hear/smell/taste? (Delete incorrect responses)	Not formed/cannot describe	
a. Voices:	Whole Faces	Familiar
b. Music:	Fragmented faces	Familiar
c. Tastes:	Whole people	Familiar
d. Smells:	Animals	
e. Skin related:	Insects/reptiles Objects	
8. Is there anything you can do to make the images/sensations disappear? (Delete incorrect response)	Yes No	
9. At what time of the day or under which lighting conditions do you experience hallucinations? (Delete incorrect responses)	A. Specific time During the day/Bright During the night/Dark Dim B. Anytime	
10. Do the images ever make any sound or noise (for visual hallucinations)? (Delete incorrect responses)	Yes No N/A (for non-visual hallucinations)	
11. Do images move (for visual hallucinations)? (Delete incorrect responses)	Yes No N/A (for non-visual hallucinations)	
12. Are the images normal size? (Delete incorrect responses)	Yes No, smaller than normal No, larger than normal N/A (for non-visual hallucinations)	

13. Are the images transparent or solid? (Delete incorrect responses)	Transparent Solid N/A (for non-visual hallucinations)
14. Are the images colored? (Delete incorrect responses)	Yes No, (black and white) N/A (for non-visual hallucinations)
15. Is the onset of hallucinations gradual or sudden? (Delete incorrect responses)	Gradual (appear-disappear slowly) Sudden (appear-disappear suddenly) I cannot tell

Appendix 2. Significant connections in the subnetwork of reduced connectivity in patients with Parkinson's and visual hallucinations (Chapter 6).

L_ventral_23ab to L_p24pr. Test stat: 3.73	L_6ma to R_s6-8. Test stat: 3.53
L_p24pr to L_8BL. Test stat: 3.15	L_2 to R_s6-8. Test stat: 3.84
L_p24pr to L_9p. Test stat: 3.32	L_p24pr to R_OP2-3. Test stat: 3.15
L_2 to L_44. Test stat: 3.57	R_7PC to R_MiddleInsular. Test stat: 3.69
L_8Av to L_44. Test stat: 3.12	R_3a to R_MiddleInsular. Test stat: 3.21
L_44 to L_52. Test stat: 3.12	R_6a to R_AnteriorAngranularInsulaComplex. Test stat: 3.12
L_a47r to L_MiddleInsular. Test stat: 3.12	R_MedialSuperiorTemporal to R_AuditoryComplex_5. Test stat: 3.22
L_55b to L_FrontalOPercular_1. Test stat: 3.19	L_VentralIntraParietalComplex to R_STSv_posterior. Test stat: 3.28
L_44 to L_PFt. Test stat: 3.44	R_7PC to R_STSv_posterior. Test stat: 3.27
L_p24pr to L_PreSubiculum. Test stat: 3.21	L_V3A to R_DorsalTransitionalVisualArea. Test stat: 3.24
L_PoI2 to L_AuditoryComplex_5. Test stat: 3.13	L_ProStriate to R_DorsalTransitionalVisualArea. Test stat: 3.35
L_AuditoryComplex_5 to L_TemporoParietoOccipitalJunction_3. Test stat: 3.22	R_PrimaryAuditory_1 to R_IntraParietaR_1. Test stat: 3.36
L_6_ventral to L_PF_opercular. Test stat: 3.17	L_V8 to R_V6A. Test stat: 3.11
L_44 to L_PF_opercular. Test stat: 3.13	L_ProStriate to R_V3CD. Test stat: 3.10
L_44 to L_PF. Test stat: 3.25	R_MedialSuperiorTemporal to R_PosteriorInsular_1. Test stat: 3.10
L_6r to L_PF. Test stat: 3.22	R_55b to R_PosteriorInsular_1. Test stat: 3.14
L_44 to L_PosteriorInsular_1. Test stat: 3.11	R_a47r to R_PosteriorInsular_1. Test stat: 3.58
L_MiddleInsular to L_FrontalOpercular_5. Test stat: 3.26	R_10pp to R_PosteriorInsular_1. Test stat: 3.10
L_44 to L_ParaInsular. Test stat: 3.27	R_PoI2 to R_LateralBeltComplex. Test stat: 3.23
L_a47r to L_ParaInsular. Test stat: 3.16	R_STSv_posterior to R_AuditoryComplex_4. Test stat: 3.13
L_8BL to R_p24. Test stat: 3.26	R_IntraParietaR_1 to R_AuditoryComplex_4. Test stat: 3.35
L_V8 to R_V6. Test stat: 3.10	R_LateralBeltComplex to R_AuditoryComplex_4. Test stat: 3.16
L_ProStriate to R_V6. Test stat: 3.45	R_V6A to R_ParaInsular. Test stat: 3.12
L_ProStriate to R_V3A. Test stat: 3.25	L_55b to L_Cerebellum. Test stat: 3.27
L_5L to R_PrimaryAuditory_1. Test stat: 3.30	L_PresylvianLanguage to L_Cerebellum. Test stat: 3.48
L_8BL to R_5m_ventral. Test stat: 3.65	L_44 to L_Cerebellum. Test stat: 3.56
L_9p to R_SupplementaryCingulateEyeField. Test stat: 3.40	
L_SupplementaryCingulateEyeField to R_6ma. Test stat: 3.54	
L_6ma to R_6ma. Test stat: 3.43	
L_33pr to R_6ma. Test stat: 3.32	
L_6a to R_6ma. Test stat: 3.46	
R_PrimaryAuditory_1 to R_LateralIntraParietalVentral. Test stat: 3.12	

L_SuperiorFrontalLanguage to R_8BM. Test stat: 3.17 R_p24 to R_10r. Test stat: 3.22 L_PoI2 to R_8BL. Test stat: 3.12 R_p24 to R_10d. Test stat: 3.35 L_10d to R_a47r. Test stat: 3.27 R_p24 to R_a47r. Test stat: 3.14 L_VentralIntraParietalComplex to R_6r. Test stat: 3.45 R_2 to R_6r. Test stat: 3.17 R_p24 to R_9-46d. Test stat: 3.39 L_33pr to R_9a. Test stat: 3.11 L_10d to R_a10p. Test stat: 3.28 R_8Av to R_47s. Test stat: 3.53 R_9-46d to R_47s. Test stat: 3.28 R_PrimaryAuditory_1 to R_6a. Test stat: 3.17 L_SuperiorFrontalLanguage to R_s6-8. Test stat: 3.14	L_AuditoryComplex_5 to L_Cerebellum. Test stat: 3.24 L_PHT to L_Cerebellum. Test stat: 3.52 L_AuditoryComplex_4 to L_Cerebellum. Test stat: 3.35 R_6r to L_Cerebellum. Test stat: 3.14 R_ParaInsular to L_Cerebellum. Test stat: 3.12 L_1 to L_Thalamus. Test stat: 3.20 L_Cerebellum to L_Thalamus. Test stat: 3.63 L_PresylvianLanguage to L_Putamen. Test stat: 3.12 L_V8 to Brain-Stem. Test stat: 3.19 L_44 to Brain-Stem. Test stat: 3.70 L_44 to L_Hippocampus. Test stat: 3.19 R_AuditoryComplex_5 to R_Cerebellum. Test stat: 3.25 R_5L to R_Thalamus. Test stat: 3.24 R_s6-8 to R_Thalamus. Test stat: 3.25 R_Cerebellum to R_Thalamus. Test stat: 3.45 R_ParaBeltComplex to R_Pallidum. Test stat: 3.19 R_STSv_posterior to R_Pallidum. Test stat: 3.52 R_AuditoryComplex_4 to R_Pallidum. Test stat: 3.12

Appendix 3. Cortical and subcortical regions and their rank controllability in controls (Chapter 6).

1	R_Cerebellum	71	L_PH	141	L_STSd_posterior
2	L_Cerebellum	72	L_PGs	142	L_45
3	L_V2	73	L_9-46d	143	R_6_ventral
4	L_V1	74	L_AuditoryComplex_4	144	R_TE1_middle
5	R_V2	75	R_AuditoryComplex_5	145	L_55b
6	R_V1	76	R_PerirhinalEctorhinalCortex	146	R_TE1_anterior
7	L_V3	77	L_VentralVisualComplex	147	L_SupplemCingulateEyeField
8	R_V3	78	L_posteriorOFC	148	L_TE1_anterior
9	R_Thalamus	79	R_PosteriorInferoTemporal	149	L_VentroMedialVisual_1
10	L_Caudate	80	R_9-46d	150	R_9p
11	L_Thalamus	81	R_PH	151	R_47s
12	L_Putamen	82	L_PerirhinalEctorhinalCortex	152	R_PGp
13	R_Putamen	83	L_AuditoryComplex_5	153	L_7PC
14	R_Caudate	84	R_OrbitoFrontalCortex	154	L_MedialIntralParietal
15	Brain-Stem	85	R_PirformCortex	155	L_9p
16	L_V4	86	L_46	156	L_IFSa
17	R_V4	87	R_FrontalEyeFields	157	L_10v
18	L_PrimaryMotorCortex_4	88	L_Amygdala	158	L_i6-8
19	R_Pallidum	89	L_AnteriorIntraParietal	159	L_OP2-3
20	L_1	90	L_PHT	160	L_IntraParietal_1
21	R_PrimaryMotorCortex_4	91	R_V8	161	R_d32
22	L_Pallidum	92	R_TemporoParietoOccipitalJunction_1	162	R_IntraParietaR_2
23	L_PrimarySenroryCortex_3b	93	R_AuditoryComplex_4	163	L_V6
24	R_1	94	R_5m	164	L_LateralOccipital_2
25	L_2	95	R_8BM	165	L_PFt
26	R_2	96	R_9m	166	L_ProStriate
27	R_VentralDC	97	R_6r	167	L_FrontalOpercular_5
28	L_VentralDC	98	L_8Ad	168	R_SuperiorTemporalVisual
29	R_PrimarySenroryCortex_3b	99	L_47s	169	R_5m_ventral
30	L_3a	100	L_PF	170	R_44
31	L_TF	101	R_8Ad	171	R_VentroMedialVisuaR_3
32	L_6_dorsal	102	R_PGs	172	R_FrontalOpercular_5
33	R_6_dorsal	103	R_ParietoOccipitalSulcus_2	173	L_8BL
34	R_TG_dorsal	104	R_ParetoOccipitalSulcus_1	174	L_47l
35	L_TE2_posterior	105	R_8BL	175	L_PFcm
36	R_TE2_anterior	106	R_6ma	176	L_PreSubiculum
37	R_3a	107	L_11l	177	L_TemporoParietoOccipitalJun_2
38	L_TE2_anterior	108	L_ParaHippocampalArea_3	178	L_FST
39	R_TF	109	R_VentralVisualComplex	179	L_V3CD
40	L_6mp	110	R_p9-46v	180	R_V6
41	R_6mp	111	R_11l	181	R_LateralOccipitaR_2
42	L_TG_dorsal	112	R_OP4	182	R_24d_ventral
43	L_V3A	113	R_AnteriorIntraParietal	183	R_7PC
44	R_V3A	114	R_posteriorOFC	184	R_45
45	R_TE2_posterior	115	L_RertroSplenialCortex	185	R_43
46	L_PFm	116	L_ParetoOccipitalSulcus_1	186	R_PFt
47	L_PGi	117	L_TemporoParietoOccipitalJunction_1	187	R_ProStriate
48	L_TG_ventral	118	L_TE1_middle	188	R_ParaHippocampalArea_3
49	L_TE1_posterior	119	R_PHT	189	L_MedialSuperiorTemporal
50	R_Hippocampus	120	L_Accumbens	190	L_7m
51	L_6a	121	L_ParietoOccipitalSulcus_2	191	L_5m_ventral
52	L_Hippocampus	122	R_TemporoParietoOccipitalJunction_2	192	L_8BM
53	R_6a	123	L_PosteriorInferoTemporal	193	L_10d
54	L_OrbitoFrontalCortex	124	R_SupplementaryCingulateEyeField	194	L_OP4
55	R_8C	125	L_V8	195	L_ParaHippocampalArea_1
56	R_TG_ventral	126	R_VentroMedialVisuaR_1	196	L_STSv_posterior
57	R_Amygdala	127	R_Accumbens	197	L_IntraParietal_2
58	L_13l	128	R_RertroSplenialCortex	198	L_VentroMedialVisual_3
59	R_TE1_posterior	129	L_5m	199	R_SuperiorFrontalLanguage
60	L_8Av	130	R_PF	200	R_p32pr
61	R_FusiformFaceComplex	131	L_9m	201	R_IFSa
62	R_24d_dorsal	132	R_a47r	202	R_9a
63	R_8Av	133	L_a47r	203	R_i6-8
64	L_FrontalEyeFields	134	L_OP1	204	R_OP1
65	R_PGi	135	L_PirformCortex	205	R_STSd_posterior
66	L_24d_dorsal	136	R_10v	206	R_DorsalTransitionalVisualArea
67	L_8C	137	R_13l	207	L_5L
68	R_46	138	L_6ma	208	L_7_lateral_area
69	R_PFm	139	L_p9-46v	209	L_LateralIntraParietalVentral
70	L_FusiformFaceComplex	140	L_9a	210	L_6_ventral

211	L_a9-46v	268	L_PGp	325	R_AnteriorVentralInsularArea
212	L_FrontalOPercular_4	269	L_PF_opercular	326	R_AnteriorAngranInsulaComplex
213	L_EntorhinalCortex	270	L_V6A	327	R_EntorhinalCortex
214	L_TemporoParietoOccipitalJunc_3	271	L_31pd	328	R_PreSubiculum
215	L_p47r	272	L_InsularGranularComplex	329	R_ParaHippocampalArea_1
216	R_MedialIntralParietal	273	L_MedialBeltComplex	330	R_V4t
217	R_10r	274	L_LateralBeltComplex	331	R_31a
218	R_10d	275	R_MedialSuperiorTemporal	332	R_InsularGranularComplex
219	R_10pp	276	R_IntraParietalSulcus_1	333	R_MedialBeltComplex
220	R_FrontalOPercular_4	277	R_LateralOccipitaR_1	334	R_STSv_anterior
221	R_FrontalOPercular_2	278	R_PresylvianLanguage	335	L_7Pm
222	R_STSd_anterior	279	R_ventraR_23ab	336	L_23d
223	R_TemporoParietoOccipitalJun_3	280	R_23c	337	L_dorsal_23ab
224	R_p47r	281	R_5L	338	L_p24pr
225	L_d32	282	R_7_lateraR_area	339	L_33pr
226	L_44	283	R_7A_medial	340	L_a24pr
227	L_ParaBeltComplex	284	R_LateralIntraParietalVentral	341	L_a24
228	L_STSd_anterior	285	R_VentralIntraParietalComplex	342	L_p32
229	L_DorsalTransitionalVisualArea	286	R_IFSp	343	L_IFJp
230	L_p10p	287	R_a10p	344	L_IFSp
231	L_STSv_anterior	288	R_TA2	345	L_52
232	R_OP2-3	289	R_FrontalOPercular_3	346	L_TA2
233	R_PFcm	290	R_ParaBeltComplex	347	L_FrontalOPercular_1
234	R_IntraParietaR_1	291	R_V6A	348	L_FrontalOPercular_3
235	R_PF_opercular	292	R_V3CD	349	L_Hippocampus
236	R_FST	293	R_VentroMedialVisuaR_2	350	L_ParaHippocampalArea_2
237	R_LateralOccipitaR_3	294	R_p10p	351	L_V4t
238	R_25	295	L_PremotorEyeFields	352	L_VentroMedialVisual_2
239	R_a32pr	296	L_IntraParietalSulcus_1	353	L_31a
240	L_V7	297	L_MiddleTemporal	354	L_s32
241	L_V3B	298	L_ventral_23ab	355	L_PosteriorInsular_1
242	L_LateralOccipital_1	299	L_31p_ventral	356	L_ParaInsular
243	L_PrimaryAuditory_1	300	L_23c	357	R_p24
244	L_PresylvianLanguage	301	L_24d_ventral	358	R_PremotorEyeFields
245	L_SuperiorFrontalLanguage	302	L_7A_medial	359	R_PrimaryAuditory_1
246	L_SuperiorTemporalVisual	303	L_10r	360	R_23d
247	L_p32pr	304	L_IFJa	361	R_dorsaR_23ab
248	L_6r	305	L_10pp	362	R_31p_ventral
249	L_a10p	306	L_s6-8	363	R_p24pr
250	L_PoI2	307	L_43	364	R_a24pr
251	L_AnteriorVentralInsularArea	308	L_RetroInsularCortex	365	R_a24
252	L_IntraParietal_0	309	L_MiddleInsular	366	R_47l
253	L_25	310	L_FrontalOPercular_2	367	R_IFJp
254	L_a32pr	311	L_STGa	368	R_LateralIntralParietalDorsal
255	R_V7	312	L_LateralOccipital_3	369	R_52
256	R_7m	313	R_55b	370	R_Hippocampus
257	R_p32	314	R_V3B	371	R_STGa
258	R_47m	315	R_MiddleTemporal	372	R_STSv_posterior
259	R_s6-8	316	R_PrecuneusVisual	373	R_ParaHippocampalArea_2
260	R_FrontalOPercular_1	317	R_7Pm	374	R_31pd
261	R_IntraParietaR_0	318	R_7P_lateral	375	R_s32
262	L_PrecuneusVisual	319	R_33pr	376	R_PosteriorInsular_1
263	L_7P_lateral	320	R_IFJa	377	R_LateralBeltComplex
264	L_VentralIntraParietalComplex	321	R_a9-46v	378	R_ParaInsular
265	L_47m	322	R_RetroInsularCortex	379	R_p24
266	L_LateralIntralParietalDorsal	323	R_PoI2		
267	L_AnteriorAngranInsulaComplex	324	R_MiddleInsular		

Appendix 4. Full Gene Ontology (GO) terms for the "Upweighted" module (Chapter 6).

Term name	GO ID	adjusted p_value	negative_log10_of adjusted_p_value	Term size
protein targeting	GO:0006605	1.38E-07	6.85985	428
viral transcription	GO:0019083	5.06E-07	6.296222	178
nuclear-transcribed mRNA catabolic process, nonsense-mediated decay	GO:0000184	5.06E-07	6.296222	122
SRP-dependent cotranslational protein targeting to membrane	GO:0006614	5.06E-07	6.296222	96
establishment of protein localization to organelle	GO:0072594	6.61E-07	6.179858	565
cotranslational protein targeting to membrane	GO:0006613	6.61E-07	6.179858	101
establishment of protein localization to membrane	GO:0090150	1.07E-06	5.970062	330
viral gene expression	GO:0019080	1.47E-06	5.833037	195
protein targeting to ER	GO:0045047	1.47E-06	5.833037	109
protein localization to organelle	GO:0033365	2.17E-06	5.66305	949
establishment of protein localization to endoplasmic reticulum	GO:0072599	2.17E-06	5.66305	113
protein targeting to membrane	GO:0006612	6.21E-06	5.207214	195
protein localization to endoplasmic reticulum	GO:0070972	6.59E-06	5.180837	137
ribosome biogenesis	GO:0042254	8.58E-06	5.066436	294
mitochondrial respiratory chain complex assembly	GO:0033108	9.5E-06	5.022327	99
translational termination	GO:0006415	1.02E-05	4.989984	104
ribonucleoprotein complex biogenesis	GO:0022613	1.88E-05	4.72641	460
peptide biosynthetic process	GO:0043043	1.88E-05	4.72641	755
mitochondrial translational elongation	GO:0070125	2.68E-05	4.572601	87
translation	GO:0006412	3.49E-05	4.457061	730
mitochondrial respiratory chain complex I assembly	GO:0032981	3.49E-05	4.457061	65
NADH dehydrogenase complex assembly	GO:0010257	3.49E-05	4.457061	65
peptide metabolic process	GO:0006518	4.22E-05	4.374345	895
cellular amide metabolic process	GO:0043603	4.51E-05	4.345481	1163
nuclear-transcribed mRNA catabolic process	GO:0000956	4.87E-05	4.312476	211
ribosome assembly	GO:0042255	5.4E-05	4.267769	62
mitochondrial translation	GO:0032543	8.28E-05	4.082008	138
RNA catabolic process	GO:0006401	0.000104	3.983372	408

oxidative phosphorylation	GO:0006119	0.000122	3.914995	144
amide biosynthetic process	GO:0043604	0.000122	3.914995	897
mitochondrial translational termination	GO:0070126	0.000122	3.914995	88
protein localization to mitochondrion	GO:0070585	0.000126	3.898519	142
mitochondrial electron transport, NADH to ubiquinone	GO:0006120	0.000128	3.8918	56
mitochondrion organization	GO:0007005	0.000155	3.809926	530
mitochondrial ATP synthesis coupled electron transport	GO:0042775	0.000163	3.786642	98
protein targeting to mitochondrion	GO:0006626	0.00017	3.769199	101
ATP synthesis coupled electron transport	GO:0042773	0.00017	3.769199	99
translational elongation	GO:0006414	0.00017	3.769199	140
mRNA catabolic process	GO:0006402	0.000193	3.715352	371
cellular protein-containing complex assembly	GO:0034622	0.000208	3.682874	1103
ribosomal small subunit biogenesis	GO:0042274	0.000229	3.639515	68
rRNA processing	GO:0006364	0.000246	3.608656	209
cellular nitrogen compound catabolic process	GO:0044270	0.000327	3.485759	592
ATP metabolic process	GO:0046034	0.000329	3.48346	306
rRNA metabolic process	GO:0016072	0.000447	3.349394	220
ribosomal small subunit assembly	GO:0000028	0.000499	3.302053	18
translational initiation	GO:0006413	0.000506	3.295726	196
protein-containing complex subunit organization	GO:0043933	0.000526	3.279023	2177
aromatic compound catabolic process	GO:0019439	0.000526	3.279023	607
cellular macromolecule catabolic process	GO:0044265	0.000542	3.265806	1194
nucleobase-containing compound catabolic process	GO:0034655	0.000606	3.217439	544
heterocycle catabolic process	GO:0046700	0.000626	3.203438	591
mitochondrial gene expression	GO:0140053	0.000626	3.203438	166
respiratory electron transport chain	GO:0022904	0.000652	3.185973	118
cellular respiration	GO:0045333	0.000652	3.185973	191
intracellular transport	GO:0046907	0.000736	3.133379	1759
anaphase-promoting complex-dependent catabolic process	GO:0031145	0.000736	3.133379	83
protein localization to membrane	GO:0072657	0.000755	3.12194	636
electron transport chain	GO:0022900	0.000909	3.041209	188
establishment of protein localization to mitochondrion	GO:0072655	0.000985	3.0065	138
organic cyclic compound catabolic process	GO:1901361	0.001319	2.879838	638
intracellular protein transport	GO:0006886	0.002004	2.698026	1162

energy derivation by oxidation of organic compounds	GO:0015980	0.002576	2.589036	287
ribonucleoprotein complex assembly	GO:0022618	0.002853	2.544704	237
maturation of SSU-rRNA from tricistronic rRNA transcript (SSU-rRNA, 5.8S rRNA, LSU-rRNA)	GO:0000462	0.00322	2.492159	35
cellular protein localization	GO:0034613	0.003883	2.410818	1945
positive regulation of viral process	GO:0048524	0.003946	2.403849	104
cellular catabolic process	GO:0044248	0.003946	2.403849	2287
cellular macromolecule localization	GO:0070727	0.004551	2.341857	1956
macromolecule catabolic process	GO:0009057	0.004739	2.324337	1431
ribonucleoprotein complex subunit organization	GO:0071826	0.005585	2.252964	251
peptidyl-serine acetylation	GO:0030920	0.005585	2.252964	2
ribosomal large subunit biogenesis	GO:0042273	0.005585	2.252964	69
N-terminal peptidyl-serine acetylation	GO:0017198	0.005585	2.252964	2
ncRNA processing	GO:0034470	0.006042	2.218833	377
viral process	GO:0016032	0.006426	2.192043	832
protein insertion into mitochondrial inner membrane	GO:0045039	0.006426	2.192043	11
establishment of protein localization to mitochondrial membrane	GO:0090151	0.006674	2.175616	18
generation of precursor metabolites and energy	GO:0006091	0.007136	2.146548	543
transcription elongation from RNA polymerase II promoter	GO:0006368	0.007879	2.103545	84
mRNA metabolic process	GO:0016071	0.007882	2.103348	860
ncRNA metabolic process	GO:0034660	0.008121	2.090408	471
protein transport	GO:0015031	0.008176	2.087435	2084
establishment of protein localization	GO:0045184	0.008271	2.08244	2199
positive regulation of viral transcription	GO:0050434	0.008486	2.071288	41
protein-containing complex assembly	GO:0065003	0.008953	2.048034	1852
cellular protein complex disassembly	GO:0043624	0.010374	1.984061	218
catabolic process	GO:0009056	0.010374	1.984061	2665
protein import into mitochondrial matrix	GO:0030150	0.010823	1.965642	19
maturation of SSU-rRNA	GO:0030490	0.011299	1.946956	47
symbiotic process	GO:0044403	0.012268	1.911241	886
N-terminal peptidyl-glutamic acid acetylation	GO:0018002	0.013397	1.873002	3
mitochondrial transport	GO:0006839	0.013956	1.855227	263
peptide transport	GO:0015833	0.013956	1.855227	2124
amide transport	GO:0042886	0.015049	1.822499	2158
macroautophagy	GO:0016236	0.015676	1.804767	294

protein polyubiquitination	GO:0000209	0.015933	1.797714	313
organonitrogen compound biosynthetic process	GO:1901566	0.016832	1.773859	1884
regulation of viral transcription	GO:0046782	0.017821	1.749068	64
maturation of LSU-rRNA	GO:0000470	0.01934	1.71354	21
regulation of viral process	GO:0050792	0.020458	1.689135	208
interspecies interaction between organisms	GO:0044419	0.020674	1.684578	936
DNA-templated transcription, elongation	GO:0006354	0.023411	1.630574	112
regulation of symbiosis, encompassing mutualism through parasitism	GO:0043903	0.024673	1.607773	224
protein-containing complex disassembly	GO:0032984	0.025342	1.596155	330
nitrogen compound transport	GO:0071705	0.027333	1.563306	2466
positive regulation of synaptic vesicle endocytosis	GO:1900244	0.029382	1.531912	8
transcription-coupled nucleotide-excision repair	GO:0006283	0.029958	1.523485	73
regulation of protein targeting	GO:1903533	0.030219	1.51972	82
protein localization	GO:0008104	0.031504	1.501628	2863
establishment of localization in cell	GO:0051649	0.032464	1.488595	2271
negative regulation of centriole elongation	GO:1903723	0.032824	1.483807	1
pigment catabolic process	GO:0046149	0.034124	1.466935	7
tetrapyrrole catabolic process	GO:0033015	0.034124	1.466935	7
porphyrin-containing compound catabolic process	GO:0006787	0.034124	1.466935	7
heme catabolic process	GO:0042167	0.034124	1.466935	7
distal tubule morphogenesis	GO:0072156	0.036247	1.440724	3
renal sodium ion absorption	GO:0070294	0.047915	1.31953	4
regulation of transcription from RNA polymerase II promoter in response to hypoxia	GO:0061418	0.04929	1.307242	78

Appendix 5. Full Gene Ontology (GO) terms for the "Downweighted" module (Chapter 6).

Term name	GO ID	adjusted p_value	negative_log10_of adjusted_p_value	Term size
mRNA processing	GO:0006397	0.001374	2.862095	517
mRNA metabolic process	GO:0016071	0.004514	2.345424	860
RNA splicing	GO:0008380	0.004514	2.345424	439
histone H3-K9 methylation	GO:0051567	0.034524	1.461884	40
histone lysine methylation	GO:0034968	0.034524	1.461884	119
negative regulation of integrin-mediated signaling pathway	GO:2001045	0.034524	1.461884	2
mRNA splicing, via spliceosome	GO:0000398	0.034524	1.461884	348
monoubiquitinated protein deubiquitination	GO:0035520	0.034524	1.461884	10
RNA splicing, via transesterification reactions	GO:0000375	0.034524	1.461884	351
chromosome organization	GO:0051276	0.034524	1.461884	1238
RNA splicing, via transesterification reactions with bulged adenosine as nucleophile	GO:0000377	0.034524	1.461884	348
negative regulation of chromatin silencing at rDNA	GO:0061188	0.034524	1.461884	2
mRNA-containing ribonucleoprotein complex export from nucleus	GO:0071427	0.044654	1.350142	111
nuclear-transcribed mRNA catabolic process, endonucleolytic cleavage-dependent decay	GO:0000294	0.044654	1.350142	2
RNA processing	GO:0006396	0.044654	1.350142	929
mRNA export from nucleus	GO:0006406	0.044654	1.350142	111
peptidyl-lysine modification	GO:0018205	0.044654	1.350142	408
histone mRNA catabolic process	GO:0071044	0.044654	1.350142	12
regulation of chromatin silencing at rDNA	GO:0061187	0.045281	1.344089	3
peptidyl-lysine methylation	GO:0018022	0.047765	1.320892	135
regulation of gene expression, epigenetic	GO:0040029	0.047765	1.320892	555
ribonucleoprotein complex localization	GO:0071166	0.047765	1.320892	130
ribonucleoprotein complex export from nucleus	GO:0071426	0.047765	1.320892	129
histone H3-K9 modification	GO:0061647	0.047765	1.320892	51
mRNA processing	GO:0006397	0.001374	2.862095	517
mRNA metabolic process	GO:0016071	0.004514	2.345424	860
RNA splicing	GO:0008380	0.004514	2.345424	439
histone H3-K9 methylation	GO:0051567	0.034524	1.461884	40
histone lysine methylation	GO:0034968	0.034524	1.461884	119
negative regulation of integrin-mediated signaling pathway	GO:2001045	0.034524	1.461884	2
mRNA splicing, via spliceosome	GO:0000398	0.034524	1.461884	348
monoubiquitinated protein deubiquitination	GO:0035520	0.034524	1.461884	10

RNA splicing, via transesterification reactions	GO:0000375	0.034524	1.461884	351
chromosome organization	GO:0051276	0.034524	1.461884	1238
RNA splicing, via transesterification reactions with bulged adenosine as nucleophile	GO:0000377	0.034524	1.461884	348
negative regulation of chromatin silencing at rDNA	GO:0061188	0.034524	1.461884	2
mRNA-containing ribonucleoprotein complex export from nucleus	GO:0071427	0.044654	1.350142	111
nuclear-transcribed mRNA catabolic process, endonucleolytic cleavage-dependent decay	GO:0000294	0.044654	1.350142	2
RNA processing	GO:0006396	0.044654	1.350142	929
mRNA export from nucleus	GO:0006406	0.044654	1.350142	111
peptidyl-lysine modification	GO:0018205	0.044654	1.350142	408
histone mRNA catabolic process	GO:0071044	0.044654	1.350142	12
regulation of chromatin silencing at rDNA	GO:0061187	0.045281	1.344089	3
peptidyl-lysine methylation	GO:0018022	0.047765	1.320892	135
regulation of gene expression, epigenetic	GO:0040029	0.047765	1.320892	555
ribonucleoprotein complex localization	GO:0071166	0.047765	1.320892	130
ribonucleoprotein complex export from nucleus	GO:0071426	0.047765	1.320892	129
histone H3-K9 modification	GO:0061647	0.047765	1.320892	51